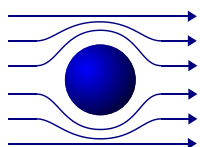


Annual Report  
Jahresbericht

2008



WALTHER-MEISSNER-INSTITUT  
für Tieftemperaturforschung  
Bayerische Akademie der Wissenschaften





**Contact:**

Prof. Dr. Rudolf Gross  
Walther-Meißner-Institut für Tieftemperaturforschung  
Bayerische Akademie der Wissenschaften  
and  
Lehrstuhl für Technische Physik – E23  
Technische Universität München

**Address:**

Walther-Meißner-Str. 8	Phone:	+49 – (0)89 289 14201
D - 85748 Garching	Fax:	+49 – (0)89 289 14206
GERMANY	e-mail:	Rudolf.Gross@wmi.badw.de
	WWW-address:	<a href="http://www.wmi.badw.de">http://www.wmi.badw.de</a>

**Secretary's Office and Administration:**

<b>Emel Dönertas</b>	Phone:	+49 – (0)89 289 14202
	Fax:	+49 – (0)89 289 14206
	e-mail:	Emel.Doenertas@wmi.badw.de Sekretariat@wmi.badw.de

<b>Ludwig Ossiander</b>	Phone:	+49 – (0)89 289 14205
	Fax:	+49 – (0)89 289 14206
	e-mail:	Ludwig.Ossiander@wmi.badw.de



## Preface

The Walther–Meißner–Institute for Low Temperature Research (WMI) of the Bavarian Academy for Sciences and Humanities (BAW) is looking back at a highly successful year 2008. On behalf of the members of WMI I am pleased to present our Annual Report 2008. The report is aiming to give an overview of the research and teaching activities of the WMI during the year 2008, as well as on recent developments in infrastructure and experimental facilities.

The WMI is participating in several long-term coordinated research programs jointly put into effect in collaboration with partners from both Munich universities and other research institutions in the greater Munich area. In some of these programs the WMI is playing a leading role and providing the spokesman of the program:

- The *Collaborative Research Center 631 (SFB 631)* of the German Science Foundation (DFG) on *Solid-State Quantum Information Processing: Physical Concepts and Materials Aspects* (spokesman: Rudolf Gross, WMI) was started in 2003 and has been extended for a second four-year funding period in 2007. Within 18 research projects subdivided into three research areas, research groups from WMI, the TU Munich (TUM), the Ludwig-Maximilians-University (LMU), the Max-Planck-Institute for Quantum Optics (MPQ), as well as the University of Regensburg and Augsburg are collaborating. In addition to the 35 principle investigators, more than 60 PhD and diploma students as well as a large number of postdocs and guests scientists are involved in the research activities. The SFB 631 (see <http://www.wmi.badw-muenchen.de/SFB631> and reports below) studies the physical concepts, materials aspects, and technological foundations of solid-state quantum information processing (SQIP). Besides the coordination of the collaborative research center, the WMI contributes to this prospering interdisciplinary research field by two projects on (i) the development of superconducting quantum circuits as basic elements for SQIP and (ii) the study of the key physics and technological problems of cavity quantum electrodynamics with superconducting devices.
- The *Research Unit FOR 538* of the German Science Foundation (DFG) on *High Temperature Superconductivity* (coordinator: Rudi Hackl, WMI) has been established in 2004 and extended by a further three-year funding period in 2007. Due to the successful research work (see <http://www.wmi.badw-muenchen.de/FG538> and reports below) the number of projects has been increased from 7 to 9 to further strengthen the research program. Besides the coordination of the Research Unit, the WMI is contributing to FOR 538 by two research projects on (i) Raman studies of competing ordering phenomena in cuprates and (ii) single crystal growth of *p*- and *n*-doped cuprate superconductors.
- The Cluster of Excellence *Nanosystems Initiative Munich – NIM* (coordinator: J. Feldmann, LMU) was started late in 2006. The WMI is deeply involved in several research areas of this coordinated program (see <http://www.nano-initiative-munich.de/> and reports below). In particular, the WMI contributes to research area A – Single Electron and Spin Systems (R. Gross, S.T.B. Gönnerwein), research area C – Quantum Information Nanosystems (R. Gross, A. Marx), and research area F – Nanoanalytics and Enabling Techniques (B.A. Hermann). Rudolf Gross of WMI is coordinator of research area A.
- The WMI also successfully continued the research project on *New Functional Thin Film Systems Based on Artificial Heterostructures of Transition Metal Oxides* (R. Gross, S.B.T. Gönnerwein, M. Opel) within the DFG Priority Programme 1157 on *Integrated Electro-ceramic Functional Systems*. This research project, which is carried out in close collaboration with the group of Prof. Mader at the University of Bonn, entered the third two-year

funding period.

- The new project on *Spin Injection, Spin Transport and Controllable Ferromagnetism in Transition Metal Doped ZnO* within the DFG Priority Programme 1285 on *Semiconductor Spin Electronics* (R. Gross, S.B.T. Gönnerwein, M. Opel) has been started in 2007. The project already provided several important scientific results and technological developments.

Besides our successful work in the *Collaborative Research Center 631*, the *Research Unit FOR 538*, the *Cluster of Excellence NIM*, and the DFG Priority Programs, various other research projects of WMI have been successfully continued in 2008 and, moreover, promising new projects could be started. The DFG project on *Local Magnetotransport Properties of Thin Ferromagnetic Layers and Heterostructures* (S.T.B. Gönnerwein) has been started in 2007 and is carried out in close collaboration with Tübingen University. Very recently, a new EU project has been started, which is part of the *Marie Curie Network for Initial Training (ITN)* on *Cavity-confined Luminophores for Advanced Photonic Materials* (R. Hackl). The high level of scientific productivity of WMI within the past year strongly profited from the collaborative atmosphere, the commitment and high motivation of its research and technical staff as well as the support of various funding agencies. We gratefully acknowledge financial support from the BAdW, the DFG, the Bavarian Ministry for Science and Arts, the BMBF and the EU.

Our successful research work in 2008 is substantiated by a large number of scientific papers in high quality journals, invited presentations at national and international conferences as well as seminar talks and colloquia. The staff of WMI was again slightly growing in 2008, although the limited lab and office space forces a saturation of growth rate. Throughout 2008, an average of 14 scientific staff members, 20 members of the administrative and technical staff, 22 doctorate candidates, more than 20 diploma/master students as well as a large number of short and long-term guests belonged to the institute. Happily, in 2008 again several acknowledgements and awards have been achieved by members of the WMI: Sebastian Gönnerwein received the Arnold Sommerfeld Award of the Bavarian Academy of Sciences and Humanities, Dietrich Einzel received the Venia Legendi in Theoretical Physics from the TU München, and, moreover, Matthias Althammer and Matthias Opel received a best poster and best presentation award, respectively, at the Joint European Magnetism Conference held from September 14 – 19, 2008 at Dublin, Ireland. Several members of WMI also have been elected members in boards and committees: Werner Biberacher has been appointed member of the Selection Panel EuroMagNet II of the Joint European High Magnetic Field Laboratories, Rudolf Gross has been appointed member of the Scientific Advisory Board of the Leibniz Institute for Solid-State and Materials Research Dresden and of the Kuratorium of the Physik Journal of the German Physical Society. He also has been appointed spokesman of the section *Low Temperature Physics* of the Condensed Matter Division of the German Physical Society.

The year 2008 not only brought very good progress in our research projects, but also several improvements of the technological infrastructure of the WMI. Despite the tight financial situation several new experimental facilities could be developed and set up during the last year. For example, new setups for measuring the ferromagnetic resonance (FMR) and the magneto-optical Kerr effect (MOKE) have been completed and our Laser-MBE system for complex transition metal oxides has been extended by an atomic oxygen/nitrogen source and an infrared laser heating system. Furthermore, one of our mK-systems has been modified to allow for the detection of weak quantum signals in the GHz regime on a single photon level. Finally, a new glove box has been added to the crystal growth lab of WMI to allow for the fabrication of the new

FeAs superconductors.

The Annual Report 2008 is aiming to provide a general overview of the scientific results of WMI to our friends and partners in research and industry. In order to be useful also for our numerous international partners the report is written in English. I finally would like to thank all the colleagues, guests, students, post-docs and cooperating partners, who contributed to the success of our research and teaching activities within the last year, and last but not least all our friends and sponsors for their interest, trust and continuous support.



Rudolf Gross

Garching, December 2008



The majority of the WMI group members

2008



# Contents

Preface . . . . .	1
The Walther–Meißner–Institute . . . . .	7
<b>Reports:</b>	<b>11</b>
<b>Joint Research Projects</b>	<b>11</b>
The Collaborative Research Center 631 . . . . .	11
The Nanosystems Initiative Munich – NIM . . . . .	13
<b>Basic Research</b>	<b>15</b>
Controlled Symmetry Breaking in Circuit Quantum Electrodynamics . . . . .	15
Two-Resonator Circuit QED: a Superconducting Quantum Switch . . . . .	18
Measuring the Zero-point Fluctuations of the Microwave Radiation . . . . .	21
Cross-Correlation Measurements of Weak Microwave Signals . . . . .	24
Electronic Raman Scattering in Non-centrosymmetric Superconductors . . . . .	27
Two-channel Conductivity in a Highly Anisotropic Layered Organic Metal . . . . .	31
A New Bifunctional Organic Superconductor $\kappa$ -(BETS) <sub>2</sub> Mn[N(CN) <sub>2</sub> ] <sub>3</sub> . . . . .	35
Quantitative Comparison of ARPES and Raman Spectra in the Cuprates . . . . .	39
Resonances in Superconductor/Insulator/Ferromagnet/Superconductor Josephson Junctions . . . . .	43
Universal Scaling between Hall and Longitudinal Conductivity in Fe <sub>3</sub> O <sub>4</sub> . . . . .	46
Magnetization and Specific Heat Measurements on YbRh <sub>2</sub> Si <sub>2</sub> . . . . .	49
Correlated Systems Investigated with Scanning Tunneling Microscopy . . . . .	51
<b>Application Oriented Research</b>	<b>57</b>
Fabrication and Characterization of Superconducting Flux Qubits . . . . .	57
Quantum Experiments on Electromechanical Systems . . . . .	61
Voltage Controlled Inversion of the Magnetic Anisotropy in a Ferromagnetic Thin Film at Room Temperature . . . . .	64
Epitaxial Zn <sub>x</sub> Fe <sub>3-x</sub> O <sub>4</sub> Thin Films: A Spintronic Material with Tunable Electrical and Magnetic Properties . . . . .	68

<b>Materials, Thin Film and Nanotechnology, Experimental Techniques</b>	<b>73</b>
Impact of Cryogen-free Revolution . . . . .	73
A Ferromagnetic Resonance Setup for the X- and the K-band . . . . .	76
Extension and Improvement of the Existing Laser-MBE System . . . . .	79
Redox Reactions, Layer Charges and Tschermak Substitution in Vermiculites from Spain	80
<b>Experimental Facilities</b>	<b>83</b>
<b>Publications</b>	<b>101</b>
<b>Theses, Appointments, Honors and Awards, Membership in Advisory Boards, etc.</b>	<b>105</b>
<b>Research Projects and Cooperations</b>	<b>111</b>
<b>Invited Conference Talks and Seminar Lectures</b>	<b>119</b>
<b>Seminars, Courses, Lectures and other Scientific Activities</b>	<b>125</b>
<b>Staff of the Walther-Meißner-Institute</b>	<b>133</b>
<b>Guest Researchers</b>	<b>135</b>
<b>Commission for Low Temperature Physics</b>	<b>137</b>

## The Walther–Meißner–Institute

### General Information

The Walther–Meißner–Institute for Low Temperature Research (WMI) is operated by the Commission for Low Temperature Research of the Bavarian Academy of Sciences and Humanities (BAdW). The commission was founded in 1946 on Walther Meißner's initiative, who was president of BAdW from 1946 to 1950. The Commissions (Research Groups) of the Academy are set up in order to carry out long-term projects, which are too ambitious for the lifetime or capacity of any single researcher, or which require the collaboration of specialists in various disciplines. At present, the Bavarian Academy of Sciences and Humanities consists of 36 Commissions with more than 300 employees.

The Commission for Low Temperature Research of the BAdW started its research activities in 1946 in the Herrsching barracks. After the retirement of Walther Meißner in 1952, Heinz Maier-Leibnitz, who followed Walther Meißner on the Chair for Technical Physics of the Technische Universität München, became the new head of the Commission for Low Temperature Research. In 1967, the commission moved to the Garching research campus after the construction of the new "Zentralinstitut für Tieftemperaturforschung" (ZTTF) was completed (director: Prof. Heinz Maier-Leibnitz, technical director: Prof. Franz Xaver Eder). Until 1972, the theory group of the Institute Laue Langevin was hosted at the ZTTF. In 1980, Prof. Dr. Klaus Andres became the new director of the ZTTF again associated with the Chair for Technical Physics (E23) at the Technische Universität München, followed by Prof. Dr. Rudolf Gross in 2000. In 1982, the ZTTF was renamed into Walther-Meißner-Institute for Low Temperature Research (WMI) on the occasion of Walther Meißner's 100. birthday.

As already mentioned, it is a long tradition that the WMI also hosts the Chair for Technical Physics (E 23) of the Technische Universität München (TUM) with the director of the WMI being full professor at the Faculty of Physics of TUM. In addition, since 2004 the WMI also hosts a new scanning probe division with the head of this division being professor at the Ludwig-Maximilians-Universität (LMU). In this way a tight collaboration has been established between WMI and research groups of both Munich universities, joining technological and human resources in the fields of experimental and theoretical solid-state and condensed matter physics, low temperature techniques, materials science as well as thin film and nanotechnology. Noteworthy, the WMI supplies liquid helium to more than 25 research groups at both Munich universities and provides the technological basis for low temperature research.

### Research Activities

The research activities of the Walther–Meißner–Institute are focused on low temperature solid-state and condensed matter physics (see reports below). The research program is devoted to both **fundamental** and **applied research** and also addresses **materials science, thin film and nanotechnology** aspects. With respect to **basic research** the main focus of the WMI is on

- superconductivity and superfluidity,
- magnetism and spin transport,
- quantum phenomena in mesoscopic systems and nanostructures,
- self-organization of molecules on surfaces,
- and the general properties of metallic systems at low and very low temperatures.

The WMI also conducts **applied research** in the fields of

- solid-state quantum information processing systems,
- superconducting and spintronic devices,
- oxide electronics,
- multi-functional and multiferroic materials,
- and the development of low and ultra low temperature systems and techniques.

With respect to **materials science, thin film and nanotechnology** the research program is focused on

- the synthesis of superconducting and magnetic materials,
- the single crystal growth of oxide materials,
- the thin film technology of complex oxide heterostructures including multi-functional and multiferroic material systems,
- the fabrication of superconducting, magnetic, and hybrid nanostructures,
- and the growth of self-organized molecular ad-layers.

The WMI also develops and operates systems and techniques for low and ultra-low temperature experiments. A successful development have been dry mK-systems that can be operated without liquid helium by using a pulse-tube refrigerator for precooling. Meanwhile, these systems have been successfully commercialized by the company VeriCold Technologies GmbH at Ismaning, Germany, which was taken over by Oxford Instruments in 2007. As further typical examples we mention a nuclear demagnetization cryostat for temperature down to below 100  $\mu\text{K}$ , or very flexible dilution refrigerator inserts for temperatures down to about 20 mK fitting into a 2 inch bore. These systems have been engineered and fabricated at the WMI. Within the last years, several dilution refrigerators have been provided to other research groups for various low temperature experiments. The WMI also operates a helium liquifier with a capacity of more than 150.000 liters per year and supplies both Munich universities with liquid helium. To optimize the transfer of liquid helium into transport containers the WMI has developed a pumping system for liquid helium that is commercialized in collaboration with a company.

To a large extent the research activities of WMI are integrated into national and international research projects such as Clusters of Excellence, Collaborative Research Centers, Research Units, or EU projects. The individual research groups of WMI offer a wide range of attractive research opportunities for diploma (graduate) students, PhD students and postdoctoral fellows.

## **Experimental Facilities and Resources**

The WMI is equipped with state of the art facilities for the preparation and characterization of superconducting and magnetic materials as well as for various low and ultra-low temperature experiments. The main experimental and technological resources of WMI are listed in the following.

### **Materials Preparation and Fabrication of Nanostructures**

- Laser Molecular Beam Epitaxy (L-MBE) system for oxide heterostructures (equipped with in-situ RHEED, Omicron AFM/STM system, atomic oxygen/nitrogen source, infrared-laser heating system, metallization)

- molecular beam epitaxy (MBE) system for metallic systems
- UHV magnetron sputtering systems for metals (e.g. Nb, Al, NiPd, ... )
- magnetron sputtering system for oxide heteroepitaxy (equipped with four sputtering guns and an oxygen ion gun)
- ion beam sputtering system
- reactive ion etching (RIE) system, Plasmalab 80 Plus with ICP plasma source, Oxford Instruments Plasma Technology
- ion beam etching (IBE) system equipped with a LN<sub>2</sub> cooled sample holder
- polishing machine for substrate preparation
- ultrasonic bonding machine
- 50 m<sup>2</sup> class 1000 clean room facility
- optical lithography (Süss maskaligner MJB 3 and projection lithography)
- electron beam lithography (based on Philips XL 30 SFEG scanning electron microscope and Raith Elphy Plus lithography system including a laser stage)
- four-mirror image furnace for crystal growth

### Characterization

- 2-circle x-ray diffractometer (Bruker D8 Advance, sample temperature up to 1 600°C)
- high resolution 4-circle x-ray diffractometer with Göbel mirror and Ge monochromator (Bruker D8 Discover)
- scanning electron microscope with EDX analysis
- UHV room temperature AFM/STM system
- 2048 u high resolution mass spectrometer (Fa. Pfeiffer, cross beam ion source, SEM)
- Low Energy Electron Diffraction (SPECTA-LEED, Fa. Omicron)
- two Raman spectroscopy systems (1.5 to 300 K, in-situ sample preparation)
- SQUID magnetometer (Quantum Design, 1.5 to 700 K, up to 7 Tesla)
- several high field magnet systems (up to 17 Tesla) with variable temperature inserts
- 7 Tesla split coil magnet systems with optical access and variable temperature insert
- experimental set-ups for the measurement of noise including low noise SQUID amplifiers and signal analyzers
- high-frequency network analyzers (up to 40 GHz) and various microwave components (sources, mixers, circulators, attenuators) for the determination of high frequency parameters
- high-frequency cryogenic probing station (up to 20 GHz,  $T > 4$  K)
- magneto-optical Kerr effect (MOKE) system
- ferromagnetic resonance (FMR) system

### Low temperature systems and techniques

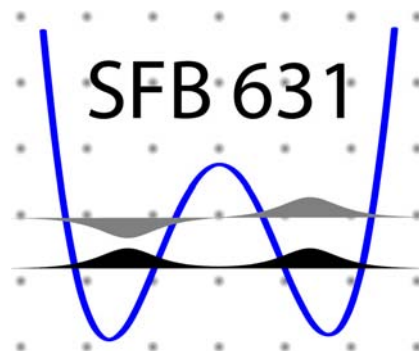
- 5 K-Scanning Tunneling Microscope (low temperature STM, Fa. Omicron)
- several <sup>3</sup>He/<sup>4</sup>He dilution refrigerator inserts for temperatures down to 10 mK

- “dry” mK-cooler based on a dilution refrigerator with pulse-tube precooling
- ultra-low temperature facility for temperatures down to below 100  $\mu$ K based on a nuclear demagnetization cryostat
- experimental set-ups for the measurement of specific heat, magnetization, thermal expansion as well as electrical and thermal transport properties as a function of temperature, magnetic field and pressure

## The Collaborative Research Center 631

Rudolf Gross, Achim Marx<sup>1</sup>

The Collaborative Research Center 631 (SFB 631) on *Solid State Based Quantum Information Processing: Physical Concepts and Materials Aspects* is one of the key research programs of the Walther–Meißner–Institute (WMI). It has been established in 2003 and a second four-year funding period has been granted by the German Science Foundation (DFG) in 2007. Within SFB 631, in 18 research projects subdivided into three research areas, research groups from the Bavarian Academy of Sciences and Humanities (BAW), the TU Munich (TUM), the Ludwig-Maximilians-University (LMU), the Max-Planck-Institute for Quantum Optics (MPQ), as well as the University of Regensburg and the University of Augsburg are collaborating. It joins 35 principle investigators, more than 60 PhD and diploma students as well as a large number of postdocs and guest scientists. The WMI is one of the main actors within SFB 631, providing the coordination of the collaborative research center (spokesman: Rudolf Gross) from the beginning. The WMI is also carrying out Project A3 on *Superconducting Quantum Circuits as Basic Elements for Quantum Information Processing* and Project A8 on *Cavity Quantum Electrodynamics with Superconducting Devices*.



The research program of WMI within SFB 631 is focussing on the fabrication and study of superconducting quantum information circuits. This includes the fabrication of superconducting flux qubits. In these ring-shaped devices quantum mechanical superposition states of clockwise and anticlockwise circulating persistent currents are used for the realization of solid state qubits. These qubits are coupled to superconducting microwave resonators. In this way fascinating quantum electrodynamic experiments with deliberately designed artificial solid state systems become possible. Since such experiments are completely analogous to quantum optical experiments on natural atoms in optical resonators, this prospering new field is called circuit quantum electrodynamics (cQED). Here, particular goals are the coupling of superconducting qubits to high-quality superconducting resonators, the generation and detection of non-classical microwave Fock states, the development of dispersive readout and quantum non-demolition measurements, and the entanglement of superconducting qubits via multiple resonators. In the field of superconducting quantum circuits the WMI team has close collaborations with the theory groups at LMU (Marquardt, Solano, von Delft), the University of Augsburg (Hänggi, Kohler) and the Canadian Institute for Quantum Computing at Waterloo (Wilhelm), as well as the experimental group at the NTT Basic Research Laboratories (Semba, Takayanagi). The research work within SFB 631 is closely linked to the activities within Research Area C of the Cluster of Excellence *Nanosystems Initiative Munich (NIM)*.

Within the past year, the WMI team made good progress in the fabrication and characterization of superconducting quantum circuits. The WMI team succeeded in the reproducible fabrication of superconducting flux qubits with a qubit splitting ranging between 2 and 5 GHz [1]. Furthermore, the electromagnetic environment of the quantum circuits was improved by implementing on-chip shunting capacitors, high-resistance bias lines and an on-chip microwave antenna. The phase coherent dynamics of flux qubits has been studied in collaboration with the

<sup>1</sup>This work is supported by the Deutsche Forschungsgemeinschaft through SFB 631.

qubit group at the NTT Basic Research Laboratories [2, 3]. In an internationally well recognized experiment we used two-photon qubit spectroscopy to study the interaction of a superconducting flux qubit with an  $LC$ -resonator. We provided experimental evidence for the presence of an anticrossing under two-photon driving, permitting us to estimate the vacuum Rabi coupling. Our experiments and theoretical analysis shed new light on the fundamental symmetry properties of quantum circuits and the nonlinear dynamics inherent to cQED. We showed that this can be exploited in a wide range of applications such as parametric up-conversion, generation of microwave single photons on demand or squeezing [4]. We also designed a superconducting quantum switch based on two-resonator cQED, permitting to switch on and off the interaction between the two resonators via a qubit population inversion or by shifting the qubit operation point [5]. Moreover, superconducting  $\pi$ -Josephson junctions with ferromagnetic interlayers have been successfully fabricated and characterized (see report by G. Wild *et al.* on *Resonances in Superconductor/Insulator/Ferromagnet/Superconductor Josephson Junctions*. Finally, the experimental techniques for measuring weak quantum systems in the GHz-regime on a single photon level at mK temperatures have been established. These techniques have been successfully applied to the measurement of zero-point fluctuations of the microwave radiation emitted by a cold  $50\ \Omega$  resistor or to perform cross-correlation measurements of weak microwave signals (see reports by M. Mariani *et al.* and E. Menzel *et al.*).

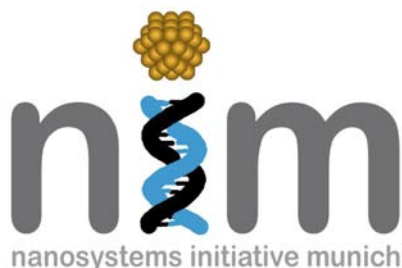
## References

- [1] T. Niemczyk, F. Deppe, M. Mariani, E.P. Menzel, E. Hoffmann, G. Wild, L. Eggenstein, A. Marx, and R. Gross, **Fabrication Technology of and Symmetry Breaking in Superconducting Quantum Circuits**, Superconductor Science and Technology, submitted for publication (2008).
- [2] F. Deppe, M. Mariani, E.P. Menzel, S. Saito, K. Kakuyanagi, H. Tanaka, T. Meno, K. Semba, H. Takayanagi, R. Gross, **Phase coherent dynamics of a superconducting flux qubit with capacitive bias readout** Phys. Rev. B **76**, 214503 (2008).
- [3] K. Kakuyanagi, T. Meno, S. Saito, H. Nakano, K. Semba, H. Takayanagi, F. Deppe, and A. Shnirman, Phys. Rev. Lett. **98**, 047004 (2007).
- [4] F. Deppe, M. Mariani, E. P. Menzel, A. Marx, S. Saito, K. Kakuyanagi, T. Meno, K. Semba, H. Takayanagi, E. Solano, and R. Gross, **Two-photon probe of the Jaynes-Cummings model and controlled symmetry breaking in circuit QED**, Nature Physics **4**, 686 (2008).
- [5] M. Mariani, F. Deppe, A. Marx, R. Gross, F.K. Wilhelm, E. Solano, **Two-resonator circuit quantum electrodynamics: A superconducting quantum switch** Phys. Rev. B **78**, 104508 (2008).

## The Nanosystems Initiative Munich – NIM

Rudolf Gross<sup>1</sup>

The Walther–Meißner–Institute (WMI) is participating in the Cluster of Excellence *Nanosystems Initiative Munich (NIM)* and is contributing to its research program by several activities. A key activity addresses the fabrication, control/manipulation of magnetization direction, and spin transport in spin-nanosystems. Furthermore, the study of solid-state based quantum information systems and the development of novel nanoanalytical techniques are in the focus of our NIM projects. Within the past year, a new activity directed towards the development of electro-mechanical nanosystems has been started in collaboration with the group of Tobias Kippenberg from Max-Planck-Institute for Quantum Optics (see report of Hocke *et al.*: *Quantum Experiments on Electromechanical Systems*).



NIM is one of the Clusters of Excellence which have been established in 2006 by the German government's *Excellence Initiative*. Within NIM, scientists from various research facilities in the greater Munich area in the fields of physics, biophysics, physical chemistry, biochemistry, pharmaceuticals, biology, electronics and medicine are collaborating. The overriding goal is to design, produce and control a series of artificial and multi-functional nanosystems. The cluster is coordinated by J. Feldmann

(CeNS, LMU Munich) and G. Abstreiter (WSI, TU Munich). It joins research groups from LMU Munich, TU Munich (TUM), WMI, the University of Augsburg, the Munich University of Applied Science, the Max-Planck-Institutes for Biochemistry and Quantum Optics, and the Deutsches Museum. NIM is aiming to realize and study nanosystems interfacing the worlds of information and communication systems on the one hand and life sciences and medical nanotechnology on the other hand. Nanosystems are already playing a major role in information and communication systems: the electronic components in computers and communication technology are becoming smaller and smaller. However, this development cannot go on forever, once the nanometer scale has been reached. At that level, novel physical phenomena often arise that may present potential problems for conventional uses – and an opportunity for innovations and new applications. Micro- and nanosystems are also becoming increasingly important in the life sciences and medicine. They can be introduced to living organisms, for instance to bring a cancer medication to tumor cells. “Programmed drug delivery” is therefore one of the ten research areas within NIM. Other research areas focus on quantum phenomena in nanosystems, connecting nanosensors to living cells and “lab on a chip” applications.

The 10 research areas of NIM are: (A) Single electron and spin nanosystems, (B) Nanophotonic systems, (C) Quantum information nanosystems, (D) Nanotransducers, (E) Functional nano-networks, (F) Nanoanalytics and enabling techniques, (G) Nanostructured surfaces and cellsubstrate interaction, (H) Single molecule biophysics, (I) Nanoagents and advanced cell imaging, (J) Programmed drug delivery. The WMI actively participates in the research program of NIM in the research areas A: *Single Electron and Spin Nanosystems* (R. Gross, S.T.B. Gönnenwein), C: *Quantum Information Nanosystems* (R. Gross, A. Marx), and F: *Nanoanalytics and Enabling Techniques* (B.A. Hermann).

In *Research Area A* (coordinated by Rudolf Gross, WMI), our research activities are focusing on the fabrication and characterization of spin-nanosystems, as well as on complex hybrid

<sup>1</sup>This work is supported by the German Excellence Initiative via the Nanosystems Initiative Munich (NIM).

nanosystems composed of normal metals (N) and correlated electron materials (e.g. superconductors (S), ferro- (F) and antiferromagnets (AF)). Regarding the former, the key goal is the control and manipulation of magnetization as well as the study of spin transport in magnetic nanosystems. To this end, considerable progress has been achieved within the last year. With respect to the latter, the main goal is the study of quantum phenomena in nanosystems with correlated electrons and spins.

In *Research Area C*, the experimental group at WMI and the theory groups at LMU (Solano, Marquardt, von Delft) and MPQ (Cirac, Giedke) are aiming at the study of superconducting qubits coupled to microwave resonators. This new and very promising field of solid-state quantum information processing is denoted as circuit quantum electrodynamics (circuit-QED) and is analogue to cavity quantum electrodynamics in atom optics. Particular goals are the use superconducting circuit-QED systems for the realization of dispersive quantum non-demolition measurements on superconducting flux qubits, the implementation of a deterministic source of microwave single photons at the output of a superconducting resonator containing a single flux qubit, or the detection of single photons using microwave quantum homodyning. In the long run the goal is to establish the basic building blocks for on-chip quantum information transfer between superconducting qubits. Within the last year, considerable progress in this direction has been achieved. Examples are the controlled symmetry breaking in circuit-QED systems consisting of a flux qubit coupled to a harmonic oscillator or the design of a superconducting quantum switch based on two-resonator circuit QED. Moreover, experimental techniques have been successfully established to measure weak quantum systems in the GHz regime on a single photon level at mK temperatures. These techniques have been applied for measuring the zero-point fluctuations of the microwave radiation or to perform cross-correlation measurements of weak microwave signals.

Over the last few years opto-mechanical systems have become a topic of considerable interest. In such systems nano-mechanical harmonic oscillators are coupled to the electromagnetic field inside a suitable cavity. At sufficiently strong coupling, such systems may allow to explore various quantum effects such as superposition and entanglement, or the generation of cat states at a macroscopic scale. Furthermore, they may allow to perform ultra-sensitive measurements on macroscopic objects or to combine opto-mechanical systems in the microwave regime with nonlinear circuit elements such as Josephson junctions or qubits. In a collaboration between the NIM research areas A, C, and D we have fabricated electro-mechanical nanosystems consisting of a superconducting nanobeam coupled to a high quality factor superconducting microwave resonator. First experiments will aim at the cooling to the quantum mechanical ground state of the vibrational mode.

In *Research Area F*, the research focus is on the development of novel nanoanalytical techniques based on functionalized cantilever arrays that act as extremely sensitive and specific receptors for (bio)chemical substances.

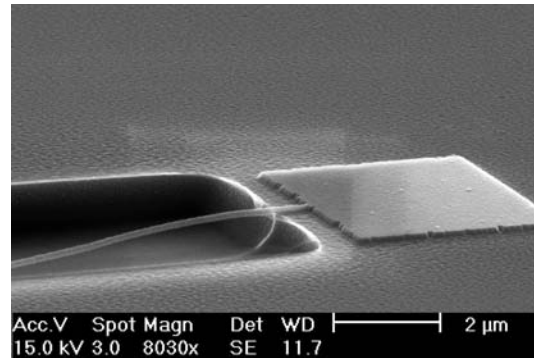


**Figure 1:** Scanning electron microscopy micrograph of first tests to suspend a superconducting Al nanomechanical resonators on a Si wafer using a reactive ion etching. The width of the nanobeam is about 200 nm.

## Controlled Symmetry Breaking in Circuit Quantum Electrodynamics

*F. Deppe, M. Mariani, E. P. Menzel, A. Marx, R. Gross*<sup>1</sup>

*S. Saito, K. Kakuyanagi, H. Tanaka, K. Semba*<sup>2</sup>

*T. Meno*<sup>3</sup>, *H. Takayanagi*<sup>4</sup>, *E. Solano*<sup>5</sup>

Superconducting qubits [1] are micrometer-sized electrical circuits, which behave as artificial two-level atoms. In addition to their possible application in quantum information processing, they are used to investigate fundamental quantum phenomena on a macroscopic scale. Regarding the latter, the study of multi-photon excitations [2–6] occupies a central role. Moreover, coupling superconducting qubits to on-chip microwave resonators has given rise to the field of circuit quantum electrodynamics (QED) [7–9]. In contrast to quantum-optical cavity QED, circuit QED offers the tunability inherent to solid-state circuits. In this work, we report on the observation of key signatures of a two-photon driven Jaynes-Cummings model in a superconducting flux qubit [10] coupled to an on-chip resonator. We show that the dispersive interaction between the qubit and the two-photon driving enables real level transitions. The nature of our experiment can be understood as an upconversion mechanism, which transforms the two-photon coherent driving into single photons of the Jaynes-Cummings dynamics. This process requires energy conservation and a not well-defined parity [11] of the interaction Hamiltonian due to the symmetry breaking of the qubit potential. Our experiment and theoretical analysis show clear evidence for the coexistence of one- and two-photon driven level anticrossings of the qubit-resonator system. In this way, we demonstrate that such symmetry breaking can be obtained in a controlled way by choosing a suitable qubit operation point. Our study provides deep insight into the interplay of multiphoton processes and symmetries in a qubit-resonator system. These results are published in Ref. [12], where also a detailed description of the setup can be found.

We extract the parameters of our quantum system from pulsed qubit microwave spectroscopy [12–14], the driving frequency is  $\omega/2\pi$ . The results are shown in Fig. 1a and Fig. 1b. Within the parameter range relevant for our experiments, the flux qubit can be modeled as a two-level system. Its energy level splitting  $\hbar\omega_q = \sqrt{\epsilon(\Phi_x)^2 + \Delta^2}$  is tunable by means of an external flux bias  $\Phi_x$  corresponding to an energy bias  $\epsilon(\Phi_x)$ . We find a qubit gap  $\Delta/h = 3.89$  GHz. The qubit is coupled to a lumped-element LC-circuit acting as a quantum harmonic oscillator with resonance frequency  $\omega_r/2\pi = 6.16$  GHz. Due to its low quality factor  $Q \simeq 100$ , its decay is the dominant channel of decoherence in the system. We observe qubit-resonator anticrossings under one-photon ( $\omega = \omega_q = \omega_r$ ) and two-photon ( $2\omega = \omega_q = \omega_r$ ) driving. Inspecting Fig. 1b, the two-photon anticrossing ( $2\omega = \omega_q = \omega_r$ ) reveals a qubit-resonator coupling constant  $g/2\pi = 115$  MHz. This value represents the vacuum coupling strength because the resonator cannot absorb a two-photon driving directly. In contrast, for the one-photon anticrossing the effective coupling strength is enhanced by a driving-induced steady-state population of  $\langle \hat{N} \rangle \simeq 10$  photons in the resonator (see Fig. 1a).

The second-order effective Hamiltonian under two-photon driving can be derived using a

<sup>1</sup>This work is supported by the Deutsche Forschungsgemeinschaft through SFB 631 and the German Excellence Initiative via the Nanosystems Initiative Munich (NIM).

<sup>2</sup>NTT Basic Research Laboratories, NTT Corporation, Kanagawa, 243-0198, Japan. Supported by CREST-JST, JSPS-KAKENHI(18201018) and MEXT-KAKENHI(18001002).

<sup>3</sup>NTT Advanced Technology, NTT Corporation, Kanagawa, 243-0198, Japan

<sup>4</sup>Tokyo University of Science, 1-3 Kagurazaka, Shinjuku, Tokyo, 162-8601, Japan. International Center for Materials Nanoarchitectronics, NIMS, Tsukuba 305-0003, Japan.

<sup>5</sup>Departamento de Química-Física, Universidad del País Vasco - Euskal Herriko Unibertsitatea, Apdo. 644, 48080 Bilbao, Spain. Supported by the EuroSQIP EU project, the Ikerbasque Foundation and UPV-EHU Grant GIU07/40.

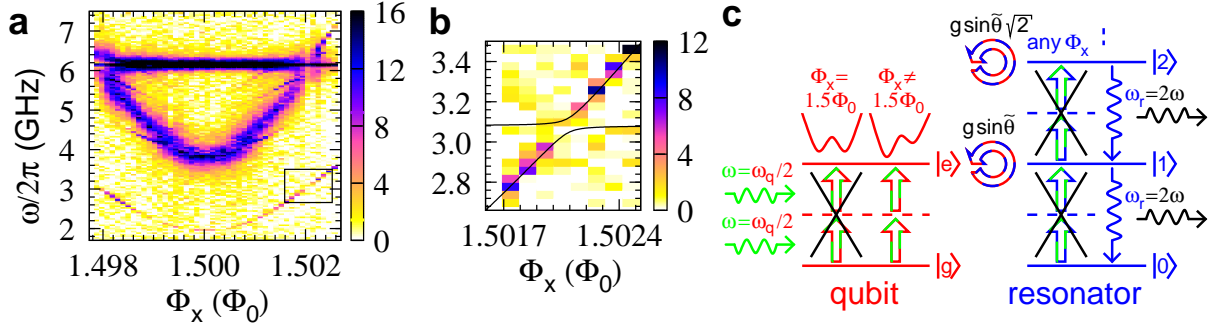


**Figure 1:** Qubit microwave spectroscopy results and two-photon upconversion dynamics. (a), Probability to find the qubit in the excited state (color code) plotted as a function of the excitation frequency  $\omega/2\pi$  and the external flux  $\Phi_x$  near the qubit optimal point. The black box marks the close-up shown in b. (b), Close-up of a. (c), Schematic representation of the upconversion dynamics described by Eq. (1), which depends on the symmetry properties of the qubit potential.  $|g\rangle$  and  $|e\rangle$  are the qubit ground and excited state, respectively. The resonator number states are  $|0\rangle, |1\rangle, |2\rangle, \dots$

Dyson-series approach [12]. An alternative derivation is presented in Ref. [15]. Neglecting the cavity driving and respecting large-detuning conditions we obtain

$$\hat{H}^{(2)} = \frac{\hbar\omega_q}{2}\hat{\sigma}_z + \frac{\Omega^2}{4\Delta}\sin^2\theta\cos\theta\left(\hat{\sigma}_+e^{-i2\omega t} + \hat{\sigma}_-e^{+i2\omega t}\right) - \hbar g \sin\theta\left(\hat{\sigma}_+\hat{a} + \hat{\sigma}_-\hat{a}^\dagger\right) + \hbar\omega_r\left(\hat{a}^\dagger\hat{a} + \frac{1}{2}\right), \quad (1)$$

where  $\hat{\sigma}_+$ ,  $\hat{\sigma}_-$ ,  $\hat{a}^\dagger$ , and  $\hat{a}$  are the qubit raising and lowering and the cavity creation and annihilation operators, respectively. We define the Bloch angle  $\theta$  via  $\sin\theta \equiv \Delta/\omega_q$  and  $\cos\theta \equiv \epsilon/\omega_q$ . The upconversion dynamics sketched in Fig. 1c is clearly described by Eq. (1). The first two terms represent the qubit and its coherent two-photon driving with angular frequency  $\omega$ . The last two terms show the population transfer via the Jaynes-Cummings interaction to the resonator. The Jaynes-Cummings interaction in this form is valid only near the anticrossings ( $\theta \approx \tilde{\theta}$ ,  $\sin\tilde{\theta} \equiv \Delta/\omega_r \simeq 0.63$ ). Finally, the resonator decays emitting radiation of angular frequency  $2\omega$ .

The model outlined above allows us to unveil the symmetry properties of our system. Even though the two-photon coherent driving is largely detuned,  $\omega_q = 2\omega \gg \Omega \sin\theta$ , a not well-defined symmetry of the qubit potential permits qubit level transitions away from the optimal point. Because of energy conservation, i.e., frequency matching, these transitions are real and can be used to probe the qubit-resonator anticrossing. The effective two-photon qubit driving strength,  $(\Omega^2 \sin^2\theta/4\Delta)\cos\theta$ , has the typical structure of a second-order dispersive interaction with the extra factor  $\cos\theta$ . The latter causes this coupling to disappear at the optimal point, where  $\epsilon(\Phi_x) = 0$ . There, the qubit potential is symmetric and the parity of the interaction operator is well defined. Consequently, selection rules similar to those governing electric dipole transitions hold [11]. This is best understood in our analytical two-level model, where the first-order interaction Hamiltonian for the driven diagonalized qubit consists of a pure  $\hat{\sigma}_x$ -term at the optimal point. In this case, one-photon transitions are allowed because  $\hat{\sigma}_x$  is an odd-parity operator. In contrast, the two-photon driving effectively couples via second-order interaction Hamiltonian, which is of a pure  $\hat{\sigma}_z$ -type. Since  $\hat{\sigma}_z$  is an even-parity operator, real level transitions are forbidden. We note that this  $\hat{\sigma}_z$ -term simply renormalizes the qubit transition frequency slightly and is neglected in Eq. (1). The intimate nature of the symmetry breaking now resides in the coexistence of second-order  $\hat{\sigma}_x$ - and  $\hat{\sigma}_z$ -terms in the interaction Hamiltonian when moving away from the qubit optimal point.

In conclusion, we use two-photon qubit spectroscopy to study the interaction of a superconducting flux qubit with an *LC*-resonator. We show experimental evidence for the presence of an anticrossing under two-photon driving, permitting us to estimate the vacuum Rabi coupling. Our experiments and theoretical analysis shed new light on the fundamental symmetry properties of quantum circuits and the nonlinear dynamics inherent to circuit QED. This can be exploited in a wide range of applications such as parametric upconversion, generation of microwave single photons on demand or squeezing.

## References

- [1] J. Clarke and F. K. Wilhelm, *Nature* **453**, 1031 (2008).
- [2] Y. Nakamura, Yu. A. Pashkin, and J. S. Tsai. *Phys. Rev. Lett.* **87**, 246601, (2001).
- [3] W. D. Oliver, Y. Yu, J. C. Lee, K. K. Berggren, L. S. Levitov, and T. P. Orlando, *Science* **310**, 1653 (2005).
- [4] S. Saito, T. Meno, M. Ueda, H. Tanaka, K. Semba, and H. Takayanagi, *Phys. Rev. Lett.* **96**, 107001 (2006).
- [5] M. Sillanpää, T. Lehtinen, A. Paila, Y. Makhlin, and P. Hakonen, *Phys. Rev. Lett.* **96**, 187002 (2006).
- [6] C. M. Wilson, T. Duty, F. Persson, M. Sandberg, G. Johansson, and P. Delsing, *Phys. Rev. Lett.* **98**, 257003 (2007).
- [7] A. Wallraff, D. I. Schuster, A. Blais, L. Frunzio, R.-S. Huang, J. Majer, S. Kumar, S. M. Girvin, and R. J. Schoelkopf, *Nature* **431**, 162 (2004).
- [8] A. Blais, R.-S. Huang, A. Wallraff, S. M. Girvin, and R. J. Schoelkopf. *Phys. Rev. A* **69**, 062320 (2004).
- [9] M. Mariani, F. Deppe, A. Marx, R. Gross, F. K. Wilhelm, and E. Solano, *Phys. Rev. B* **78**, 104508 (2008).
- [10] T. P. Orlando, J. E. Mooij, L. Tian, C. H. van der Wal, L. S. Levitov, S. Lloyd, and J. J. Mazo, *Phys. Rev. B* **60**, 15398 (1999).
- [11] Yu-xi Liu, J. Q. You, L. F. Wei, C. P. Sun, and F. Nori, *Phys. Rev. Lett.* **95**, 087001 (2005).
- [12] F. Deppe, M. Mariani, E. P. Menzel, A. Marx, S. Saito, K. Kakuyanagi, T. Meno, K. Semba, H. Takayanagi, E. Solano, and R. Gross, *Nature Physics* **4**, 686 (2008).
- [13] K. Kakuyanagi, T. Meno, S. Saito, H. Nakano, K. Semba, H. Takayanagi, F. Deppe, and A. Shnirman, *Phys. Rev. Lett.* **98**, 047004 (2007).
- [14] F. Deppe, M. Mariani, E. P. Menzel, S. Saito, K. Kakuyanagi, H. Tanaka, T. Meno, K. Semba, H. Takayanagi, and R. Gross, *Phys. Rev. B* **76**, 214503 (2007).
- [15] T. Niemczyk, F. Deppe, M. Mariani, E. P. Menzel, E. Hoffmann, G. Wild, L. Eggenstein, A. Marx, and R. Gross, unpublished.

## Two-Resonator Circuit QED: a Superconducting Quantum Switch

*E. Hoffmann, M. Mariantoni, F. Deppe, T. Weißl, T. Niemczyk, E.P. Menzel, A. Marx, and R. Gross*<sup>1</sup>

In the past few years, there has been a tremendous experimental progress in the flourishing realm of circuit quantum electrodynamics (QED) [1]. There, different types of superconducting qubits have been strongly coupled to on-chip microwave resonators, which act as quantized cavities. Recently, a quantum state has been stored and coherently transferred between two superconducting phase qubits via a microwave resonator [2] and two transmon qubits have been coupled utilizing an on-chip cavity as a quantum bus [3]. Schemes to perform quantum information processing based on circuit QED implementations have been suggested e.g. in ref. [4] where a two-dimensional array of on-chip resonators coupled to qubits is considered. In this or any other multi-cavity setup, it is highly desirable to switch on and off an interaction between two resonators or to compensate their spurious crosstalk. Therefore, investigating the basic properties of two-resonator circuit QED, where two resonators are coupled to one qubit, is a highly relevant subject to study. When operating such a system in a regime dominated by second-order (dispersive) interactions, the requirements on the qubit coherence properties are considerably relaxed. We have theoretically studied a three-circuit network where a superconducting charge or flux qubit interacts with two on-chip microwave cavities, a two-resonator circuit QED setup. In this three-circuit network, the qubit mediates a geometric second-order circuit interaction between the otherwise decoupled resonators. In the dispersive regime, it also gives rise to a dynamic second order perturbative interaction. The geometric and dynamic coupling strengths can be tuned to be equal, thus permitting to switch on and off the interaction between the two resonators via a qubit population inversion or by shifting the qubit operation point. This work has recently been published [5]. We have recently started to design, simulate and fabricate two on-chip microwave resonators which will be simultaneously coupled to the same superconducting flux qubit.

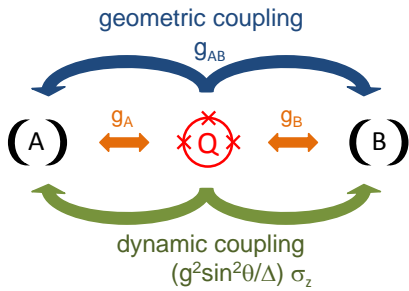


**Figure 1:** Schematic representation of the couplings in the three-node network. First-order coupling: two resonators A and B equally interact with a superconducting flux qubit Q ( $g_A = g_B = g$ ). The second-order coupling consists of a geometric part with coupling constant  $g_{AB}$  and a dynamic part with coefficient  $\frac{g^2 \sin^2 \theta}{\Delta} \hat{\sigma}_z$ . The direct first-order coupling between the two resonators is assumed to be small.

In the following we will first consider the tunable coupling between the individual network components in the *three-node network* as sketched in Fig. 1. Here, the microwave resonators (in this case two  $\lambda/2$  resonators) are represented by symbolic mirrors A and B. The superconducting flux qubit is characterized by two energies, the qubit energy bias  $\hbar\epsilon$  and the qubit gap  $\delta_Q$ . While the qubit energy bias is tunable by an external applied flux  $\Phi_x^{\text{DC}}$ , the qubit gap is fixed by the fabrication. The eigenenergies  $\hbar\Omega_Q/2$  of the flux qubit are mixtures of the qubit energy bias and the qubit gap with the qubit's transition frequency  $\Omega_Q = \sqrt{\epsilon^2 + \delta_Q^2}$ . The qubit mixing angle is defined as  $\theta = \arctan(\delta_Q/\epsilon)$ . The two resonators A and B have the eigenfrequency  $\omega$ . For the quantum switch the effective hamiltonian

$$H = \hbar \left( \frac{g^2 \sin^2 \theta}{\Delta} \hat{\sigma}_z + g_{AB} \right) (\hat{a}^\dagger \hat{b} + \hat{a} \hat{b}^\dagger) \quad (1)$$

<sup>1</sup>This work is supported by the Deutsche Forschungsgemeinschaft through SFB 631 and the German Excellence Initiative via the Nanosystems Initiative Munich (NIM).

can be derived [5], with  $\Delta = \Omega_Q - \omega$  being the qubit-resonator detuning. Furthermore,  $\hat{a}^\dagger$  ( $\hat{b}^\dagger$ ) and  $\hat{a}$  ( $\hat{b}$ ) are the bosonic creation and annihilation operators for the field in cavity A (B). This hamiltonian is the key ingredient for the implementation of a quantum switch between the two resonators. It represents a tunable interaction between A and B characterized by an effective coupling coefficient

$$g_{sw}^{(g)} = g_{AB} - \frac{g^2 \sin^2 \theta}{\Delta}, \quad g_{sw}^{(e)} = g_{AB} + \frac{g^2 \sin^2 \theta}{\Delta} \quad (2)$$

for the qubit's eigenstates  $|g\rangle$  and  $|e\rangle$ . The coupling constant in Eq. (1) consists of two parts: the purely geometric one,  $g_{AB}$ , and the dynamic part  $\frac{g^2 \sin^2 \theta}{\Delta} \hat{\sigma}_z$ . The geometric coupling is constant and qubit-state independent while the dynamic part depends on the qubit state and the external applied flux. Thus, the *switch setting condition*

$$g_{AB} = \frac{g^2 \sin^2 \theta}{\Delta} \quad (3)$$

can easily be fulfilled by varying  $\Delta$  and changing  $\sin \theta$  such that  $g_{sw}^{(g)} = 0$ . This adjustment can be achieved by initializing the qubit in it's ground state and choosing the appropriate detuning  $\Delta$  by changing the quasi-static bias of the qubit.

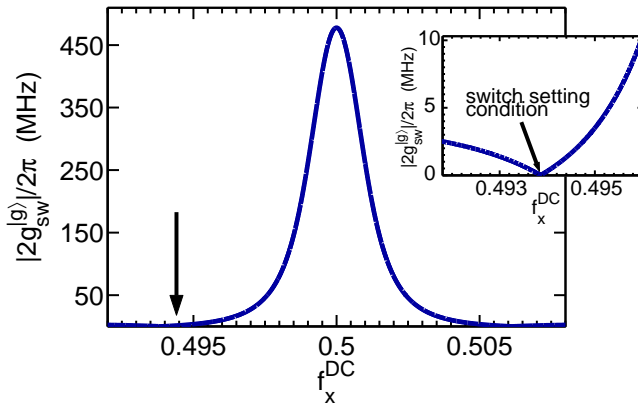


**Figure 2:** Simulation of the quantum switch hamiltonian: the coupling coefficient  $g_{sw}^{(g)}$  strongly depends on the external applied flux ( $f_x^{dc} = \Phi_x^{DC}/\Phi_0$ ). Inset: close-up of the region marked by the black arrow.

also change the quasi-static bias of the qubit by applying an adiabatic pulse. In this way, the detuning  $\Delta$  and the mixing angle  $\theta$  change such that  $g_{sw}^{(g)} \neq 0$ . This means that the geometric and dynamic part of the coupling coefficient in Eq. (1) are not balanced against each other anymore and we get a finite coupling between the two microwave resonators.

During the last year we have designed, simulated and fabricated different types of on-chip coupled microwave resonators. Initial measurements indicate a strong first-order coupling between two microstrip resonators (see Fig. 3 (a)). This first-order coupling induces a splitting of the peaks in the measured transmission spectra which can be seen in Fig. 3(b). Here, the red curve shows the transmission spectrum of resonator A for the coupled system, the blue curve shows the transmission from A to B where resonator A is excited and the output of resonator B is detected. On the other hand, the blue curve shows the transmission spectrum of resonator A with a center frequency of 3.88 GHz when resonator B is removed. The width of the splitting is proportional to the coupling strength and will be investigated in further experiments. The next

Figure 2 visualizes the coupling coefficient  $g_{sw}^{(g)}$  of the system when the qubit is in its ground state. The switch setting condition  $g_{sw}^{(g)} = 0$  is reached at  $f_x^{dc} \sim 0.4938$ . In this case, the resonators are decoupled. Changing the state of the quantum switch from off to on can be achieved in two different ways. On the one hand, the state of the qubit can be changed from the ground state  $|g\rangle$  to the excited state  $|e\rangle$ . Then, the coupling constant changes from  $g_{sw}^{(g)} = 0$  to  $g_{sw}^{(e)} = 2g_{AB} = g_{sw}^{on}$ . Under these conditions, the two resonators are effectively coupled and the A-to-B transfer time is  $t = \pi/2g_{sw}^{on}$ . On the other hand, we can

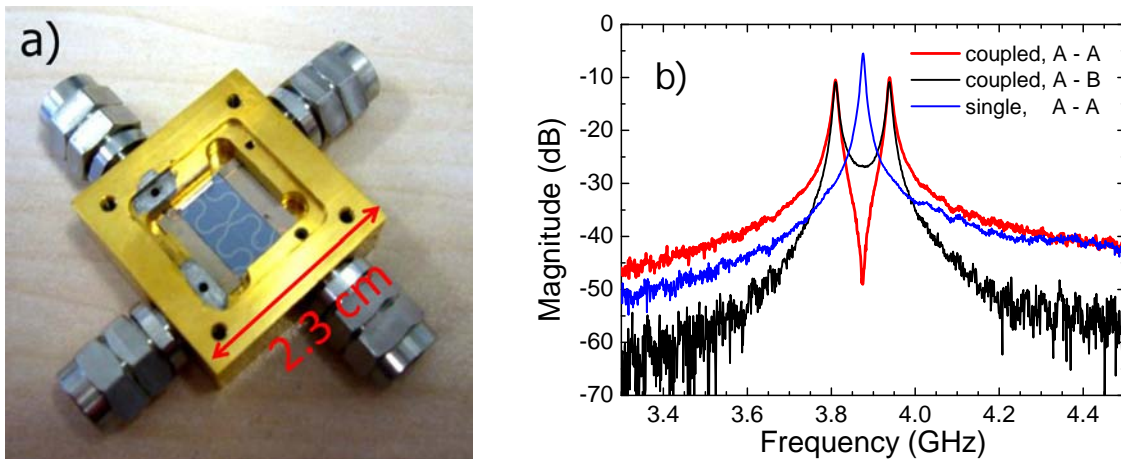


**Figure 3:** (a) Silicon chip with two on-chip microwave resonators mounted in the specially designed gold plated box. (b) Transmission measurement of the coupled resonators: the red curve shows the transmission of resonator A while resonator B is not excited. The black curve depicts the transmission from resonator A to resonator B whereas the blue curve shows the transmission of resonator A with resonator B removed.

step will be to implement a superconducting ring between two weakly coupled resonators to characterize the geometric second-order coupling. The dimensions of this ring are similar to the dimensions of the qubit which will eventually be implemented between the two resonators. This should enable us to experimentally discriminate between geometric and dynamic second order coupling.

## References

- [1] A. Wallraff, D. I. Schuster, A. Blais, L. Frunzio, R.-S. Huang, J. Majer, S. Kumar, S. M. Girvin, and R. J. Schoelkopf, *Nature* **431**, 162 (2004).
- [2] M. A. Sillanpää, J. I. Park, and R. W. Simmonds, *Nature*, **449**, 438 (2007).
- [3] J. Majer, J. M. Chow, J. M. Gambetta, J. Koch, B. R. Johnson, J. A. Schreier, L. Frunzio, D. I. Schuster, A. A. Houck, A. Wallraff, A. Blais, M. H. Devoret, S. M. Girvin, and R. J. Schoelkopf, *Nature*, **449**, 443 (2007).
- [4] F. Helmer, M. Mariantoni, A. G. Fowler, J. v. Delft, E. Solano, and F. Marquardt, arXiv:cond-math.mes-hall/0706.3625v (2007).
- [5] M. Mariantoni, F. Deppe, A. Marx, R. Gross, F. K. Wilhelm, and E. Solano, *Phys. Rev. B* **78**, 104508 (2008).

## Measuring the Zero-point Fluctuations of the Microwave Radiation

*M. Mariani, E. P. Menzel, M. Á. Araque Caballero, F. Deppe, E. Hoffmann, T. Niemczyk, A. Marx, and R. Gross*<sup>1</sup>  
*E. Solano*<sup>2</sup>

The measurement of the zero-point fluctuations of the electromagnetic field in the microwave regime represents a demanding experimental task. It allows for a deep understanding of the quantum properties of radiation. Furthermore, it has recently become possible to encode the quantum state of superconducting qubits into the states of microwave fields. Therefore, measuring microwave signals with (almost) quantum-limited sensitivity is highly desirable. Here, we report on an experimental setup designed for the measurement of extremely weak microwave signals. We show first experimental results providing clear evidence for the detection of vacuum fluctuations at microwave frequencies. This is realized by measuring the Planck distribution of the photons emitted by a  $50\ \Omega$  resistor in the range between 4 and 7 GHz down to the mK regime [1, 2].

The experimental setup is sketched in Fig. 1. As a noise source we utilize a  $50\ \Omega$  resistor  $R$ . The temperature of this resistor could be precisely controlled by means of a heater and a thermometer. The resistor is initially cooled down to the base temperature of our dilution refrigerator ( $\approx 20\ \text{mK}$ ). It is used to terminate one end of a  $50\ \Omega$

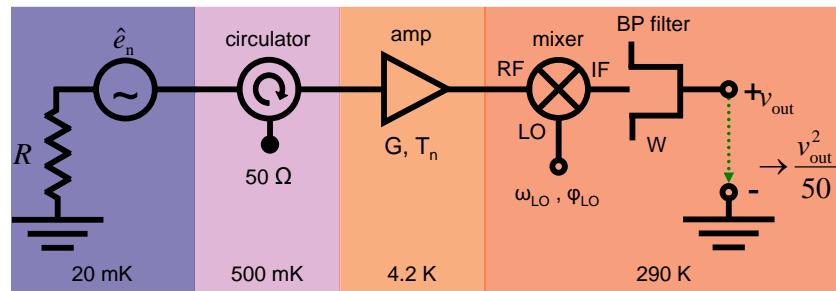


**Figure 1: Microwave homodyne/heterodyne detection apparatus.** The noise  $e_n$  generated by a resistor  $R$  in the GHz regime is amplified by means of a cryogenic amplifier and downconverted with a mixer. The output voltage  $v_{out}$  is post-processed in order to obtain the corresponding noise power and, hence, its Planck distribution. The temperature of the noisy resistor is opportunely controlled.

transmission line. This line is then connected to a circulator, which is heat sunk at a temperature of approximately 500 mK. The circulator is a special microwave device characterized by a non-reciprocal scattering matrix. As a consequence, the circulator effectively breaks the symmetry of the transmission line. This property allows the signal, i.e., the noise generated by the resistor, to be transmitted through the circulator and then to the transmission line following it (see Fig. 1). However, any signal coming from the output port of the circulator cannot be transmitted back into the coldest stage of the experiment. Such signals are instead absorbed by a  $50\ \Omega$  load positioned at the third port of the circulator (see Fig. 1). This fact plays an important role when considering the fact that the next stage of our detection chain is represented by a cryogenic amplifier thermally anchored at 4.2 K. The amplifier has a gain  $G$  and generates noise because of its finite internal resistance. Such noise, typically expressed in an equivalent noise temperature  $T_n$ , could go back into the experiment. However, the isolation provided by the circulator largely reduces this undesirable effect. In this manner, we substantially improve on the performances of our measurement apparatus. The last stage of the detection scheme is located at room temperature and consists of a mixer followed by a bandpass filter with band-

<sup>1</sup>This work is supported by the Deutsche Forschungsgemeinschaft through SFB 631 and the German Excellence Initiative via the Nanosystems Initiative Munich (NIM).

<sup>2</sup>Departamento de Química-Física, Universidad del País Vasco - Euskal Herriko Unibertsitatea, Apdo. 644, 48080 Bilbao, Spain.

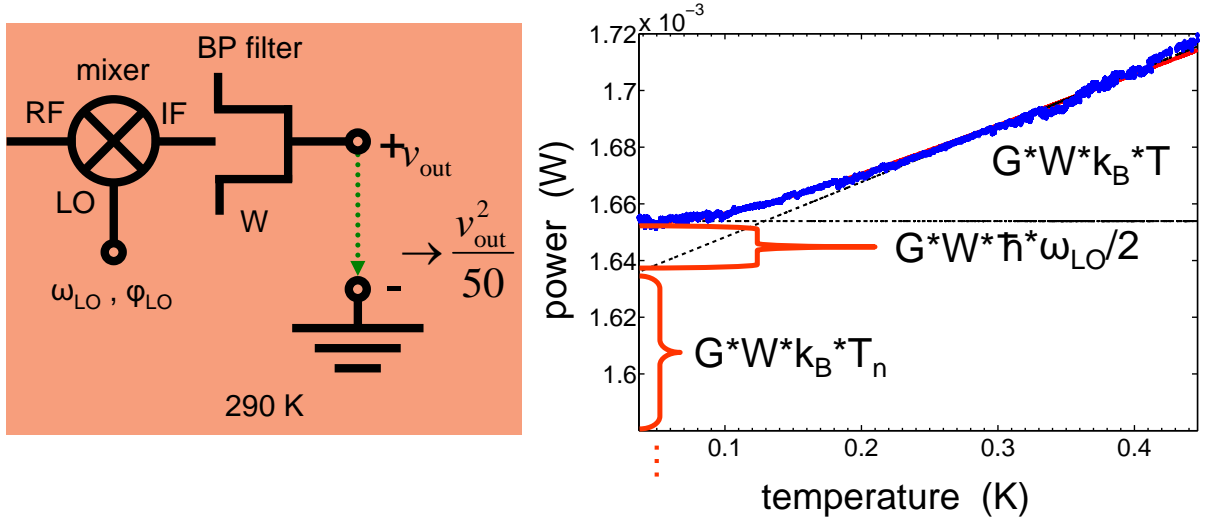


**Figure 2: Experimental results.** The Planck distribution for the noise generated by a resistor  $R$ . This distribution allows to extract the gain and noise of the cryogenic amplifier. Moreover, from it we can infer information on the vacuum fluctuations of the microwave radiation.

width  $W$ . The mixer is a three-port device. The input signal is fed into the radio-frequency port (RF), a sinusoidal pump signal with frequency  $\omega_{\text{LO}}$  and phase  $\varphi_{\text{LO}}$  is fed into the local oscillator port (LO), and an output signal is obtained at the intermediate frequency port (IF). The basic principle of a mixer is to multiply the RF and the LO signals, resulting in a down-conversion of the RF signal to the IF frequency. Usually, the noise we are interested in (the RF signal) is white Gaussian noise centered at a frequency of approximately 6 GHz. The LO can be chosen to possess exactly the same frequency or to be slightly detuned. In the first case, the detection is referred to as homodyne, in the second case as heterodyne. In the homodyne case, the IF signal is a pure DC signal. In the heterodyne case, the IF signal has a frequency of a few MHz. The bandpass filter is then used to define the desired frequency window for the white Gaussian noise we want to measure. The final output of our detector is a voltage  $v_{\text{out}}$ , which can be opportunely post-processed in order to obtain useful information. For instance, we can square it and divide it by the characteristic impedance of our network ( $50 \Omega$ ), thus computing a noise power,  $v_{\text{out}}^2/50$ .

The knowledge of the noise power is very important. In fact, it allows us to measure the Planck distribution of thermal noise. First, we represent our noise source with quantum mechanical operators

$$e_n = \frac{1}{2} (a^\dagger + a), \quad (1)$$

where  $a$  and  $a^\dagger$  are the usual bosonic creation and annihilation operators. The noise power is then proportional to

$$\langle e_n^2 \rangle = \frac{1}{2} \left( \langle a^\dagger a \rangle + \frac{1}{2} \right). \quad (2)$$

The proportionality constant is given by the amplification gain  $G$  and the bandwidth of the bandpass filter  $W$ . For thermal noise, the quantity  $\langle a^\dagger a \rangle$  follows the Bose-Einstein distribution

$$n(\omega) = \frac{1}{e^{\frac{\hbar\omega}{k_B T}} - 1}, \quad (3)$$

where  $\omega$  is the frequency of the RF signal,  $T$  the temperature of the noisy resistor  $R$ , which we can control, and  $k_B$  the Boltzmann constant. It is important to notice that the offset quantity  $1/2$

in Eq. (2) is exquisitely due to the fact that at very low temperatures the electromagnetic radiation possesses vacuum fluctuations. Evidently, measuring the Planck distribution of noise at a particular frequency down to very low temperatures ( $k_B T < \hbar\omega$ ) allows us to infer information about the vacuum fluctuations.

Our experimental results are summarized in Fig. 2, which shows the measured noise power between about 20 mK and 0.5 K. Evidently, the measured temperature dependence nicely follows the Planck distribution. We can clearly observe a cross-over from thermal noise into quantum vacuum noise. Given a bandwidth  $W \approx 20$  MHz, from the slope of the linear region of the measured curve we extract the gain of our amplification chain,  $G \approx 118$  dB. From the intercept of the linear slope with the  $y$ -axis, we obtain the noise temperature  $T_n$  of the cryogenic amplifier to  $T_n \approx 8.54$  K. Last but not least, from the little triangle formed by the linear slope and the flat region of the Planck distribution after the cross-over point, we can extract the quantum vacuum noise level. The experimental value of  $1.77 \times 10^{-24}$  J is only 9% away from the theoretical value of  $1.93 \times 10^{-24}$  J expected for vacuum noise centered at about 6 GHz.

In conclusion, we have experimentally implemented a homodyne detection apparatus for the measurement of weak quantum signals in the microwave regime. The setup was used to measure the Planck distribution of microwave photons emitted by a  $50 \Omega$  resistor down to very low temperatures. From our measurements we directly can infer information on the vacuum fluctuations of the microwave radiation.

## References

- [1] M. Mariani *et al.*, unpublished arXiv:cond-mat/0509737 (2005).
- [2] R. Movshovich *et al.*, Phys. Rev. Lett. **65**, 1419 (1990).

## Cross-Correlation Measurements of Weak Microwave Signals

*E. P. Menzel, M. Mariantoni, M. Á. Araque Caballero, F. Deppe, E. Hoffmann, T. Niemczyk, C. Probst, K. Uhlig, A. Baust, M. Häberlein, C. Rauch, A. Marx, R. Gross<sup>1</sup>  
E. Solano<sup>2</sup>*

The interaction between matter and light plays a central role in the realm of cavity QED, in which a real atom interacts with the electromagnetic field inside a cavity. Concepts developed for the optical domain have been successfully transferred and applied to the microwave regime, establishing the rapidly evolving field of circuit QED. Here, superconducting quantum circuits, acting as tunable, artificial atoms, are strongly coupled to the microwave field of a superconducting transmission line resonator [1]. For a deeper understanding of the properties of microwave radiation it is necessary to investigate the fields in these systems by a direct detection instead of indirectly inferring information on them by measuring the artificial atoms. However, concepts like optical homodyning in the quantum regime rely on the existence of detectors with single photon resolution. Unfortunately, the smaller energy scale of microwave radiation prevents processes used in the optical domain to detect photons. This lack of suitable detectors has driven the development of a cross-correlation measurement scheme [3], which can resolve the mean value and variance of propagating microwave fields with minimum noise disturbance. Its concept is based on amplification of the opportunely split signal with independent amplification chains. In this way, the inevitably added noise  $\chi$  of the amplifiers can be canceled using cross-correlation. For the clean detection of the mean value a single amplification chain together with averaging is sufficient, as the mean value of the noise vanishes:  $\langle \chi \rangle = 0$ . This is not the case for the variance. Here, the second moment of the noise,  $\langle \chi^2 \rangle$ , which is related to the noise power, plays an important role as it does not average out. However, using two amplification chains and cross-correlation changes  $\langle \chi^2 \rangle$  to  $\langle \chi_1 \chi_2 \rangle$  (the index refers to the individual chain), which cancels if the noise signals added by the two chains are statistically independent.

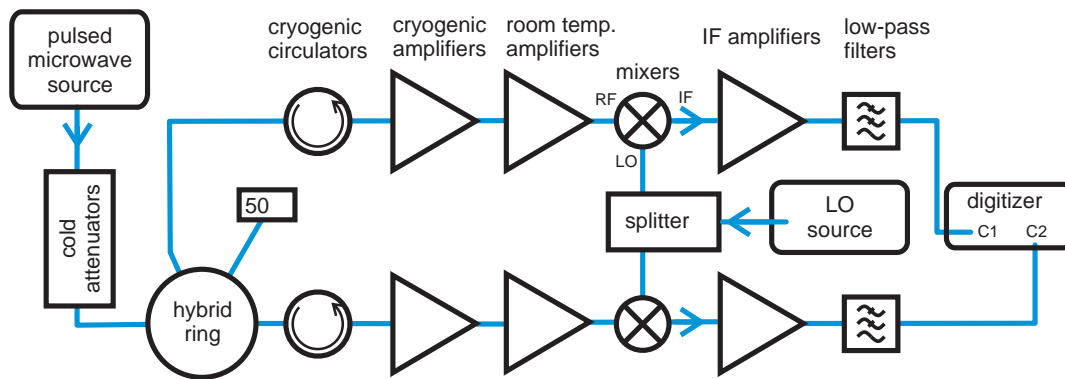


**Figure 1: Experimental setup.** The signal is split by a microwave hybrid and fed into two independent amplification chains. After down conversion by a mixer and amplification it is digitized and processed.

Here, we describe a first characterization of our experimental setup (see Fig. 1) with pulsed coherent signals. Part of it is located in a dilution refrigerator with a base temperature of 15 mK. The pulsed microwaves are damped by cold attenuators, which are heat sunk at the different temperature stages of the fridge. Thus, the unavoidable thermal noise added is much smaller than in the case of attenuation at room temperature resulting in a better signal-to-noise ratio.

<sup>1</sup>This work is supported by the Deutsche Forschungsgemeinschaft through SFB 631 and the German Excellence Initiative via the Nanosystems Initiative Munich (NIM).

<sup>2</sup>Departamento de Química-Física, Universidad del País Vasco - Euskal Herriko Unibertsitatea, 48080 Bilbao, Spain.

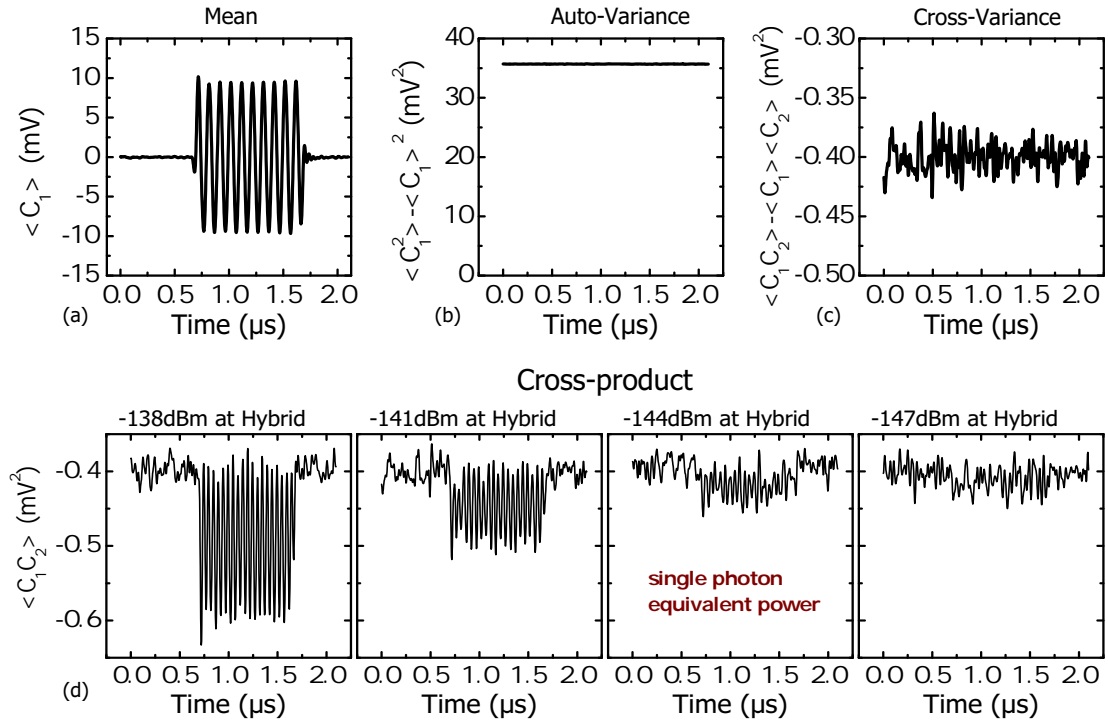


**Figure 2: Experimental Results.** (a), (b), (c) show the mean, the auto-variance and the cross-variance of a pulsed coherent signal, respectively. The power at the hybrid input is -141 dBm. In (d), the power dependence of the cross-product is plotted. All measurements are the average of 10 million traces.

The signal is split by means of a hybrid ring, which acts as a beam splitter for microwaves. This four port device does not only ensure a balanced division of the signal with minimum loss, but also provides an isolation of approximately 40 dB between its output ports. This, together with the isolation of the cryogenic circulator, ensures that noise from one of the cold amplifiers can not go back and enter the other amplification chain. Thus, the noises of the amplification chains are independent. In order to sample the amplitudes with an acquisition card, the signals are down converted with mixers from the GHz- to the MHz-regime. Details on the amplification chain, circulators and mixers can be found in the report by Mariani *et al.* on *Measuring the Zero-point Fluctuations of the Microwave Radiation*.

Figure 2 summarizes our experimental results. The time dependence of the mean of 10 million coherent pulses after down conversion to an intermediate frequency of 10 MHz is shown in Fig. 2a. The original frequency is 5.85 GHz and the power within the pulse -141 dBm at the hybrid input. The pulse duration of  $1 \mu\text{s}$  simulates a typical cavity decay rate in circuit QED experiments of 1 MHz. The energy in such a RF-pulse is approximately  $8 \times 10^{-24}$  J or two microwave photons. The auto-variance (Fig. 2b) resulting from only one channel and the cross-variance (Fig. 2c) are as expected constant except for statistical fluctuations. Evidently, the auto-variance contains a huge offset due to the noise of the chain, whereas this is suppressed in the case of the cross-variance. The minus sign of the cross-variance and the cross-product is a result of the  $180^\circ$  phase shift imposed on the signals by the hybrid. As the variance of coherent states is the one of the vacuum, one cannot decide on the resolution limit looking at the variance alone. However, the variance is defined as the second moment minus the square of the mean values. Thus, we have to consider the power dependence of the cross-product plotted in Fig. 2d. The signal is clearly visible at a power of -144 dBm, which is equivalent to a single photon on average.

In conclusion, we have shown that our setup is capable to detect variances of signals down to powers equivalent to that of a single microwave photon on average. Together with the fact that mean values can be retrieved in a more simple way we can fully describe all sorts of Gaussian states, e.g. squeezed states. A further promising application of this tool is the investigation of entanglement of the electromagnetic fields inside two resonators, whose mutual coupling is mediated by a flux qubit [2].

## References

- [1] A. Wallraff, D. I. Schuster, A. Blais, L. Frunzio, R.- S. Huang, J. Majer, S. Kumar, S. M. Girvin, and R. J. Schoelkopf, *Nature* **431**,162 (2004).
- [2] M. Mariani, F. Deppe, A. Marx, R. Gross, F. K. Wilhelm, and E. Solano, *Phys. Rev. B* **78**,104508 (2008).
- [3] M. Mariani, M. J. Storcz, F. K. Wilhelm, W. D. Oliver, A. Emmert, A. Marx, R. Gross, H. Christ, and E. Solano. [arXiv:cond-mat/0509737](https://arxiv.org/abs/cond-mat/0509737), (2006).

## Electronic Raman Scattering in Non-centrosymmetric Superconductors

*D. Einzel, L. Klam<sup>1</sup> and D. Manske<sup>1</sup>*

We formulate a theory for the polarization-dependence of the electronic (pair-breaking) Raman response for the recently discovered non-centrosymmetric superconductors in the clean limit at zero temperature. Possible applications include the systems CePt<sub>3</sub>Si and Li<sub>2</sub>Pd<sub>x</sub>Pt<sub>3-x</sub>B which reflect the two important classes of the involved spin-orbit coupling. We provide analytical expressions for the Raman vertices for these two classes and calculate the polarization dependence of the electronic spectra. We predict a two-peak structure and different power laws with respect to the unknown relative magnitude of the singlet and triplet contributions to the superconducting order parameter, revealing a large variety of characteristic fingerprints of the underlying condensate.

The order parameter of conventional and unconventional superconductors is usually classified as either spin singlet (even parity) or spin triplet (odd parity) by the Pauli exclusion principle. A necessary prerequisite for such a classification is, however, the existence of an inversion center. Something of a stir has been caused by the discovery of the bulk superconductor CePt<sub>3</sub>Si without inversion symmetry, which initiated extensive theoretical and experimental studies. In such systems the existence of an antisymmetric potential gradient causes a parity-breaking antisymmetric spin-orbit coupling (ASOC) that leads to a splitting of the Fermi surface and, moreover, gives rise to the unique possibility of having admixtures of spin-singlet and spin-triplet pairing states. At present, however, the relative magnitude of both contributions to the superconducting order parameter is unknown. In this letter (for more details see Ref. [1] and references therein), we propose that inelastic (Raman) light scattering provides a powerful tool to solve this problem and, in general, to investigate the underlying condensate in such parity-violated, non-centrosymmetric superconductors (NCS). This is because various choices of the photon polarization with respect to the location of the nodes on the Fermi surface allow one to draw conclusions about the node topology and hence the pairing symmetry. Therefore, our predictions of the polarization dependence of Raman spectra enable one to draw conclusions about the internal structure of the parity-mixed condensate in a given NCS.

The model Hamiltonian for noninteracting electrons in a non-centrosymmetric crystal reads

$$\hat{H} = \sum_{\mathbf{k}\sigma\sigma'} \hat{c}_{\mathbf{k}\sigma}^\dagger [\zeta_{\mathbf{k}}\delta_{\sigma\sigma'} + \mathbf{g}_{\mathbf{k}} \cdot \boldsymbol{\tau}_{\sigma\sigma'}] \hat{c}_{\mathbf{k}\sigma'} \quad (1)$$

where  $\zeta_{\mathbf{k}}$  represents the bare band dispersion,  $\sigma, \sigma' = \uparrow, \downarrow$  label the spin state and  $\boldsymbol{\tau}$  are the Pauli matrices. The second term describes an ASOC with a coupling  $\mathbf{g}_{\mathbf{k}}$ . In NCS two important classes of ASOCs are realized reflecting the underlying point group  $\mathcal{G}$  of the crystal. Therefore, we shall be interested in the tetragonal point group  $C_{4v}$  (application to CePt<sub>3</sub>Si, for example) and the cubic point group  $O(432)$  (applicable to the system Li<sub>2</sub>Pd<sub>x</sub>Pt<sub>3-x</sub>B). For  $\mathcal{G} = C_{4v}$  the ASOC reads  $\mathbf{g}_{\mathbf{k}} = g_{\perp}(\hat{\mathbf{k}} \times \hat{\mathbf{e}}_z) + g_{\parallel}\hat{k}_x\hat{k}_y\hat{k}_z(\hat{k}_x^2 - \hat{k}_y^2)\hat{\mathbf{e}}_z$ . In the purely two-dimensional case ( $g_{\parallel} = 0$ ) one recovers what is known as the Rashba interaction. For the cubic point group  $\mathcal{G} = O(432)$   $\mathbf{g}_{\mathbf{k}}$  reads  $\mathbf{g}_{\mathbf{k}} = g_1\hat{\mathbf{k}} - g_3 \left[ \hat{k}_x(\hat{k}_y^2 + \hat{k}_z^2)\hat{\mathbf{e}}_x + \hat{k}_y(\hat{k}_z^2 + \hat{k}_x^2)\hat{\mathbf{e}}_y + \hat{k}_z(\hat{k}_x^2 + \hat{k}_y^2)\hat{\mathbf{e}}_z \right]$  where the ratio  $g_3/g_1$  can be estimated to be  $\simeq 3/2$ .

Diagonalizing the Hamiltonian one finds the eigenvalues  $\zeta_{\mathbf{k}\pm} = \zeta_{\mathbf{k}} \pm |\mathbf{g}_{\mathbf{k}}|$ , which physically correspond to the lifting of the Kramers degeneracy between the two spin states at a given

<sup>1</sup>Max-Planck-Institut für Festkörperforschung, D70569 Stuttgart, Germany

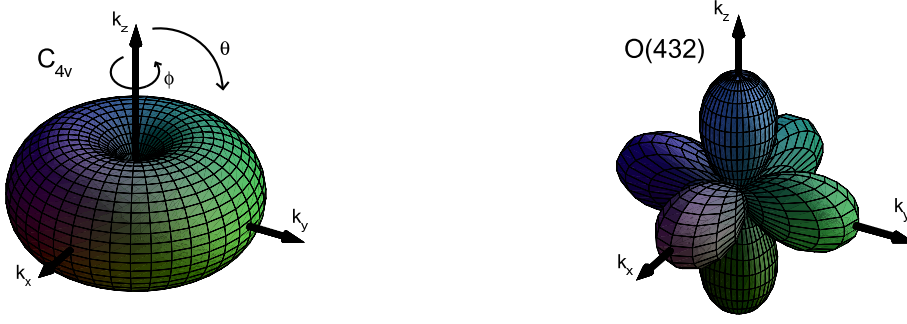


**Figure 1:** The angular dependence of  $|\mathbf{g}_{\mathbf{k}}|$  for the point groups  $C_{4v}$  and  $O(432)$ . Since  $\mathbf{d}_{\mathbf{k}} \parallel \mathbf{g}_{\mathbf{k}}$ , these plots show also the magnitude of the gap function in the pure triplet case for both point groups.

**k.** Sigrist and co-workers have shown that the presence of the ASOC generally allows for an admixture between a spin-triplet order parameter and a spin-singlet pairing gap. This implies that we can write down the following ansatz for the energy gap matrix in spin space  $\Delta_{\mathbf{k}\sigma\sigma'} = [(\psi_{\mathbf{k}}(T)\mathbf{1} + \mathbf{d}_{\mathbf{k}}(T) \cdot \boldsymbol{\tau})i\tau^y]_{\sigma\sigma'}$ , where  $\psi_{\mathbf{k}}(T)$  and  $\mathbf{d}_{\mathbf{k}}(T)$  reflect the singlet and triplet part of the pair potential, respectively. It is then easy to see that the ASOC is not destructive for triplet pairing if one assumes  $\mathbf{d}_{\mathbf{k}} \parallel \mathbf{g}_{\mathbf{k}}$ . This results in the following ansatz for the gap function on both bands (+, -)  $\Delta_{\mathbf{k}\pm} = \psi \pm d|\mathbf{g}_{\mathbf{k}}| = \psi(1 \pm p|\mathbf{g}_{\mathbf{k}}|) \equiv \Delta_{\pm}$  where the parameter  $p = d/\psi$  represents the unknown triplet-singlet ratio. Note that for  $\text{Li}_2\text{Pd}_x\text{Pt}_{3-x}\text{B}$  this parameter seems to be directly related to the substitution of platinum by palladium, since the larger spin-orbit coupling of the heavier platinum is expected to enhance the triplet contribution. This seems to be confirmed by penetration depth experiments. The  $T = 0$  electronic Raman response in a single band is given by the imaginary part of  $\chi_{\gamma\gamma}(\omega) = \chi_{\gamma\gamma}^{(0)}(\omega) - \chi_{\gamma 1}^{(0)2}(\omega)/\chi_{11}^{(0)}(\omega)$  where the index  $\gamma = \gamma_{\mathbf{k}}$  denotes the momentum-dependent Raman vertex that describes the coupling of polarized light to the sample. Since the ASOC leads to a splitting of the Fermi surface, the total Raman response is given by  $\chi_{\gamma\gamma}^{\text{total}} = \sum_{\lambda=\pm} \chi_{\gamma\gamma}^{\lambda}$  with  $\chi_{\gamma\gamma}^{\pm} = \chi_{\gamma\gamma}(\Delta_{\pm})$ , in which the usual summation over the spin variable  $\sigma$  is replaced by a summation over the pseudo-spin (band) index  $\lambda$ . The unscreened Raman response for both bands can be written as

$$\Im\chi_{\gamma\gamma}^{(0)\pm} = \frac{\pi N_{\text{F}}^{\pm} \psi}{\omega} \Re \left\langle \gamma_{\mathbf{k}}^2 \frac{|1 \pm p|\mathbf{g}_{\mathbf{k}}|^2}{\sqrt{(\frac{\omega}{2\psi})^2 - |1 \pm p|\mathbf{g}_{\mathbf{k}}|^2}} \right\rangle_{\text{FS}} \quad (2)$$

where we allow for a different density of states  $N_{\text{F}}^{\pm}$  on both bands and  $\langle \dots \rangle_{\text{FS}}$  denotes an average over the Fermi surface. For small momentum transfers and nonresonant scattering, the Raman tensor is given by  $\gamma_{\mathbf{k}} = m \sum_{\alpha,\beta} \mathbf{e}_{\alpha}^S (\partial^2 \epsilon(\mathbf{k}) / \partial k_{\alpha} \partial k_{\beta}) \mathbf{e}_{\beta}^I$  where  $\mathbf{e}^{S,I}$  denote the scattered and incident polarization light vectors. The light polarization selects elements of this Raman tensor, where  $\gamma_{\mathbf{k}}$  can be decomposed into its symmetry components and, after a lengthy calculation, expanded into a set of basis functions on a spherical Fermi surface. In what follows, we neglect higher harmonics and thus use only the leading term in the expansions of  $\gamma_{\mathbf{k}}$  (for details see Ref. [1]).

Before studying the mixed-parity case, it is instructive to analyze the Raman response for pure triplet  $p$ -wave pairing. Some representative examples are the Balian-Werthamer (BW) state, the Anderson-Brinkman-Morel (ABM or axial) state, and the polar state. The simple pseudoisotropic BW state has  $\mathbf{d}_{\mathbf{k}} = d_0 \hat{\mathbf{k}}$  [equivalent to  $\mathbf{g}_{\mathbf{k}}$  for  $C_{4v}$  with  $g_3 = 0$ , see Fig. 1]. In 3D we obtain more interesting results for the axial state with  $\mathbf{d}_{\mathbf{k}} = d_0(\hat{k}_y \hat{\mathbf{e}}_x - \hat{k}_x \hat{\mathbf{e}}_y)$  [equivalent to  $\mathbf{g}_{\mathbf{k}}$  for  $O(432)$  with  $g_{\parallel} = 0$ ]. The Raman response for this axial state in  $B_1$  and  $B_2$  polarizations for

$\mathcal{G} = C_{4v}$  is given then by

$$\chi''_{B_{1,2}}(x) = \frac{\pi N_F \gamma_0^2}{128} \left( -10 - \frac{28}{3}x^2 - 10x^4 + \frac{5 + 3x^2 + 3x^4 + 5x^6}{x} \ln \left| \frac{x+1}{x-1} \right| \right) \quad (3)$$

with the reduced frequency  $x = \omega/2d_0$ . An expansion for low frequencies reveals a characteristic exponent [ $\chi''_{B_{1,2}} \propto (\omega/2d_0)^6$ ] which is due to the overlap between the gap and the vertex function. Moreover, we calculate the Raman response for the polar state with  $\mathbf{d}_k = d_0 \hat{k}_z \hat{\mathbf{e}}_x$ , where one equatorial line node crosses the Fermi surface:

$$\chi''_{B_{1,2}}(x) = \frac{\pi N_F \gamma_0^2}{8x} \begin{cases} \frac{\pi}{2}x^2 - \frac{3\pi}{4}x^4 + \frac{5\pi}{16}x^6 & x \leq 1 \\ (x^2 - \frac{3}{2}x^4 + \frac{5}{8}x^6) \arcsin \frac{1}{x} - (\frac{1}{3} - \frac{13}{12}x^2 + \frac{5}{8}x^4) \sqrt{x^2 - 1} & x > 1 \end{cases} \quad (4)$$

with the trivial low frequency expansion  $\chi''_{B_{1,2}} \propto \omega/2d_0$ . Whereas the pair-breaking peaks for the BW and ABM state were both located at  $\omega = 2d_0$  (similar to the  $B_{1g}$  polarization in the singlet  $d$ -wave case, which is peaked at  $2\Delta_0$ ), for the polar state this peak is significantly shifted to lower frequencies. The maximum is given by  $\omega = 1.38d_0$ , which looks similar to the response for  $B_{2g}$  polarization in singlet  $d$ -wave superconductors, where it is also peaked at  $\omega < 2\Delta_0$ .

In general, due to the mixing of a singlet and a triplet component to the superconducting condensate, one expects a two-peak structure in parity-violated NCS, reflecting both pair-breaking peaks for the linear combination of the singlet order parameter  $\psi_k$  and the triplet order parameter  $\mathbf{d}_k$  respectively. The ratio  $p = d/\psi$ , however, is unknown for both types of ASOCs.

In Fig. 2 we show the calculated Raman response using  $\mathbf{g}_k$  ( $C_{4v}$ ) with  $g_{\parallel} = 0$ . This Rashba-type of ASOC splits the Fermi surface into two bands; while on the one band the gap function is  $\Delta_k = \psi(1 + p|\mathbf{g}_k|) \equiv \Delta_+$ , it is  $\Delta_- \equiv \psi(1 - p|\mathbf{g}_k|)$  on the other band. Thus, depending on the ratio  $p = d/\psi$ , four different cases (see polar diagrams in the insets) have to be considered: (a) no nodes; (b) one (equatorial) line node ( $\Delta_-$  band); (c) two line nodes ( $\Delta_-$  band); and (d) two point nodes on both bands. Since the Raman intensity in NCS is proportional to the imaginary part of  $\chi_{\gamma\gamma}^{\text{total}} = \chi_{\gamma\gamma}(\Delta_-) + \chi_{\gamma\gamma}(\Delta_+)$ , it is interesting to display both contributions separately (blue and red, respectively). Even though (except for  $\psi = 0$ ) we always find two pair-breaking peaks at  $\omega/2\psi = |1 \pm p|$  we stress that our results for NCS are not just a superposition of a singlet and a triplet spectra. This is clearly demonstrated in Fig. (2a), for example, in which we show the results for a small triplet contribution ( $p = 1/2$ ). For  $\chi_{\gamma\gamma}(\Delta_-)$  we find a threshold behavior with an adjacent maximum value of  $\chi''_{B_{1,2}}(\Delta_-) = N_F^- \gamma_0^2 \pi^2 / 8 \sqrt{p^{-1} - 1}$  and for  $\chi_{\gamma\gamma}(\Delta_+)$  a zero Raman signal to twice the singlet contribution followed by a smooth increase and a singularity. For the special case (b), where the singlet contribution equals the triplet one ( $p = 1$ ), the gap function  $\Delta_-$  displays an equatorial line node without sign change. Because of this nodal structure and strong weight from the vertex function ( $\propto \sin^2 \theta$ ), many low energy quasiparticles can be excited, which leads to this square-root-like increase in the Raman intensity. In this special case the pair-breaking peak is located very close to elastic scattering ( $\omega = 0.24\psi$ ). In Fig. (2c) the gap function  $\Delta_-$  displays two circular line nodes. The corresponding Raman response for  $p > 1$  shows two singularities with different low frequency power laws  $\chi''_{B_{1,2}}(\Delta_-) \propto \omega/2\psi$  and  $\chi''_{B_{1,2}}(\Delta_+) \propto (\omega/2\psi - 1)^{11/2}$ . Finally, for  $p \gg 1$  one recovers the pure triplet cases (d) which is given analytically by Eq. (3).

The Raman response for the point group  $O(432)$  is shown in Fig. 3. We again consider four different cases: (a) no nodes; (b) six point nodes ( $\Delta_-$  band); (c) six connected line nodes ( $\Delta_-$  band); and (d) 8 point nodes (both bands) as illustrated in the insets. Obviously, the pronounced angular dependence of  $|\mathbf{g}_k|$  leads to a strong polarization dependence. Thus we get different

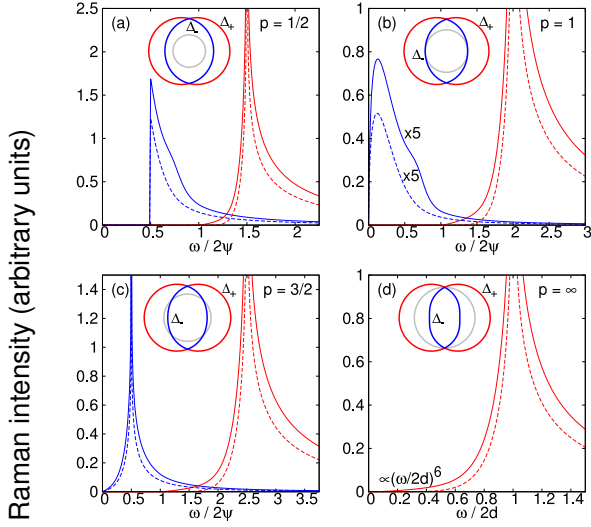


**Figure 2:** Theoretical prediction of the Raman spectra  $\chi''_{\gamma\gamma}(\Delta_-)$  [blue] and  $\chi''_{\gamma\gamma}(\Delta_+)$  [red] for  $A_1$  (solid lines) and for  $B_{1,2}$  (dashed lines) polarizations for the point group  $C_{4v}$ . We obtain the same spectra for the  $B_1$  and  $B_2$  symmetry. The polar diagrams in the insets demonstrate the four qualitative different cases.

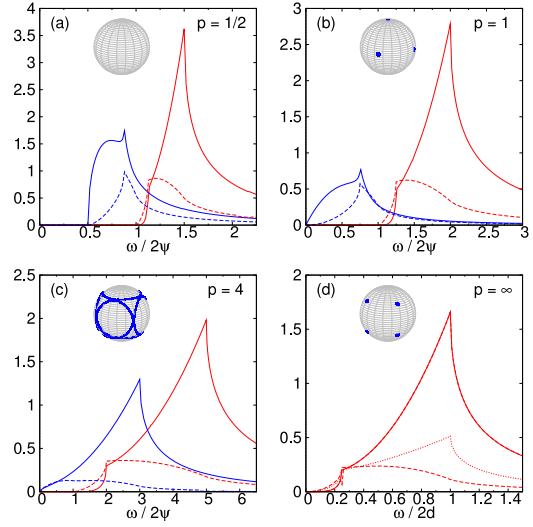


**Figure 3:** Theoretical prediction of the Raman spectra  $\chi_{\gamma\gamma}(\Delta_-)$  [blue] and  $\chi_{\gamma\gamma}(\Delta_+)$  [red] for E (solid lines),  $T_2$  (dashed lines) and  $A_1$  [dotted line, only in (d)] polarizations for the point group  $O(432)$ . The insets display the point and line nodes of the gap function  $\Delta_-$ .

peak positions for the E and  $T_2$  polarizations in  $\chi''_{\gamma\gamma}(\Delta_+)$ . As a further consequence, the Raman spectra reveals up to two kinks on each band (+, -) at  $\omega/2\psi = |1 \pm p/4|$  and  $\omega/2\psi = |1 \pm p|$ . Furthermore, no singularities are present. Nevertheless, the main feature, namely the two-peak structure, is still present and one can directly deduce the value of  $p$  from the peak and kink positions. Finally, for  $p \gg 1$  one recovers the pure triplet case (d), in which the unscreened Raman response is given by

$$\chi''_{\gamma\gamma}(\omega) \propto \frac{2d}{\omega} \Re \left\langle \gamma_{\mathbf{k}}^2 \frac{|\mathbf{g}_{\mathbf{k}}|^2}{\sqrt{(\omega/2d + |\mathbf{g}_{\mathbf{k}}|)(\omega/2d - |\mathbf{g}_{\mathbf{k}}|)}} \right\rangle_{\text{FS}}. \quad (5)$$

Clearly, only the area on the Fermi surface with  $\omega/2d > |\mathbf{g}_{\mathbf{k}}|$  contributes to the Raman intensity. Since  $|\mathbf{g}_{\mathbf{k}}| \in [0, 1]$  has a saddle point at  $|\mathbf{g}_{\mathbf{k}}| = 1/4$ , we find kinks at characteristic frequencies  $\omega/2d = 1/4$  and  $\omega/2d = 1$ . In contrast to the Rashba-type ASOC, we find a characteristic low energy expansion  $\propto (\omega/2d)^2$  for both the  $A_1$  and E symmetry, while  $\propto (\omega/2d)^4$  for the  $T_2$  symmetry.

In summary, we have calculated for the first time the electronic (pair-breaking) Raman response in the newly discovered NCS such as  $\text{CePt}_3\text{Si}$  ( $\mathcal{G} = C_{4v}$ ) and  $\text{Li}_2\text{Pd}_x\text{Pt}_{3-x}\text{B}$  ( $\mathcal{G} = O(432)$ ). Taking the pronounced ASOC into account, we provide various analytical results for the Raman response function and cover all relevant cases from weak to strong triplet-singlet ratio  $p$ . Our theoretical predictions can be used to analyze the underlying condensate in parity-violated NCS and allow the determination of  $p$ .

## References

- [1] L. Klam, D. Einzel and D. Manske, arXiv:0809.5170v1 [cond-mat.supr-con] 30 Sep 2008 (accepted by Physical Review Letters)

## Two-channel Conductivity in a Highly Anisotropic Layered Organic Metal

*M. V. Kartsovnik, W. Biberacher*<sup>1</sup>

Dimensional crossovers and their influence on transport properties and electronic states is a long-standing and still controversial issue in the field of highly anisotropic correlated conductors, such as superconducting cuprates, cobaltates, organics, intercalated compounds, etc. One of the most frequently discussed mechanisms of breaking the interlayer band transport in a layered metal is due to scattering. If the characteristic interlayer hopping time  $\tau_h$  is larger than the transport scattering time  $\tau$ :

$$\tau_h \sim t_z/\hbar \lesssim \tau, \quad (1)$$

where  $t_z$  is the effective interlayer transfer integral, the size of the electron wave packet in the interlayer direction becomes comparable to or even smaller than the layer thickness. In this situation, quasiparticle momentum and Fermi surface are only defined within conducting layers, i.e. become strictly two-dimensional (2D). Nevertheless, as long as the charge transfer between two adjacent layers is determined by direct one electron tunneling (so-called "weakly incoherent" regime [1]), the interlayer resistivity  $\rho_{\perp}(T)$  is predicted to be identical to that in the fully coherent three-dimensional (3D) case [2, 3]. Indeed, the low-temperature interlayer resistivity shows a metalliclike positive derivative,  $d\rho_{zz}/dT > 0$ , in many compounds satisfying the "two-dimensionalization" condition (1). However, by contrast to the theoretical predictions, the resistivity anisotropy in these materials continuously grows upon cooling [4–7].

Our recent studies of the anomalous magnetotransport in the layered organic metal  $\alpha$ -(BEDT-TTF)<sub>2</sub>KHg(SCN)<sub>4</sub> [8, 9] have given evidence of two parallel contributions to the interlayer field-dependent conductivity:

$$\sigma_{zz}(\mathbf{B}, \tau) = \sigma_c(\mathbf{B}, \tau) + \sigma_i(B_{\perp}, \tau). \quad (2)$$

The first term on the right-hand side of Eq. (2) is the conventional coherent Boltzmann conductivity depending in a usual way on both the strength and orientation of a magnetic field [10]. The second term of Eq. (2) is insensitive to the inplane magnetic field component. It has been proposed to originate from an incoherent interlayer charge transfer although its exact mechanism is not yet clear. Here we report on new studies of the interlayer resistance of  $\alpha$ -(BEDT-TTF)<sub>2</sub>KHg(SCN)<sub>4</sub> providing further support for the two-channel conductivity model and discuss a possible mechanism of the incoherent interlayer charge transfer in this compound.

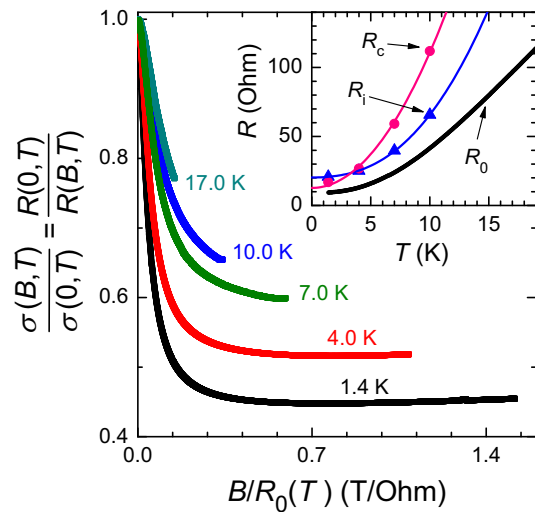


**Figure 1:** Kohler plot of the normalized interlayer conductivity of  $\alpha$ -(BEDT-TTF)<sub>2</sub>KHg(SCN)<sub>4</sub> for the field aligned parallel to layers obtained from field sweeps at different temperatures. Inset: temperature dependence of the zero-field resistance  $R_0$  (thick line) and the resistances of the coherent,  $R_c \propto 1/\sigma_c$ , (circles) and incoherent,  $R_i \propto 1/\sigma_i$ , (triangles) channels. The red and blue lines are, respectively, a quadratic fit of the coherent channel and fit of the incoherent channel according to Eq. (4)

<sup>1</sup>This work was done in collaboration with P. D. Grigoriev (L.D. Landau Institute for Theoretical Physics, Chernogolovka, Russia) and N. D. Kushch (Institute for Problems of Chemical Physics, Chernogolovka, Russia). Financial support from DFG-RFBR Grant No. 436 RUS 113/926 is gratefully acknowledged.

The main panel of Fig. 1 shows results of the interlayer resistance measurements performed at sweeping magnetic field up to 14 T in a direction parallel to conducting layers, at different fixed temperatures. The data is presented in the form of a Kohler plot. Here,  $R_0(T) \equiv R(0, T)$  is the zero-field resistance (shown in the inset) and the normalized field-dependent interlayer conductivity  $\sigma(B, T)/\sigma(0, T)$  is obtained from the resistance  $R(B, T)$ , taking into account that  $\sigma(B) \propto 1/R(B)$  in our quasi-2D material. The argument in Fig. 1 is  $B/R_0(T) \propto \omega_c \tau$ , where  $\omega_c \propto B$  is the characteristic frequency of orbital motion in a magnetic field and the transport  $\tau$  is inversely proportional to the zero-field resistance  $R_0(B)$ . According to Kohler's rule, the magnetoresistance or, in our representation, magnetoconductivity at different fields and temperatures should be just a function of  $B/R_0(T)$ . This rule is strongly violated in Fig. 1: the curves corresponding to different temperatures rapidly diverge from each other. On the other hand, all the curves (at least, those from 1.4 to 10 K) tend to saturation at approximately the same  $B/R_0$  value.

The described behavior can be interpreted in terms of the two-channel model proposed above. Starting from the curve taken at  $T = 1.4$  K, the coherent channel contributes  $\approx 55\%$  of the total conductivity at zero field. In a field parallel to layers it decreases proportional to  $(\omega_c \tau)^\alpha$  with  $1 \leq \alpha \leq 2$  [10] and, at a high enough field, the second, incoherent term in Eq. (2) becomes dominant and the curve saturates at the level determined by  $\sigma_i$ . Evaluating the relative contribution of  $\sigma_i$  to the total zero-field conductivity  $\sigma(0, T)$  at different temperatures and using the  $R_0(T)$  data plotted in the inset of Fig. 1, one can extract separately the temperature dependencies of the coherent (circles in the inset) and incoherent (triangles) channels. Note that even the anomalous, incoherent channel shows a metallic behavior, although its temperature dependence is considerably weaker than for  $\sigma_c$ .

Having separated contributions from the two channels, we can now make a Kohler plot individually for the coherent channel  $\sigma_c(B, T)$ . The result is shown in Fig. 2. Since  $\sigma_i$  is not a classical Boltzmann conductivity, it must not be proportional to the scattering time  $\tau$ . Therefore, the argument in the Kohler plot, which is a characteristic of  $\omega_c \tau$ , should include only the resistance  $R_c(0, T)$  associated with the coherent channel rather than the total resistance  $R_0$ . In the new coordinates, the Kohler scaling works perfectly for the coherent conductivity, thus strongly supporting the two-channel model.

Turning to a possible origin of the incoherent conduction channel, its metallic behavior apparently comes into conflict with the existing theories of incoherent interlayer charge transfer (see [3, 11–13] and references therein) predicting an insulating temperature dependence. In addition, those theories do not account for the significant dependence of  $\sigma_i$  on magnetic field normal to layers [8, 9]. To comply with the experimental observations, we propose to consider elementary events of incoherent interlayer hopping via local centers, such as resonance impurities [3, 13], in combination with diffusive intralayer transfer from one hopping center to another. Our model assumes the volume concentration of hopping centers  $n_i$  to be small, so that the average distance  $l_i$  between them along the 2D layers is much larger than the inplane mean free path  $l_\tau = v_F \tau$ :  $l_i = (n_i d)^{-1/2} \gg l_\tau$ . This condition, being opposite to the model [3], looks reasonable, since

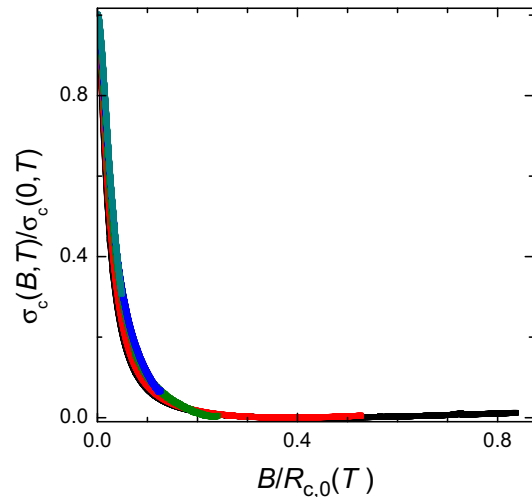


**Figure 2:** Kohler plot of the normalized coherent conductivity. Colours are the same as in the main panel of Fig. 1.

the concentration of resonant impurities is definitely much lower than the concentration of all kinds of impurities. The current through each hopping center is limited by the resistance  $R_{\perp}$ , which contains two in-series elements:

$$R_{\perp} = R_{\text{hc}} + R_{\parallel}. \quad (3)$$

The first part,  $R_{\text{hc}}$ , is the hopping-center resistance itself, which is almost independent of magnetic field and can have a weak nonmetallic temperature dependence  $R_{\text{hc}}(T)$ . The second part,  $R_{\parallel}$ , is the intralayer resistance, which comes up because the electrons must travel along the conducting layer over a distance  $\sim l_i$ . In the limit  $l_i \gg l_{\tau}$ , the 2D intralayer current density  $\mathbf{j}(\mathbf{r})$  at each point is proportional to the electric field  $\mathbf{E}(\mathbf{r})$  at this point:  $\mathbf{j} = \sigma_{\parallel} d \mathbf{E}$ , where an isotropic in-plane conductivity is assumed for simplicity. Assuming further that all the hopping centers are identical, one can obtain, after straightforward calculations, the expression for the interlayer conductivity:

$$\sigma_i = \frac{\pi \sigma_{\parallel} n_i d^3}{\pi d \sigma_{\parallel} R_{\text{hc}} + \ln(l_i/l_{\tau})}. \quad (4)$$

This expression provides a good fit to the temperature dependence of the incoherent channel as shown by the blue line in the inset in Fig. 1. For fitting, we evaluated the  $T$ -dependent intralayer conductivity using the fit of the coherent channel  $R_c = a + bT^2$  red line in the inset in Fig. 1 and the relationship between the intralayer and coherent interlayer conductivities [2]:  $\sigma_{\parallel}(T) = \sigma_{c,\perp}(T)(t_{\parallel}/t_{\perp})^2(a/d)^2 \propto 1/R_c \cdot (t_{\parallel}/t_{\perp})^2(a/d)^2$ , where  $t_{\parallel}$  and  $t_{\perp}$  are the effective intra- and interlayer transfer integrals,  $t_{\parallel}/t_{\perp} = 670$ , [8] and  $a \approx 1.0$  nm and  $d \approx 2.0$  nm are the unit cell parameters along and across layers. The intralayer mean free path was evaluated from  $\sigma_{\parallel}$  using the Drude-Lorentz formula:  $l_{\tau}(T) \simeq \sigma_{\parallel}(T) m v_F / n e^2$  with the effective mass  $m = 1.4 m_0$  ( $m_0$  is the free electron mass) and carrier concentration  $n = 1.5 \times 10^{20} \text{ cm}^{-3}$  taken from de Haas – van Alphen experiments. With that, we have two free parameters,  $l_i$  and  $R_{\text{hc}}$ , to fit  $R_i(T)$ . Assuming  $R_{\text{hc}}$  to be independent of temperature, we obtain an excellent fit of the experimental data, yielding reasonable values:  $l_i = 0.43 \mu\text{m}$  and  $R_{\text{hc}} \approx 400 \text{ Ohm}$ .

The present simple model can be generalized by including the distribution of the hopping centers  $n[R_{\text{hc}}(T)]$  and performing integration over  $R_{\text{hc}}(T)$ . The exact result will depend on the particular physical model of the hopping centers. In the trivial case of short-circuiting the layers (e.g., by dislocations),  $R_{\text{hc}} \approx 1/d\sigma_{\parallel}$  and  $\sigma_i$  should be just proportional to the intralayer conductivity. The fact that the temperature dependence of the incoherent channel is metallic-like, however, considerably weaker than that of the coherent one (inset in Fig. 1), implies that  $R_{\text{hc}}$  is larger than  $1/d\sigma_{\parallel}$  and only slightly varies with (or is independent of) temperature. Such conditions can be fulfilled if the hopping occurs via resonance impurities [3]. Further, both  $R_{\text{hc}}$  and  $1/\sigma_{\parallel}$  are largely insensitive to the inplane magnetic field in the incoherent regime whereas the significant dependence on the out-of-plane field component obviously comes from the intralayer conductivity. Thus, the proposed mechanism is consistent with the main features of the incoherent channel observed in the present experiment as well as in the previous works [8, 9].

## References

- [1] R. H. McKenzie and P. Moses, Phys. Rev. Lett. **81**, 4492 (1998).
- [2] N. Kumar and A. M. Jayannavar, Phys. Rev. B **45**, 5001 (1992).
- [3] D. B. Gutman and D. L. Maslov, Phys. Rev. Lett. **99**, 196602 (2007); Phys. Rev. B **77**, 035115 (2008).
- [4] A. N. Lavrov, M. Y. Kameneva, and L. P. Kozeeva, Phys. Rev. Lett. **81**, 5636 (1998).
- [5] C. H. Wang, et al., Phys. Rev. B **71**, 224515 (2005).
- [6] L. Buravov et al., J. Phys. I **2**, 1257 (1992).
- [7] V. N. Zverev et al., Phys. Rev. B **74**, 104504 (2006).

- [8] M. V. Kartsovnik et al., Phys. Rev. Lett. **96**, 166601 (2006).
- [9] M. V. Kartsovnik and W. Biberacher, WMI Annual report, 2007, p. 32; M. V. Kartsovnik P. D. Grigoriev and W. Biberacher, Arxiv: 0811.4323, submitted to Phys. Rev. Lett.
- [10] M. V. Kartsovnik, Chem. Rev. **104**, 5737 (2004).
- [11] U. Lundin and R. H. McKenzie, Phys. Rev. B **68**, 081101(R) (2003).
- [12] A. F. Ho and A. J. Schofield, Phys. Rev. B **71**, 045101 (2005).
- [13] A. A. Abrikosov, Physica C **317-318**, 154 (1999).

## A New Bifunctional Organic Superconductor $\kappa$ -(BETS)<sub>2</sub>Mn[N(CN)<sub>2</sub>]<sub>3</sub>

M. V. Kartsovnik and W. Biberacher<sup>1</sup>

A new trend in the field of molecular conductors appeared and has been developed over the past decade, aiming at the design of hybrid multi-functional materials combining conducting and magnetic properties in the same crystal lattice. In most of such materials, electrical conductivity is provided by an organic radical cation subsystem while magnetism is provided by an anionic subsystem, containing magnetic transition metal ions. The combination of conductivity and magnetism and their synergism give rise, in some cases, to unique materials and novel physical properties. For example, magnetic field induced superconductivity has been found in  $\lambda$ -(BETS)<sub>2</sub>FeCl<sub>4</sub> [1] and  $\kappa$ -(BETS)<sub>2</sub>FeBr<sub>4</sub> [2]. Such materials are of high interest as possible objects for spintronics due to their gigantic magnetoresistance effect. By now, among radical cation salts, a number of metals and superconductors with localized magnetic moments as well as molecular antiferromagnetic (AFM) metals and superconductors [2, 3] and ferromagnetic metals [4] have been synthesized and intensely studied.

We have studied the transport and magnetic properties of a new layered organic conductor based on  $\pi$ -donor BETS (bis(ethylene-dithio)tetraselenafulvalene) with an anion layer containing magnetic ion Mn<sup>2+</sup>:  $\kappa$ -(BETS)<sub>2</sub>Mn[N(CN)<sub>2</sub>]<sub>3</sub> [5]. This compound is found to be a superconductor at  $P \simeq 0.3$  kbar with  $T_c \simeq 5$  K. At ambient pressure, it exhibits a metal-insulator (MI) transition at  $T_1 \simeq 21$  K and an AFM ordering at  $T_0 \simeq 5$  K. A comparison between resistive and magnetic properties suggests that the exchange interaction between conducting  $\pi$  electrons and localized  $3d$  electrons of Mn<sup>2+</sup> plays an important role in this new conductor.

The crystal structure of  $\kappa$ -(BETS)<sub>2</sub>Mn[N(CN)<sub>2</sub>]<sub>3</sub> comprises alternating conducting layers of BETS radical cations, arranged in the characteristic fishbone  $\kappa$ -type packing, and insulating polymeric anion layers incorporating the magnetic Mn<sup>2+</sup> ion [5]. This leads to a strong electronic anisotropy with the highest conductivity in the crystallographic **bc** plane (parallel to the BETS layers),  $\sigma_{\parallel} \simeq 5 - 30$  (Ohm · cm)<sup>-1</sup> at room temperature; the conductivity in the direction perpendicular to layers is 4 orders of magnitude lower. Four-probe resistance measurements were performed on single crystals with typical dimensions of  $1 \times 0.4 \times 0.04$  mm<sup>3</sup>, with a current directed along the plane of conducting layers and perpendicular to them. Magnetic measurements were done on a crystal with a mass of 95  $\mu$ g in magnetic fields up to 7 T applied parallel to the **b** axis using a SQUID magnetometer MPMS XL7 Quantum Design, and in fields up to 15 T using a home made cantilever beam torqueometer.

A typical behavior of the temperature dependent resistance of  $\kappa$ -(BETS)<sub>2</sub>Mn[N(CN)<sub>2</sub>]<sub>3</sub> is displayed in Fig. 1. The inplane resistance decreases by approximately a factor of two at lowering  $T$  from 295 K down to  $T_{\min} \simeq 28$  K and then rapidly grows (curve 1 in Fig. 1). The interplane resistance (curve 2 in Fig. 1) gradually increases at cooling from room temperature till  $\sim 100$  K and decreases at further cooling down to  $T_{\min}$ . Such a behavior of interlayer resistance  $R_{\perp}(T)$  is typical of many layered organic metals and is most likely caused by a breakdown of the interlayer transport coherence and strong electron-phonon interactions [6]. Below  $T_{\min}$  the interlayer resistance shows a dramatic increase, like in the case of the inplane measurements, indicating a MI transition. The transition temperature defined as that of the minimum in the logarithmic derivative  $d(\ln R)/dT$  is  $T_1 \simeq 21$  K.

<sup>1</sup>This work was done in collaboration with N. D. Kushch and L. I. Buravov (Institute for Problems of Chemical Physics, Chernogolovka, Russia). Financial support from DFG-RFBR Grant No. 436 RUS 113/926 is gratefully acknowledged.

The observed transition is extremely sensitive to pressure. Curve 3 in Fig. 1 shows the resistance  $R_{\perp}(T)$  of a crystal placed inside a drop of silicon oil GKZh-136. Due to a difference in thermal contractions, a pressure of 0.2-0.4 kbar is generated by cooling to low temperatures. As a result, the low-temperature increase of resistance is almost completely suppressed and the sample undergoes a superconducting transition at  $T_c \approx 4.5$  K. This behavior has been reproduced on several samples. As an example, the inset in Fig. 1 shows the low-temperature inter-layer resistance of another crystal placed in GKZh oil, recorded in different magnetic fields. For this sample, the resistance does not reach zero below  $T_c$ , saturating at the level of 4% of the normal-state resistance. Nevertheless, the superconducting nature of the transition is ascertained by its high sensitivity to a magnetic field.

A qualitatively similar behavior has been observed on another organic conductor  $\lambda$ -(BETS) $_2$ FeCl $_4$ . In that compound, the MI transition at 8.3 K is associated with an AFM ordering in the system of Fe $^{3+}$  ions and an exchange interaction between 3d electrons of iron and conducting  $\pi$  electrons in cation layers [1, 7]. The AFM insulating state can be suppressed by a magnetic field of 12 T [7]; moreover, in fields  $17\text{T} < \mu_0 H < 42\text{ T}$  parallel to layers a superconducting state is observed. Further, the  $\pi$ -d interaction is weakened under pressure: a pressure  $\geq 3$  kbar stabilizes the metallic state with a superconducting transition at 2 K [8]. Noteworthy, in comparison to  $\lambda$ -(BETS) $_2$ FeCl $_4$ , the MI transition in our compound is suppressed by a much lower pressure and the pressure-induced superconducting state shows a higher  $T_c$ . On the other hand, a magnetic field of 15 T shifts the MI transition temperature by no more than  $\sim 0.5$  K. The relative weakness of the field effect in our compound in comparison to that in  $\lambda$ -(BETS) $_2$ FeCl $_4$  is not surprising, keeping in mind the 3 times higher temperature of the MI transition.

Given the presence of magnetic ions Mn $^{2+}$  in  $\kappa$ -(BETS) $_2$ Mn[N(CN) $_2$ ] $_3$  one can also expect here interesting effects of an interaction between the magnetic and conducting subsystems. It should be noted, however, that, by contrast to the (BETS) $_2$ FeX $_4$  salts, in our case, the polymeric structure of the anion layer favors a direct exchange interaction between 3d electrons of Mn $^{2+}$  ions linked to each other via dicyanamide bridges. On the other hand, an analysis of shortened contacts between anion and radical cation layers in the structure of the present salt suggests a possibility of  $\pi$ -d interactions via nitrogen 2p orbitals. With this in mind, we have performed a study of magnetic properties of this compound.

Figure 2(a) shows the temperature dependence of molar magnetic susceptibility of a single crystal with a mass of 95  $\mu\text{g}$  obtained on a SQUID magnetometer. The magnetic field,  $\mu_0 H = 7$  T is applied parallel to conducting layers, along the crystallographic short axis **b**. In the whole temperature range, except the lowest temperatures, susceptibility nicely follows the Curie-Weiss law for localized paramagnetic spins,  $\chi = C_m / (T - \theta)$  (a small peak at  $\sim 50$  K was

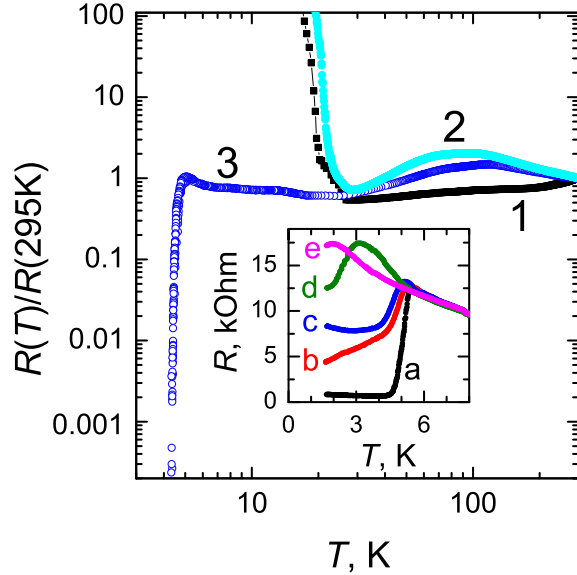


**Figure 1:** Temperature dependence of the resistance of  $\kappa$ -(BETS) $_2$ Mn[N(CN) $_2$ ] $_3$  measured parallel to conducting layers (curve 1) and perpendicular to them (curve 2) at ambient pressure, and the interlayer resistance under a pressure of  $\sim 0.3$  kbar created by cooling in GKZh oil (curve 3). Inset: Superconducting transition in the interlayer resistance of another sample cooled in GKZh, at magnetic fields, (a) to (e): 0, 0.01, 0.03, 0.7, and 1.6 T, directed perpendicular to layers.

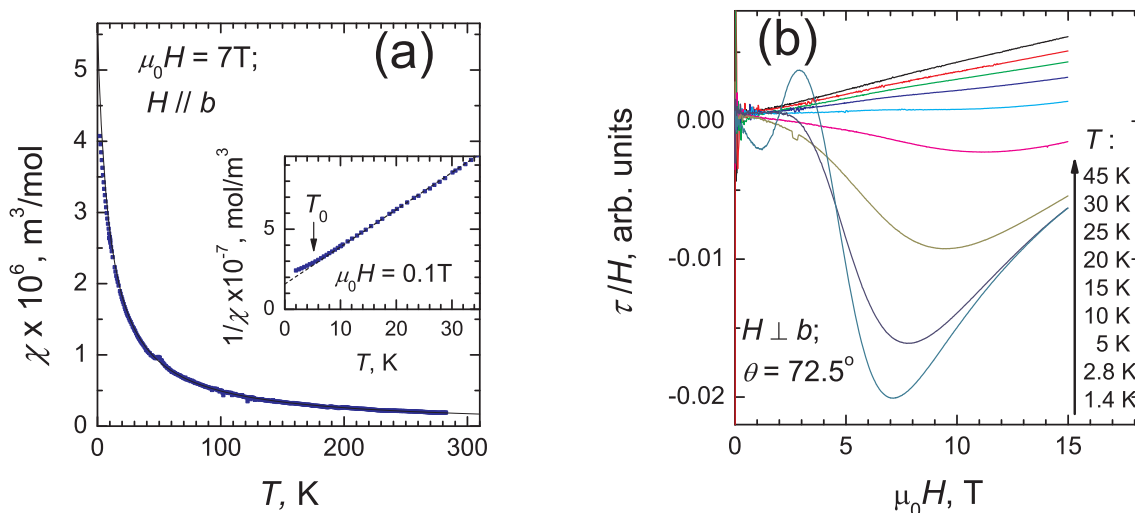


**Figure 2:** (a) Temperature dependence of magnetic susceptibility in the field parallel to the **b** axis; the solid line is a fit to the Curie-Weiss law (see text). Inset: Inverse susceptibility  $1/\chi(T)$  in a weak magnetic field,  $\mu_0 H = 0.1\text{T} \ll k_B T/g\mu_{\text{eff}}$ . The deviation from the linear dependence below  $T_0$  indicates an onset of AFM ordering. (b) Magnetic torque, scaled to the field strength, as a function of the field aligned in the **ac** plane, at different temperatures;  $\theta$  is the angle between the **c** axis and the magnetic field direction.

not reproduced in successive measurements in the interval 35-60 K; it is, most likely, associated with oxygen remnant in the sample space). The Curie constant,  $C_m = (5.2 \pm 0.2) \times 10^{-5} \text{ m}^3 \cdot \text{K}/\text{mol}$ , yields an effective magnetic moment,  $\mu_{\text{eff}} = (5.8 \pm 0.1)\mu_B$  ( $\mu_B$  being the Bohr magneton), indicating that magnetization is dominated by the high-spin,  $S = 5/2$ , state of  $\text{Mn}^{2+}$  ions. The negative Curie-Weiss temperature,  $\theta = 9.7 \text{ K}$ , reveals AFM correlations between the paramagnetic spins. No significant changes in the susceptibility behavior occurs in the temperature range corresponding to the MI transition; the inverse susceptibility,  $1/\chi$ , keeps the linear temperature dependence, as shown in the inset in Fig. 2(a). However, at cooling below  $T_0 \approx 5 \text{ K}$ , a considerable deviation from the Curie-Weiss behavior signaling an onset of AFM ordering is observed.

The AFM ordering is also clearly manifested in magnetic torque  $\tau$  measured in a magnetic field inclined with respect to the principal axes of the susceptibility tensor. The results of torque measurements in the field directed in the crystallographic **ac** plane, at an angle of  $\sim 73^\circ$  from the **c** axis are presented in Fig. 2(b). The ratio  $\tau(H)/H$  plotted along the Y axis is proportional to the magnetization component perpendicular to the external field,  $M_\perp$  (taking into account that  $M \ll H$ ). At cooling below  $T_0$ , in fields below 4 T an anomaly originating most likely from the spin-flop transition in the AFM state rapidly develops. In addition, the curves  $\tau(H)/H$  exhibit a nonmonotonic shape in higher fields, with a minimum at 7-10 T. The corresponding deviations from a usual paramagnetic monotonic field dependence arise already at a temperature  $\sim 20 \text{ K}$ , i.e. around the MI transition. One can, therefore, suggest a correlation between the phase transformation in the conduction system and the evolution of magnetic properties of insulating layers.

The origin of the anomalous high-field behavior of magnetic torque at temperatures  $T \leq 20 \text{ K}$  is not clear at present. The absence of anomalies in the  $\chi(T)$  curve taken on the SQUID magnetometer from the same sample [see inset in Fig. 2(a)] implies that a reorientation of spins takes place most likely in the plane perpendicular to the **b** axis. Further detailed studies in magnetic fields are necessary for clarifying the nature of the low-temperature magnetic state and its influence on the conduction system in the  $\kappa\text{-(BETS)}_2\text{Mn}[\text{N}(\text{CN})_2]_3$ .

## References

- [1] S. Uji et al., *Nature* **410**, 908 (2001); L. Balicas, et al., *Phys. Rev. Lett.* **87**, 067002 (2001).
- [2] H. Kobayashi, H. Cui, and A. Kobayashi, *Chem. Rev.* **104**, 5265 (2004).
- [3] H. Tanaka, et al., *J. Am. Chem. Soc.* **121**, 11243 (1999).
- [4] E. Coronado, et al., *Nature* **408**, 447 (2000); A. Alberola, et al., *J. Am. Chem. Soc.* **125**, 10774 (2003).
- [5] N.D. Kushch, et al., *J. Am. Chem. Soc.* **130**, 7238 (2008).
- [6] A.F. Ho and A.J. Schofield, *Phys. Rev. B* **71**, 045101 (2005); U. Lundin and R.H. McKenzie, *Phys. Rev. B* **71**, 045101 (2003).
- [7] L. Brossard, et al., *Eur. Phys. J. B* **1**, 439 (1998).
- [8] T. Otsuka, et al., *J. Mat. Chem.* **14**, 1682 (2004).

## Quantitative Comparison of ARPES and Raman Spectra in the Cuprates

W. Prestel, B. Muschler, N. Munnikes, A. Erb, M. Lambacher, R. Hackl<sup>1</sup>  
S.V. Borisenko<sup>2</sup>, Shimpei Ono<sup>3</sup>, Yoichi Ando<sup>4</sup>, A. Damascelli<sup>5</sup>, H. Eisaki<sup>6</sup>, M. Greven<sup>7</sup>

The copper-oxygen compounds (cuprates) [1] are highly correlated nearly two-dimensional metals which become superconducting above 100 K. There is no consensus yet on the origin of their superconductivity: Is the condensed state a low-temperature instability of the normal metal as in conventional systems or a new ground state?

In the first case the weak or strong coupling approaches proposed by Bardeen, Cooper, and Schrieffer (BCS) [2] and Eliashberg [3], respectively, should provide an at least qualitative description in terms of intermediary bosons making the electrons to condense into Cooper pairs. Signatures of the coupling boson should also influence if not determine the properties above  $T_c$ . Traditionally, one looks at renormalization effects in the single-particle or transport responses as a function of temperature, specifically around  $T_c$  where abrupt changes are to be expected [4, 5]. The results in the cuprates are far from converging into a unified picture. The unsuccessful search for clear signatures of a dominating retarded interaction was one reason why new ground states were and are being studied intensively [6, 7].

There were early proposals that the superconductivity in the cuprates could be a property of the electrons alone. A prominent example is the resonating valence bond (RVB) state with antiferromagnetic coupling of nearest neighbor spins [8] which emerges from the Néel state upon doping [6]. From an experimental point of view this proposal is much harder to pin down than superconductivity as an instability or a small perturbation of the normal state. There is indeed an arsenal of methods to analyze data in terms of an Eliashberg-type strong coupling approach [3, 9, 10] while ideas for “Smoking Gun” experiments unveiling new ground states are scarce.

Our Raman experiments aim at disentangling strong coupling effects evolving mainly in the temperature domain [10] from phase transitions and cross-over phenomena occurring as a function of doping  $p$ . As a tool we use a phenomenological description of the response. Starting from single-particle properties observed by angle-resolved photoemission spectroscopy (ARPES) we calculate the electronic Raman response (ERS) in both the normal and the superconducting states. While ARPES measures occupied single-electron states ERS yields - similarly as, e.g., optical transport (IR) - a weighted convolution of occupied and empty states. Therefore, the two-particle spectra contain additional information originating from the interaction between the hole and the electron created in the scattering process.

In the Raman process an electron is scattered through an intermediate high-energy state into an unoccupied level. The energy transferred to the electron corresponds to the difference between the incoming and the outgoing photon  $\Omega = \omega^I - \omega^S$ . As a result of the Coulomb interaction only charge fluctuations within a unit cell can be observed. The resulting selection rules lead to form factors  $\gamma(\mathbf{k})$  weighing out symmetry-specific regions of the Brillouin zone. For crossed

<sup>1</sup>This work is supported by the DFG via Research Unit FOR 538 (grant no. Ha 2071/3-4).

<sup>2</sup>IFW-Dresden, 01069 Dresden, Germany

<sup>3</sup>CRIEPI, Komae, Tokyo 201-8511, Japan

<sup>4</sup>Institute of Scientific and Industrial Research, Osaka University, Ibaraki, Osaka 567-0047, Japan

<sup>5</sup>Department of Physics & Astronomy, University of British Columbia, Vancouver, BC V6T 1Z4, Canada

<sup>6</sup>Nanoelectronic Research Institute, AIST, Tsukuba 305-8568, Japan

<sup>7</sup>Department of Applied Physics and Photon Science, Stanford University, Stanford, CA 94305, USA

photon polarizations aligned along the principle axes the  $B_{2g}$  symmetry is projected out and  $\gamma_{\mathbf{k}}^{B_{2g}} \propto \sin k_x \sin k_y$ . In  $B_{1g}$  symmetry with both polarizations rotated by  $45^\circ$  the form factor reads  $\gamma_{\mathbf{k}}^{B_{1g}} \propto \cos k_x - \cos k_y$  (see insets in Fig. 3). The Raman response function  $\chi''_{\gamma\gamma}(\Omega)$  in the simplest representation is a generalized susceptibility reading [11]

$$\chi''_{\gamma\gamma}(\Omega) = \frac{2}{N} \sum_{\mathbf{k}} \gamma^2(\mathbf{k}) \int \frac{d\omega}{\pi} G''(\mathbf{k}, \omega) G''(\mathbf{k}, \omega + \Omega) [f(\omega, T) - f(\omega + \Omega, T)] \quad (1)$$

with  $G''(\mathbf{k}, \omega) = -\pi A(\mathbf{k}, \omega)$  the imaginary part of the renormalized Green function, which is proportional to the spectral function  $A(\mathbf{k}, \omega)$  and  $f(\omega, T)$  the Fermi distribution.  $G$  is related to the bare Green function  $G_0$  via the Dyson equation  $G^{-1} = G_0^{-1} - \Sigma$ , where  $\Sigma$  is the self energy including all interactions of the electron and  $G_0^{-1} = \omega - \zeta_{\mathbf{k}} + i\delta$ . Since we need both occupied and empty states for the calculation of  $\chi''_{\gamma\gamma}(\Omega)$  model functions for  $A(\mathbf{k}, \omega)$  must be derived from the experimental ARPES spectra  $A_{exp}(\mathbf{k}, \omega)$  being cut off at the chemical potential  $\mu$  by  $f$ . Ideally, one has to microscopically derive expressions for the bare band structure  $\zeta_{\mathbf{k}} = \epsilon_{\mathbf{k}} - \mu$  and for  $\Sigma$  in order to obtain a spectral function  $A(\mathbf{k}, \omega)$  which, after multiplication with the matrix element  $|M_{f,i}|^2$  and convolution with the resolution function  $R$ , reproduces  $A_{exp} = (f A |M_{f,i}|^2) \otimes R$ . In *praxi* we use models of the form

$$\Sigma'' = -[\max(\alpha|\omega|, \beta T) + c_{\mathbf{k}}] \quad (2)$$

and tight-binding fits for  $\zeta_{\mathbf{k}}$  [12]. For a set of parameters<sup>8</sup> optimized for  $\text{La}_{1.74}\text{Sr}_{0.26}\text{CuO}_4$  and using Eq. (1) we arrive at the Raman spectra shown in Fig. 1. The agreement is remarkable since only a single intensity is set at 150 K. Symmetry and temperature dependence follow then within the model.

It has been shown before that the longitudinal and the Hall resistivity can be reproduced in a Boltzmann approach with similar assumptions [13]. Here, we use full  $\mathbf{k}$  sums to calculate the spectra at finite energies. The limitation to the Fermi surface would suppress essential structures of the spectra due to the anisotropy of  $\zeta_{\mathbf{k}}$  and the proximity of a van Hove singularity to  $\mu$ . The agreement reaches beyond the energy range shown here and leaves only little spectral weight unexplained up to 1 eV.

The agreement between various single- and two-particle probes at high doping demonstrates that the self energy alone captures the essential physics and that the lowest order approximation (Eq. 1) is sufficient for the calculation of response functions. Yet, there is no microscopic model for  $\Sigma(\mathbf{k}, \omega, T)$  which would link the variation with momentum, energy, and temperature to some interaction or fluctuation. Only the marginal Fermi-liquid model (mFL) [14] predicts expressions similar to Eq. (2) with the momentum dependence coming from impurities. Other models lead to more Fermi liquid like variations of  $\Sigma$  but include an intrinsic momentum dependence due to the underlying fluctuations [15, 16].

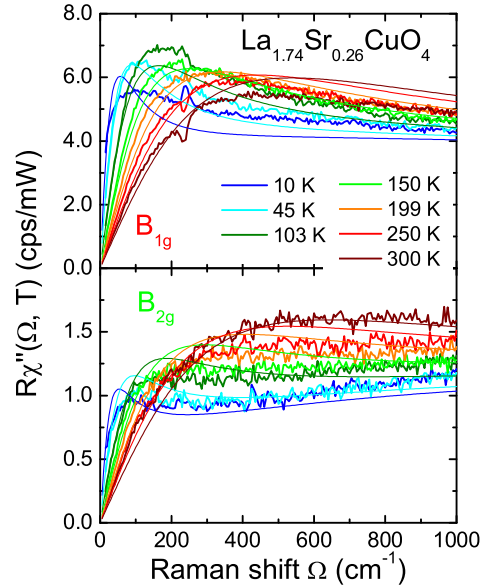


**Figure 1:** Temperature dependence of the electronic Raman response of overdoped non-superconducting  $\text{La}_{1.74}\text{Sr}_{0.26}\text{CuO}_4$ . The smooth lines represent the phenomenology described in the text and are based on an analytic approximation to the photoemission results.

<sup>8</sup>For  $t = 0.25$  eV,  $t'/t = 0.35$ ,  $\mu/t = 1.3$ ,  $\alpha = 1.1$ ,  $\beta = 2.5$ , and  $c_{\mathbf{k}}/t = 0.04$  we get the proper filling and satisfactory agreement with the ARPES spectra. In addition, the temperature dependence of the resistivity is well reproduced.

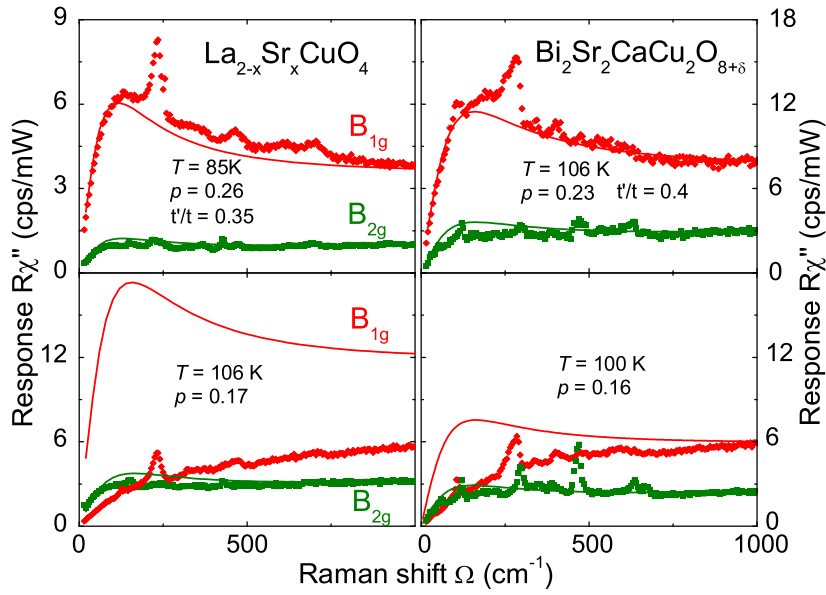


**Figure 2:** Doping dependence of the electronic Raman response of  $\text{Bi}_2\text{Sr}_2\text{CaCu}_2\text{O}_{8+\delta}$  ( $p \approx 2\delta - 0.24$ ) and  $\text{La}_{2-x}\text{Sr}_x\text{CuO}_4$  ( $p = x$ ). There is little variation for the  $B_{2g}$  spectra. The  $B_{1g}$  response changes abruptly at  $p \simeq 0.2$  and cannot be described by spectral functions derived from the ARPES results.

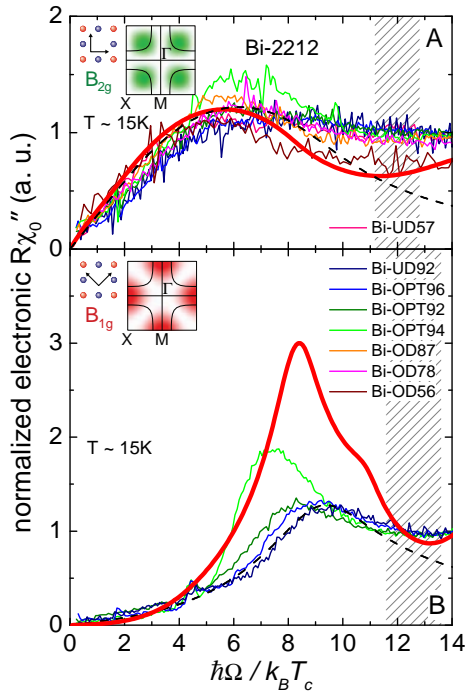


**Figure 3:** Electronic Raman response of  $\text{Bi}_2\text{Sr}_2\text{CaCu}_2\text{O}_{8+\delta}$  below  $T_c$ . In  $B_{1g}$  symmetry only spectra close to  $p = 0.16$  are shown. The energy is given in units of  $k_B T_c$ . The hatched area indicates the energy range, where superconducting and normal spectra merge.

Upon decreasing the doping level we expect little changes on the basis of the ARPES spectra. Even around optimal doping there are still well defined quasiparticle peaks on the entire Fermi surface, and all changes are continuous [17]. In contrast, the  $B_{1g}$  Raman spectra change abruptly close to  $p = 0.2$  [18]. Since there is no discontinuity in the ARPES spectra around  $p = 0.2$  we can use the same model for  $\Sigma$  and  $\zeta_{\mathbf{k}}$  on either side of the transition. The comparison between the prediction on the basis of the ARPES results and the observed  $B_{1g}$  Raman spectra for samples above and below  $p = 0.2$  are shown in Fig. 2. In  $B_{2g}$  symmetry the spectra are well described at both doping levels and, beyond that, down to the lowest doping inside the superconducting dome. The  $B_{1g}$  spectra drop considerably below the simulation in the range below  $1000 \text{ cm}^{-1}$ . While the spectral shapes are similar in Bi-2212 and LSCO the overall intensity in LSCO is subject to variations of the cross section due to resonance effects.

The most remarkable result here is the continuous versus abrupt change in the ARPES and Raman spectra, respectively, across a critical doping level of  $p \simeq 0.20$ . Apparently, we encounter a transition from an essentially conventional metallic state to one of strongly interacting electrons. The origin of the dichotomy of single- vs two-particle properties has to remain open at the moment.

Below  $T_c$  an additional complication arises since the superconductivity-induced features ex-

hibit a statistically significant sample dependence as shown in Fig. 3 B. On the basis of results obtained with applied pressure [20] we speculate that internal strain induced by quenched disorder [19] leads to the variation of the  $B_{1g}$  spectra below  $T_c$ . More quantitatively, the response at the two symmetries shows distinctly different variations: while the  $B_{2g}$  response (Fig. 3 A) is universal and scales with the individual  $T_c$  for all doping levels and samples the  $B_{1g}$  spectra (Fig. 3 B) clearly reflect sample specific behavior and, beyond that, do not scale with  $T_c$  but rather as  $(1 - p)$ . This experimental fact escaped attention so far but may shed light on the origin of the  $B_{1g}$  spectra. It is indeed hard to understand their origin in terms of a pure pair-breaking effect.

This qualitative reasoning is fully corroborated by the simulations derived from the ARPES spectra. Here, Eq. (1) must be extended to superconductivity, where we need the normal and the anomalous part of the Green functions [11] and self energies derived in the spirit of a strong coupling approach [10, 21, 22]. Although sample Bi-UD92 came from the same source as the one used for ARPES there is no agreement between the simulations and the Raman spectra (Fig. 3 B). Results for samples from other sources lie more or less inside the pair-breaking peak derived from ARPES but, similarly as in the normal state, the overall intensity is generally too small.

In summary, the quantitative comparison of ARPES and Raman spectra revealed satisfactory agreement above  $p \simeq 0.2$  in lowest order approximation and increasing discrepancies in  $B_{1g}$  symmetry for  $p \leq 0.2$ . At optimal doping the pair-breaking features observed by Raman scattering reflect properties of the individual samples and are inconsistent with the single-particle results. The abrupt onset of the renormalization effects in the  $B_{1g}$  Raman spectra indicates a phase transition in the middle of the superconducting dome and highlights the importance of higher order (vertex) corrections for a full understanding of the loss of coherence close to the  $(\pi, 0)$  points in the Brillouin zone.

## References

- [1] J.G. Bednorz and K.A. Müller, *Z. Phys. B* **64**, 189 (1986).
- [2] J. Bardeen, L. N. Cooper, and J. R. Schrieffer, *Phys. Rev.* **108**, 1175 (1957).
- [3] For a review see: J. Carbotte, *Rev. Mod. Phys.*, **62**, 1062 (1990).
- [4] S. Engelsberg and J.R. Schrieffer, *Phys. Rev.*, **131**, 993 (1963).
- [5] P.B. Allen and M.L. Cohen, *Phys. Rev. Lett.*, **29**, 1593 (1972).
- [6] For a review see: Patrick A. Lee, Naoto Nagaosa, and Xiao-Gan Wen, *Rev. Mod. Phys.* **78**, 17 (2006).
- [7] P. W. Anderson, *Science*, **317**, 1705 (2007).
- [8] P. W. Anderson, *Science*, **237**, 1196 (1987).
- [9] W. L. McMillan and J. M. Rowell, *Phys. Rev. Lett.* **14**, 108 (1965).
- [10] J. Carbotte, E. Schachinger, and D. N. Basov, *Nature* **401**, 354 (1999).
- [11] T. P. Devereaux and R. Hackl, *Rev. Mod. Phys.* **79**, 175 (2007).
- [12] F. Venturini, Doctoral Thesis, Technische Universität München (2003).
- [13] S. Nakamae *et al.*, *Phys. Rev. B* **68**, 100502 (2003).
- [14] C. M. Varma *et al.*, *Phys. Rev. Lett.* **63**, 1996 (1989).
- [15] W. Metzner, D. Rohe, and S. Andergasen, *Phys. Rev. Lett.* **91**, 066402 (2003).
- [16] S. Caprara *et al.*, *Phys. Rev. B* **59**, 14980 (1999).
- [17] A. Damascelli, Z. Hussain, and Z.-X. Shen, *Rev. Mod. Phys.* **75**, 473 (2003).
- [18] F. Venturini *et al.*, *Phys. Rev. Lett.* **89**, 107003 (2002).
- [19] H. Eisaki *et al.*, *Phys. Rev. B* **69**, 064512 (2004).
- [20] A. F. Goncharov and V. V. Struzhkin, *J. Raman Spectrosc.* **34**, 532 (2003).
- [21] M. R. Norman *et al.*, *Phys. Rev. B* **63**, 140805 (2001).
- [22] D. Inosov *et al.*, *Phys. Rev. B* **75**, 172505 (2007)

## Resonances in Superconductor/Insulator/Ferromagnet/Superconductor Josephson junctions

G. Wild, A. Marx, C. Probst, R. Gross<sup>1</sup>

Josephson junctions with ferromagnetic interlayers recently attracted much interest because they potentially improve the performance of various classical and quantum circuits. In contrast to conventional Josephson junctions, showing no phase difference between the macroscopic phases of the superconducting electrodes at zero bias current, Josephson junction with ferromagnetic interlayer may show up a phase difference of exactly  $\pi$  for an appropriate thickness of the ferromagnetic interlayer. Hence, for superconducting flux qubits the requirement of applying an external flux bias to induce a phase shift of  $\pi$  required to reach the degeneracy point is eliminated by inserting a  $\pi$ -phase shift element into the flux qubit loop. However, superconductor/ferromagnet/superconductor (SFS) Josephson junctions based on metallic ferromagnets usually have a very low normal resistance resulting in low junction quality factors  $Q$ . The related damping is expected to reduce the qubit coherence times. Fortunately, this problem can be relaxed by introducing an additional insulating barrier, resulting in superconductor/insulator/ferromagnet/superconductor (SIFS) Josephson junctions with a higher junction resistance and, in turn, a higher junction quality factor.

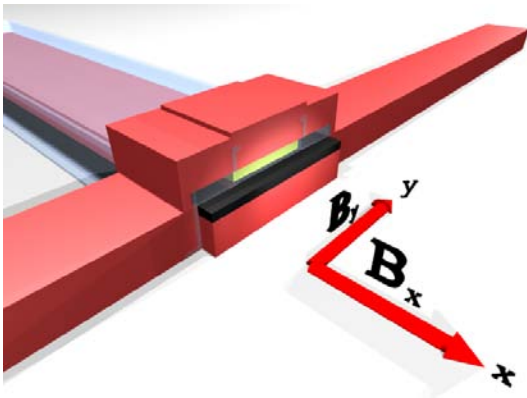


**Figure 1:** Geometry of our  $50 \times 50 \mu\text{m}^2$  SIFS Josephson junctions. The overhang of the wiring layer in  $x$ -direction is negligible, while in  $y$ -direction there is a considerable overhang influencing the propagation of electromagnetic modes.

influenced by plasmonic damping and thus the niobium quality in the vicinity of the ferromagnet. Hence, in the following we will examine the current-voltage characteristics (IVCs) of a  $50 \times 50 \mu\text{m}^2$  junction in detail and characterize the quality of the intrinsic resonance at the plasma frequency  $\omega_p$  as well as the Fiske resonances at higher frequencies  $\omega_n = 2\pi f_n = \frac{2\pi}{\Phi_0} \cdot V_n = \frac{2e}{\hbar} \cdot V_n$ , which are given by the Fiske voltage step position  $V_n$ . Here,  $\Phi_0 = 2.06 \cdot 10^{-15}$  Vs is the flux quantum and  $e = 1.602 \cdot 10^{-19}$  C the elementary charge.

Figure 1 shows the geometry of our  $50 \times 50 \mu\text{m}^2$   $\pi$ -coupled Josephson junctions. The overhang of the wiring layer over the mesa structure forming the junction is negligible in  $x$ -direction, while it is considerable in  $y$ -direction. The IVCs of a  $\pi$ -junction measured with a magnetic field applied in  $x$ - and  $y$ -direction as illustrated in Fig. 1 are shown in Fig. 2. They give clear

The study of the dynamic properties of the SIFS Josephson junctions, especially of the quality of the junction plasma resonance, provide valuable information on the damping properties of the junction. This information is a prerequisite for the estimate of the effect of  $\pi$ -junctions on the decoherence time of flux qubits, when incorporating such junctions as  $\pi$ -phase shift elements in the qubit loop. Therefore, we studied the self-resonant modes of the electromagnetic fields in SIFS  $\pi$ -Josephson junctions based on a multilayer consisting of 50 nm niobium, 3 nm oxidized aluminum, 8 nm  $\text{Pd}_{0.82}\text{Ni}_{0.18}$  and 250 nm niobium. Details of the fabrication process have been described already in annual report 2007. High-frequency damping is predominantly

<sup>1</sup>This work is supported by the Deutsche Forschungsgemeinschaft through SFB 631 and the German Excellence Initiative via the Nanosystems Initiative Munich (NIM).

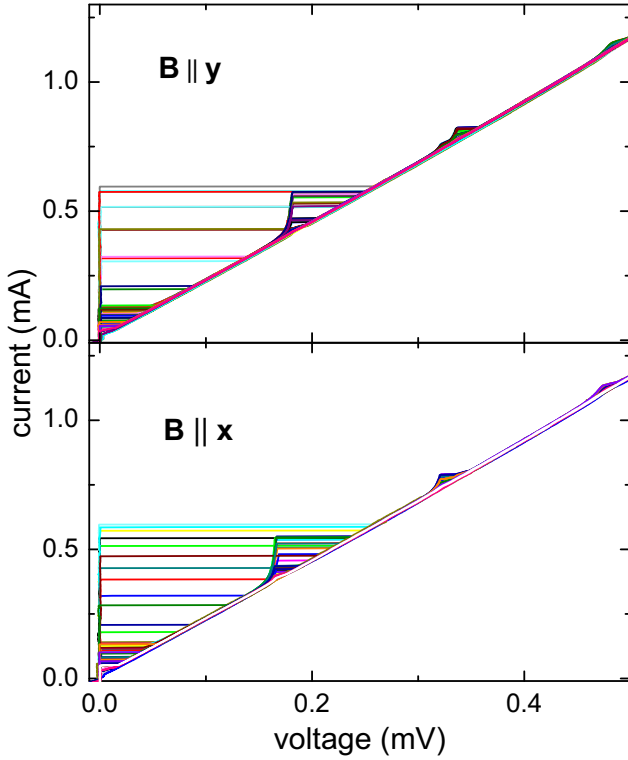


**Figure 2:** IVCs measured at 500 mK for different magnetic fields applied in  $y$ - (top) and  $x$ -direction (bottom) parallel to the multilayer structure (cf. Fig. 1). The Fiske steps measured with a magnetic field applied in  $y$ -direction occur at higher voltages due to the influence of the overhanging wiring layer as explained in the text.

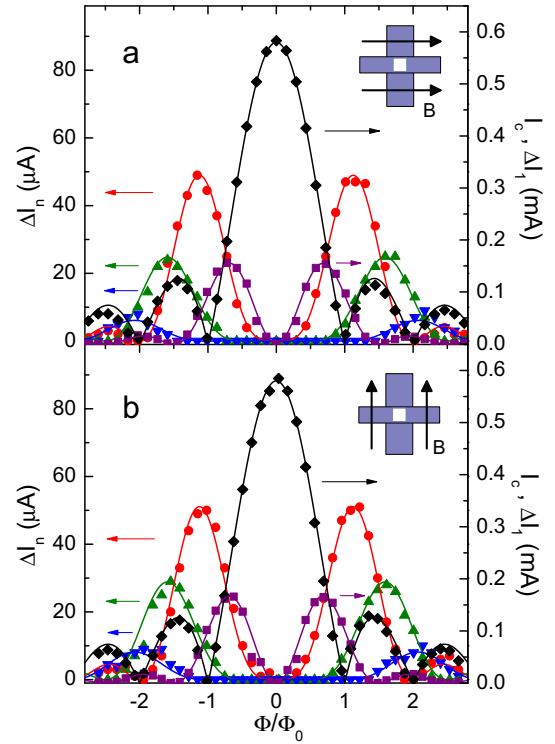


**Figure 3:** Critical current (black line) and current step height of the first four Fiske current steps (increasing number of order: violet, red, green and blue line) measured at 500 mK with the magnetic field applied in  $y$ - (a) and  $x$ -direction (b). The lines are fits to Kulik's theory.  $I_c$  and the current height of the first Fiske step are given by the right axis.

evidence for the presence of self-resonant Fiske modes, manifesting themselves as current steps at voltages  $V_n = \Phi_0 f_n$ . In principal, the frequency of the  $n$ -th Fiske step is given by  $f_n = \bar{c}n/2L$ , where  $\bar{c}$  is the Swihart velocity and  $L$  the junction length perpendicular to the magnetic field direction. The fact that the Fiske steps for the magnetic field applied in  $x$ -direction occur at lower voltages than for the field applied in  $y$ -direction can be explained by an increased Swihart velocity in  $x$ -direction due to the overhanging wiring layer in  $y$ -direction [3]. In turn, this increased Swihart velocity – probed with the magnetic field applied in  $y$ -direction – results in an increase of the Fiske resonance frequency  $f_n$  and the related voltage  $V_n$ .

The height of the current steps can be fitted by Kulik's theory [1] using the quality of the resonance as the fit parameter. The measured height of the current steps together with the fits are shown in Fig. 3 as a function of the applied magnetic field applied in  $x$ - and  $y$ -direction. Figure 4 shows the quality factors derived for the first five resonances by fitting the data obtained for the magnetic field applied in  $x$ - and  $y$ -direction. The values are plotted versus the resonance frequency which is obtained from the voltage position of the resonances. The quality of the intrinsic plasma resonance is determined from the hysteresis of the IVCs ( $Q_{IVC}$ ) and from the Fiske step voltage position ( $Q_{Swihart}$ ). The overestimation of the plasma resonance quality extracted from the Fiske voltage step position may be due to strong non-equilibrium phenomena in these junctions.

At low frequencies the damping is dominated by the finite quasiparticle tunneling current. Therefore, it is expected that the quality factor of both the intrinsic resonance and the Fiske

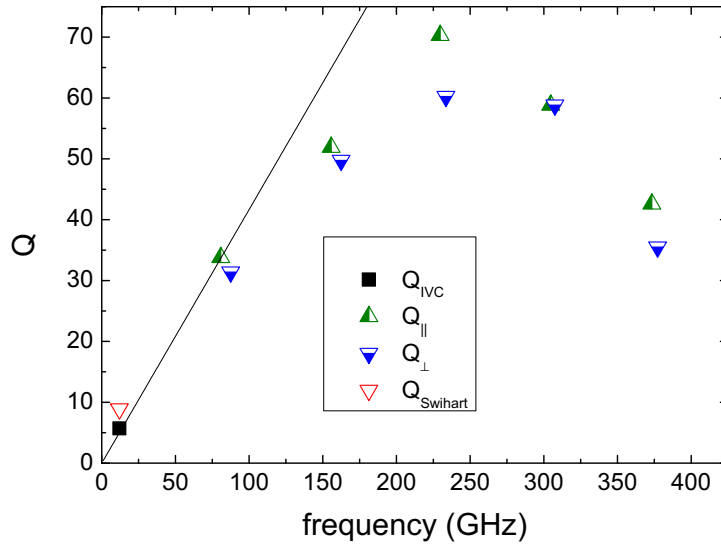


**Figure 4:** The intrinsic quality factor of a SIFS Josephson junction determined from the IVCs  $Q_{IVC}$  and the Fiske current step position  $Q_{Swihart}$  at the plasma frequency  $\omega_p$  and the quality of the Fiske resonances at the appropriate frequencies (all data at 500 mK). The solid black line indicates the expected linear dependence of the quality factor on frequency in the low frequency limit.

resonances is determined by a common quality factor  $Q_{qp}$  determined by the about frequency independent quasiparticle tunneling resistance. Since  $Q_{qp} \propto f/\Delta f$  and  $\Delta f$  is about independent of frequency due to the frequency independent quasiparticle damping, the quality factor is expected to increase linearly with frequency. As shown in Fig. 4, this is in good agreement with our data. At higher frequencies plasmonic damping described by the quality  $Q_p$  becomes dominant, cutting off the linear increase of the quality factor. The crossover in the resulting quality factor for the Fiske resonances can be described as

$$Q = \left( \frac{1}{Q_{qp}} + \frac{1}{Q_p} \right)^{-1}.$$

This behavior can be seen in Fig. 4. Comparing the plasmonic damping in our SIFS Josephson junctions to the quality factors reported in literature for pure niobium Josephson junctions [2] indicates an increased damping in our junctions. This most likely is caused by the additional thin ferromagnetic interlayer causing additional damping.

## References

- [1] I. O. Kulik, JETP Lett. **2**, 84 (1965).
- [2] J. Gijsbertsen, E. Houwman, J. Flokstra, H. Rogalla, J. le Grand, and P. de Korte, IEEE Trans. Appl. Supercond. **3**, 2100 (1993).
- [3] G. Lee, IEEE Trans. Appl. Supercond. **1**, 121 (1991).

## Universal Scaling between Hall and Longitudinal Conductivity in $\text{Fe}_3\text{O}_4$

A. Nielsen, D. Venkateshwaran, M. Althammer, S.T.B. Goennenwein, M. Opel, R. Gross<sup>1</sup>  
M.S. Ramachandra Rao<sup>2</sup>

The physics of the Hall effect in ferromagnetic materials is discussed intensively and controversially since the 1950s. Early experimental work on ferromagnetic metals suggested that the Hall resistivity can be described by the empirical relation  $\rho_{xy} = R_O\mu_0H + R_A\mu_0M$ , where  $H$  is the applied magnetic field and  $M$  the spontaneous magnetization of the ferromagnet. The first term, proportional to  $H$  and characterized by the ordinary Hall coefficient  $R_O$ , describes the ordinary Hall effect (OHE), whereas the second term, proportional to  $M$  and characterized by the anomalous Hall coefficient  $R_A$ , represents the anomalous Hall effect (AHE). Although the AHE is generally observed in ferromagnetic metals and semiconductors, its origin has been one of the most intriguing and controversial issues in solid-state physics. Whereas the extrinsic origins of the AHE are based on skew scattering [1] and side jump [2] mechanisms due to spin orbit interaction connecting the spin polarization with the orbital motion of electrons, the intrinsic origin of the AHE is closely related to the Berry phase [3] of the Bloch electrons.

A powerful experimental test for AHE models is the measurement of the scaling of the anomalous Hall resistivity (conductivity)  $\rho_{xy}^{\text{AHE}}$  ( $\sigma_{xy}^{\text{AHE}}$ ) with the longitudinal resistivity (conductivity)  $\rho_{xx}$  ( $\sigma_{xx}$ ). The skew scattering and side jump mechanisms are known to yield  $\rho_{xy}^{\text{AHE}} \propto \rho_{xx}$  ( $\sigma_{xy}^{\text{AHE}} \propto \sigma_{xx}$ ) and  $\rho_{xy}^{\text{AHE}} \propto \rho_{xx}^2$  ( $\sigma_{xy}^{\text{AHE}} \sim \text{const.}$ ), respectively. Recently, a unified theory of the AHE has been developed for multiband ferromagnetic metals with dilute impurities, taking into account resonant contributions from band crossings. In the dirty limit, the intrinsic contribution is strongly damped, leading to a scaling relation  $\sigma_{xy}^{\text{AHE}} \propto \sigma_{xx}^{1.6}$  [4]. This behavior has been reported for several low-conductivity materials independent of the details of the underlying transport mechanism [5, 6]. In a recent report [7], we addressed the question whether or not the same scaling relation  $\sigma_{xy}^{\text{AHE}} \propto \sigma_{xx}^{1.6}$  also holds for low-conductivity ferromagnetic oxides with hopping type conductivity. To this end, we performed a systematic study of the AHE in Zn-substituted magnetite ( $\text{Fe}_{3-x}\text{Zn}_x\text{O}_4$ ). In particular, we checked whether the scaling relation is universal or depends on specific sample properties such as the crystallographic structure, the charge carrier density, or the Zn content.

Epitaxial thin films of  $\text{Fe}_{3-x}\text{Zn}_x\text{O}_4$  with  $x = 0, 0.1$ , and  $0.5$  were grown by laser molecular beam epitaxy at a base pressure of  $3.7 \times 10^{-3}$  mbar in pure Ar atmosphere or an Ar/O<sub>2</sub> (99:1) mixture.

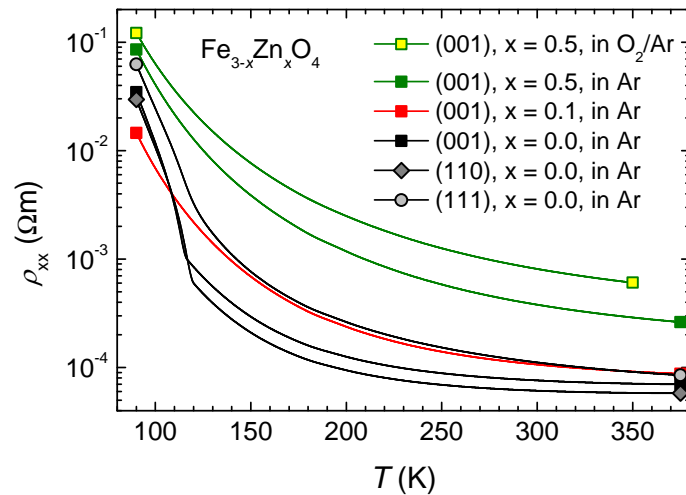


**Figure 1:** Longitudinal resistivity versus temperature for epitaxial  $\text{Fe}_{3-x}\text{Zn}_x\text{O}_4$  films.

<sup>1</sup>This work is supported by the DFG via the priority program SPP 1285 (GR 1132/14) and by the DAAD.

<sup>2</sup>Materials Science Research Centre, Indian Institute of Technology Madras, Chennai 600036, India

We used MgO(001), MgO(110), and Al<sub>2</sub>O<sub>3</sub>(0001) substrates to obtain (001), (110), and (111) oriented films with different amount of epitaxial coherency strain. X-ray diffraction reveals a high epitaxial quality of our samples as demonstrated by a FWHM of the rocking curves of the (004) reflection smaller than 0.05°. Magnetotransport measurements as a function of temperature  $T$  and magnetic field  $H$  were performed using a standard 4-probe technique with  $H$  applied perpendicular to the film plane. The Hall resistivity  $\rho_{xy}$  was obtained by anti-symmetrization of the values measured for opposite magnetic field directions to eliminate offsets due to e.g. a geometric misalignment of the Hall probes. The respective conductivities were derived by inversion of the resistivity tensor.

The longitudinal resistivity  $\rho_{xx}(T)$  increases by more than two orders of magnitude on decreasing  $T$  from 350 to below 100 K (Fig.1). Furthermore,  $\rho_{xx}$  sensitively depends on the Zn substitution, the growth atmosphere and the crystallographic orientation. An increasing Zn content increases resistivity. It is also seen that the resistivity increases by growing the films in an Ar/O<sub>2</sub> mixture. The Hall resistivity  $\rho_{xy}(H)$  scales with the magnetization  $M(H)$  of the samples (not shown here). This is expected according to the empirical relation  $\rho_{xy} = \rho_{xy}^{\text{OHE}} + \rho_{xy}^{\text{AHE}} = R_O\mu_0H + R_A\mu_0M$ , if the anomalous contribution  $\rho_{xy}^{\text{AHE}}$  dominates. To derive  $\rho_{xy}^{\text{AHE}}(M_s) = R_A\mu_0M_s$ , where  $M_s$  is the saturation magnetization, from the measured  $\rho_{xy}(H)$  curve, one has to separate the ordinary and anomalous contributions. Fortunately,  $\rho_{xy}^{\text{OHE}} \sim 2 \times 10^{-9} \Omega\text{m}$  at 1 T is very small and therefore can be safely neglected compared to the contribution  $\rho_{xy}^{\text{AHE}}$  of the AHE which is about two orders of magnitude larger.

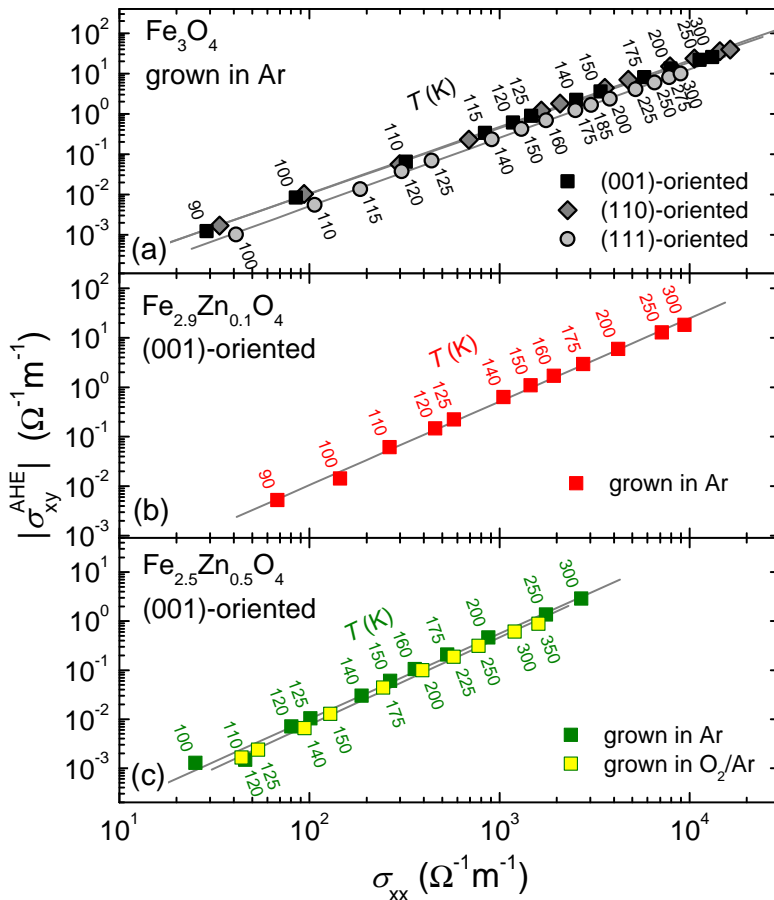


**Figure 2:** Modulus of the anomalous Hall conductivity,  $|\sigma_{xy}^{\text{AHE}}|$ , plotted versus longitudinal conductivity  $\sigma_{xx}$  in a double logarithmic representation.

The  $\sigma_{xy}^{\text{AHE}}$  and  $\sigma_{xx}$  values of our epitaxial Fe<sub>3-x</sub>Zn<sub>x</sub>O<sub>4</sub> thin films change over almost five and three orders of magnitude, respectively, as a function of the crystallographic orientation, the growth atmosphere, and the Zn content. Irrespective of these pronounced differences, however, all data follow the same scaling law (see Fig. 2)

$$|\sigma_{xy}^{\text{AHE}}| = a \cdot \sigma_{xx}^{\alpha} \quad (1)$$

with  $\alpha = 1.69 \pm 0.08$ . This even holds on moving across the Verwey transition in Fe<sub>3</sub>O<sub>4</sub> at about 120 K associated with a structural phase transition (cubic to monoclinic) as well as charge and/or orbital ordering. With respect to the scaling exponent  $\alpha$  our systematic data is in good agreement with theoretical predictions [4]. Our results also agree well with those obtained from polycrystalline [8] and epitaxial Fe<sub>3</sub>O<sub>4</sub> films of different thickness [6] as well as

from single crystals [9]. We further note that scaling relations with about the same exponent but different prefactors have been found for  $\text{Ti}_{1-x}\text{Co}_x\text{O}_{2-\delta}$  and a number of other oxide materials [5].

The origin of the observed scaling relation is still controversial. A recent theoretical model [4] was developed for multiband ferromagnetic metals with dilute impurities in the dirty limit and does not cover the case of low-conductivity ferromagnetic oxides where electric transport is dominated by hopping. Our results together with the available literature data [5, 6] suggest that the scaling relation holds for low-conductivity materials independent of the details of the specific material parameters and the underlying transport mechanism (hopping or metallic conduction) and, therefore, can be considered universal.

## References

- [1] J. Smit, *Physica (Amsterdam)* **21**, 877 (1955); **24**, 39 (1958); J. M. Luttinger, *Phys. Rev.* **112**, 739 (1958).
- [2] L. Berger, *Phys. Rev. B* **2**, 4559 (1970); *Phys. Rev. B* **5**, 4559 (1970); P. Nozières, *J. Phys. (Paris)* **34**, 901 (1973).
- [3] M. V. Berry, *Proc. R. Soc. London, Ser. A* **392**, 45 (1984).
- [4] S. Onoda *et al.*, *Phys. Rev. Lett.* **97**, 126602 (2006); S. Onoda *et al.*, *Phys. Rev. B* **77**, 165103 (2008).
- [5] T. Miyasato *et al.*, *Phys. Rev. Lett.* **99**, 086602 (2007); H. Toyosaki *et al.*, *Nature Mater.* **3**, 221 (2004); K. Ueno *et al.*, *Appl. Phys. Lett.* **90**, 072103 (2007); T. Fukumura *et al.*, *J. J. Appl. Phys.* **46**, L642 (2007).
- [6] A. Fernández-Pacheco *et al.*, *Phys. Rev. B* **77**, 100403(R) (2008).
- [7] D. Venkateshvaran, W. Kaiser, A. Boger, M. Althammer, M.S. Ramachandra Rao, S.T.B. Gönnenwein, M. Opel, R. Gross, *Phys. Rev. B* **78**, 092405 (2008).
- [8] J. S. Feng, R. D. Pashley, and M. A. Nicolet, *J. Phys. C: Solid State Phys.* **8**, 1010 (1975).
- [9] S. Todo, K. Siratori, and S. Kimura, *J. Phys. Soc. Japan* **64**, 2118 (1995).

## Magnetization and Specific Heat Measurements on $\text{YbRh}_2\text{Si}_2$

*E. Schuberth, M. Kath, M. Tippmann*

$\text{YbRh}_2\text{Si}_2$ , a Heavy Fermion compound, is in the center of interest for its unconventional behavior around a quantum critical point (QCP) which can be tuned by a small magnetic field. A QCP marks a continuous phase transition at  $T=0$  in the vicinity of which pronounced deviations from the conventional Landau Fermi liquid state have been found. It can be reached e.g. by suppressing magnetic order by pressure (including chemical pressure through doping) and in some cases by magnetic field. In  $\text{YbRh}_2\text{Si}_2$  a weak antiferromagnetic phase was found below 70 mK [1] which can be driven towards a QCP by a moderate magnetic field of only 60 mT in the  $B \parallel (a, b)$  crystal orientation and of 0.6 T in the  $B \perp (a, b)$  direction. To find the thermodynamic ground state we studied the system at the lowest possible temperatures. Especially we have measured the dc magnetization in magnetic fields up to 60 mT and down to 1 mK using an rf SQUID magnetometer. Both field cooled (fc) and zero field cooled (zfc) data were taken. We found a sharp transition to a low magnetization ground state at 2.2 mK and differences between the fc - zfc traces below 11 mK indicating two new phases in this temperature regime.

The experiments were done in our nuclear demagnetization cryostat with a final temperature of 0.4 mK. Temperatures were measured by pulsed NMR on Pt and Cu rods thermally anchored at the nuclear stage. The samples were clamped in a 5N Ag rod, see Fig. 1, and screwed to the nuclear stage and extending into the pick-up coil of a conventional flux transformer which transferred the signal into an rf Nb SQUID. Since the electrical conductivity of the samples is high (of the order of 5000 Sm) we have no indication that their temperature deviates from that of the nuclear stage by more than a few tens of  $\mu\text{K}$ , at least above the new transitions which we found in this work.

We find a drop of the magnetization below 2.2 mK ( $B \parallel (a, b)$  orientation, see Fig. 2) which is largest for very small magnetic fields of order 0.1 mT. The associated phase transition extends up to 23 mT, see Fig.4. Beyond this field it is suppressed to below 800  $\mu\text{K}$ , and we cannot detect it any more. Obviously, there is a new phase transition at 2.2 mK below which an ordered state exists, different from the AF state at higher temperatures. An extrapolation of the new phase boundary to higher fields even leaves the possibility that it could extend all the way up to the QCP, 60 mT. A kink in this phase boundary around 6 mT is also remarkable.



**Figure 1:** The largest sample of  $\text{YbRh}_2\text{Si}_2$  used in this work mounted in a 5N Ag clamp.

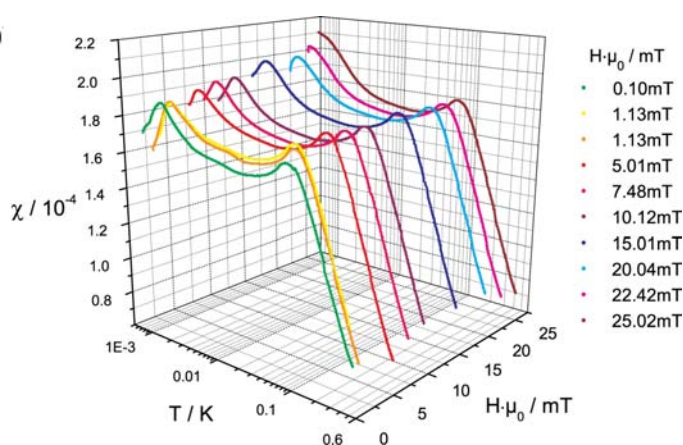


**Figure 2:** Magnetic susceptibility of  $\text{YbRh}_2\text{Si}_2$  in different magnetic fields.

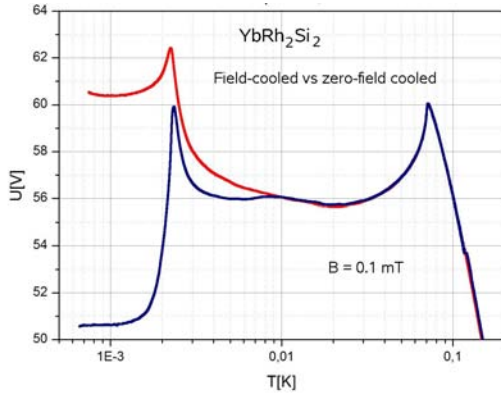


**Figure 3:** DC magnetization of  $\text{YbRh}_2\text{Si}_2$  vs temperature. The two traces correspond to a field-cooled and a zero-field cooled measurement respectively.

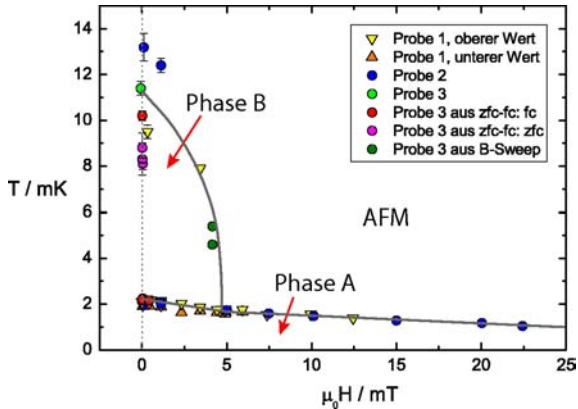


**Figure 4:** Resulting phase diagram measured with three probes, see different symbols. Two new phases, named A and B were found. The lowest temperatures were around  $800 \mu\text{K}$ .

involves moments of similar magnitude as those which order below  $70 \text{ mK}$  [2]. Whether parts of the latter become free again at low temperatures which would indicate a weakened Kondo interaction, or whether new moments are showing up is yet unclear. Although the exact nature of this new state of  $\text{YbRh}_2\text{Si}_2$  is unknown so far, we have shown that the magnetism of this unique compound reveals a very rich phase diagram down to the lowest accessible temperatures. A fascinating question arises as for the properties of the QCP. There could well be a connection between the suppression of the new state at the QCP and the QCP itself. The latter could be driven not by antiferromagnetic fluctuation as is assumed now but by quantum fluctuations of the A-state.

## References

- [1] P. Gegenwart, J. Custers, C. Geibel, K. Neumaier, T. Tayama, K. Tenya, O. Tovarelli, and F. Steglich, Phys. Rev. Lett. **89** 056402 (2002).
- [2] K. Ishida, K. Okamoto, Y. Kawasaki, Y. Kitaoka, O. Trovarelli, C. Geibel, and F. Steglich, Phys. Rev. Lett. **89**, 107202-1 (2002).

Field-cooled (fc) and zero-field-cooled (zfc) data start to deviate from each other below  $11 \text{ mK}$  where a second phase, B, sets in, see Fig. 3. Both data increase at first below this temperature and while the fc trace only shows a drop of about 30 % of the maximum magnetization below  $2.2 \text{ mK}$ , the zero field cooled data had lowest end values in the "virgin state", i.e., when no other magnetic field was run in the cryostat except the field used for demagnetization which acts on a different part of the cryostat. On warming from the lowest temperatures the zfc data begin near zero magnetization and are temperature independent below the new transition A. On further warming a sharp increase with a peak at  $2.2 \text{ mK}$  is observed followed by a decrease until at  $11 \text{ mK}$  the field-cooled trace is met (Fig. 3). The uprise of  $M(T)$  below  $11 \text{ mK}$  can be fitted with a pure Curie law with  $\Theta_{\text{Weiss}} = 0$  and  $\mu = 0.02 \mu_{\text{Bohr}}$ .

In summary, we show that for the Heavy Fermion compound  $\text{YbRh}_2\text{Si}_2$  there are two new phases of which A is possibly the thermodynamic ground state. It is characterized by a pronounced drop of the magnetization. The reduction is largest in magnetic fields below  $100 \mu\text{T}$ . It is unlikely that this marks just a change in the antiferromagnetic order as there exists a large hysteresis between the zfc and the fc magnetization. On the other hand, the  $2.2 \text{ mK}$  transition is preceded by an upturn of  $M$  towards lower temperatures which

## Correlated Systems Investigated with Scanning Tunneling Microscopy

Nanoscale systems offer the unique opportunity to study correlation effects on a fundamental level. Correlation in the microscopic realm, may it be spatial, steric, electronic or magnetic in nature, giving rise to such fascinating properties as magnetism, superconductivity or chiral assemblies. The following questions immediately arise: Can local correlations be analyzed and eventually be influenced? Which role do natural or deliberate defects play in the examined materials and assemblies? How does the system behave under the influence of changing temperature, magnetic field or surrounding conditions? Due to its supreme spatial resolution combined with the ability to probe local electronic properties of a sample, scanning tunneling microscopy has emerged as an invaluable tool to intricately probe those systems.

In various in-house, Munich wide and international collaborations, the group currently focuses on structural and electronic properties of molecular assemblies and superconductors in order to pursue various material driven and (bio)chemical applications as well as to understand the properties of the studied compounds or composite structures on a fundamental level. As one example of the possible applications of our knowledge on molecular self-organization, spatially correlated surface functionality is transferred to nano-mechanical sensor systems as e.g. the cantilever sensor platform.

A short description of the different areas of research on molecular assemblies, superconductors and on (bio)sensing with cantilever arrays is following.

### Complex Self-Assembly of Fréchet-Dendron-Monolayers

*C. Rohr, K. Gruber, C. Höhl, B. A. Hermann*<sup>1</sup>  
*L. Scherer, M. Malarek, E.C. Constable, C.E. Housecroft*<sup>2</sup>  
*E. Frey, T. Franosch, M. Bálbás Gamba*<sup>3</sup>

Self-assembled monolayers on surfaces can undergo restructuring and reorganization - a control thereof is highly anticipated. Additional complexity in molecular monolayers is introduced by multi-component assembly. Such heterogeneous mixtures offer the unique opportunity to store guest-molecules in supporting networks, allowing free rotation of these guest molecules in controlled local environments as well as introducing spacing in molecular assemblies. High precision, sub-molecularly resolved images obtained by scanning tunneling microscopy (STM) promote such studies. On top of that, local conductance can be characterized via scanning tunneling spectroscopy and the STM-tip can directly interact with adsorbed molecules on a nanometer scale via its inhomogeneous electrical field. Proceeding towards increasing complexity, the lack of a fundamental theoretical understanding of the long range correlations triggered by intermolecular interactions is ever apparent. Would on the other hand such an understanding be gained from clever and complementary experimental analysis, a new stage of surface design could be entered leaving behind a trial and error approach.

<sup>1</sup>This work was supported by the German Excellence Initiative via the Nanosystems Initiative Munich (NIM) Area F, CENS, and the Studienstiftung des deutschen Volkes.

<sup>2</sup>Dept. of Inorganic Chemistry, University of Basel, Switzerland.

<sup>3</sup>Dept. of Theoretical Physics, Arnold-Sommerfeld-Center, Ludwig-Maximilians-University Munich.

A multitude of ordering motifs have been found on highly oriented pyrolytic graphite (HOPG) [1] for alkyl-substituted-Fréchet-dendrons. To study and understand the factors in experimental conditions that lead to this extraordinary diversity, a multi-faceted approach has been taken that consists of the following steps: a) The length of the alkylchains on one side of the molecule was systematically varied not altering the overall nature of the Fréchet-dendrons b) The effects of solvent properties, e.g. their electrostatic influence on the

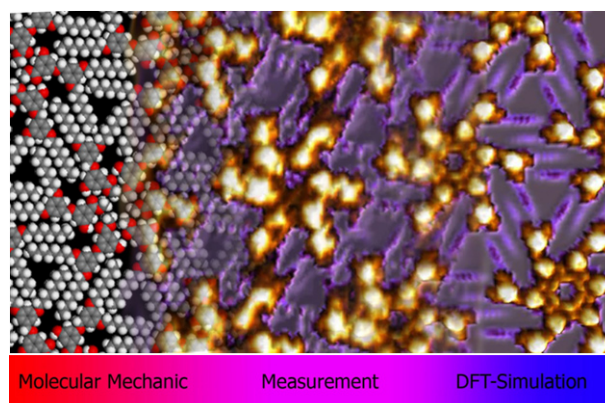


**Figure 1:** Here an STM measurement (middle part) of an octyl-decorated Fréchet-dendron is faded into a corresponding molecular mechanics simulation on the left and a DFT-simulation on the right. STM image matches very well to the DFT simulation pronouncing the high resolution of the measurement.

resulting patterns, was studied in detail [2, 3]. c) Also, the influence of the substrate, in particular, its effect on the 2-D crystal symmetry and on the adsorption energy of the molecular layers, was investigated [2, 4]. d) Furthermore, the complexity of the system was increased by systematically examining heterogeneous molecular assemblies. Host-guest architectures were also realized via the use of template molecules (three molecular components). Besides that new polymorph heterogeneous structures [4] could be obtained. e) Molecular mechanics modeling was performed based on the sub-molecularly resolved STM-images providing a detailed knowledge of the exact molecular conformation (see Fig. 1 left). Moreover, the involved interaction strength within a specific pattern can be deduced. f) Density functional theory (DFT) simulations were computed further enhancing the knowledge on the electronic properties of the Fréchet-dendrons (see Fig. 1, right). In particular the DFT-calculations allow a simulation of STM-images at different specific bias-voltages. g) In collaboration with the group of Prof. E. Frey the formation of and relationship between different structural phases of Fréchet-dendrons is explored on the basis of statistical mechanics, deepening our theoretical understanding of the self-organization process.

This work is currently compiled for a manuscript intended for Physical Review Letters.

## Nano-Mechanical Detection of Bio-Molecular Recognition

*K. Gruber, C. Rohr, F. Trixler, S. Jannuzzi, B. A. Hermann<sup>4</sup>  
T. Horlacher, P. Seeberger,<sup>5</sup> A. Rubio,<sup>6</sup> T. Sobey, F. Simmel<sup>7</sup>*

Based on the development of the atomic force microscope, the cantilever array technique monitors physical, chemical and biochemical processes taking place on the surface of a cantilever sensor. Reactions occurring at this surface can be measured directly without fluorescent or radioactive labels, and chemical reactions can be followed in real-time allowing analysis of reaction dynamics and determination of e.g. kinetic constants. By employing cantilevers, wafer-

<sup>4</sup>This work is supported by the DFG via ERA-Chemistry (HE 5162/1-1) and the German Excellence Initiative via the Nanosystems Initiative Munich (NIM) Area F.

<sup>5</sup>Department Biomolecular Systems, Max Planck Institute of Colloids and Interfaces, Potsdam, Germany

<sup>6</sup>Department of Material Physics, University of The Basque Country, San Sebastián, Spain

<sup>7</sup>Department of Physics, Technical University Munich, Munich, Germany

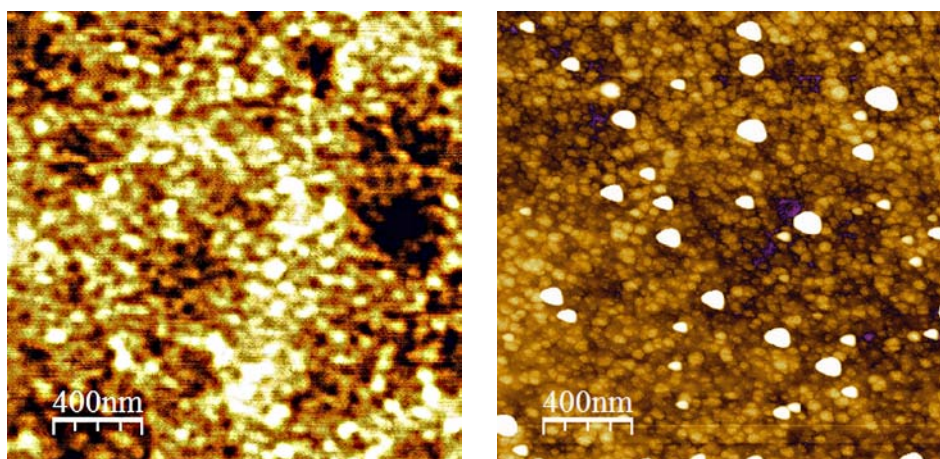


**Figure 2:** AFM height images of Cantisens Cantilever before (left) and (right) after UV-Ozone treatment.

thin and extremely sensitive silicon springs, the Hermann group transfers their knowledge of molecular self-organization to sensor applications. The goal is to understand the chemical transduction process of a (bio)molecular key-lock-recognition in a deflection signal by performing well defined experiments. We additionally employ our microscopy methods for nanoscopic control of the molecules adsorbed on the sensor surface. Typically a microarray of eight differently functionalized cantilever sensors allows the simultaneous detection of multiple substances dissolved in an analyte solution. Unspecific binding is taken into account by employing one or more cantilevers as reference channels.

The specificity and sensitivity of our new cantilever apparatus was tested by setting up a DNA hybridization experiment, where the signals of two single stranded DNAs differing only in eight from 22 base pairs (or 25 respectively) should be distinguished. For that a cantilever array ( $500 \mu\text{m} \times 100 \mu\text{m} \times 1 \mu\text{m}$ ) was functionalized with four cantilevers of each type of the two single stranded DNA sequences. Hence, only those cantilevers that bear the exact complementary to a matching single strand, offered in the sample solution, should show deflection. The hybridization for both sets of single stranded DNA could be successfully and reproducibly detected for several independently functionalized cantilever arrays.

### Functionalization Process Optimization

In order to reach a high reproducibility and efficiency in detecting proteins with cantilever array sensors, it is mandatory to work with well cleaned and carefully prepared cantilever arrays. Also during the functionalization process (the insertion of the cantilevers into micro-capillaries) optimized conditions are desirable. It is crucial for the detection process to form ideal sensing layers, especially when the sensing molecules are attached by sulfur-gold-bonds to the gold-layer of the cantilever array. Therefore protocols had to be developed in order to establish the required performance of the cantilever surface.

*Camera Controlled Functionalization:* For the functionalization the cantilevers are inserted into micro-capillaries filled with a buffer solution containing the sensing molecules. Once dried out, even for a short time period, the delicate assembly of the molecular layer is severely disturbed, rendering the sensor useless for further applications. A camera coupled to a high resolution optical microscope allows time lapse imaging and monitoring of the critical filling level of the capillaries during the entire functionalization process.

*UV-Ozone cleaning:* Our new Novascan UV-Ozone cleaning facility allows a fast in-house preparation of the cantilever arrays according to the newly established protocols. Prior to the

UV-ozone treatment, the cantilever is pre-cleaned by rinsing with ethanol and ultrapure water as well as by plasma etching [5]. In order to find efficient time cycles of the UV-ozone cleaning process, the effectiveness of the treatment was studied on several cantilever arrays with scanning electron microscopy (SEM) and atomic force microscopy (AFM) on different length scales.

The SEM image in Fig. 3 shows the side of a single cantilever, revealing fabrication related indentations. The AFM images depicted in Fig. 2 allow a closer look on the typical surface topology before and after UV-ozone cleaning. How this change in surface topology affects the success of the functionalization process is currently systematically tested with various sensing molecular layers.

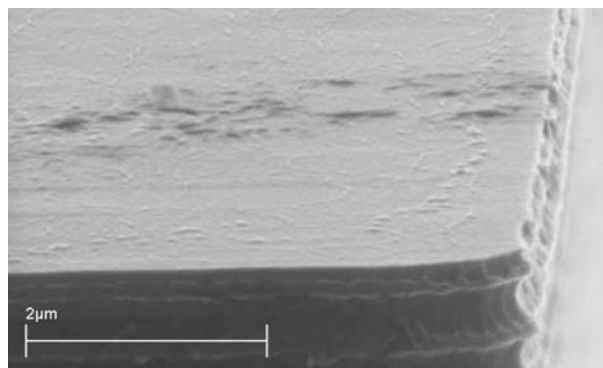


**Figure 3:** SEM of Cantisens Cantilever: typical gold clustering after coating with Au. Image: K. Macknapp, Deutsches Museum, U = 20 kV.

### Current Research

A new project was started in collaboration with the Simmel group, Technical University Munich: a translation of a well-established solution-DNA-protein binding assay onto the cantilever surface. In solution, this system consists of a DNA-aptamer that has been proofed to repeatedly catch and release thrombin [6]. We are currently modifying the cantilever sensor surface in order to facilitate the thrombin recognition. As a first step we successfully attached the DNA-aptamer to a gold coated cantilever via sulfur linker chemistry.

The main research on the cantilever sensor platform focuses on protein-carbohydrate interactions which are relevant for most of the processes occurring on a cell surface [7]. On this topic we collaborate with Prof. P. Seeberger, MPI Potsdam, and Prof. A. Rubio, University of San Sebastian. We identified a basic protein-carbohydrate model system helping to identify the crucial protocol steps. It appears that centrifuge time and speed had to be optimized in order to facilitate reproducible and selective binding in the background of similar sugar derivatives. Meanwhile the molecular recognition is sensitive down to micro molar protein concentrations and the observed signal size of the cantilever deflection was proofed to increase with higher protein concentrations. These, to the best of our knowledge, are the first protein-carbohydrate-interactions reported with cantilever arrays.

### Aging of Organic Superconductors

*J. Büttner, F. Palitschka, C. Rohr, B. A. Hermann  
N. D. Kushch,<sup>8</sup> M. V. Kartsovnik, and W. Biberacher*

Organic superconductors of the BEDT-TTF family have a layered nature and show a pseudogap [8]. Because of that, these materials are of high interest for the understanding of the nature and physics of high-temperature superconductors [9]. The crystal structure facing the cation-layer is shown on the right (see Fig. 4); the anion layer is faded out for better clarity. Due to the fragility of organic superconductor crystals as a result of the weak charge-transfer bonding, we conducted a study on crystals of drastically different age.

<sup>8</sup>Institute of Chemical Physics, Russian Academy of Science, Chemogolovka, Moscow-Region, Russia.

### Topographic Images of $(\text{ET})_2\text{Cu}(\text{NCS})_2$

New crystals of  $\kappa\text{-(BEDT-TTF)}_2\text{Cu}(\text{NCS})_2$  were synthesized during a guest stay of N.D. Kushch at the WMI in November 2007. Figure 5(a) displays a room temperature STM image of a b-c plane of such a recently grown single crystal. While the distance of the stripes in the STM picture agrees well with a unit cell length of 1.31 nm, the inner details of a such defined unit cell can not straightforwardly be attributed to an inner structure of the molecule, as a comparison with the above depicted crystal structure reveals.

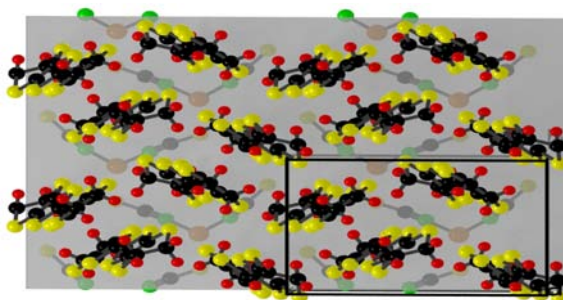
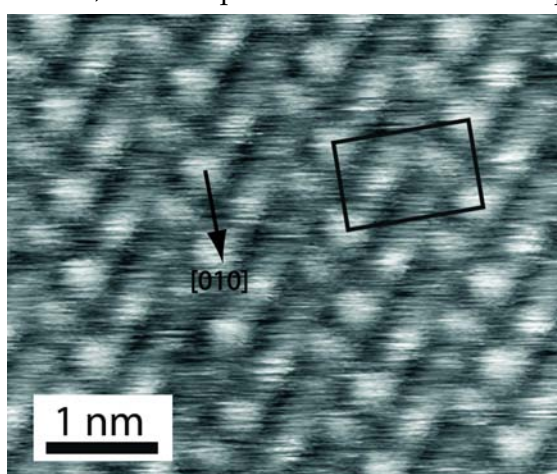
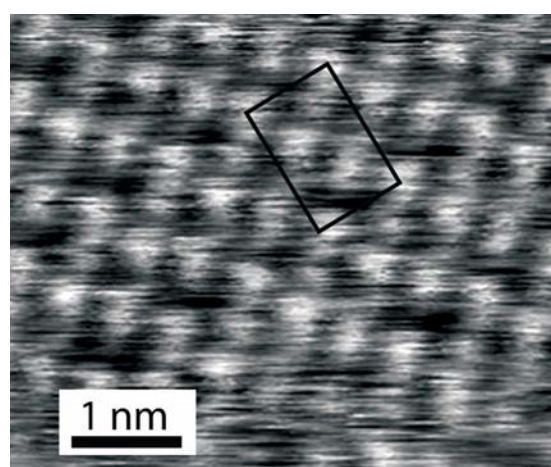


Figure 4: Molecular arrangement of the cation layer (anion layer faded) within a  $\kappa\text{-(BEDT-TTF)}_2\text{Cu}(\text{NCS})_2$ -crystal.



(a) Newly synthesized sample.



(b) Ten year old sample.

Figure 5: Samples of  $\kappa\text{-(BEDT-TTF)}_2\text{Cu}(\text{NCS})_2$  of different age in comparison.

### Density-Functional-Theory

To clarify the molecular positions observed in the STM measurements, density functional theory (DFT)-calculations as exemplified in Fig. 6 were performed with a newly upgraded CASTEP DFT package. In order to mimic the behavior of a finite tip size, the images were afterwards blurred with a Gaussian filter. Based on these simulations the molecular position could be determined with high accuracy.

### Aging

An image of a more than 10 year old  $\kappa\text{-(BEDT-TTF)}_2\text{Cu}(\text{NCS})_2$ -crystal is depicted in Fig. 5(b): No degeneration or aging effect in any way can be observed. Even after ten years the STM images reveal a surface in sub-molecular resolution, agreeing well with the DFT-calculations.

### Discussion

We confirmed the recently reported symmetry breaking [10–12] as well as the enhanced bright-

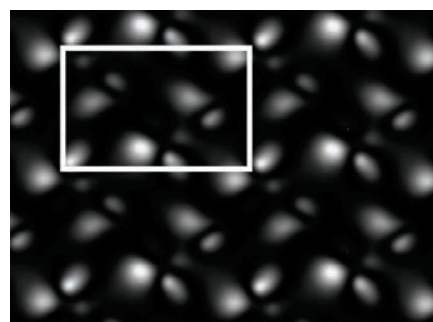


Figure 6: DFT-calculation

ness along the [010] direction and find a close match of these properties in the here newly presented DFT-surface simulations of the *bc* plane (cation layer) of  $\kappa$ -(BEDT-TTF)<sub>2</sub>Cu(NCS)<sub>2</sub> crystals. This suggests that the symmetry breaking and enhanced brightness lies in the surface electronic properties rather than in tip-molecule interactions or insulation layers or slight position relaxation of the surface molecules as suggested before [13]. The collaborations currently proceeds on investigations of the anion-layer and on spectroscopic insights of these materials.

## References

- [1] L. Merz, H.-J. Güntherodt, L. Scherer, E.C. Constable, C.E Housecroft, M. Neuburger, and B.A. Hermann, Chem. Eur. J. **11**, 2307 (2005).
- [2] C. Rohr, Diploma thesis LMU (2007).
- [3] C. Höhl, Diploma thesis LMU (2008).
- [4] K. Gruber, Diploma thesis LMU (2007).
- [5] J. R. Vig, J. Vac. Sci. Technol.A **3**, 1027 (1985).
- [6] W. U. Dittmer, A. Reuter, and F. C. Simmel, Angew. Chem. Int. Ed. **43**, 3549 (2004).
- [7] E.W. Adams, J. Ueberfeld, D.M. Ratner, B.R. O’Keefe, D.R. Walt, and P.H. Seeberger, Angew. Chem. Int. Ed. **42**, 5317 (2003).
- [8] T. Arai, K. Ichimura, K. Nomura, S. Takasaki, J. Yamada, S. Nakatsuji, and H. Anzai, Solid State Commun. **116**, 679 (2000).
- [9] K. Ichimura, T. Arai, K. Nomura, S. Takasaki, J. Yamada, S. Nakatsuji, H. Anzai, T. Nakamura, T. Takahashi, B. Hilti, and J.S. Zambounis, J. Supercond. **12**, 519 (1999).
- [10] M. Ishida, O. Takeuchi, T. Mori, and H. Shigekawa, Phys. Rev. B **64**, 153405 (2001).
- [11] S. Yoon, W.F. Smith, M. Yoo, A.L. deLozanne, R. Fainchtein, T.J. Kistenmacher, S.T. D’Arcangelis, and D.O. Cowan, Phys. Rev. B **47**, 4802 (1993).
- [12] M. Ishida, O. Takeuchi, T. Mori, and H. Shigekawa, Jap. J. Appl. Phys. **39**, 3823 (2000).
- [13] F. Palitschka, J.M. Büttner, C.L. Rohr, N.D. Kuschsch, M.V. Kartsovnik, W. Biberacher, and B.A. Hermann, Eur. Phys. J., (accepted).

## Fabrication and Characterization of Superconducting Flux Qubits

T. Niemczyk, L. Eggenstein, E. Hoffmann, E. Menzel, F. Deppe, M. Mariani, C. Probst, A. Marx, R. Gross<sup>1</sup>

In 1994, the field of Quantum Information Processing (QIP) emerged when Peter W. Shor published an efficient algorithm for prime factorization of large integers using a theoretical quantum computer. During the last years, different experimental realizations of the fundamental building blocks – the so-called ‘qubits’ – of future quantum computers made QIP one of the most active research topics in physics. The main areas of interest include quantum computation, quantum cryptography, and quantum communication.

Among the various different realizations of quantum bits, solid-state based superconducting qubits have gained increasing interest during the last years. One particular advantage of superconducting qubits – compared to other solid-state based realizations of quantum bits – is the fact that the superconducting condensate is decoupled from quasiparticle excitations by an energy gap. At WMI, we focus on the design and realization of superconducting flux qubits. The solid state circuits behave as ‘artificial atoms’ and are characterized by microwave spectroscopy at mK temperatures in our experiments [1].

The flux qubits [2–4] consist of a superconducting loop interrupted by three nm-sized Josephson junctions (JJs). Two of these JJs have the same area  $A$  ( $\simeq 0.02 \mu\text{m}^2$ ) and critical current  $I_c$ , while the other junction is designed to be smaller by a factor of  $\alpha$  with  $\alpha \sim 0.6 - 0.8$ . The two characteristic energies of this system are the Josephson coupling energy  $E_J = \hbar I_c / 2e$  and the charging energy  $E_c = e^2 / 2C_J$ .  $E_J$  is associated with the storage of a flux quantum  $\Phi_0 = h / 2e$  in the Josephson inductor while  $E_c$  is associated with the storage of a single electron charge  $e$  on the junction capacitance  $C_J$ . For low enough temperatures ( $k_B T \ll E_J, E_c$ ) and  $E_J / E_c$  ratios between 10 - 100, the circuit effectively behaves like a two-level quantum system. The ground  $|g\rangle$  and first excited state  $|e\rangle$  can be distinguished by opposite circulating persistent currents  $I_p$  which produce a measurable flux signal ( $\sim 10^{-3} \Phi_0$ ) due to the finite inductance of the qubit loop. For readout of this small flux signal the qubit loop is surrounded by a dc SQUID with large shunting capacitors. The level splitting  $\Delta_{ge}$  between  $|g\rangle$  and  $|e\rangle$  should be much larger than the thermal energy,  $\Delta_{ge} \gg k_B T$ , to avoid thermal population of the first excited state. Because  $T \sim 30$  mK corresponds to an energy and frequency of about  $2 \mu\text{eV}$  and  $600$  MHz,  $\Delta_{ge} / h \gtrsim 2$  GHz is desired. Since  $\Delta_{ge} \propto \hbar \omega_p \exp(-a \sqrt{E_J / E_c})$ , where  $\omega_p \propto E_c \sqrt{E_J / E_c}$  is the plasma frequency and  $a$  a constant of the order of unity, large  $E_c$  (small junction area) is required. At the same time one has to keep  $E_J / E_c$  large enough to have well-defined flux states with a measurable circulating current. These requirements are demanding regarding junction fabrication technology, asking for junctions with high critical current densities  $J_c \simeq 10^3$  A/cm<sup>2</sup> and areas down to a few  $0.01 \mu\text{m}^2$ .

Figure 1(a) shows a scanning electron microscopy (SEM) micrograph of a three-junction flux qubit based on Al/AlO<sub>x</sub>/Al junctions. The qubit is surrounded by the readout dc SQUID. Figures 1(d) and (e) show an enlarged view of the so-called  $\alpha$ -junction, which has a reduced area  $\alpha A$  with  $\alpha = 0.7$ , and one of the regular qubit junctions, respectively. The area of the  $\alpha$ -junction is only about  $0.02 \mu\text{m}^2$ . The qubits are fabricated on thermally oxidized (50 nm SiO<sub>2</sub>) Si wafers by electron beam lithography using a Philips XL30 SFEG field emission SEM and a Raith Elphy Plus nanolithography system. For producing free-standing resist masks we used a double-layer resist system. Typical cross-sectional views of the resist stencils are shown in

<sup>1</sup>This work is supported by the Deutsche Forschungsgemeinschaft through SFB 631 and the German Excellence Initiative via the Nanosystems Initiative Munich (NIM).

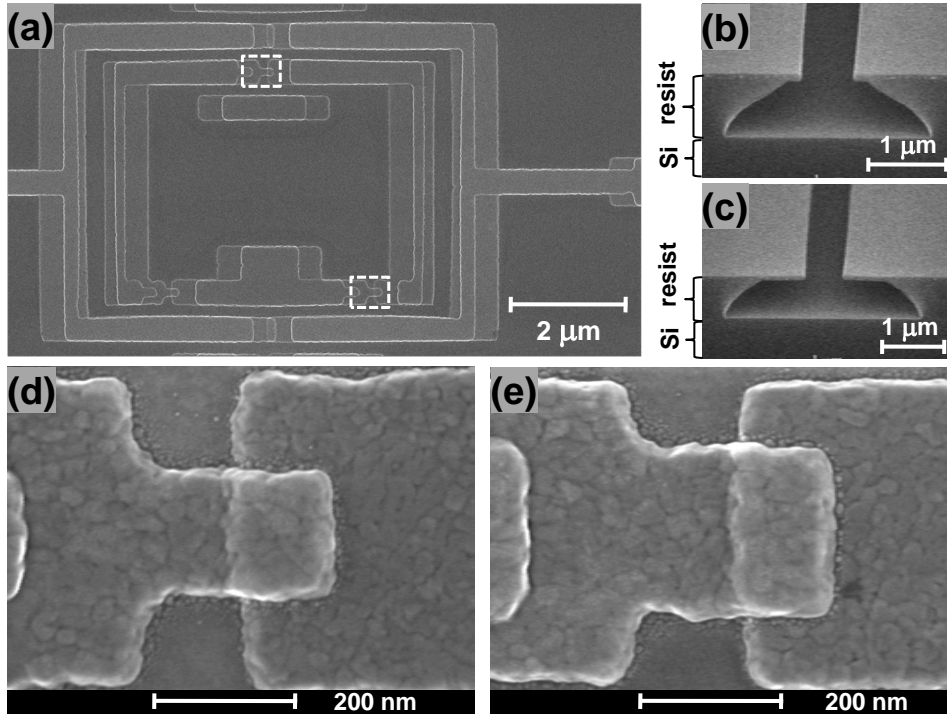


**Figure 1:** (a) SEM micrograph of a three-junction flux qubit (inner loop) surrounded by the readout dc SQUID (outer loop with two junctions). The white rectangles mark the regions of the  $\alpha$ -junction (upper) with a reduced area ( $\alpha = 0.7$ ) and a regular junction (lower) shown on an enlarged scale in (d) and (e), respectively. (b) and (c) show cross-sectional views of double-layer resist structures obtained with different exposure times. Large undercuts can be obtained, resulting in free-standing resist parts required for the shadow evaporation technique.

Figs. 1(b) and (c). Due to the larger sensitivity of the underlayer resist, large undercuts can be generated in a controlled way. The two-angle shadow evaporation of Al was done by electron beam evaporation in a UHV system with a base pressure in the  $10^{-9}$  mbar range. The bottom layer was thermally oxidized *in situ* in pure oxygen at  $p = 2 \cdot 10^{-4}$  mbar. In order to achieve high current densities we used small products  $L$  of oxygen pressure and oxidation time ranging between 0.25 and 0.26 mbar  $\cdot$  s. With these values we achieved  $J_c(50 \text{ mK}) \simeq 1500 \pm 500 \text{ A/cm}^2$  with a high yield of 85%. By optimizing the electron beam lithography process we could reduce the spread in the junction area down to 10%.

Figure 2 shows the current-voltage characteristics (IVC) and the flux dependence of the critical current of a readout dc SQUID fabricated with the process described above. From  $I_c = 1.44 \mu\text{A}$  and the measured junction area  $A = 0.035 \mu\text{m}^2$  we obtain  $J_c = 2 \text{ kA/cm}^2$ . Furthermore, from  $R_n = 169 \Omega$  the product  $I_c R_n = 243 \mu\text{V}$  is obtained. The measured gap voltage  $V_g \simeq 360 \mu\text{V}$  is close to the BCS value  $V_g = 2\Delta/e = 3.53k_B T_c/e = 365 \mu\text{V}$  using  $T_c = 1.2 \text{ K}$  for the critical temperature of Al. Furthermore, the measured  $I_c R_n$  product agrees well with the Ambegaokar-Baratoff value  $\pi V_g/4 = 287 \mu\text{V}$ .

The  $I_c(\Phi_{\text{ex}}^*)$  dependence of a readout dc SQUID is shown in Fig. 2(b). Here,  $\Phi_{\text{ex}}^*$  is the applied magnetic flux threading the SQUID loop, which is to be distinguished from the flux  $\Phi_{\text{ex}}$  threading the qubit loop. With the ratio of 1.37 between the SQUID and the qubit loop we estimate  $\Phi_{\text{ex}}^* = 0.685\Phi_0$  in good agreement with the experiment. The measured  $I_c(\Phi_{\text{ex}}^*)$  curve is close to the ideal  $|\cos(\pi\Phi_{\text{ex}}^*/\Phi_0)|$  dependence expected for an ideal dc SQUID with  $\beta_L = 2\pi L_s I_c / \Phi_0 = L_s / L_c \ll 1$ , for which the Josephson inductance  $L_c = \hbar/2eI_c$  dominates the geometric inductance  $L_s$ . However, there are small deviations, originating from the additional flux due to the persistent current  $I_p$  circulating clock- or counterclockwise in the qubit loop.

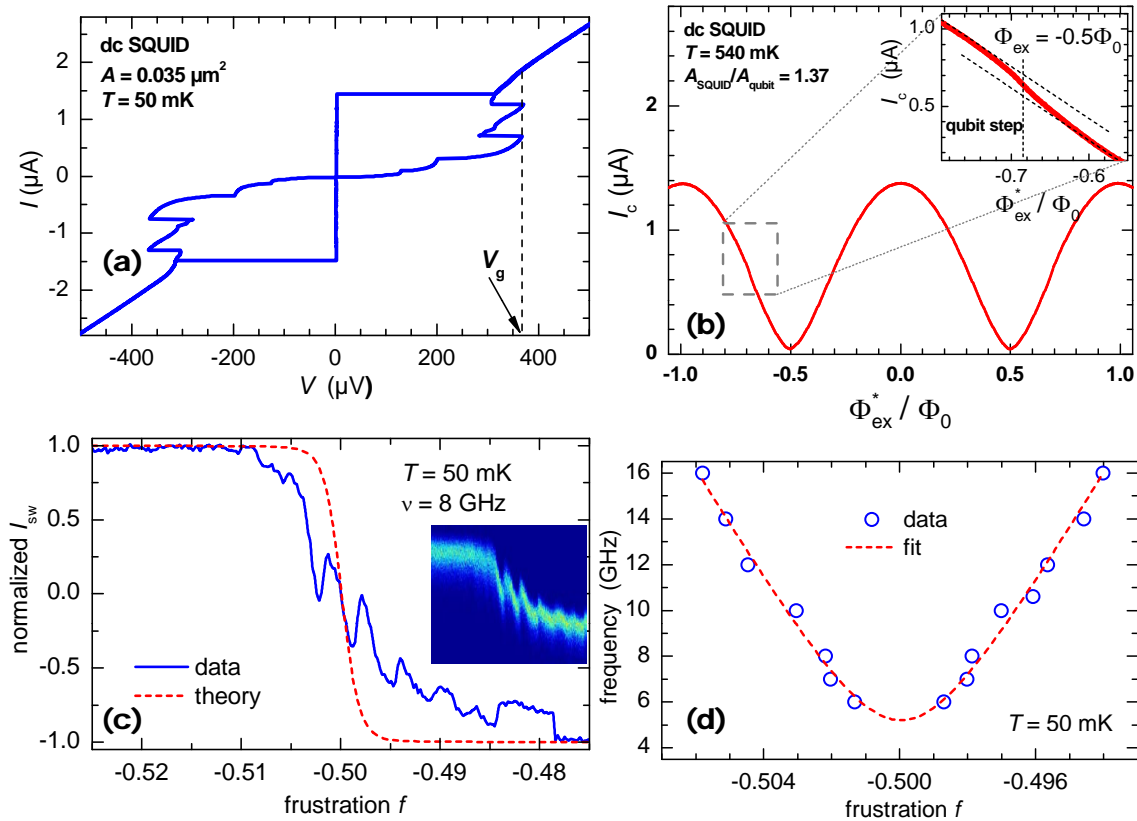


**Figure 2:** (a) Current-voltage characteristics of a readout dc SQUID based on Al/AIO<sub>x</sub>/Al tunnel junctions with  $A = 0.035 \mu\text{m}^2$  at  $T = 50 \text{ mK}$ . (b) Critical current  $I_c$  of a readout dc SQUID as a function of the applied magnetic flux  $\Phi_{\text{ex}}^*$  threading the SQUID loop at  $T = 540 \text{ mK}$ . The inset shows an enlarged view of the region around  $\Phi_{\text{ex}} = -\gamma\Phi_0/2$ , where the qubit persistent current changes sign. Here,  $\gamma = 1.37$  is the ratio of the loop areas of the SQUID and the qubit. (c) Normalized switching current  $I_{\text{sw}}$  of the readout dc SQUID plotted versus the frustration  $f = \Phi_{\text{ex}}/\Phi_0$  in the region around the qubit step at  $T = 50 \text{ mK}$ . The qubit is irradiated by a microwave signal ( $\nu = 8 \text{ GHz}$ ). The dashed curve shows the theoretically expected curve without microwave irradiation for  $\Delta_{\text{ge}}/h = 5.2 \text{ GHz}$ . The inset shows the switching current distribution in a color coded image. (d) Qubit transition frequency  $E_{\text{ge}}/h$  (symbols) plotted versus the frustration  $f$ . The line is a numerical fit to the data yielding  $\Delta_{\text{ge}}/h = 5.2 \text{ GHz}$  and  $I_p = 450 \text{ nA}$ .

In the region around  $\Phi_{\text{ex}} = \Phi_0/2$ ,  $I_p$  changes sign. This results in a step-like feature superimposed on the regular  $I_c(\Phi_{\text{ex}}^*)$  dependence. This so-called qubit step is shown in the inset of Fig. 2(b).

The qubit level structure has been investigated by microwave spectroscopy. Figure 2(c) shows the normalized switching current of the readout SQUID around the qubit step plotted versus the frustration  $f = \Phi_{\text{ex}}/\Phi_0$ . Note that the switching of the SQUID from the zero-voltage into the voltage state is by quantum tunneling and, hence, is a statistical process. Therefore, the normalized switching current  $I_{\text{sw}}(f)$  is obtained from the switching current distribution measured for every  $f$ . This distribution is shown in a color-coded image in the inset of Fig. 2(c). The  $I_{\text{sw}}(f)$  curve shows a pronounced peak-dip structure due to resonant transitions between the qubit levels induced by the applied microwave irradiation with frequency  $\nu = 8 \text{ GHz}$ . Note that multi-photon transitions are observed depending on the applied microwave power. The position of the peaks/dips (one-photon transitions) as a function of frequency and frustration is shown in Fig. 2(d). The data follow the expected  $E_{\text{ge}} = \sqrt{\epsilon^2 + \Delta_{\text{ge}}^2}$  dependence, where  $\epsilon =$

$2I_p\Phi_0(f + 0.5)$  is the energy bias and  $\Delta_{ge}$  the level splitting at the degeneracy point  $f = -0.5$ . Fitting the data yields  $I_p = 450$  nA and a qubit gap of  $\Delta_{ge}/h = 5.2$  GHz.

In summary, we fabricated superconducting flux-qubits with energy splittings ranging from 2 to 5 GHz. Furthermore, we improved the electromagnetic environment of our circuits by implementing on-chip shunting capacitors, high-resistance bias lines and an on-chip microwave antenna.

## References

- [1] T. Niemczyk, F. Deppe, M. Mariani, E.P. Menzel, E. Hoffmann, G. Wild, L. Eggenstein, A. Marx, R. Gross, **Fabrication Technology of and Symmetry Breaking in Superconducting Quantum Circuits**, Superconductor Science and Technology, submitted for publication (2008).
- [2] J. E. Mooij, T. P. Orlando, L. S. Levitov, L. Tian, C. H. van der Wal and S. Lloyd, *Science* **285**, 1036 (1999).
- [3] T. P. Orlando, J. E. Mooij, L. Tian, C. H. van der Wal, L. S. Levitov, S. Lloyd and J. J. Mazo, *Phys. Rev. B* **60**, 15398 (1999).
- [4] C. H. van der Wal, A. C. J. ter Haar, F. K. Wilhelm, R. N. Schouten, C. J. P. M. Harmans, T. P. Orlando, S. Lloyd and J. E. Mooij, *Science* **290**, 773 (2000).

## Quantum Experiments on Electromechanical Systems

F. Hocke, T. Niemczyk, A. Marx, R. Gross<sup>1,2</sup>

During the last few years optomechanical systems have become a topic of considerable interest. In such a system a micro- or nanomechanical harmonic oscillator is coupled to the electromagnetic field inside a suitable cavity. Optomechanical systems, in which the coupling is sufficiently strong, may eventually allow to explore quantum effects such as superposition and entanglement, or the generation of cat states at a macroscopic scale. Thus, they are expected to provide new insight into phenomena at the boundary between quantum and classical physics. The cooling of mechanical modes by the light field in the cavity is a particularly interesting effect. Here, the cooling is achieved by the radiation pressure of the light field onto the mechanical oscillator. The oscillator's movement changes the intensity of the light field. The variation of the intensity has a certain delay to the mechanical motion. This leads to a force enhancing or damping the motion, depending on the frequency of the incident light. In principle, even cooling to the quantum mechanical ground state of the vibrational mode is possible [1]. Another interesting field of research is the design of ultra-sensitive measurements of a macroscopic object. Finally, the combination of optomechanical systems in the microwave regime with nonlinear circuit elements such as Josephson junctions or qubits open a new playground. The latter already have been successfully coupled to superconducting microwave transmission line resonators.

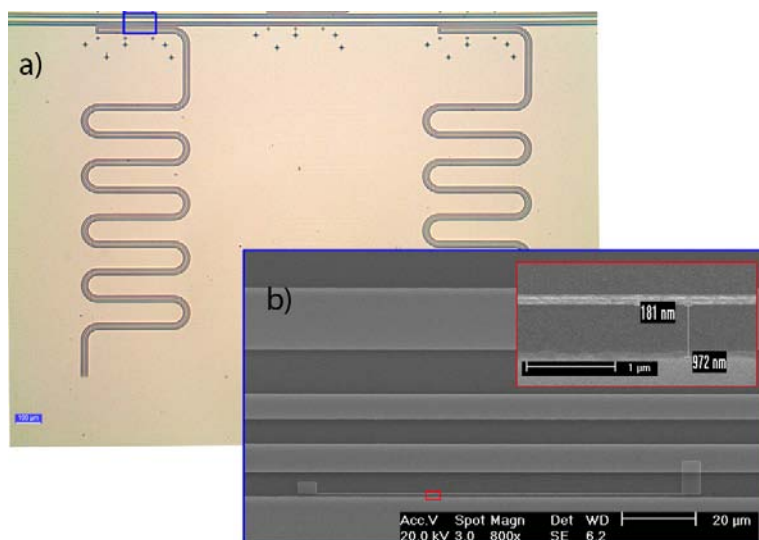


**Figure 1:** a) Optical micrograph of two  $\lambda/4$  Nb microwave cavities which are coupled to a microwave transmission line. The resonators are meandered to fit on the chip. The blue rectangle marks the area where the mechanical resonator will be placed. b) Scanning electron beam microscope image of a nanobeam coupled to a microwave cavity. The area marked by the red rectangle is shown on an enlarged scale in the inset, giving the dimensions of the beam and its distance to the groundplane.

resonator to a single electron transistor [2].

Recently, Regal *et al.* coupled a superconducting on-chip microwave transmission line resonator capacitively to a mechanical resonator (nanobeam) on a chip [10]. The motion of the

Until today, many different approaches have been considered for the realization of an optomechanical system. For example, the interaction of the radiation pressure of a light field inside a cavity with the vibrational degree of freedom of a movable micro-mirror [3–7] or a membrane inside the cavity [8] have been used. In an other attempt, the radiation field of a whispering gallery mode of a toroidal micro-cavity with its vibrational mode [9] has been successfully employed. In a recent experiment, the mechanical mode could be cooled to an occupation number of less than 60 phonons by coupling a suspended, nanomechanical

<sup>1</sup>This work is supported by the German Excellence Initiative via the Nanosystems Initiative Munich (NIM).

<sup>2</sup>in collaboration with the group of T. Kippenberg at the MPQ, Garching.

nanobeam modulates the resonance frequency of the microwave transmission line resonator, almost in the same way as the optical resonance is shifted by the mechanical motion in the usual optomechanical set-ups. The idea of using resonators in the microwave regime instead of optical cavities is very promising. It allows to perform on-chip measurements of optomechanical effects at cryogenic temperatures. The nanomechanical resonator is much lighter than the typical micro-mirrors. Moreover, it is not necessarily constrained to be larger than the radiation wavelength, and it is naturally strongly coupled to the microwave resonator.

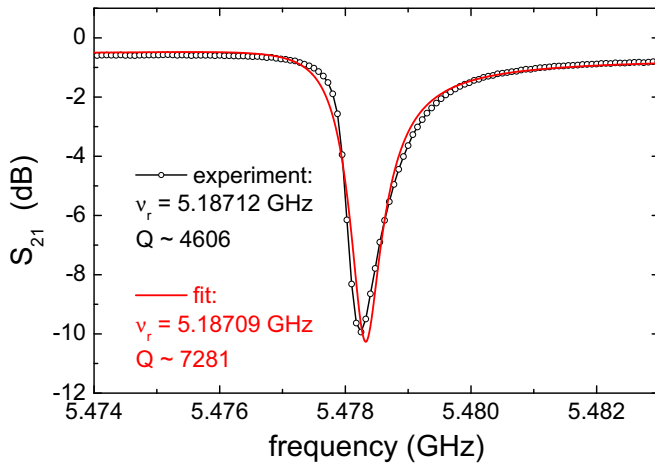


**Figure 2:** Transmission spectrum ( $S_{21}$  scattering parameter) of a microwave resonator measured at 4.2 K (black) together with a fit to the data (red). The coupling capacity is, according to simulations, approximately 7 fF. The applied microwave power was  $-20$  dBm.

tion of nm-sized metal structures required for the nanobeams we made use of the well established nanofabrication tools (electron beam lithography, electron beam evaporation, and lift-off process) already available for Al. As an additional process step, an underetching process is required to obtain suspended nanobeams which are clamped at both ends. This underetching can be achieved much more straight forwardly with Al than with Nb. The microwave resonators are fabricated by rf-sputter depositing Nb films onto Si substrates. The frequency multiplexed design shown in Fig. 1, where a number of  $\lambda/4$  microwave resonators with different lengths are coupled to a microwave transmission line, allows to study multiple cavities on a single chip in one cool down process. The cavities are defined by optical lithography and reactive ion etching (RIE) in a  $\text{SF}_6$  plasma. During the last year we designed and fabricated microwave resonators with varying coupling strength to the microwave feedline on silicon wafers.

The fabricated LC resonator were demonstrated to work with a reasonable quality factor (cf. Fig. 2), although the Nb layer was only 50 nm thick. This is only half of the thickness we intend to use in the final setup and gives rise to increased losses compared to thicker films. The mechanical resonators are produced by electron lithography, electron beam evaporation of Al on top of the exposed resist, and a final lift-off

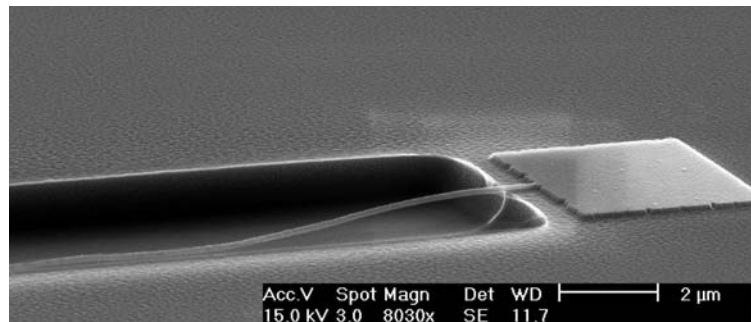


**Figure 3:** Scanning electron microscopy micrograph of first tests to suspend the mechanical resonators using a RIE process. In this process the beam is elongated.

process. To optimize the geometrical parameters, several resists with varying thickness were tested. After this optimization we can fabricate Al nanobeams up to a length of  $210\ \mu\text{m}$  with a width down to around  $130\ \text{nm}$ . For a shorter beam length of only  $110\ \mu\text{m}$ , we even can achieve a smaller beam width down to  $70\ \text{nm}$ . At present, the first experiments fabricating Al nanobeams on an existing LC circuit are under way (cf. Fig. 1).

To produce free standing Al nanobeams the Si substrate was chemically etched close to the nanobeam. Here, both a RIE process with small ion energies to minimize the physical etching contribution and a purely chemical etching in  $\text{XeF}_2$  atmosphere<sup>3</sup> were used. The former process was found to result in an elongation and, in turn, bending of the beams (cf. Fig. 3). Although the reason for this behavior is not yet clear, a likely origin is the finite heat load during the etching process, causing a temperature increase and irreversible stretching of the nanobeams. In contrast, the purely chemical  $\text{XeF}_2$  etching does not seem to affect the beams. Interestingly, the Nb layer which is present in close vicinity to the Al nanobeam is found to enhance the etching rates. This effect is investigated in more detail presently. Although some details of the fabrication process needs further clarification, we succeeded to fabricate suspended nanobeams suitable for mechanical resonators.

In summary, we managed to realize the individual building blocks of a set-up allowing the study of various effects arising from optomechanical coupling [10]. At present, all components are characterized, further optimized, and finally combined into a fully operating system. Especially the etching process to produce suspended nanobeams represents a critical step and needs more detailed analysis.

## References

- [1] F. Marquardt, J. P. Chen, A. A. Clerk, and S. M. Girvin, *Phys. Rev. Lett.* **99**, 093902 (2007).
- [2] M. D. LaHaye, O. Buu, B. Camarota, and K. C. Schwab, *Science* **304**, 74 (2004).
- [3] C. Höhberger Metzger and K. Karrai, *Nature* **432**, 1002 (2004).
- [4] O. Arcizet, P.-F. Cohadon, T. Briant, M. Pinard, and A. Heidmann, *Nature* **444**, 71 (2006).
- [5] S. Gigan, H. R. Böhm, M. Paternostro, F. Blaser, G. Langer, J. B. Hertzberg, K. C. Schwab, D. Bauerle, M. Aspelmeyer, and A. Zeilinger, *Nature* **444**, 67 (2006).
- [6] D. Kleckner and D. Bouwmeester, *Nature* **444**, 75 (2006).
- [7] T. Corbitt, Y. Chen, E. Innerhofer, H. Müller-Ebhardt, D. Ottaway, H. Rehbein, D. Sigg, S. Whitcomb, C. Wipf, and N. Mavalvala, *Phys. Rev. Lett.* **98**, 150802 (2007).
- [8] J. D. Thompson, B. M. Zwickl, A. M. Jayich, F. Marquardt, S. M. Girvin, and J. G. E. Harris, *Nature* **452**, 72 (2008).
- [9] A. Schliesser, R. Riviere, G. Anetsberger, O. Arcizet, and T. J. Kippenberg, *Nature Physics* **4**, 415 (2008).
- [10] C. A. Regal, J. D. Teufel, and K. W. Lehnert, *Nature Physics* **4**, 555 (2008).

---

<sup>3</sup>This etching process was performed in the group of T. Kippenberg at the MPQ, Garching.

## Voltage Controlled Inversion of the Magnetic Anisotropy in a Ferromagnetic Thin Film at Room Temperature

M. Weiler, A. Brandlmaier, S. Geprägs, M. Althammer, M. Opel, S.T.B. Goennenwein, and R. Gross<sup>1</sup>  
C. Bihler, H. Huebl, M.S. Brandt<sup>2</sup>

Multifunctional material systems unite different, e.g., electric and magnetic, functionalities in either a single phase or a heterostructure. They are of great fundamental and technological interest, as they allow to control magnetic properties by electric fields or vice versa. An electric field control of magnetization orientation is particularly appealing, as it removes the need to generate magnetic fields of sufficient strength for magnetization switching on small length scales – thus enabling novel concepts for high density magnetic data storage applications.

One possibility to achieve such an electric field control of magnetization is to use a material system that unites piezoelectric and magnetoelastic properties. Piezoelectric materials deform if they are exposed to an electric field, whereas in ferromagnets that show magnetoelasticity (magnetostriction) the magnetization orientation changes upon mechanical deformation. Hence, in a hybrid system that consists of a piezoelectric and magnetoelastic constituent, one can control the magnetization orientation of the magnetoelastic phase by applying an electric field to the mechanically coupled piezoelectric phase [1–4].

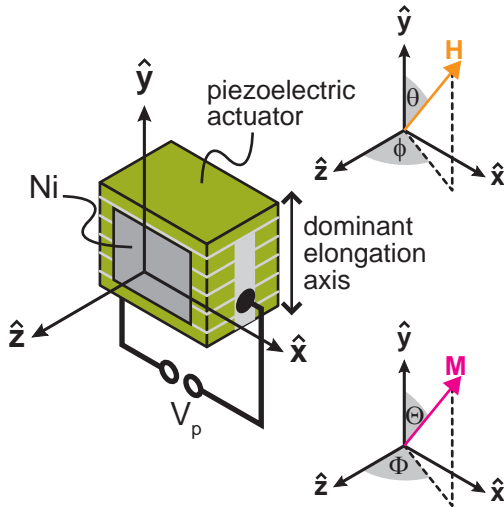


**Figure 1:** Schematic illustration of the Ni thin film/piezoelectric actuator hybrid together with the definition of angles denoting the orientations of the external magnetic field and the magnetization.

In this spirit, we fabricated ferromagnetic thin film/piezoelectric actuator structures by depositing 70 nm of nickel onto piezoelectric actuators [5] of dimensions  $x \times y \times z = 3 \times 2.6 \times 2 \text{ mm}^3$ . Nickel was chosen as the ferromagnetic constituent as it is a prototype 3d itinerant ferromagnet with a Curie temperature  $T_c = 627 \text{ K}$  well above room temperature, a high bulk saturation magnetization  $M_s = 411 \text{ kA/m}$  and sizeable volume magnetostriction  $\bar{\lambda} = -32.9 \times 10^{-6}$ . The resulting hybrid is sketched in Fig. 1(a) together with the definition of the angles that describe the orientation of the magnetization  $\mathbf{M} = (M, \Theta, \Phi)$  and the external magnetic field  $\mathbf{H} = (H, \theta, \phi)$  in the sample-affixed coordinate system. In this hybrid, it becomes possible to control the orientation of the magnetization vector by applying appropriate voltages  $V_p$  to the actuator as the actuator exhibits a hysteretic mechanical stroke of up to  $1.3 \times 10^{-3}$  [5] along its dominant elongation axis (cf. Fig. 1) if voltages  $-30 \text{ V} \leq V_p \leq +150 \text{ V}$  are applied.

To phenomenologically describe the impact of this lattice strain on the Ni magnetization orientation we use a magnetic free energy density approach. The free energy  $F_{\text{tot}}$  is a measure for the angular dependence of the magnetic hardness, with maxima in  $F_{\text{tot}}$  corresponding to magnetically hard directions and minima to magnetically easy directions. In equilibrium, the mag-

<sup>1</sup>This work is supported by the German Excellence Initiative via the “Nanosystems Initiative Munich (NIM)” and the Deutsche Forschungsgemeinschaft via SPP 1157 (project GR 1132/13) and project GO 944/3.

<sup>2</sup>Walter Schottky Institut, Technische Universität München, 85748 Garching, Germany

netization always resides in a local minimum (easy direction) of  $F_{\text{tot}}$ . The magnetic anisotropy of our Ni film is described by the magnetic free energy density

$$F_{\text{tot}} = F_{\text{stat}} + F_{\text{demag}} + F_{\text{magel}}. \quad (1)$$

The first term  $F_{\text{stat}} = -\mu_0 MH(\sin \Theta \sin \Phi \sin \theta \sin \phi + \cos \Theta \cos \theta + \sin \Theta \cos \Phi \sin \theta \cos \phi)$  in Eq. (1) describes the influence of an external magnetic field  $\mathbf{H}$  on the orientation of  $\mathbf{M}$ . The uniaxial demagnetization term  $F_{\text{demag}} = \frac{\mu_0}{2} M^2 \sin^2 \Theta \cos^2 \Phi$  is the anisotropy caused by the thin-film shape of the sample. Due to this large contribution to  $F_{\text{tot}}$ , the magnetization always resides within the Ni film plane. The last contribution to Eq. (1),

$$F_{\text{magel}} = \frac{3}{2} \bar{\lambda} \left( c_{12}^{\text{Ni}} - c_{11}^{\text{Ni}} \right) \left[ \varepsilon_1 (\sin^2 \Theta \sin^2 \Phi - 1/3) + \varepsilon_2 (\cos^2 \Theta - 1/3) + \varepsilon_3 (\sin^2 \Theta \cos^2 \Phi - 1/3) \right], \quad (2)$$

describes the influence of the lattice strains on the magnetic anisotropy. The pure strains along the  $\hat{\mathbf{x}}$ -,  $\hat{\mathbf{y}}$ - and  $\hat{\mathbf{z}}$ -axis are denoted as  $\varepsilon_1, \varepsilon_2$  and  $\varepsilon_3$ , respectively. Furthermore,  $c_{11}^{\text{Ni}} = 2.5 \times 10^{11} \text{ N/m}^2$  and  $c_{12}^{\text{Ni}} = 1.6 \times 10^{11} \text{ N/m}^2$  are the elastic moduli of Ni.

The strains  $\varepsilon_i$  are linked by the Poisson ratio  $\nu = 0.45$  of the actuator [5] and the elasticity of the Ni film [4] according to

$$\begin{aligned} \varepsilon_1 &= -\nu \varepsilon_2 \\ \varepsilon_3 &= -\frac{c_{12}^{\text{Ni}}}{c_{11}^{\text{Ni}}} (\varepsilon_1 + \varepsilon_2). \end{aligned} \quad (3)$$

With Eqs. (3) and (2) we can now calculate the magnetic free energy density of the Ni film for any given strain  $\varepsilon_2$  along the actuator's dominant elongation axis [cf. Fig. 1(a)]. While the exact voltage-strain relation  $\varepsilon_2(V_p)$  of the actuator is known from its data sheet [5] one can roughly estimate it as being linear as

$$\varepsilon_2 = \frac{\delta L}{L} \frac{V_p}{180 \text{ V}}, \quad (4)$$

where  $\delta L/L = 1.3 \times 10^{-3}$  is the nominal full actuator stroke for the full voltage swing  $-30 \text{ V} \leq V_p \leq +150 \text{ V}$ .

To determine the magnetic anisotropy of the ferromagnetic thin film/piezoelectric actuator hybrid experimentally, we rely on ferromagnetic resonance (FMR) spectroscopy. FMR is the resonant absorption of a microwave frequency magnetic field in a ferromagnet exposed to an external static magnetic field. Technically, the microwave frequency is kept constant while the external magnetic field is slowly varied. Ferromagnetic resonance occurs at the resonant magnetic field  $\mu_0 H_{\text{res}}$ . Hereby, smaller resonance fields correspond to magnetically easier directions and larger resonance fields to magnetically harder directions.

We obtained the full magnetic anisotropy of the ferromagnetic thin film/piezoelectric actuator hybrid by recording FMR traces at constant  $V_p \in \{-30 \text{ V}, +20 \text{ V}\}$  for several different  $\mathbf{H}$  orientations. The FMR fields thus determined in experiment are shown as symbols in the polar plot in Fig. 2(a). In this plot the distance of the FMR field from the plot origin is a direct measure of the magnetic hardness of the respective direction. The open blue triangles represent the resonance fields obtained for  $V_p = -30 \text{ V}$  and the full red circles those obtained for  $V_p = +20 \text{ V}$ . The lines represent simulations of the resonance field using the magnetic free energy density in Eq. (2) as explained in more detail in [3].

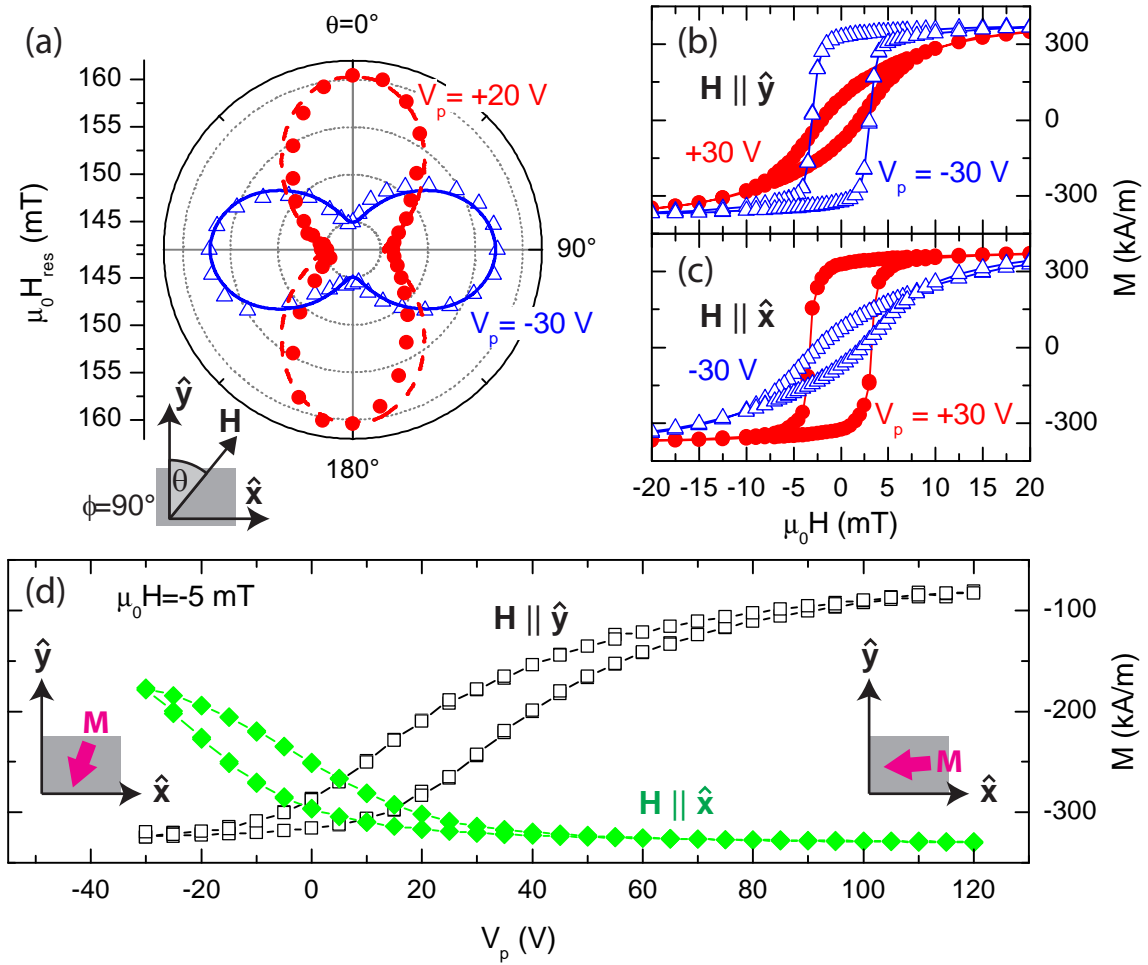


**Figure 2:** (a) FMR yields a uniaxial ( $180^\circ$  periodic) anisotropy of  $\mu_0 H_{\text{res}}(\theta)$  for  $V_p = +20$  V and  $V_p = -30$  V. However, its easy axis is rotated by  $90^\circ$  as  $V_p$  is changed from  $+20$  V to  $-30$  V. (b) SQUID  $M(H)$ -loops recorded with  $\mathbf{H} \parallel \hat{y}$  show a higher remanent magnetization for  $V_p = -30$  V than for  $V_p = +30$  V, thus the  $\hat{y}$ -axis is magnetically easier for  $V_p = -30$  V than for  $V_p = +30$  V. (c) The  $\hat{x}$ -axis is magnetically easier for  $V_p = +30$  V than for  $V_p = -30$  V. (d) SQUID  $M(V_p)$ -loops at constant external magnetic field strength  $\mu_0 H = -5$  mT show that  $\mathbf{M}$  exhibits a reversible rotation of approximately  $70^\circ$  as a function of  $V_p$ .

The obtained  $\mu_0 H_{\text{res}}(\theta)$  show minima at  $\theta = 0^\circ$  and  $\theta = 180^\circ$  for  $V_p = -30$  V and at  $\theta = 90^\circ$  and  $\theta = 270^\circ$  for  $V_p = +20$  V, respectively. Thus, a clear  $180^\circ$  periodicity of the resonance fields and hence a uniaxial magnetic anisotropy is observed for both  $V_p$ . As the orientations  $\theta$  corresponding to minima of  $\mu_0 H_{\text{res}}$  for one voltage coincide with maxima for the other voltage, we conclude that the direction of the easy axis is rotated by  $90^\circ$  if  $V_p$  is changed from  $V_p = -30$  V to  $V_p = +20$  V. In other words, for  $V_p = -30$  V the  $\hat{y}$  axis is the easy axis and for  $V_p = +20$  V the  $\hat{x}$  axis is the easy axis.

While we have shown so far that the in-plane uniaxial anisotropy of the Ni film can be inverted by applying appropriate voltages  $V_p$  to the actuator, in the following we demonstrate that the magnetization vector actually rotates to follow the minimum in the magnetic free energy density as a function of  $V_p$ . To this end, we employ superconducting quantum interference device (SQUID) magnetometry to record the projection  $m$  of the total magnetic moment  $\mathbf{m}$  onto the direction of the external magnetic field  $\mathbf{H}$ .

In a first series of experiments we recorded  $m$  as a function of the external magnetic field magnitude  $\mu_0 H$  at fixed orientations of  $\mathbf{H}$  and fixed voltages  $V_p$  at  $T = 300$  K. Figure 2(b)

shows  $M = m/V$  (with the Ni film volume  $V = 3.5 \times 10^{-13} \text{ m}^3$ ) measured with  $\mathbf{H} \parallel \hat{\mathbf{y}}$  as a function of the external magnetic field strength at constant voltage  $V_p = +30 \text{ V}$  (full red circles) and  $V_p = -30 \text{ V}$  (open blue triangles). The Ni film exhibits a rectangular  $M(H)$ -loop for  $V_p = -30 \text{ V}$ , while for  $V_p = +30 \text{ V}$  the remanent magnetization is lowered by a factor of approximately three. The rectangular loop for  $V_p = -30 \text{ V}$  indicates a magnetically easy axis, while the smooth, s-shaped loop for  $V_p = +30 \text{ V}$  indicates a magnetically harder axis. Thus, Fig. 2(b) shows that the  $\hat{\mathbf{y}}$ -direction is magnetically *easier* for  $V_p = -30 \text{ V}$  and *harder* for  $V_p = +30 \text{ V}$  – as expected from the FMR experiments. Changing the orientation of  $\mathbf{H}$  to  $\mathbf{H} \parallel \hat{\mathbf{x}}$  yields the  $M(H)$ -loops shown in Fig. 2(c). Following the same line of argument we can conclude that the  $\hat{\mathbf{x}}$ -direction is magnetically *easier* for  $V_p = +30 \text{ V}$  and *harder* for  $V_p = -30 \text{ V}$ . Altogether these results demonstrate that we observe a uniaxial in-plane anisotropy, the easy axis of which is parallel to  $\hat{\mathbf{y}}$  for  $V_p = -30 \text{ V}$  and parallel to  $\hat{\mathbf{x}}$  for  $V_p = +30 \text{ V}$ . These observations are fully consistent with the FMR results.

We now turn to the experimental measurement of the voltage control of  $\mathbf{M}$  orientation. To verify that  $\mathbf{M}$  can be rotated by varying  $V_p$  alone, we varied  $V_p$  at constant external magnetic bias field  $\mu_0 H = -5 \text{ mT}$ . We obtained the results shown in Fig. 2(d). The open black squares measured with  $\mathbf{H} \parallel \hat{\mathbf{y}}$  show that while the projection of  $\mathbf{M}$  to the negative  $\hat{\mathbf{y}}$  direction is large for negative  $V_p$ , it vanishes for positive  $V_p$ . At the same time, for  $\mathbf{H} \parallel \hat{\mathbf{x}}$  (full green diamonds), the projection of  $\mathbf{M}$  to the negative  $\hat{\mathbf{x}}$  direction is large for positive  $V_p$  and vanishes for negative  $V_p$ . Taken together, the opposing trend in the  $M(V_p)$ -loops observed for  $\mathbf{H} \parallel \hat{\mathbf{y}}$  and  $\mathbf{H} \parallel \hat{\mathbf{x}}$  evidences that  $\mathbf{M}$  rotates from mainly antiparallel to  $\hat{\mathbf{y}}$  at  $V_p = -30 \text{ V}$  to mainly antiparallel to  $\hat{\mathbf{x}}$  at  $V_p = +120 \text{ V}$ . As shown by the two schematic insets we thus observe a  $\mathbf{M}$  rotation of approximately  $70^\circ$ . The fact that both  $M(V_p)$ -loops shown in Fig. 2(d) are closed demonstrates that this purely voltage controlled rotation of  $\mathbf{M}$  is reversible. The hysteresis visible in Fig. 2(d) is caused by the hysteretic voltage-strain relation of the actuator [5]. We note that these  $M(V_p)$  experiments can be quantitatively modeled using a Stoner-Wohlfarth type of approach as shown in [3].

In conclusion, we have investigated the magnetic properties of a ferromagnetic thin film/piezoelectric actuator hybrid. FMR experiments demonstrated that the in-plane magnetic anisotropy of the hybrid is inverted if the sign of  $V_p$  is changed (cf. Fig. 2(a)). The SQUID magnetometry results shown in Fig. 2(d) demonstrate that it is possible to reversibly control the magnetization orientation in a range of approximately  $70^\circ$  by simply changing  $V_p$  at a constant small external magnetic bias field. This approach could be implemented and exploited in a variety of existing spintronic devices, e.g. to control the magnetization orientation in individual magnetic random access memory bits.

## References

- [1] C. Bihler, M. Althammer, A. Brandlmaier, S. Geprägs, M. Weiler, M. Opel, W. Schoch, W. Limmer, R. Gross, M.S. Brandt, S.T.B. Gönnerwein, Phys. Rev. B **78**, 045203 (2008).
- [2] S.T.B. Gönnerwein, M. Althammer, C. Bihler, A. Brandlmaier, S. Geprägs, M. Opel, W. Schoch, W. Limmer, R. Gross, M.S. Brandt, Phys. Status Solidi (RRL) **2**, 96 (2008).
- [3] M. Weiler, A. Brandlmaier, S. Geprägs, M. Althammer, M. Opel, C. Bihler, H. Hübl, M.S. Brandt, R. Gross, S.T.B. Gönnerwein, New J. Phys. **10**, *in press* (2008)
- [4] A. Brandlmaier, S. Geprägs, M. Weiler, A. Boger, M. Opel, H. Huebl, C. Bihler, M.S. Brandt, B. Botters, D. Grundler, R. Gross, S.T.B. Gönnerwein, Phys. Rev. B **77**, 104445 (2008).
- [5] *Low voltage co-fired multilayer stacks, rings and chips for actuation*, Piezomechanik GmbH, Munich, 2006, Model Pst 150/2x3/5, low temperature.

# Epitaxial $\text{Zn}_x\text{Fe}_{3-x}\text{O}_4$ Thin Films: A Spintronic Material with Tunable Electrical and Magnetic Properties

*D. Venkateshvaran, M. Althammer, A. Nielsen, S. Geprägs, S.T.B. Goennenwein, M. Opel, and R. Gross*<sup>1</sup>

*M.S. Ramachandra Rao*<sup>2</sup>

Spintronic materials and devices are in the focus of current research activities [1]. Regarding functionality, transition metal oxides are promising candidates. In this respect, the ferrimagnetic spinel oxide  $\text{Zn}_x\text{Fe}_{3-x}\text{O}_4$  combines high Curie temperature and spin polarization with tunable electronic and magnetic properties [2]. The parent compound magnetite ( $\text{Fe}_3\text{O}_4$ ) is known to have an inverse spinel structure (Fig. 1(a)). Eight *A* sites per unit cell surrounded by oxygen tetrahedra are occupied by trivalent  $\text{Fe}_A^{3+}$  ions ( $3d^5, S = 5/2$ ), whereas on 16 octahedrally coordinated *B* sites  $\text{Fe}_B^{2+}$  ( $3d^6, S = 2$ ) and  $\text{Fe}_B^{3+}$  ( $3d^5, S = 5/2$ ) ions are located in equal numbers. The density of itinerant charge carriers is determined by the density of the  $t_{2g}$  spin-down electron on the *B* site, i.e. by the density of  $\text{Fe}_B^{2+}$ . The magnetic exchange in magnetite is governed by a combination of antiferromagnetic superexchange (SE) between the  $\text{Fe}^{3+}$  ions on the *A* and *B* sites and ferromagnetic double exchange (DE) mediated by the itinerant spin-down  $t_{2g}$  electrons hopping between the mixed-valent Fe ions on the *B* sites (cf. Fig. 1). Since the antiparallel  $\text{Fe}_A^{3+}$  and  $\text{Fe}_B^{3+}$  moments compensate each other, a saturation magnetization of  $4\mu_B$  per formula unit (f.u.) is expected from the remaining  $\text{Fe}_B^{2+}$  ( $S = 2$ ) moments (Fig. 1(b)).

To tailor the magnetic and electronic properties, Fe ions can be substituted by nonmagnetic divalent ions such as  $\text{Zn}^{2+}$  ( $3d^{10}, S = 0$ ) [2] which preferably occupy the tetrahedrally coordinated *A* sites in the inverse spinel structure (Fig. 1(c)). Some of the antiferromagnetically coupled moments on the *A* sites are removed, leading to an initial increase of the saturation magnetization at low Zn substitution [2, 3]. Moreover, this substitution also converts  $\text{Fe}_B^{2+}$  into  $\text{Fe}_B^{3+}$  on the *B* sites due to charge neutrality, thus weakening the ferromagnetic DE. This leads to spin canting and a reduction of the saturation magnetization when going to larger substitution levels (Fig. 1(d)) [3]. Taken together, with increasing Zn substitution the electrical conductivity is expected to decrease by a reduction of both the density of itinerant charge carriers and their hopping amplitude due to spin canting. On the

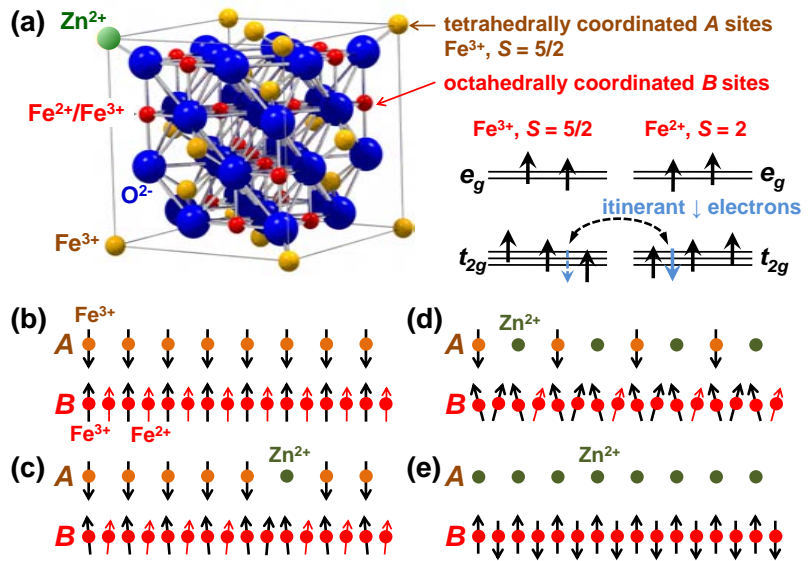


**Figure 1:** (a) Inverse spinel structure of magnetite. Also shown is the occupation of the  $\text{Fe}_B^{2+}$  and  $\text{Fe}_B^{3+}$   $3d$  states with  $t_{2g}$  and  $e_g$  symmetry separated by the crystal field splitting due to the octahedral oxygen surrounding. For details see text. (b) - (e) show the *A* and *B* sublattice configuration for (b)  $x = 0$ , (c)  $x = 1/8$ , (d)  $x = 0.5$ , and (e)  $x = 1$ .

<sup>1</sup>This work is supported by the Deutsche Forschungsgemeinschaft via the priority program SPP 1285 (project GR 1132/14) and by the DAAD.

<sup>2</sup>Materials Science Research Centre, Indian Institute of Technology Madras, Chennai 600036, India

other hand, by preparing  $\text{Fe}_3\text{O}_4$  samples in an  $\text{O}_2$ -rich atmosphere Fe vacancies on the  $B$  sites can be introduced [4]. Charge neutrality again requires a reduced amount of  $\text{Fe}_B^{2+}$  ions on the  $B$  sites weakening the ferromagnetic DE. In the same way as Zn substitution, this is expected to result in a reduced saturation magnetization together with a reduced electrical conductivity.

In a recent work [5], we studied the growth and the structural, magnetic, and magnetotransport properties of epitaxial thin film samples of  $\text{Zn}_x\text{Fe}_{3-x}\text{O}_4$  deposited by laser molecular beam epitaxy. At the same total pressure of  $3.7 \times 10^{-3}$  mbar, two sets of samples were grown in two different atmospheres. In Ar, thin films with  $x = 0, 0.1, 0.5$ , and  $0.9$  were deposited at a substrate temperature of  $320^\circ\text{C}$ . In an Ar/ $\text{O}_2$  (99:1) mixture, thin films with  $x = 0.5$  were deposited at  $320^\circ\text{C}$  and with  $x = 0, 0.33$ , and  $0.9$  at  $400^\circ\text{C}$ . A detailed x-ray diffraction analysis revealed a very high epitaxial quality of all thin film samples. Our  $\text{Zn}_x\text{Fe}_{3-x}\text{O}_4$  thin films are coherently strained and show a very small mosaic spread. Zn substitution results in an increase of the unit cell volume, causing the in-plane epitaxial strain to change from tensile to compressive on increasing the Zn content  $x$ . Growth in excess oxygen results in a reduction of the unit cell volume most likely due to the formation of Fe vacancies.

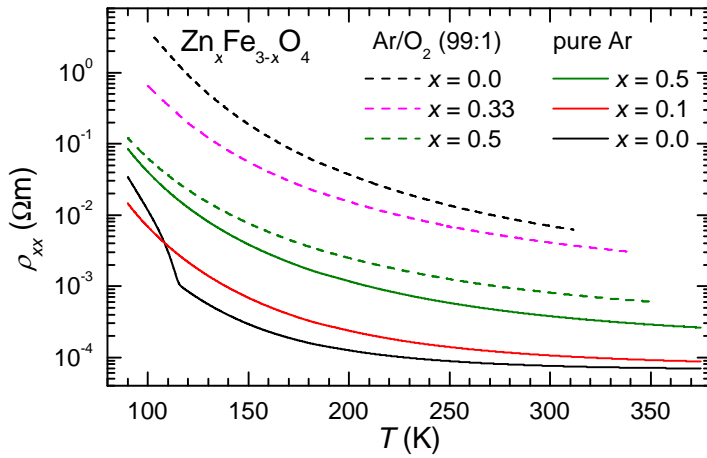
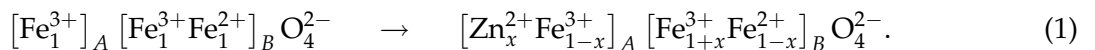


**Figure 2:** Longitudinal resistivity  $\rho_{xx}$  as a function of temperature  $T$  for samples grown in Ar (solid lines) or in Ar/ $\text{O}_2$  (99:1) (dashed lines).

decreasing  $T$  from 375 K down to 90 K. A pronounced change in the  $\rho_{xx}(T)$  curves due to the so-called *Verwey* transition in magnetite [6] is observed only for  $\text{Fe}_3\text{O}_4$  ( $x = 0$ ) grown in Ar. There, a clear kink is visible in  $\rho_{xx}(T)$  at about 115 K. In bulk material, the *Verwey* transition, associated with a cubic to monoclinic structural phase transition, occurs at  $T_V = 123$  K. It is known that the observability of the *Verwey* transition sensitively depends on perfect stoichiometry [4, 7]. Its absence for the films substituted with Zn or grown in finite oxygen partial pressure provides evidence for the presence of an unequal number of  $\text{Fe}_B^{2+}$  and  $\text{Fe}_B^{3+}$  ions on the  $B$  sublattice. As  $\text{Zn}^{2+}$  preferably occupies the tetrahedrally coordinated  $A$  site the substitution of  $\text{Fe}_A^{3+}$  by  $\text{Zn}^{2+}$  reduces the amount of  $\text{Fe}_B^{2+}$  as



That is, the density of itinerant electrons on the  $B$  sublattice is reduced, resulting in an increase of the resistivity with increasing  $x$  in perfect agreement with our observation and with literature data [2].

The  $\rho_{xx}(T)$  curves of the  $\text{Zn}_x\text{Fe}_{3-x}\text{O}_4$  ( $0 \leq x \leq 0.5$ ) films grown in Ar/ $\text{O}_2$  show a similar overall temperature dependence, however, with resistivity values that are much higher than those measured for the films grown in Ar. Furthermore, their resistivity decreases with increasing  $x$

The longitudinal resistivity  $\rho_{xx}$  has been measured as a function of temperature  $T$  and applied magnetic field  $H$  using a standard four-probe technique (Fig. 2). Despite a similar shape of all  $\rho_{xx}(T)$  curves, it is evident that the absolute magnitude of  $\rho_{xx}$  sensitively depends on the Zn substitution level  $x$  and the growth atmosphere. For both sample sets grown in Ar and an Ar/ $\text{O}_2$  (99:1) mixture,  $\rho_{xx}(T)$  increases by more than two orders of magnitude with

in contrast to what is observed for the films grown in Ar. Since growth of magnetite in excess oxygen is known to create Fe vacancies  $X^0$  [4], equivalent to two (three) missing electrons per  $\text{Fe}^{2+}$  ( $\text{Fe}^{3+}$ ) vacancy, the requirement of charge neutrality shifts the 1:1 balance between  $\text{Fe}_B^{2+}$  and  $\text{Fe}_B^{3+}$  towards  $\text{Fe}_B^{3+}$  as



Evidently, Fe vacancies in the same way as Zn substitution result in a reduction of  $\text{Fe}_B^{2+}$ . Hence, the density of itinerant electrons on the  $B$  sublattice decreases and, in turn, the resistivity increases with increasing  $\delta$ . This is exactly what is observed in our experiments and reported in literature [8]. However, Zn substitution in our films grown in an Ar/ $\text{O}_2$  mixture now leads to a decrease of resistivity in contrast to what is observed for the films grown in Ar. Since Zn substitution also results in an increase of the unit cell volume due to the larger ionic radius of  $\text{Zn}^{2+}$  compared to  $\text{Fe}^{3+}$ , it is expected that Zn substitution removes part of the Fe vacancies. This is intuitive since now Fe can be more easily incorporated into the expanded lattice. Then, it is expected that  $\text{Zn}^{2+}$  does not only remove an electron by substituting  $\text{Fe}_A^{3+}$  on an  $A$  site, but also adds two/three electrons by removing a vacancy on a  $\text{Fe}_B^{2+}/\text{Fe}_B^{3+}$  site. Evidently, in total this leads to an effective increase of the carrier density with increasing  $x$  in agreement with our experimental data in the range up to  $x = 0.5$ .

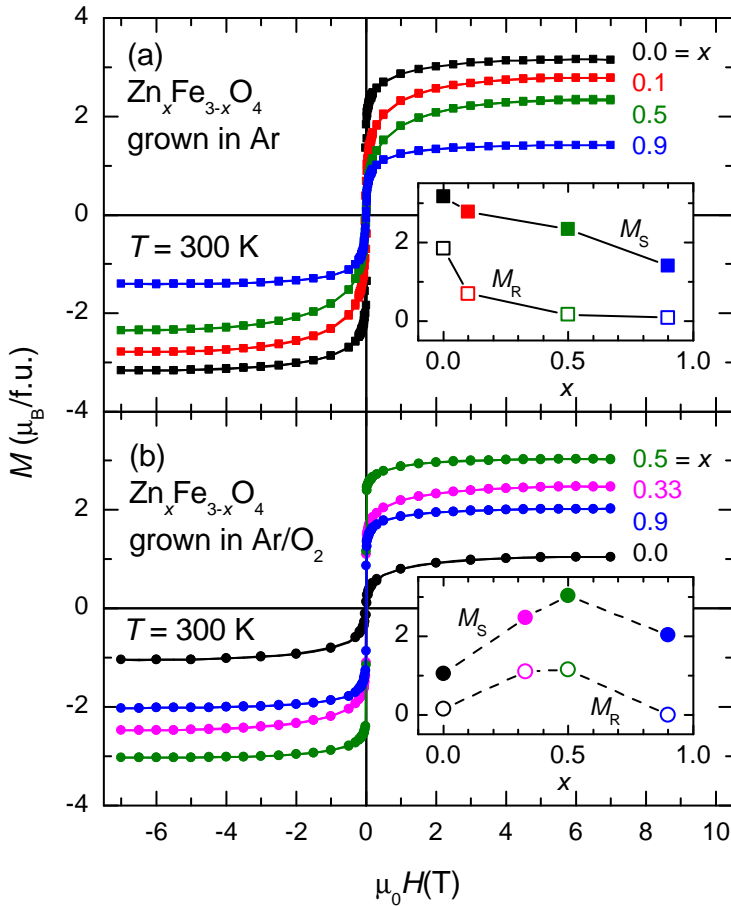


**Figure 3:** Room temperature magnetization  $M$  versus magnetic field  $H$  applied in the film plane for samples grown in (a) Ar and (b) in an Ar/ $\text{O}_2$  (99:1) mixture. The insets show the saturation magnetization  $M_S$  (full symbols) and the remanence  $M_R$  (open symbols) as a function of the Zn substitution level  $x$ .

The magnetic characterization was performed using SQUID magnetometry with magnetic fields  $\mu_0 H$  up to 7 T applied in the film plane. At room temperature, the  $M(H)$  loops show ferromagnetic behavior for all samples (Fig. 3). However, the measured saturation magnetization  $M_S$  as well as the remanent magnetization  $M_R$  and coercive field was found to strongly depend on both the Zn substitution level  $x$  and the growth atmosphere. The stoichiometric  $\text{Fe}_3\text{O}_4$  film grown in Ar, serving as a reference, shows the highest values for the saturation magnetization ( $M_S = 3.16 \mu_B/\text{f.u.}$ ) and remanence ( $M_R = 1.83 \mu_B/\text{f.u.}$ ) (Fig. 3(a)). As shown in the inset of Fig. 3(a), both  $M_S$  and  $M_R$  were found to decrease with increasing  $x$ . Recalling eq.(1), the substitution of  $\text{Fe}_A^{3+}$  ( $3d^5, S = 5/2$ ) by  $\text{Zn}^{2+}$  ( $3d^{10}, S = 0$ ) results in a decrease of the magnetization on the  $A$  sublattice. That is, since

the compensating magnetization of the  $A$  sublattice is removed, one would expect an increase of the total magnetization of the ferrimagnet. However, Zn substitution also weakens the  $A$ - $O$ - $B$  SE by diluting the  $A$  site moments. Furthermore, it converts  $\text{Fe}_B^{2+}$  ( $3d^6$ ,  $S = 2$ ) into  $\text{Fe}_B^{3+}$  on the  $B$  sublattice, resulting in a reduction of the itinerant charge carrier density. This weakens the ferromagnetic  $B$ - $O$ - $B$  DE, competing with the antiferromagnetic SE interaction on the  $B$  sublattice. As discussed in the introduction, taken together this leads to an increase of the spin canting on the  $B$  sublattice with increasing  $x$  (cf. Fig. 1), explaining the observed reduction of the total magnetization of the ferrimagnetic  $\text{Zn}_x\text{Fe}_{3-x}\text{O}_4$  films.

The magnetic properties of the  $\text{Zn}_x\text{Fe}_{3-x}\text{O}_4$  films grown in an Ar/ $\text{O}_2$  (99:1) mixture are shown in Fig. 3(b). For  $x = 0$ , both  $M_S$  and  $M_R$  are much lower than for the films grown in Ar.  $M_S$  and  $M_R$  is found to increase with increasing  $x$  for  $0 \leq x \leq 0.5$  and then to decrease again for  $x = 0.9$  as shown in the inset of Fig. 3(b). The  $M_S(x)$  dependence can be straightforwardly explained by the presence of Fe vacancies in films grown in finite oxygen partial pressure and their removal by Zn substitution. For  $x = 0$ , the Fe vacancies shift the  $\text{Fe}_B^{2+}/\text{Fe}_B^{3+}$  1:1 balance towards  $\text{Fe}_B^{3+}$ , removing itinerant charge carriers and weakening the ferromagnetic DE at the expense of antiferromagnetic SE on the  $B$  sublattice. This results in spin canting on the  $B$  sublattice, giving rise to a reduced saturation magnetization. On Zn substitution, part of the Fe vacancies are removed. This shifts the  $\text{Fe}_B^{2+}/\text{Fe}_B^{3+}$  ratio back towards a 1:1 balance. The related increase of the itinerant charge carrier density and DE interaction on the  $B$  sublattice reduces the spin canting with increasing  $x$ . This explains the increase of the room temperature saturation magnetization from  $M_S = 1.05 \mu_B/\text{f.u.}$  ( $x = 0$ ) up to  $3.02 \mu_B/\text{f.u.}$  ( $x = 0.5$ ). At 10 K (not shown here),  $M_S$  increases from  $1.26 \mu_B/\text{f.u.}$  ( $x = 0$ ) up to  $3.92 \mu_B/\text{f.u.}$  ( $x = 0.5$ ). For even larger  $x$ , the  $\text{Fe}_A^{3+}$  moments on the  $A$  sublattice are strongly diluted, resulting in a strong weakening of the antiferromagnetic SE between the  $A$  and  $B$  sublattices. Furthermore, Zn substitution may over-compensate the Fe vacancies again shifting the  $\text{Fe}_B^{2+}/\text{Fe}_B^{3+}$  balance towards  $\text{Fe}_B^{3+}$ . Taken together, this explains the decrease of  $M_S$  above the critical value of  $x \approx 0.5$ , which of course depends on the oxygen partial pressure during growth and the corresponding amount of Fe vacancies.

In conclusion, the magnetic properties of the  $\text{Zn}_x\text{Fe}_{3-x}\text{O}_4$  films grown under different oxygen partial pressure strongly depend on whether the films were grown in Ar or at finite oxygen partial pressure. In full agreement with the transport data these differences can be explained by the following effects: (i) For films grown in Ar, Zn substitution on the  $A$  site removes  $\text{Fe}_A^{3+}$  moments from the  $A$  sublattice and, due to charge neutrality, itinerant electrons from the  $B$  sublattice. The resulting weakening of both the antiferromagnetic  $A$ - $O$ - $B$  SE and the ferromagnetic DE on the  $B$  sublattice results in an increasing spin canting on the  $B$  sublattice with increasing  $x$ . This causes a reduction of the saturation magnetization with increasing  $x$ . (ii) For films grown in oxygen partial pressure, the magnetic properties are strongly influenced by the presence of Fe vacancies. They reduce the density of itinerant electrons on the  $B$  sublattice, thereby weakening the ferromagnetic DE at the expense of antiferromagnetic SE. This causes spin canting on the  $B$  sublattice and, in turn, a reduced saturation magnetization. The effect of additional

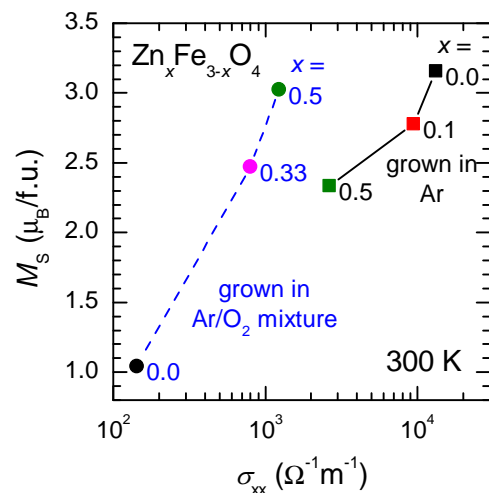


**Figure 4:** Saturation magnetization  $M_S$  versus longitudinal conductivity  $\sigma_{xx}$  for samples with different Zn substitution  $x \leq 0.5$  grown in Ar (squares) or an Ar/ $\text{O}_2$  (99:1) mixture (circles).

Zn substitution is the partial removal of the Fe vacancies. This effectively increases the density of itinerant electrons on the  $B$  sublattice, thereby strengthening the ferromagnetic DE. The result is an increase of the saturation magnetization with increasing  $x$ .

We finally link the magnetic properties to the transport data by plotting the saturation magnetization  $M_S$  versus the electrical conductivity  $\sigma_{xx}$  for films with various  $x$  and grown in Ar or Ar/O<sub>2</sub> (Fig. 4). Evidently, there is a clear correlation between  $M_S$  and  $\sigma_{xx}$ . Samples with high  $M_S$  have large  $\sigma_{xx}$  and vice versa. Again, this correlation can be straightforwardly explained within the scenario presented above. Charge transport is dominated by the hopping of the itinerant  $t_{2g}$  electrons between the mixed-valent  $\text{Fe}_B^{2+}/\text{Fe}_B^{3+}$  ions on the  $B$  sublattice. Due to the strong on-site Hund's rule coupling the spin of the hopping spin-down electron is aligned anti-parallel to the local moment of the spin-up electrons (cf. Fig. 1). Therefore, the hopping amplitude is significantly suppressed if the moments of neighboring  $B$  sites are not parallel. That is, any spin canting on the  $B$  sublattice reducing the saturation magnetization also results in a reduction of the electrical conductivity.

In summary, the possibility of tailoring the electronic and magnetic properties in a wide range by Zn substitution makes magnetite a promising material for spin injection into semiconductors within multi-functional heterostructures and spintronic devices.

## References

- [1] S.A. Wolf *et al.*, *Science* **294**, 1488 (2001); I. Zutic, J. Fabian, and S. Das Sarma, *Rev. Mod. Phys.* **76**, 323 (2004).
- [2] J. Takaobushi *et al.*, *Appl. Phys. Lett.* **89**, 242507 (2006); J. Takaobushi *et al.*, *Phys. Rev. B* **76**, 205108 (2007).
- [3] Y. Li, Q. Li, M. Wen, Y. Zhang, Y. Zhai, Z. Xie, F. Xu, and S. Wei, *J. Elect. Spectrosc.* **160**, 1 (2007).
- [4] R. Aragón, D.J. Buttrey, J.P. Shepherd, and J.M Honig, *Phys. Rev. B* **31**, 430 (1985).
- [5] D. Venkateshvaran, M. Althammer, A. Nielsen, S. Geprägs, M.S.R. Rao, S.T.B. Goennenwein, M. Opel, and R. Gross, *submitted to Phys. Rev. B* (2008); arXiv:0808.3642.
- [6] E. J. W. Verwey, *Nature (London)* **144**, 327 (1939).
- [7] D. T. Margulies *et al.*, *Phys. Rev. B* **53**, 9175 (1996).
- [8] M. L. Paramês *et al.*, *Appl. Surf. Sci.* **252**, 4610 (2006).

## Impact of Cryogen-free Revolution

*K. Uhlig*

The “impact of cryogen-free revolution” was the topic of a workshop held at the Ultralow Temperature Conference ULT2008 in London, where our newest results on cryogen-free dilution refrigeration were presented. The interest in our dilution refrigerators (DR) is remarkable, and the number of international cryo-engineering companies offering cryogen-free dilution refrigerators has further increased to seven [1]. The most important demand comes from quantum computer scientists. They need easy to use, economical and reliable mK-coolers with high cooling capacity. Quite a number of renowned institutions has ordered cryogen-free DRs (ETH Zurich, Yale University, NIST Gaithersburg, Univ. of Florida, Univ. of California (Berkeley), Los Alamos Nat. Lab., IBM, Harvard University).

So far, all manufacturers we are aware of follow our original construction plan, with “dry” DRs consisting of a commercial two-stage pulse tube refrigerator (PTR) [2], an intermediate cooling stage (JT-stage) and a DR stage [3]. Last year, dry DRs sold outnumbered traditional DRs with liquid helium pre-cooling by a wide margin [4].

### Recent developments

To condense the  $^3\text{He}$  efficiently in a dry DR, it is desirable to run the PTR near its lowest temperature. Besides, the inner vacuum can of the DR which also serves as a radiation shield, is thermally anchored at the second stage of the PTR and should be as cold as possible. So far, the  $^3\text{He}$  flow was cooled at the two stages of the PTR which operate at temperatures of about 50 K at the first stage and 2.5 K to 5 K at the second stage (Fig. 2). The temperature of the second stage depends on the  $^3\text{He}$  flow of the DR, which poses a considerable heat load to this stage (Fig. 3, curve C):

$$\dot{Q} = n_3 * [H_3(p_{in}, T_{PT1}) - H_3(p_{in}, T_{PT2})] \quad (1)$$

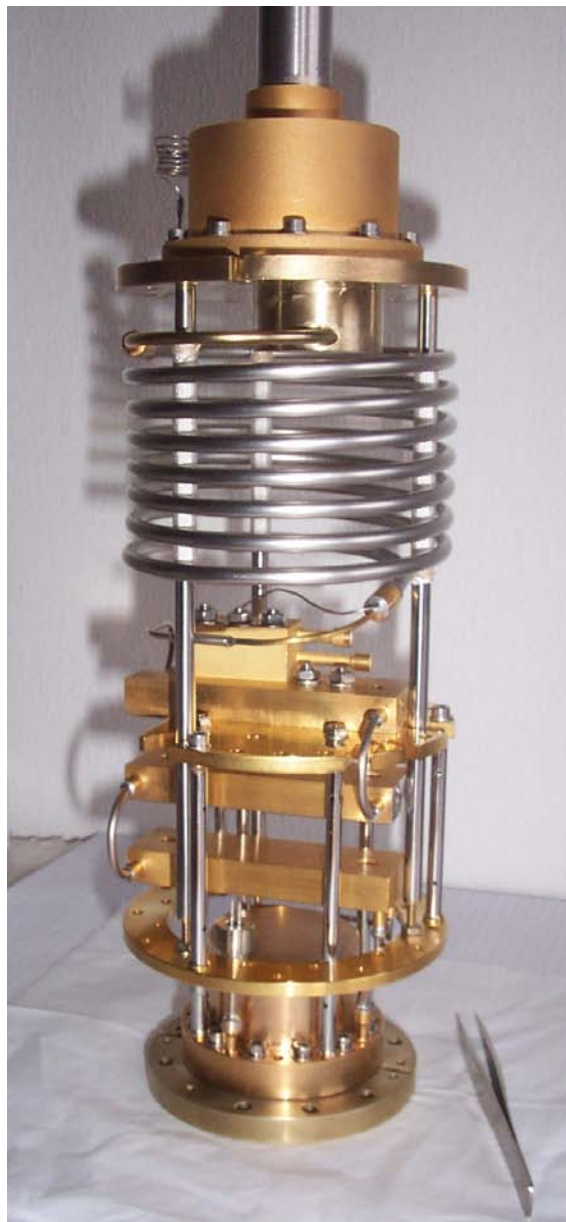


**Figure 1:** Medium-sized dilution unit with three discrete heat exchangers and concentric tube heat exchanger. In our cryostat, this dilution unit produced a cooling capacity of  $250 \mu\text{W}$  at a temperature of 100 mK. The base temperature was 10 mK.

Here,  $\dot{Q}$  is the heat load,  $n_3$  the flow rate of the  $^3\text{He}$ ,  $H_3$  its enthalpy,  $p_{in}$  its pressure ( $\approx 0.5$  bar) and  $T_{PTR1(2)}$  are the temperatures of the two stages of the PTR.

It has been shown in recent work [5, 6] that in addition to the two stages of the PTR extra cooling power is available with two-stage PTRs in the regenerator of the second stage (RE2). This effect is a result of the non-ideality of the  $^4\text{He}$  gas at low temperatures. In last year's report we explained that by adding a heat exchanger (hex) to RE2, use could be made of the extra refrigeration capacity of RE2 to cool the inflowing  $^3\text{He}$  of the DR.

The first version of this hex was made from 8 pipe sections which were clamped on the outside of RE2 (Fig. 2). The  $^3\text{He}$  inlet line was soft soldered to these pipe sections. The pre-cooling temperatures of the  $^3\text{He}$  flow are shown in Fig. 3 (curve A); instead of a temperature of  $\approx 50$  K which corresponds to the temperature of the first stage, the  $^3\text{He}$  temperature is now reduced to below 5 K when it enters the second pulse tube hex; curve B is the temperature of the second stage of the PTR.

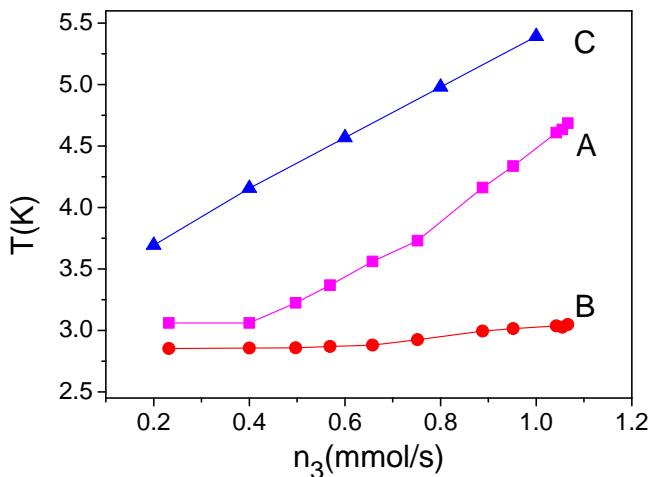


**Figure 3:** Temperatures of the PTR as a function of the  $^3\text{He}$  flow of the DR. A: Temperature of the  $^3\text{He}$  at the outlet of the heat exchanger at RE2. B: Temperature of the second stage of the PTR with the  $^3\text{He}$  pre-cooled at RE2. C: Temperature of the second stage of the PTR with no heat exchanger installed at RE2.

heat exchanger is even more efficient, and several cryo-companies have started to utilize this kind of hex in their DRs.

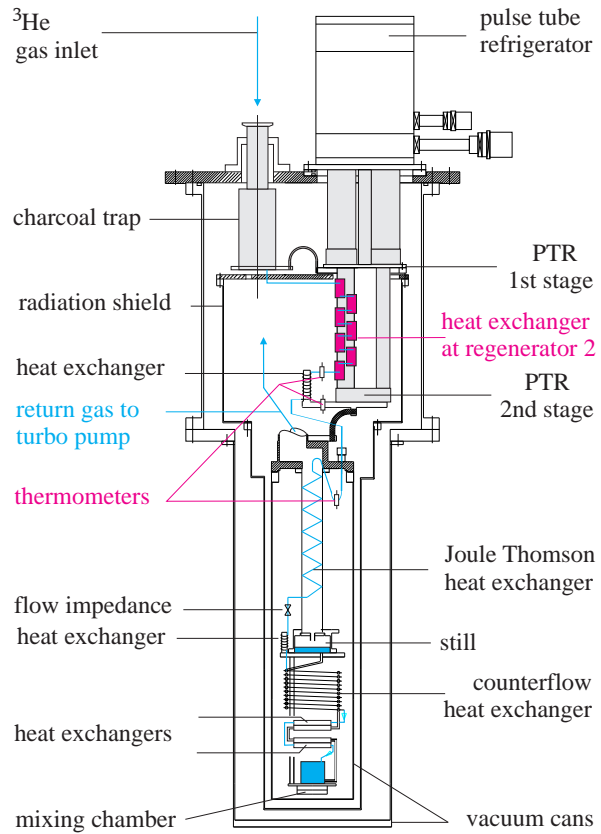


**Figure 2:** Sectional drawing of our cryogen-free DR. The heat exchanger attached to the second regenerator is in red.

From Fig. 3 we see that most of the enthalpy of the  $^3\text{He}$  stream can be dumped onto RE2 and so the temperature of the second stage of the PTR is almost unaffected by the  $^3\text{He}$  flow. Clearly, even higher  $^3\text{He}$  circulation rates could be cooled by a relatively small PTR. The type of hex made from pipe sections can easily be installed in existing dry DRs without disassembling the cryostat. Details of the experiment were published in [7].

In the following we returned our PTR to the manufacturer [8] and had a heat exchanger soldered to RE2 which was made from stainless steel tubing (Fig. 4). For the soldering chore, the PTR had to be taken apart and the regenerator material removed. The new



**Figure 4:** Lower half of our PTR. At the top of the photo is its first stage, at the bottom the second stage, and in between the second pulse tube and the regenerator with the hex made from a stainless steel capillary.

are required in important low temperature applications; we will continue our efforts in this direction.

## References

- [1] For manufacturers of cryogen-free DRs see the annual report 2007; new in the field : Blue Fors Cryogenics ([www.bluefors.com](http://www.bluefors.com))
- [2] R. Radebaugh, Development of the pulse tube refrigerator as an efficient and reliable cryocooler. [http://cryogenics.nist.gov/Papers/Institute\\_of\\_Refrig.pdf](http://cryogenics.nist.gov/Papers/Institute_of_Refrig.pdf)
- [3] K. Uhlig, *Cryogenics* **42**, 73 (2002).
- [4] J. Hoehne, VeriCold Inc., private communication; H. Albrecht, Oxford Instruments, private communication.
- [5] S. Zhu, M. Ichikawa, M. Nogawa, and T. Inoue, *Adv. Cryo. Eng.* **47A**, 633 (2002).
- [6] A. Ravex, T. Trollier, J. Tanchon, and T. Prouvé, *Cryocooler* **14**, 157 (2006); <http://www-conferences.library.wisc.edu/index.php-icc/article/download/21/21>.
- [7] K. Uhlig, *Cryogenics* **48**, 138 (2008).
- [8] Cryomech Inc., 113 Falso Drive, Syracuse, NY 13211, USA
- [9] K. Uhlig, *Adv. Cryo. Eng.* **53B**, 1287 (2007).

In Fig. 5 several temperatures of the cryogen free DR are depicted. Curve A is the pre-cooling temperature of the  $^3\text{He}$  using a hex made from pipe sections. Curve B shows the pre-cooling temperature for the hex in Fig. 4 (stainless steel tube); here, the pre-cooling temperature is about 0.5K lower. Curve C is the temperature of the cold end of the second pulse tube; in this test, the hex made from tubing was used. Finally, curves D and E give the temperatures of the still and the mixing chamber.

In summary, with the use of the hex at RE2, all of the refrigeration capacity of the PTR is used to pre-cool a subsequent refrigeration stage, in our application a  $^3\text{He}/^4\text{He}$  dilution stage. With the added hex, higher  $^3\text{He}$  flows can be cooled and hence higher cooling capacities of the DR accomplished [9]. In the future, the new hex at RE2 will be a basic component of cryogen-free  $^3\text{He}/^4\text{He}$  dilution cryostats with high cooling capacity. High cooling powers

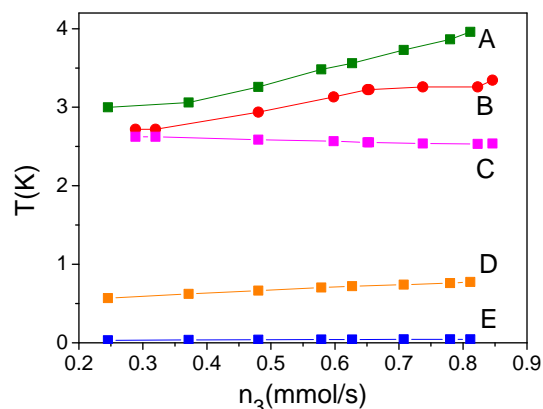


**Figure 5:** Temperatures of our dry fridge as a function of the  $^3\text{He}$  circulation rate. Curves A and B are the pre-cooling temperatures for our two hexs; instead of about 50 K, the temperature of the  $^3\text{He}$  is below 5 K. For details see text.

## A Ferromagnetic Resonance Setup for the X- and the K-band

*M.J. Schwarz, A. Brandlmaier, F. Czeschka, M. Weiler, M. Opel, S.T.B. Goennenwein, and R. Gross<sup>1</sup>*

*G. Woltersdorf<sup>2</sup> C. Bihler, H. Huebl, M.S. Brandt<sup>3</sup>*

The magnetic anisotropy is a fundamental property of ferromagnetic materials – for example, it determines the orientation of the magnetization vector  $\mathbf{M}$ . Therefore, a quantitative knowledge about magnetic anisotropy is of importance for both the basic understanding of ferromagnetic materials, as well as for the realization of magneto-electronic devices.

Today, a variety of techniques for the spectroscopy of magnetic anisotropy are established. In last years' annual report, we discussed that anisotropic magnetoresistance measurements allow to quantitatively determine the magnetic anisotropy of magnetic micro- and nanostructures [1]. For the routine characterization of ferromagnetic thin films or heterostructures, on the other hand, a contact-free measurement method is advantageous. For such purposes, ferromagnetic resonance (FMR) is the method of choice, as FMR quantitatively yields the magnetic anisotropy without requiring any particular sample preparation or treatment [2].

In the framework of a Diploma thesis, we have assembled a FMR measurement setup at the Walther-Meissner-Institut. As depicted in Fig. 1, the setup consists of a conventional electromagnet, into which the FMR microwave assembly is mounted. To accommodate the electromagnet – a rather bulky instrument with a mass of nearly 4 tons – a part of the basement boiler room was renovated and converted into laboratory space. A four-quadrant power supply (funded by the Deutsche Forschungsgemeinschaft within project GO 944/3) allows to generate magnetic fields in the range  $-2 \text{ T} \leq \mu_0 H \leq 2 \text{ T}$  in a 28 mm air gap in the electromagnet, with an accuracy of better than  $10^{-5}$ . The control over magnetic field polarity provided by the power supply enables the simul-

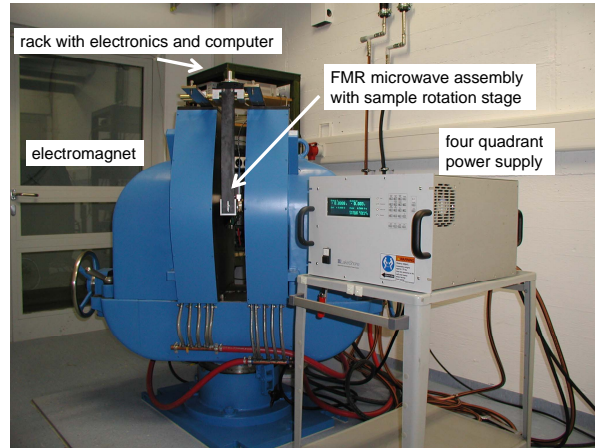


**Figure 1:** The large electromagnet and the four-quadrant power supply used in the ferromagnetic resonance setup in the new laboratory.

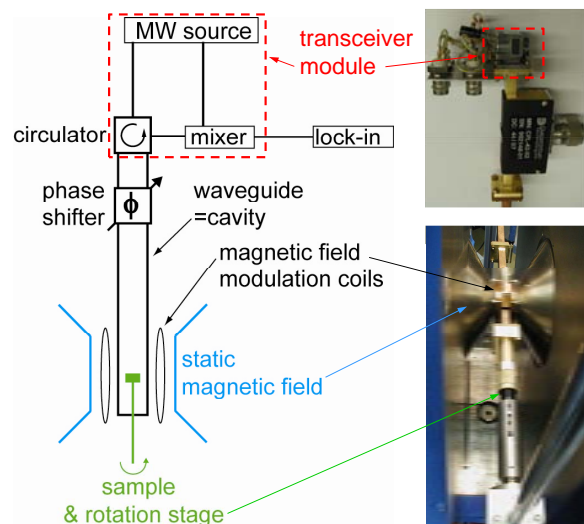


**Figure 2:** Schematic diagram of the FMR microwave assembly.

<sup>1</sup>This work is supported by the German Excellence Initiative via the “Nanosystems Initiative Munich (NIM)” and the Deutsche Forschungsgemeinschaft via project GO 944/3.

<sup>2</sup>Institut für Experimentelle und Angewandte Physik, Universität Regensburg, 93040 Regensburg, Germany

<sup>3</sup>Walter Schottky Institut, Technische Universität München, 85748 Garching, Germany

taneous detection of both FMR and magnetotransport traces, so that the information content of the two complementary measurement techniques can be compared and exploited [3].

A schematic illustration of the FMR microwave assembly is shown in Fig 2. A voltage-controlled transceiver module, commonly used in radar speed measurement devices and usually referred to as a *gunnplexer*, is used as a combined microwave source/detection unit. The transceiver module is connected to an approximately 130 cm long piece of rectangular waveguide, in which a standing microwave mode pattern with a mode frequency separation of  $\approx 100$  MHz is sustained. In other words, the long waveguide can be considered as a simple microwave cavity with a quality factor of several 100. The impedance matching between transceiver module and waveguide cavity is ensured by means of a phase shifter. The sample is mounted on a glass rod and inserted into the waveguide from the bottom end in such a fashion that the sample is located in a region of maximal microwave magnetic field [4]. A stepper motor rotation stage, which is connected to the sample mount via a mechanical transmission, allows to rotate the sample in situ in the waveguide. Furthermore, we modulate the magnetic field strength using a pair of coils to enable phase-sensitive detection. We have set up and tested two such microwave assemblies, one for the X-band (waveguide frequency range  $8.2 \text{ GHz} \leq \nu \leq 12.4 \text{ GHz}$ , transceiver module emitting at 10.3 GHz), and one for the K-band (waveguide frequency range  $18 \text{ GHz} \leq \nu \leq 26.5 \text{ GHz}$ , transceiver module emitting at 24.1 GHz).

Figure 3(a) shows the FMR signal of a ferromagnetic thin film heterostructure recorded at room temperature with the X-band assembly. The heterostructure was deposited onto a glass substrate using magnetron sputtering at the Universität Regensburg, and consists of Co (10 nm) / Cu (7 nm) / CoFeB (6 nm) / Nb(10 nm). The top Nb layer prevents the oxidation of the ferromagnetic layers beneath. As evident from Fig. 3(a), the FMR lines of the thin ferromagnetic Co and CoFeB layers are resolved with good signal to noise ratio in one single magnetic field sweep in this FMR setup. Due to the magnetic field modulation, the shape of the ferromagnetic resonance lines corresponds to a peak-dip feature, i.e. to the first derivative of a conventional (Lorentzian) absorption line with respect to magnetic field.

To quantify the magnetic anisotropy of the two ferromagnetic layers, we have measured the evolution of the FMR resonance fields  $\mu_0 H_{\text{res}}$  as a function of the orientation of the external magnetic field  $\mu_0 \mathbf{H}$ . From a series of FMR traces recorded for different orientations of  $\mu_0 \mathbf{H}$  within the plane of the thin film heterostructure, we obtain the resonance fields depicted by the symbols in Fig. 3(b). Using a standard free energy approach [4], these resonance fields can

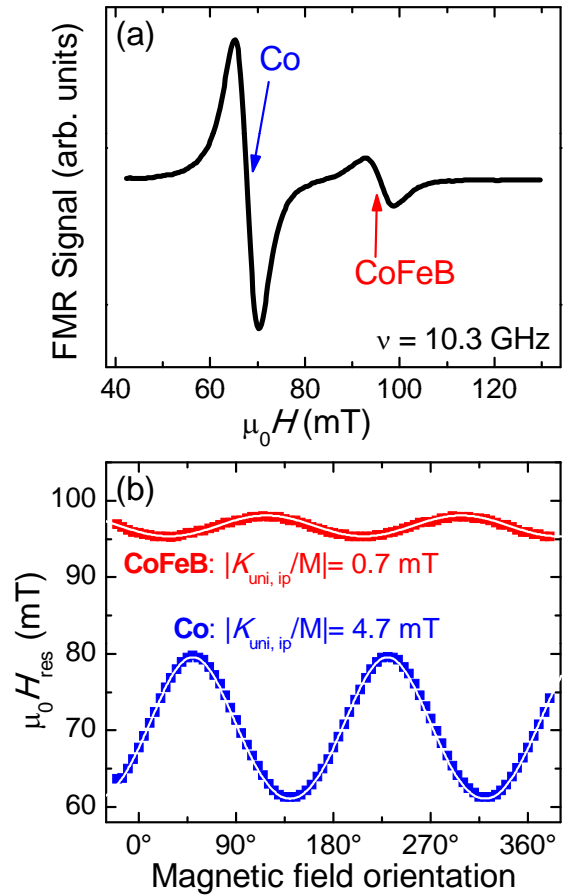


**Figure 3:** (a) Ferromagnetic resonance spectrum of a CoFeB/Cu/Co spin valve recorded with the X-band FMR assembly. The arrows indicate the ferromagnetic resonance fields  $\mu_0 H_{\text{res}}$ . (b) The resonance fields (symbols) observed for different orientations of the external, in-plane magnetic field are well reproduced using a free energy model (full lines).

be quantitatively modeled using the uniaxial in-plane anisotropy fields  $K_{\text{uni,ip}}/M = 4.7$  mT and  $K_{\text{uni,ip}}/M = 0.7$  mT for the Co and the CeFeB layer, respectively;  $M$  is the saturation magnetization of the respective ferromagnets. In particular, the FMR experiments show that the two uniaxial in-plane easy axes enclose an angle of about  $68^\circ$  [4], which naturally explains the complex magneto-transport properties of this spin valve structure.

In summary, we have assembled and tested transceiver-based ferromagnetic resonance setups for both the X- and the K-band. The setups are fully operational and allow for a quantitative spectroscopy of magnetic anisotropy in thin ferromagnetic films.

## References

- [1] W. Limmer, M. Glunk, J. Daeubler, T. Hummel, W. Schoch, R. Sauer, C. Bihler, H. Huebl, M. S. Brandt, and S. T. B. Goennenwein, *Phys. Rev. B* **74**, 205205 (2006).
- [2] A. H. Morrish, *The Physical Principles of Magnetism*, IEEE Press, New York (2001).
- [3] S. T. B. Goennenwein, S. W. Schink, A. Brandlmaier, A. Boger, M. Opel, R. Gross, R. S. Keizer, T. M. Klapwijk, A. Gupta, H. Huebl, C. Bihler, and M. S. Brandt, *Appl. Phys. Lett.* **90**, 162507 (2007).
- [4] M. J. Schwarz, *Aufbau und Charakterisierung eines FMR-Spektrometers für X- und K-Band*, Diplomarbeit, Technische Universität München (2008).

## Extension and Improvement of the Existing Laser-MBE System

*M. Althammer, S. Geprägs, T. Brenninger, S.T.B. Gönnenwein, M. Opel, and R. Gross*<sup>1</sup>

For the preparation of *p*-type ZnO thin films by nitrogen doping, the use of a repeated temperature modulation technique is an interesting and promising approach. To establish this new technique, the existing laser-MBE system at the WMI was equipped with a new infrared laser heating system (Fig. 1) and an atomic source for oxygen, nitrogen, or hydrogen (Fig. 2). The main part of the laser heating system consists of an infrared laser diode array with a maximum output power of 140 W at a wavelength of 940 nm. The laser diode array is water-cooled and mounted together with the power supply and a Linux micro-PC with pyrometer card for temperature measurement into the main control unit. This unit is connected to the laser-MBE deposition chamber via two, 7 m long glass fibers for the infrared heating power and the temperature measurement.

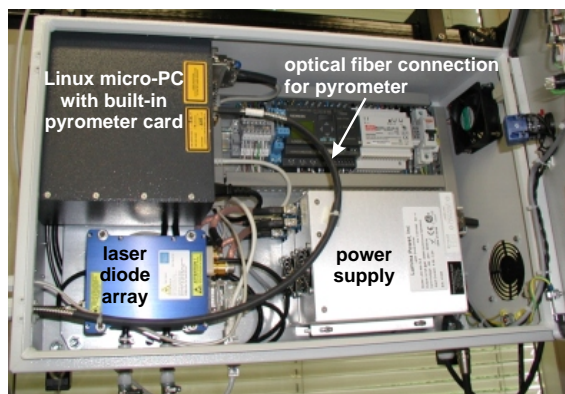


**Figure 1:** Main control unit of the infrared laser heating system (940 nm, 140 W) with built-in pyrometer

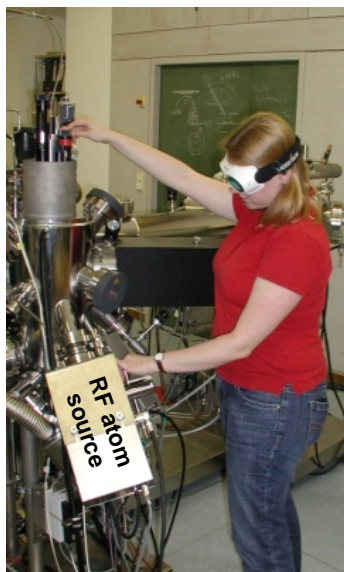


**Figure 2:** Oxford rf atom source for nitrogen, oxygen, or hydrogen (front), attached to the existing UHV cluster of the laser-MBE system

A specially designed optics unit with beam splitter attached to the laser-MBE chamber focuses the infrared laser beam onto the back side of the substrate as well as collects its thermal radiation which is sent back to the micro-PC in the control unit. There, a dual wavelength pyrometer device sensitive at 1711 nm and 1941 nm measures the substrate temperature without requiring any correction for emissivity. The temperature range of the pyrometer is 300 K to 1400 K. The micro-PC can be accessed via ethernet/LAN and allows for several control modes of the laser heating system. Stable temperatures as well as temperature sweeps can be programmed easily via a graphical user interface. In addition, the micro-PC can be accessed directly using the commercial LASCON software interface. Sequences consisting of different sequential temperature sweeps/ramps may be stored on the harddisk of the micro-PC and remotely executed at any time.

In addition, an Oxford radio frequency (rf) atom source was attached to the laser-MBE chamber. This source can be operated with N<sub>2</sub>, O<sub>2</sub>, or H<sub>2</sub> gases. It is water-cooled and UHV compatible. It operates with a maximum power of 600 W at an rf frequency of 13.56 MHz. It is equipped with an optical emission detector together with a plasma controller and an automatic tuning unit to allow for stable operation on a timescale of several hours.

<sup>1</sup>This work is supported by the Deutsche Forschungsgemeinschaft via the priority program SPP 1285 (GR 1132/14).

## Redox Reactions, Layer Charges and Tschermak Substitution in Vermiculites from Spain

A. Lerf, A. Erb<sup>1</sup>,  
F.E. Wagner,<sup>2</sup> J. Poyato,<sup>3</sup> J.L. Pérez-Rodríguez<sup>3</sup>

Natural clay minerals of the 2:1 type very often contain Fe ions in the octahedral and/or tetrahedral layers. It has been known for fifty years that at least the octahedral iron ions are easily accessible to redox reactions; a striking example for this are the color reactions of some amines intercalated into smectites [1]. Oxidation of the octahedral structural iron ions has also been considered as an important step in the weathering of micas to vermiculite [2]. To evaluate the extent of redox reactions one needs to know the  $\text{Fe}^{2+}/\text{Fe}^{3+}$  ratio before and after the reaction. However, it is notoriously difficult to determine this ratio in natural and modified clay minerals by wet chemical methods. The most suitable method to derive reliable  $\text{Fe}^{2+}/\text{Fe}^{3+}$  ratios is Mössbauer spectroscopy.

We report here the Mössbauer parameters measured mainly at room temperature for the vermiculites of Ojén and Santa Olalla, Spain, after various chemical modifications. The emphasis is mainly on the determination of the  $\text{Fe}^{2+}/\text{Fe}^{3+}$  ratio. We investigated the maximum extent of reduction in the two vermiculites mentioned above and the iron uptake in the Santa Olalla vermiculite.

In previous experiments we carried out reduction only in aqueous solutions [3]. In these experiments on the vermiculite of Santa Olalla not more than 25% of  $\text{Fe}^{2+}$  could be obtained. The possible degree of reduction is remarkably higher in case of the vermiculite from Ojén, but does not exceed 40% of  $\text{Fe}^{2+}$  if the sample is reduced in aqueous solution. The reason for this restriction and the difference of both vermiculites is not clear at the moment. However, we could increase the  $\text{Fe}^{2+}$  content dramatically when the hydrazinium intercalation compounds were heated up to 400 °C and the ammonium compounds to 700 °C. An even higher degree of reduction has been obtained by treating the sodium vermiculite in a stream of  $\text{H}_2/\text{N}_2$  (5:95). The highest amount of  $\text{Fe}^{2+}$  thus obtained is in the order of 60%. The change in oxidation state from  $\text{Fe}^{3+}$  to  $\text{Fe}^{2+}$  leads to a reduction of the positive excess charge of the octahedral layer and to an increase of the total layer charge since the negative charge due to the  $\text{Al}^{3+}/\text{Si}^{4+}$  ratio is not influenced by the reduction reaction. There are two possibilities to compensate the increase of this layer charge: the uptake of additional cations in the interlayer space or uptake of protons by octahedral oxygen ions forming OH groups. To distinguish between these alternatives one needs an independent proof of the cation content in the interlayer space.

The samples reduced at room temperature with hydrazinium have taken up hydrazinium ions in the interlayer space. The nitrogen content of the solid after reduction does not allow an unambiguous determination of the layer charge because it is indicative for a mixture of  $\text{NH}_4^+$  and  $\text{N}_2\text{H}_5^+$  ions in the interlayer space may be due to the partial destruction of the hydrazinium ions. A complete replacement by another cation, usually used for layer charge determination, was not successful up to now. However, the hydrazinium Santa Olalla vermiculite heated up to 400 °C contains ammonium ions only, and the nitrogen content of 2.5% is in fair agreement with a constant layer charge.

<sup>1</sup>This work was supported in part by the German Academic Exchange Service (DAAD) in the framework of the Acciones Integradas Program. The financial support from project MAT 2005-04838 of the Spanish Government is also acknowledged.

<sup>2</sup>Physik-Department der Technischen Universität München, 85748 Garching, Germany

<sup>3</sup>Instituto de Ciencia de Materiales de Sevilla, Consejo Superior de Investigaciones Científicas-Universidad de Sevilla, c/ Américo Vespucio 49, 41092 Sevilla, Spain.

If the reduction is carried out at temperatures up to 600 °C, the Fe<sup>2+</sup> site with the higher quadrupole splitting increases more strongly than the other. In the samples treated at 700 °C or even higher temperatures the opposite effect is observed. In addition the Fe<sup>2+</sup> sites with low quadrupole splitting show a rather broad Gauss distribution. Such a Mössbauer spectrum is obtained also for biotites treated at 850 °C and interpreted as a consequence of oxygen defect formation [4]. Thus, it could be possible that the high temperature reduction is accompanied with dehydration of the octahedral layer. Further hints for a destruction of the vermiculites cannot be deduced from the Mössbauer spectra, even at the highest temperature investigated (850 °C). This is surprising, since one has to be aware that at temperatures above 750 °C the reduction could be superimposed by the decomposition of the vermiculites.

Reduction with hydrogen at 600 °C should not affect the integrity of the vermiculite layers. In agreement with this expectation the X-ray fluorescence analysis shows only a small variation of the composition with respect to the starting vermiculites. These changes are in accordance with movement of Al<sup>3+</sup> ions from the tetrahedral layer to the octahedral layer. A bit puzzling is the slight reduction of the total layer charge despite the increased amount of Fe<sup>2+</sup>. By X-ray diffraction it could be shown that the samples rehydrate after hydrogen treatment completely and have a layer spacing of about 14.5 Å, which is in perfect agreement with the layer spacings of fully hydrated phases.

In samples reduced at higher temperatures the stoichiometry deviates strongly from that of the original vermiculites. Again the total layer charge decreases despite the high degree of reduction. Especially the tetrahedral charge is reduced considerably, and instead the Al<sup>3+</sup> content of the octahedral sheets increases correspondingly. This fits quite well with the statement of Cole and Walker [5] that the thermal decomposition of vermiculites goes via the uncharged talk-like phases towards an enstatite. The Santa Olalla vermiculite reduced at 700 °C still rehydrate completely whereas the Ojén vermiculite treated at the same temperature shows a strong perturbation of the layer stacking. At even higher temperature both materials get amorphous but the final product enstatite is still not detectable. The mechanism of the thermal transformation of vermiculites is not thoroughly investigated up to now. The ion movements could be an indication for a reduction triggered Tschermak substitution (<sup>[6]</sup>Fe + <sup>[4]</sup>Si = <sup>[6]</sup>Al + <sup>[4]</sup>Al, numbers in brackets assign the coordination numbers of the elements) which is often observed in high temperature reactions of silicate minerals [6]. However, in our experiments the restructuring of the materials is still not complete.

## References

- [1] E.A. Hauser and M.B. Leggett, *J. Amer. Chem. Soc.* **62**, 1811 (1940).
- [2] K. Norrish K, in: J.M. Serratosa(ed), *Proc. Int. Clay Conf.*, pp. 417, Madrid 1972.
- [3] A. Lerf, F.E. Wagner, and J. Poyato, *Solid State Ionics* **141-142**, 479 (2001).
- [4] C.S. Hogg and R.E. Meads, *Miner. Mag.* **40**, 79 (1975).
- [5] G.F. Walker and W.F. Cole, in: R.C. Mackenzie (ed), *Thermal Investigation of Clays*, pp. 191, Mineralogical Society, London (1957).
- [6] J.B. Thompson, *Amer. Miner.* **63**, 239 (1978).



## Experimental Facilities and Infrastructure

In the following basic information on the key experimental facilities and components of the technical infrastructure installed at the Walther-Meißner-Institute (WMI) is given.

### UHV-Laser-MBE

The WMI operates a UHV-Laser-Molecular Beam Epitaxy (L-MBE) system for the growth of complex oxide heterostructures. The system has been designed to meet the special requirements of oxide epitaxy. The UHV cluster tool consists of the following main components:

- central transfer chamber;
- load-lock chamber with heater system for substrate annealing;
- laser deposition chamber with in-situ reflection high energy electron diffraction (RHEED) system, laser substrate heating system, and atomic oxygen source, the RHEED system has been modified to allow for the operation at high oxygen partial pressure up to 0.5 mbar;
- surface characterization chamber with UHV scanning force microscope (Omicron);
- metallization chamber with a four heart electron gun system and a liquid nitrogen cooled sample stage. The sample holder can be tilt for shadow evaporation;
- KrF excimer laser.

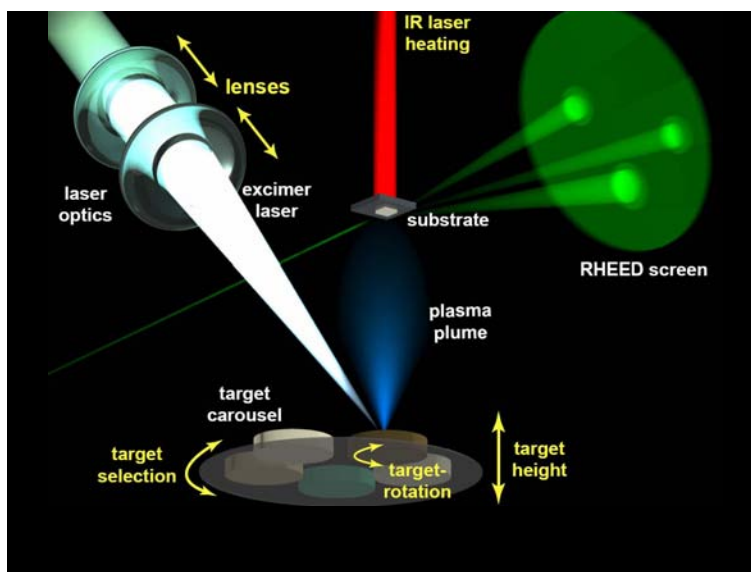
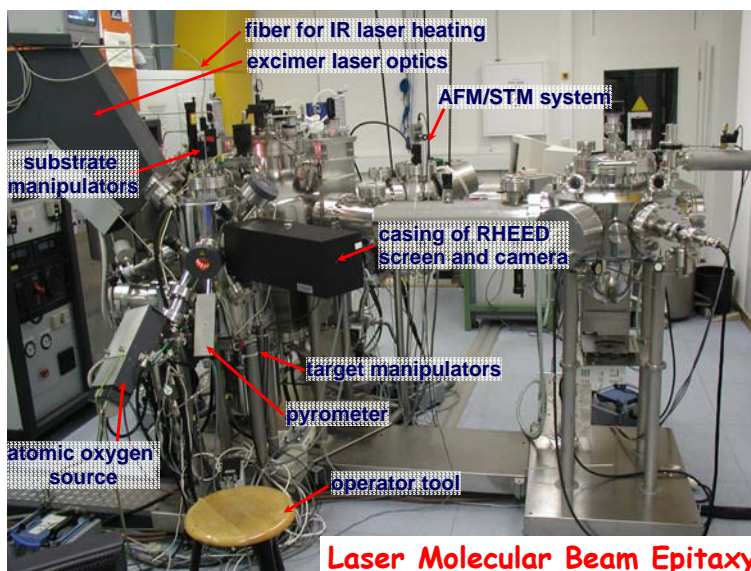
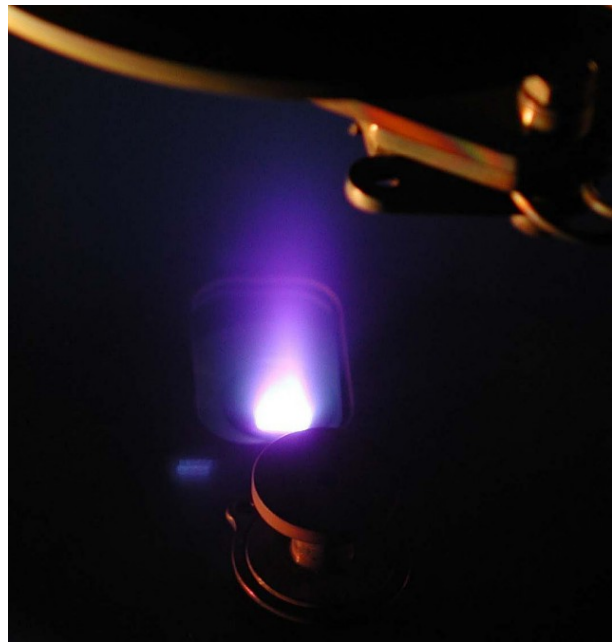


Figure 1: Top: UHV-Laser-Molecular Beam Epitaxy System. Bottom: Principle of the deposition process.

The system is used for the growth of complex oxide heterostructures consisting of superconducting, magnetic and dielectric materials such as the high-temperature superconductors, the doped manganites, the double perovskites, magnetite etc..

The original laser molecular beam epitaxy system (laser-MBE) designed already in 1995/96 until now has been permanently extended and modified. In particular, the substrate heating system and the temperature control unit was changed from a resistive radiation heater to a new infrared laser heating system (see Fig.3, left) including a pyrometer for determining the sample temperature. In addition, a source for atomic oxygen has been added. The main advantage of the new heating system is that only the substrate is heated while the surrounding parts are hardly affected (Fig.3, right). In this way one can achieve an essentially better vacuum at temperatures well above 1000°C. The achievable substrate temperature is limited by the melting point and the size of the substrate material (approx. 1410°C for a  $5 \times 5 \text{ mm}^2$  silicon substrate). The laser heating system has already been successfully used for removing the amorphous silicon oxide layer from the surface of silicon substrates at 1150°C. This is required for the epitaxial growth of oxide thin films on this substrate.



**Figure 2:** Pulsed Laser Deposition (PLD): When the pulse of the UV laser (KrF excimer laser, 248 nm) hits the target, the target material is ablated and the so-called laser “plume” containing highly excited atoms and molecules is formed.

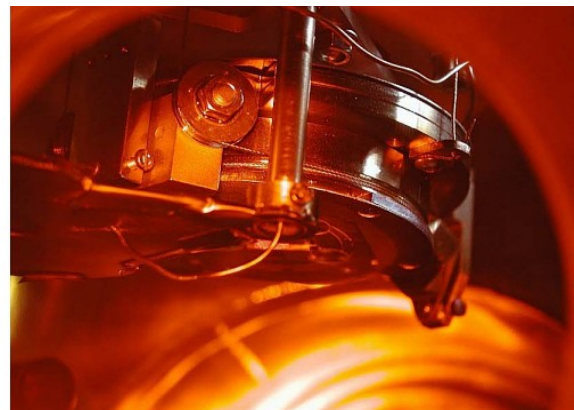
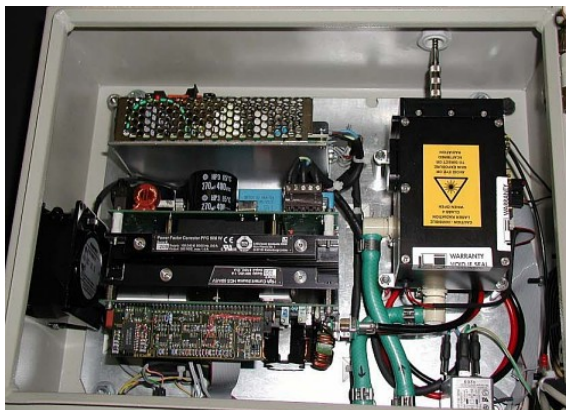


**Figure 3:** Components of the laser heating system: The substrate is heated using an IR diode laser head that is located in a separate box far away from the deposition chamber (left). The laser light is brought to the substrate (right) via an optical fiber.

## Single Crystal Growth and Synthesis of Bulk Materials

Transition metal oxides are of great interest due to their various interesting physical properties (e.g. high temperature superconductivity, colossal magnetoresistance, ferroelectricity, nonlinear optical properties etc.) and their high potential for applications. Therefore, the WMI operates a laboratory for the synthesis of bulk materials and single crystals of transition metal oxides. Besides various chamber- and tube furnaces a four-mirror image furnace is used in the crystal growth of various oxide systems. With this furnace crystals of many different compounds of the high temperature superconductors and various other transition metal oxides have been grown as single crystals using the traveling solvent floating zone technique. The furnace consists basically of 4 elliptical mirrors with a common focus on the sample rod and with halogen lamps in their other focus. By irradiation of the focused light the sample rod is locally heated and eventually molten. The molten zone can be moved up and down along the entire sample rod under simultaneous rotation. Due to the anisotropic growth velocity a preferential growth of those grains with the fastest growth velocity along the pulling direction is obtained and the formerly polycrystalline rod is transformed into a single crystal. Single crystal growth can be performed with this furnace at maximum temperatures up to 2200°C in the pressure range from  $10^{-5}$  mbar up to 10 bar and in oxidizing, reducing as well as inert atmosphere.



**Figure 4:** The four-mirror image furnace installed at the crystal laboratory of the WMI. Crystals can be grown by the floating zone and traveling solvent floating zone technique at temperatures up to 2200°C and pressures up to 10 bar.

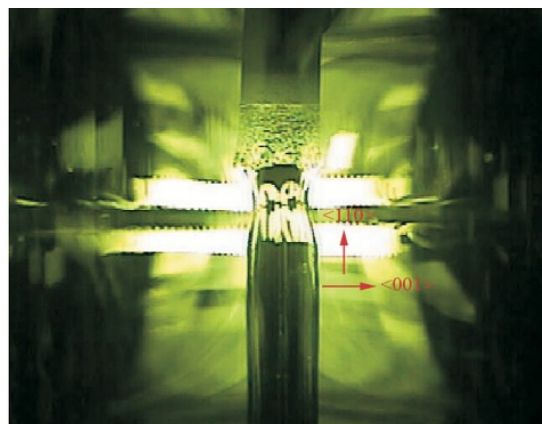
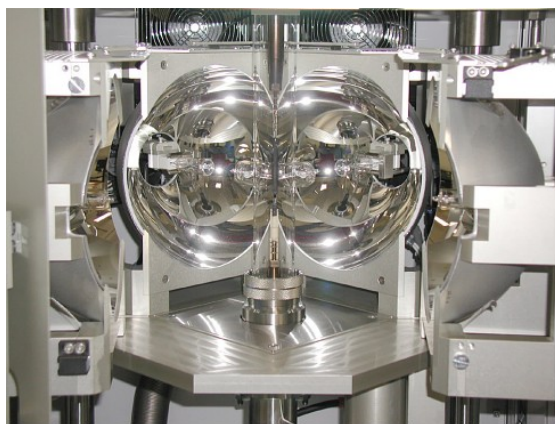


**Figure 5:** Left: Central part of the image furnace with the four elliptical mirrors. In the center one can see the quartz tube with the poly-crystalline rod. Right: View on the molten zone of  $\text{Pr}_{2-x}\text{Ce}_x\text{CuO}_4$  (melting point: 1280°C) obtained by a CCD camera.

### The X-ray diffraction systems

For x-ray analysis the Walther-Meissner-Institute operates two X-ray diffractometers (Bruker D8 Advance and D8 Discover). The two-circle system is used for powder diffraction. In this system the samples can be heated in oxygen atmosphere up to 1600°C. It is equipped with a Göbel mirror and an area detector to save measuring time. The second system is a high resolution four-circle diffractometer that can be used for reciprocal space mappings. It is equipped with a Göbel mirror and an asymmetric two-fold monochromator and allows for the texture analysis of thin film superlattices and single crystalline materials. In both systems measurements can be carried out fully computer controlled.



Figure 6: The two-circle X-ray diffractometer Bruker D8 Advance.

Beyond these two Bruker x-ray systems a Laue camera for single crystal analysis and a Debye-Scherrer camera are available.

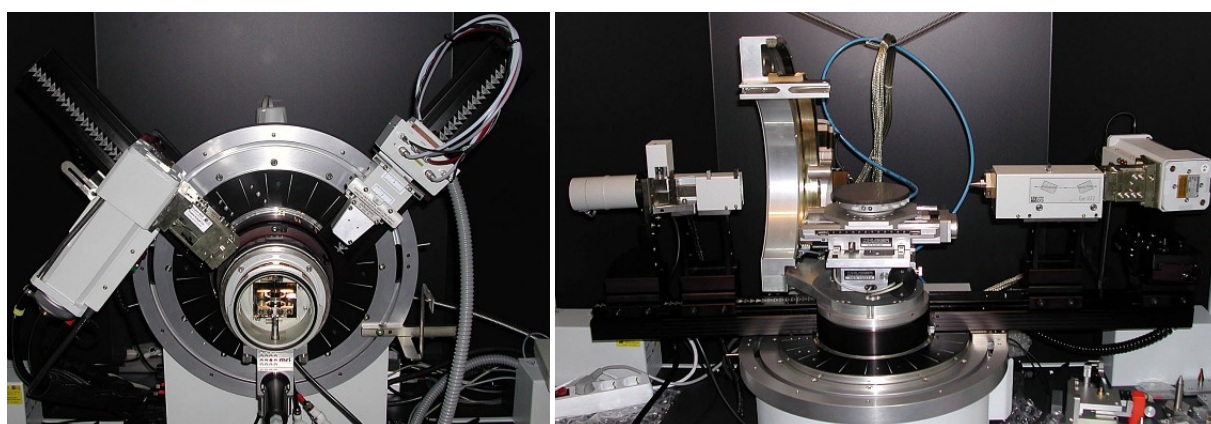


Figure 7: Left: High temperature sample holder of the D8 Advance system. Right: Four-circle high resolution X-ray diffractometer Bruker D8 Discover.



Figure 8: Quantum Design SQUID magnetometer.

### The SQUID-magnetometer

For the analysis of the magnetic properties of materials, a Quantum Design SQUID magnetometer system as shown in Fig. 8 is used at the WMI. The SQUID magnetometer allows for measurements in the temperature regime from 1.5 to 400 K and provides excellent sensitivity particularly in the low field regime. Due to the excellent sensitivity of the system, thin film samples with a very small sample volume can be analyzed. In a special inset, samples can be measured up to temperatures well above room temperature (up to 700°C). For this option the sample volume has to be reduced.

The SQUID magnetometer is equipped with a superconducting solenoid allowing for a maximum field of 7 T. At present, the magnetometer is used for the characterization of magnetic materials (both in bulk and thin film form). Examples are the doped manganites, magnetite, the double perovskites or magnetic semiconductors.

### The High Field Laboratory

Transport and thermodynamic properties of samples are often studied as a function of applied magnetic field. For such measurements several superconducting magnets are available at the WMI. Two of them (8/10 and 15/17 Tesla magnet system) are located in the high magnetic field laboratory in the basement of the WMI. The magnet systems are lowered below the ground level to facilitate the access



Figure 9: High field laboratory with Oxford 17 T magnet system.

to the top flange and the change of the sample sticks. The magnet systems are decoupled from the building to avoid noise due to mechanical vibrations. A variety of sample holders can be mounted allowing for e.g. sample rotation during the measurement. For standard sample holders the accessible temperature regime is  $1.5 \text{ K} < T < 300 \text{ K}$ . However, also  $^3\text{He}/^4\text{He}$  dilution refrigerator inserts ( $T > 20 \text{ mK}$ ) or high temperature units ( $T < 700 \text{ K}$ ) can be mounted. All measurements are fully computer controlled (by the use of the LabView software tool) allowing for remote control and almost continuous measurements.



**Figure 10:** Top: Part of the clean room facility with optical lithography equipment and clean room benches. Bottom: Resist coater and hot plates.

### The Clean Room Facility

For the fabrication of nanostructures and superconducting as well as spintronic devices the WMI operates a class 1000 clean room facility with an area of about 50 m<sup>2</sup>. This clean room facility has been put into operation at the WMI within the year 2001. The clean room is subdivided into two parts for optical lithography and electron beam lithography, respectively. The clean room facility is equipped with the standard tools for optical lithography such as resist coaters, hot plates, wet benches, a Karl Süss MJB3 mask aligner and an optical projection lithography system. The technical infrastructure for the clean room is located in the basement of the WMI directly below the clean room area.

Since 2005 the clean room also is equipped with a reactive ion etching system, Plasmalab 80 Plus with ICP plasma source (Oxford Instruments Plasma Technology).

### Electron Beam Lithography

The Electron Beam Lithography System is installed in one part of the clean room facility. It consists of a Philips XL 30 SFEG scanning electron microscope (SEM) with a Raith Elphy Plus electron beam lithography system and a laser interferometer table for precise stitching of writing fields.

The SEM is equipped with a hot field emitter and typically provides a beam diameter of less than 1.5 nm at  $\geq 10$  keV or about 2.5 nm at 1 keV. The lithography unit allows the fabrication of nanostructures down to about 10 nm. We have realized the controlled fabrication of metallic strip patterns with a strip width of about 20 nm. The electron beam lithography is used for the fabrication of nanostructures in metallic and oxide systems required for the study of quantum effects in mesoscopic samples.

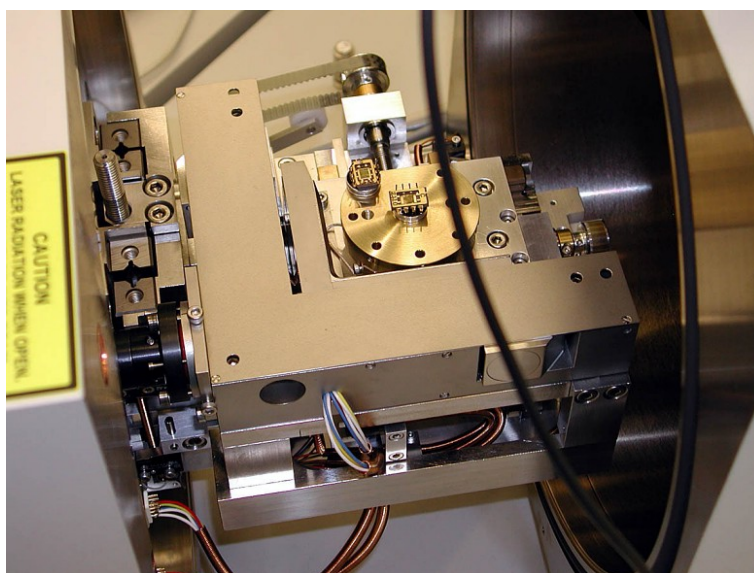
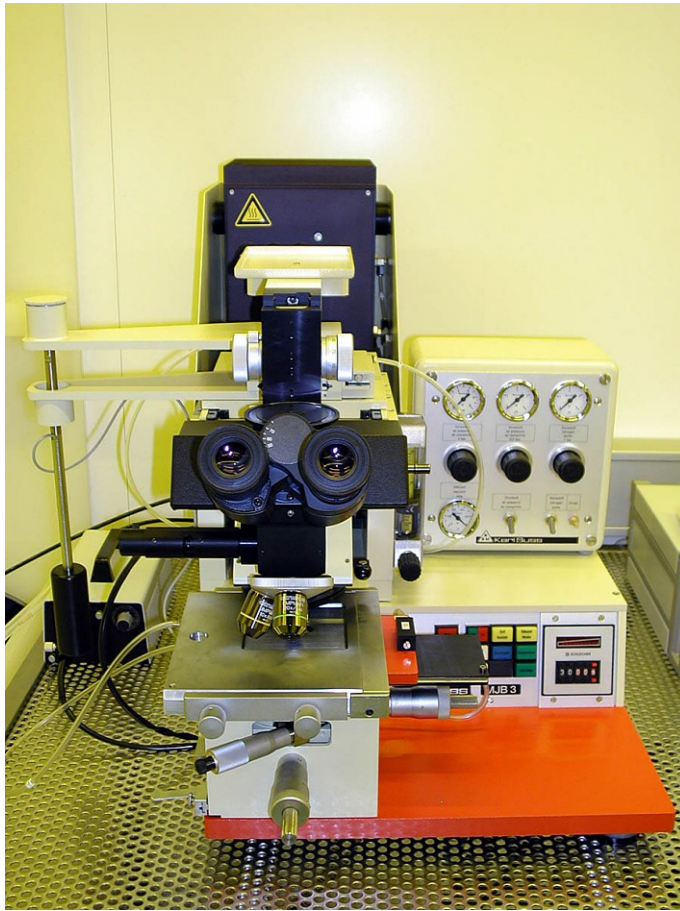


**Figure 11:** Top: Philips XL 30 SFEG Scanning Electron Microscope with Raith Elphy Plus Lithography System. Bottom: Raith Laser Stage.



### Optical Lithography

For optical lithography a Karl Süss MJB 3 maskaligner or an optical microscope based projection system are used. The maskaligner is operating in the 1 : 1 soft or hard contact mode and is using chromium metal masks. In the projection system the mask pattern is demagnified by a factor of 5 to 100. Therefore, cheap foil masks can be used. With both systems microstructures with a lateral dimension down to  $1\mu\text{m}$  can be fabricated.



**Figure 12:** Top: Süss MJB 3 maskaligner for optical lithography. Bottom: Optical projection lithography based on an optical microscope.

### Low and Ultra-low Temperature Facilities

The WMI operates several low and ultra-low temperature facilities that have been developed and fabricated in-house.

The lowest temperature is achieved by the nuclear demagnetization cryostat "Bayerische Millimühle 2". This ultra-low temperature facility consists of an in-house built dilution refrigerator and originally of two nuclear demagnetization stages. The first of those is based on a hyperfine enhanced van Vleck paramagnet  $\text{PrNi}_5$  (0.9 mole), the second, which has been removed a few years ago, was based on purified copper (0.2 mole). The lowest temperature reached with this system was slightly below  $30 \mu\text{K}$  in the copper nuclear spin system. At the moment, the first stage can be cooled to below  $400 \mu\text{K}$  and, due to the large heat capacity of  $\text{PrNi}_5$ , it stays below the mixing chamber temperature (5 mK) for nearly 3 weeks. In this cryostat three measuring sites are provided, two in a magnetic field compensated region and one in the center of an 8 T magnet. They are suitable for specific heat measurements, for capacitive torque- and SQUID magnetometry, as well as for transport measurements (electrical and thermal conductivity). The cryostat is also equipped with a pressure cell for liquid and solid  $^3\text{He}$ , which at the moment is used for nuclear spin resonance measurements below 1 mK.

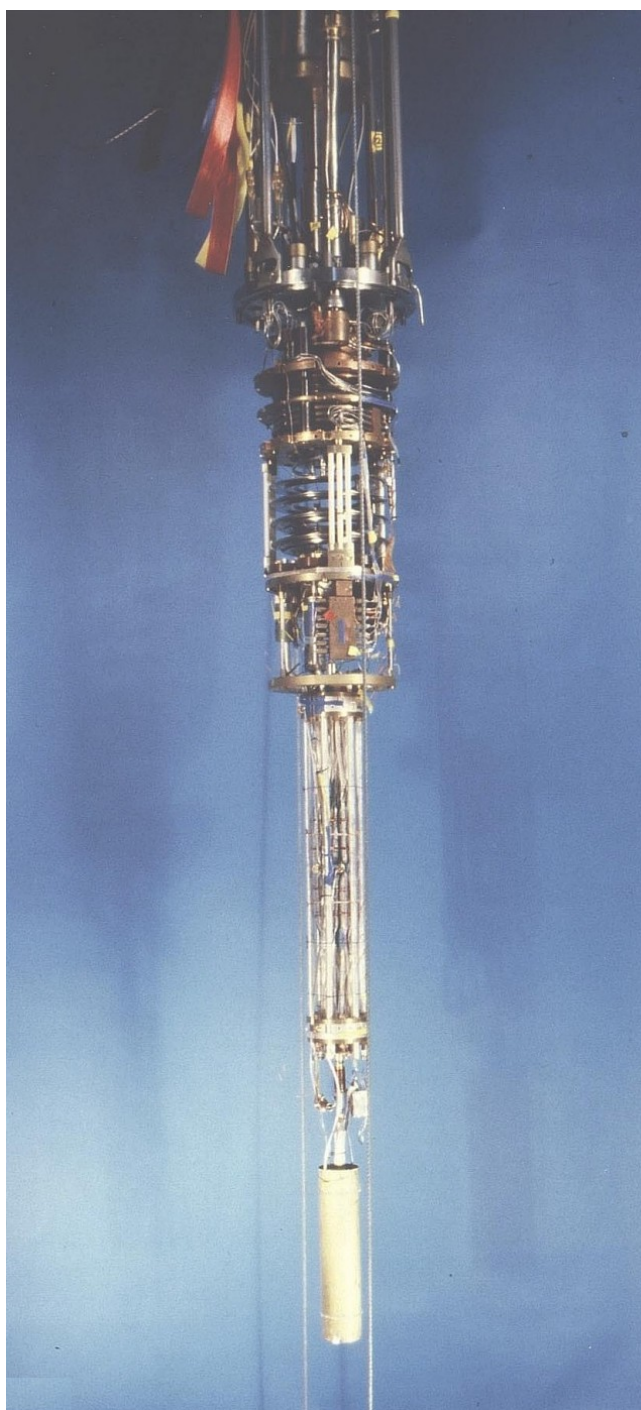


**Figure 13:** The dilution refrigerator and the nuclear demagnetization stage of the nuclear demagnetization cryostat "Bayerische Millimühle 2".

Some years ago, at the WMI, we have constructed the first dilution refrigerator with pulse tube pre-cooling for ultra-low temperature experiments. This type of refrigerator works without cryo-liquids, and thus is a lot more practical, more economical and more reliable than cryostats with liquid helium pre-cooling. These days, all major cryo-engineering firms are offering commercial versions of this milli-Kelvin cooler, and these so-called "dry" refrigerators outsell conventional refrigerators by a wide margin. The general construction concept of most manufacturers is unchanged from our original



**Figure 14:** The "dry" dilution refrigerator of the WMI.



**Figure 15:** Low-temperature unit of a WMI dilution refrigerator ready to go into a cryostat.

prototype, where the refrigerator consists of three basic components. The first cooling stage is a commercial pulse tube cryocooler which reaches a base temperature of 2.5 K. The second stage is a Joule-Thomson stage, and the last stage is a dilution refrigeration stage, where the lowest temperature of the cryostat is about 0.01 K (Fig. 14).

In many low temperature applications high refrigeration capacities are required. Our design allows for a high circulation rate of  $^3\text{He}$  which in the end determines the cooling power of a dilution refrigerator. Presently our "dry" fridge reaches a refrigeration capacity of  $700 \mu\text{W}$  at a temperature of the mixing chamber of 0.1 K, seven times the cooling power of the WMI nuclear demagnetization cryostat. Goals of our present work are a further increase of cooling power and a lower base temperature of the dry dilution refrigerator.



**Figure 16:** Two mixing chamber mounting plates with silver sponges. Those are needed to overcome the thermal resistance (Kapitza resistance) between the liquid  $^3\text{He}$  and the mounting plate of the mixing chamber. To fabricate the mounting of the sponge (square pins embedded in the sponge) a spark erosion technique has been employed.

A smaller version of our cryogen-free fridge has become commercially available at VeriCold Technologies, Ismaning. It has a refrigeration capacity of  $250 \mu\text{W}$  at a mixing chamber temperature of 0.1 K (Fig.15).



**Figure 17:** Dilution refrigerator insert with the Joule-Thompson stage, the heat exchanger and the mixing chamber.

The WMI also develops and fabricates dilution refrigerator inserts for temperatures down to about 20 mK. The inserts fit into all cryogenic systems (e.g. superconducting magnets) having a two inch bore. They allow fast sample change and rapid cool down cycles of less than five hours.

The dilution refrigerator inserts are engineered and fabricated in-house and are also provided to other low temperature laboratories for ultra low temperature experiments.

## Low Temperature Scanning Tunneling Microscope with Ultra-High-Vacuum Characterization and Preparation Facilities

The low temperature scanning tunneling microscope (LT-STM) allows investigation of low dimensional systems such as self-organized molecules, superconductors, magnetic and hetero-structure surfaces. The LT-STM is integrated into an ultra-high vacuum (UHV) chamber together with a variety of analytical as well as preparation tools. The Hermann-group operates the LT-STM and the here listed preparation facilities at the WMI. Besides being part of the WMI, Prof. Hermann heads a workgroup of experimental physics at the LMU-Munich and is at the same time ordinary member of the Center for Nano Science (CeNS) as well as principal investigator in the Nanosystems Initiative Munich Excellence-Cluster (NIM).

### The Microscope

The LT-STM (top picture) is designed for easy handling under UHV as well as low temperature conditions. We control the Omicron STM by an electronics from the company RHK (bottom picture, left side). In the following, some technical features are listed:

- In-situ sample and tip exchange (manipulator see bottom picture, right side).
- Vibration isolation ensured by a spring suspension system with eddy current damping and pneumatic damping legs.
- Variable temperatures from 5 K (pumped 2 K) up to room temperature ( $\approx 300$  K).
- Fast system cool-down (5 K within  $\approx 6$  hours).
- Sample pre-cooling to 50 K on the manipulator stage.
- Fast sample cool-down (5 K within  $\approx 2$  hours).
- On-line optical access.
- On-line four terminal transport measurements.
- Up to 6 samples can be stored at low temperature (77 K).



## Preparation and Characterization Facilities

In addition to the LT-STM analysis chamber another UHV-preparation chamber (see top picture, in the middle) allows for sample preparation and characterization under UHV-conditions. Substrates can be prepared by an argon sputter gun and thermal annealing. A three crucible evaporator allows the deposition of molecules onto the surface. For sample characterization low-energy-electron-diffraction (LEED) and quadrupole mass spectrometry are available.

### Argon Sputter Gun

Inside the preparation chamber clean single crystalline substrates are prepared by ion-sputtering and subsequent thermal annealing which can be controlled by a three grid LEED (middle picture) in a vacuum of  $10^{-11}$  mbar.

### Evaporator for Organic Material

A microprocessor controlled evaporator allows deposition of up to three different organic materials at the same time (bottom picture). Crucibles are refilled without breaking the vacuum of the main chamber.

### Sample Heating/Cooling Stage

The preparation facilities allow a direct current and indirect heating of the sample up to 1073 K and sample cooling down to 50 K on the manipulator (top picture, far right in the back).

### Low Energy Electron Diffraction (LEED)

The surface ordering of (reconstructed) substrate/single crystal surfaces or molecular adlayers can be analyzed by low energy electron diffraction (middle picture).

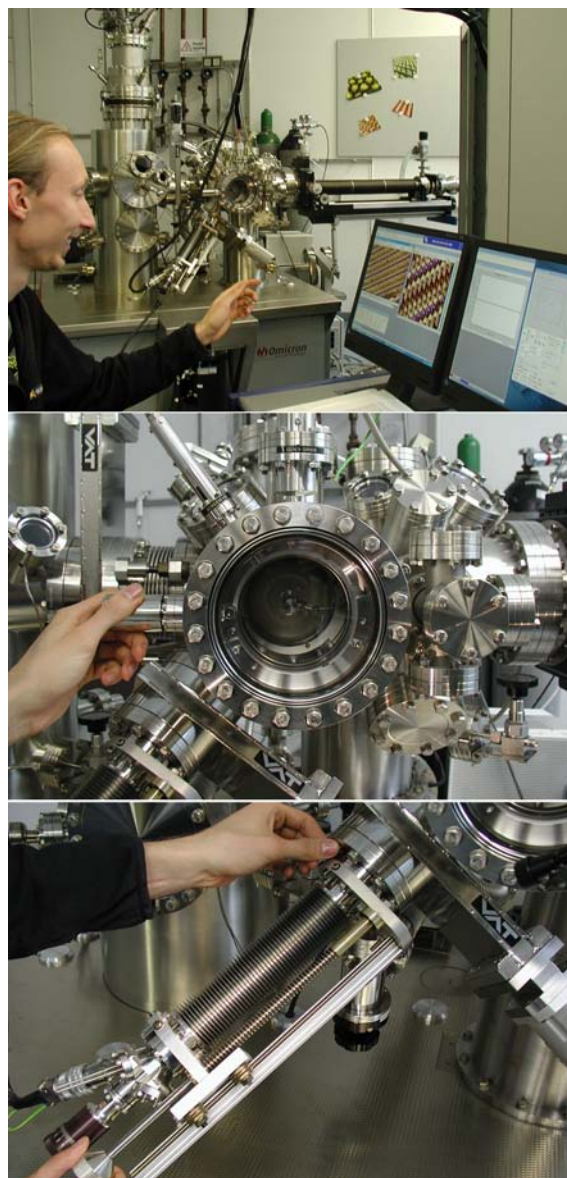
### Quadrupole Mass Spectrometer

Samples are additionally characterized by desorption spectroscopy with a quadrupole mass spectrometer. The desorbing molecules are ionized in a crossbeam ion source and accelerated in the quadrupole mass spectrometer, which either uses a Faraday cup or secondary electron multiplier (SEM) as detector with a mass resolution up to 2048 u.

Multiple additional vacuum ports allow further extensions of the Omicron STM in the future.

### Tip etching facility

The standard procedure for preparing STM tips suitable for STM measurements is of cutting an PtIr-wire with scissors. Other tip materials (e.g. Tungsten, Gold, Iron, ...) have to be etched in order to give the necessary tip radii. A newly constructed tip etching facility allows the use of other tip material than PtIr.



## Magnetic Field Low Temperature Ultra-High-Vacuum (UHV) Scanning Tunneling Microscope (STM)

The homebuilt low temperature scanning tunneling microscope with an external field up to 4 Tesla is specialized on tunneling spectroscopy measurements. Built under the guidance of B. A. Hermann in the group of Prof. Dr. H.-J. Güntherodt in Basel, the system was very recently completed in its components at the WMI in Munich. The high stability of the instrument as well as temperatures as low as 2.7 K allow the investigation of high temperature superconductor (HTSC) and organic superconductors as well as conventional superconductors. In a collaboration with A. Erb, M. Lambacher, R. Hackl as well as M. Kartsovnik and W. Biberacher, the group of B. A. Hermann currently investigates  $Y_1Ba_2Cu_3O_{8-ff}$ , NbSe<sub>2</sub> and ET<sub>2</sub>Cu(NCS)<sub>2</sub>.



The STM is optimized for low temperature tunneling imaging and spectroscopy in high magnetic fields under UHV-conditions (see picture: STM in the cryostat). A self-built electronics allows scanning tunneling spectroscopy at points along lines, in grids and in a high density mode.

### Technical Features of the STM:

- Imaging resolution: 0.01 nm in x-y-direction and 0.005 nm in z-direction.
- Current-voltage spectroscopy (I-V) (voltage resolution: 0.05 meV).
- Current-distance curves (I-d).
- Maximum scan size: 1  $\mu\text{m}$  x 1  $\mu\text{m}$  at 4.2 K.
- Superconducting magnet up to 4 T with persistent switch.
- Vibration damping through spring suspension.
- Temperature range from room temperature down to liquid helium temperature at 4.2 K (pumped 2.7 K).
- Cryostat with LHe durability of one week (without thermal load).

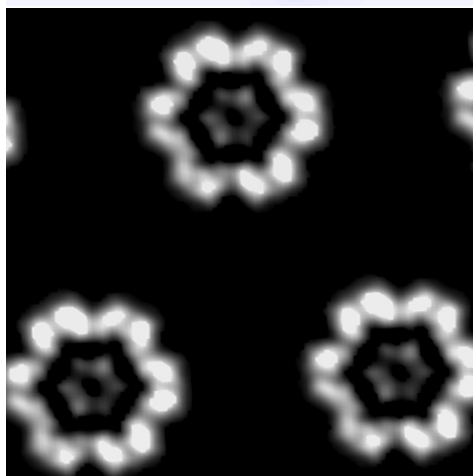
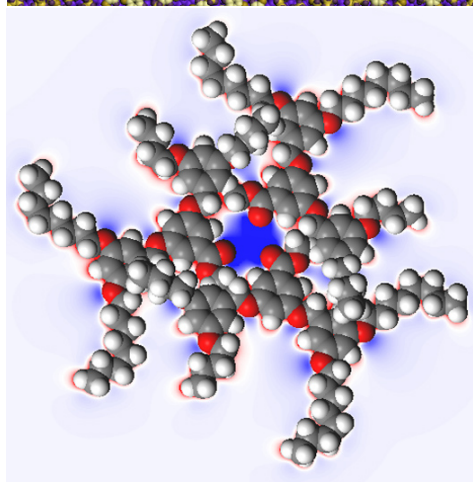
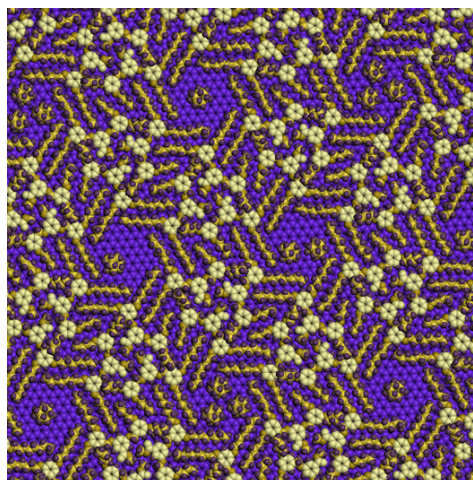
## Molecular Mechanics (MM), Molecular Dynamics (MD) and Density Functional Theory (DFT) Simulation Software

Commercial simulation software available for materials science applications allows experimental groups to predict and understand the studied materials in a complementary way. Materials Studio provides an easy access interface to codes of the United Kingdom Car-Parinello Consortium in order to crosscheck experimental data on a day to day basis.

The Materials Studio is a modular simulation software consisting of Forcite Plus (molecular mechanics and molecular dynamics simulations), DMol<sup>3</sup> (computational efficient DFT based calculations) and CASTEP (high accuracy DFT calculations).

### Characteristics of Forcite Plus (MM and MD):

- Single energy point properties.
- Energy minimization of molecular structures.
- Problem optimized force fields (Universal, Dreiding, COMPASS etc.).
- Non-periodic, 2D and 3D-periodic structures are supported.
- MD-simulation (see upper right) in different thermodynamic ensembles (*NVT*, *NVE*, *NPH*, *NPT*) at a wide range of temperatures.
- Quenching/annealing allowing search for global energy minimum.
- Simulation of mechanical stress properties.



### Characteristics of DMol<sup>3</sup> (DFT):

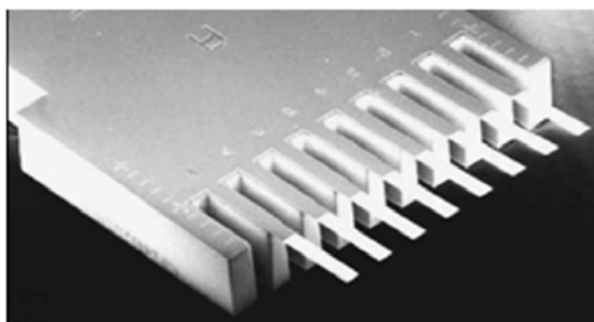
- Calculation of single energy point properties: bandstructure, density of states, electrostatic potential (see lower right), orbitals etc.
- Problem oriented usage via two local density approximation (*LDA*) functionals and eight generalized gradient approximation (*GGA*) functionals.
- MM-geometry optimization using the energies and forces calculated by DFT.
- Dynamical simulation of electronic sample properties in up to two thermodynamic ensembles (*NVT*, *NVE*).
- Continuous solvation model for as much as 15 different solvents.
- Search for the inversion point (transition state) in the energy landscape of a chemical reaction (energy barrier, reaction pathway).

### Characteristics of CASTEP (DFT):

- High precision calculation of single energy point properties: bandstructure, local density of states, orbital, NMR, optical properties, phonons, stress etc.
- One *LDA* and four *GGA* functionals as well as five nonlocal-exchange-correlation functionals (better description of semiconductors and insulators).
- MM-geometry optimization using the energies and forces calculated by DFT.
- Simulation of various dynamic sample properties (bandstructure,... see above) in four different thermodynamic ensembles or under elastic stress.
- Simulation of constant height STM-images: integrated local density of states at various bias voltage (see right).
- Search for transition states (e.g. in chemical reactions).

### Cantilever Sensor System with Integrated Liquid Handling and Temperature Control

With their small size, fast response time, and direct signal transduction without the need for labeling, cantilever sensors hold an enormous potential for applications in the field of biomolecular and chemical recognition and investigation of biomolecular interactions. Advantages of this technology in addition to their high sensitivity are parallel detection of multiple analytes (multiplexed assays), flexibility with respect to the choice of systems to be investigated, real-time analysis and on-line reference channels.



With a core competence in molecular self-organization and scanning probe microscopy, the Hermann group pursues application of this knowledge towards enabling and controlling a Concentris® cantilever array setup for the detection of (bio-)chemical key-lock interactions. (Bio)sensing devices are developed based on arrays of functionalized cantilevers that act as extremely sensitive and highly specific receptors for chemical or biological substances under accurate temperature control.

This research on protein-carbohydrate, bacterial, cell and gene interactions is integrated in the ERA Chemistry project with Prof. P. Seeberger, MPI Potsdam, and A. Rubio, University of The Basque Country, San Sebastián, and the Excellence Cluster "Nanosystems Initiative Munich" (NIM).

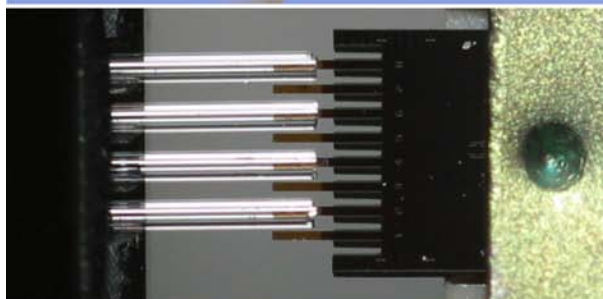
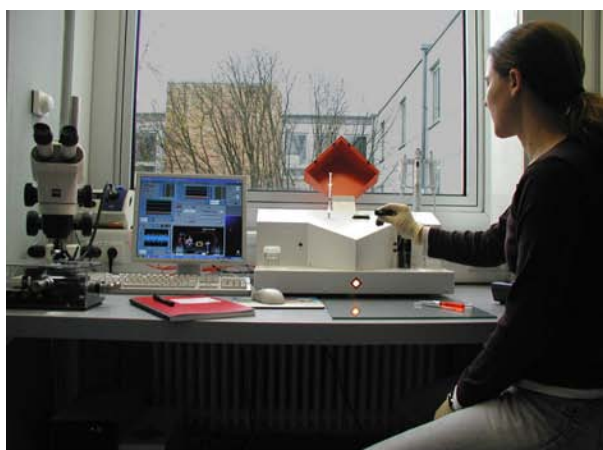
Cantilever sensors are small and extremely thin, long silicon beams (typically 500  $\mu\text{m}$  long, 100  $\mu\text{m}$  wide and 0.5-0.7  $\mu\text{m}$  thick), which are coated with a functional layer. This layer can e.g. consist of specific receptor molecules, lipid bilayers, polymer layers or others. All (bio)chemistry linked to gold or silicon oxide surfaces can potentially be applied to cantilever arrays.

### Modes of Operation

A reaction occurring at the functional cantilever surface, e.g. molecular rearrangements or binding of specific target molecules, is transduced into a mechanical deflection in the nanometer regime. This deflection is caused by surface stress (lateral force), which is due to electrostatic interaction or steric effects. In addition, shifts in the resonance frequency of a cantilever can be measured with high precision allowing the simultaneous determination of mass adsorption to or desorption from the cantilever surface. The combination of these two complementary measurement modes - deflection caused by surface stress (static mode), and resonance frequency shifts caused by changing mass load (dynamic mode) - is a unique feature, which sets cantilever sensors apart from any other technologies used in the life science field (forces below  $10^{-9}$  N and masses in the sub-picogram range can be detected).

### Functionalization of Cantilever Arrays

Typically a microarray of eight differently functionalized sensors allows to detect multiple substances within a mixture simultaneously and to take into account unspecific bindings by employing one or more cantilevers as reference channels. The functionalization is technically



realized by inserting the cantilevers into an array of liquid-filled micro capillaries in a functionalization unit. The process of chemical functionalization then takes place within minutes or hours controlled through a high resolution optical microscope by a camera.

### Handling Cartridge for Cantilever Arrays

The cantilever arrays are handled in a cartridge (which also contains the piezo actuator) allowing mounting and laser adjustment in the Concentris Cantisens® Research system. Following, the features of the Concentris cantilever sensor system are listed.

- Temperature control from 290 K to 340 K.
- Preheating stage allowing temperature stability better than 0.05 K.
- Vibration damping.
- Force ( $F$ ) or surface stress ( $\sigma$ ) resolution in static mode:  $F = 10^{-9}$  N;  $\sigma = 10^{-4}$  N/m.
- Frequency resolution 0.1 ppm in the dynamic mode (10mHz@100kHz).  
Dynamic range from 10 kHz to 2 MHz.
- Example of mass load detection in the dynamic mode in vacuum:  
0.025 fg/mm<sup>2</sup>/Hz corresponding to  
 $m = 10^{-18}$  g (from B. Illic et al., *J. Appl. Phys.*, **95**, 7 (2004)).
- Real-time dynamic measurements.
- Simultaneous measurements of static mode signals and dynamic mode signals in liquids (0.1 to 10 Hz sampling rate).
- Resolution of differential deflection  
< 2 nm (best case) or < 5 nm (average case).
- Optical beam deflection system.
- Arrays of 8 parallel, stabilized single-mode vertical-cavity surface-emitting lasers (VCSEL®, wavelength 850 nm) for optical read-out.
- Bio-compatible measurement cell with a volume of only 5  $\mu$ l.
- Capable of measuring (bio-) chemical reaction dynamics.
- Integrated liquid handling system: liquid flow rates ranging from 0.4  $\mu$ l/sec to 50.0  $\mu$ l/sec.  
Figure shows: set-up, handling cartridge, close-up on capillaries and the mechanics of the functionalization unit.

### Cleaning of the Sensor Surface:

For the reproducibility of results very clean sensor surfaces are mandatory prior to functionalization. Applying UV-ozone treatment guarantees an efficient attachment of the sensing layer. The new Novascan Benchtop UV-Ozone Cleaner features an adjustable sample stage and a UV lamp that emits both at 185 and 254 nm.

## Publications

1. F. Deppe, M. Mariani, E.P. Menzel, A. Marx, S. Saito, K. Kakuyanagi, H. Tanaka, T. Meno, K. Semba, H. Takayanagi, E. Solano, R. Gross,  
**Two-photon probe of the Jaynes-Cummings model and controlled symmetry breaking in circuit QED**  
Nature Physics **4**, 686-691 (2008).
2. M. Wagenknecht, D. Koelle, R. Kleiner, S. Graser, N. Schopohl, B. Chesca, A. Tsukada, S.T.B. Gönnerwein, R. Gross,  
**Phase diagram of the electron-doped  $\text{La}_{2-x}\text{Ce}_x\text{CuO}_4$  cuprate superconductor from Andreev bound states at grain boundary junctions**  
Phys. Rev. Lett. **100**, 227001 (2008).
3. F. Deppe, M. Mariani, E.P. Menzel, S. Saito, K. Kakuyanagi, H. Tanaka, T. Meno, K. Semba, H. Takayanagi, R. Gross,  
**Phase coherent dynamics of a superconducting flux qubit with capacitive bias readout**  
Phys. Rev. B **76**, 214503 (2008).
4. M. Mariani, F. Deppe, A. Marx, R. Gross, F.K. Wilhelm, E. Solano,  
**Two-resonator circuit quantum electrodynamics: A superconducting quantum switch**  
Phys. Rev. B **78**, 104508 (2008).
5. D. Venkateshvaran, W. Kaiser, A. Boger, M. Althammer, M.S. Ramachandra Rao, S.T.B. Gönnerwein, M. Opel, R. Gross,  
**Anomalous Hall effect in magnetite: Universal scaling relation between Hall and longitudinal conductivity in low-conductivity ferromagnets**  
Phys. Rev. B **78**, 092405 (2008).
6. A. Brandlmaier, S. Geprägs, M. Weiler, A. Boger, M. Opel, H. Huebl, C. Bihler, M.S. Brandt, B. Botters, D. Grundler, R. Gross, S.T.B. Gönnerwein,  
**In situ manipulation of magnetic anisotropy in magnetite thin films**  
Phys. Rev. B **77**, 104445 (2008).
7. L. Tassini, W. Prestel, A. Erb, M. Lambacher, R. Hackl,  
**First-order-type effects in  $\text{YBa}_2\text{Cu}_3\text{O}_{6+x}$  at the onset of superconductivity**  
Phys. Rev. B **78**, 020511 (2008).
8. J. S. White, S. P. Brown, E. M. Forgan, M. Laver, C. J. Howell, R. J. Lycett, D. Charalambous, V. Hinkov, A. Erb, and J. Kohlbrecher  
**Observations of the configuration of the high-field vortex lattice in  $\text{YBa}_2\text{Cu}_3\text{O}_7$ : Dependence upon temperature and angle of applied field**  
Phys. Rev. B **78**, 174513 (2008).
9. D. Einzel, L. Klam,  
**Response, Relaxation and Transport in Unconventional Superconductors**  
J. Low Temp. Phys. **150**, 57-81 (2008).
10. D. Einzel, R. Hackl,  
**Robert Doll zum 85. Geburtstag**  
Akademie Aktuell **01**, 44-45 (2008).
11. S.T.B. Gönnerwein, M. Althammer, C. Bihler, A. Brandlmaier, S. Geprägs, M. Opel, W. Schoch, W. Limmer, R. Gross, M.S. Brandt,  
**Piezo-voltage control of magnetization orientation in a ferromagnetic semiconductor**  
Phys. Stat. Sol. (RRL) **2**, 96-98 (2008).
12. R. Ranjan, R. Hackl, A. Chandra, E. Schmidbauer, D. Trots, H. Boysen,  
**High-temperature relaxor ferroelectric behavior in Pr-doped  $\text{SrTiO}_3$**   
Phys. Rev. B **76**, 224109 (2008).
13. K. Uhlig,  
**Dry dilution refrigerator with high cooling power**

- CP 985, *Advances in Cryogenic Engineering: Transactions of the Cryogenic Engineering Conference-CEC 53*, edited by J.G. Weisend II, 1287-1291 (2008).
14. Yu. A. Ossipyan, N.S. Sidorov, A.V. Palnichenko, O.M. Vyaselev, M.V. Kartsovnik, M. Opel, V.V. Avdonin, D.V. Shakhrai, N.V. Biktimirova, A.A. Golyshev,  
**Superconductivity of C<sub>60</sub> fullerite intercalated with Ca by means of shock-wave pressure technique**  
Chem. Phys. Lett. **457**, 74-77 (2008).
  15. M. Opel, K.-W. Nielsen, S. Bauer, S.T.B. Gönnerwein, J.C. Cezar, D. Schmeisser, J. Simon, W. Mader, R. Gross,  
**Nanosized superparamagnetic precipitates in cobalt-doped ZnO**  
Eur. Phys. J. B **63**, 437-444 (2008).
  16. N.D. Kushch, E.B. Yagubskii, M.V. Kartsovnik, L.I. Buravov, A.D. Dubrovskii, A.N. Chekhlov, W. Biberacher,  
 **$\pi$ -Donor BETS Based Bifunctional Superconductor with Polymeric Dicyanamidomanganate (II) Anion Layer:  $\kappa$ -(BETS)<sub>2</sub>Mn[N(CN)<sub>2</sub>]<sub>3</sub>**  
J. Am. Chem. Soc. **130**, 7238-7240 (2008).
  17. C. Bihler, M. Kraus, M.S. Brandt, S.T.B. Gönnerwein, M. Opel, M.A. Scarpulla, R. Farshchi, D.M. Estrada, O.D. Dubon,  
**Suppression of hole-mediated ferromagnetism in Ga<sub>1-x</sub>Mn<sub>x</sub>P by hydrogen**  
J. Appl. Phys. **104**, 013908 (2008).
  18. K. Uhlig,  
**Condensation stage of a pulse tube precooled dilution refrigerator**  
Cryogenics **48**, 138-141 (2008).
  19. R. Ranjan, R. Gang, R. Hackl, A. Senyshyn, E. Schmidbauer, D. Trots, H. Boysen,  
**Onset of spontaneous electrostrictive strain below 520 K in Pr-doped SrTiO<sub>3</sub>**  
Phys. Rev. B **78**, 092102 (2008).
  20. A. Nielsen, A. Brandlmaier, M. Althammer, W. Kaiser, M. Opel, J. Simon, W. Mader, S.T.B. Gönnerwein, R. Gross,  
**All oxide ferromagnet/semiconductor epitaxial heterostructures**  
Appl. Phys. Lett. **93**, 162510 (2008).
  21. R.B. Lyubovskii, S.I. Pesotskii, W. Biberacher, E.I. Zhilyaeva, O.A. Bogdanova, R.N. Lyubovskaya,  
**De Haas-Van Alphen Oscillations in the Quasi-Two-Dimensional Organic Metal (BEDO-TTF)<sub>5</sub>[CsHg(SCN)<sub>4</sub>]<sub>2</sub>**  
Sov. Phys. Solid State **50**, 1560-1564 (2008).
  22. M. Weiler, A. Brandlmaier, S. Geprägs, M. Althammer, M. Opel, C. Bihler, H. Hübl, M.S. Brandt, R. Gross, S.T.B. Gönnerwein,  
**Voltage controlled inversion of magnetic anisotropy in a ferromagnetic thin film at room temperature**  
New Journal of Physics **11**, in press (2008).
  23. C. Bihler, M. Althammer, A. Brandlmaier, S. Geprägs, M. Weiler, M. Opel, W. Schoch, W. Limmer, R. Gross, M.S. Brandt, S.T.B. Gönnerwein,  
**Ga<sub>1-x</sub>Mn<sub>x</sub>As/piezoelectric actuator hybrids: A model system for magnetoelastic magnetization manipulation**  
Phys. Rev. B **78**, 045203 (2008).
  24. M.V. Kartsovnik,  
**Layered organic conductors in strong magnetic fields**  
General Review in *The Physics of Organic Superconductors and Conductors*, ed. by A.G. Lebed (Springer Series in Materials Science **110**, 185-246 (2008).
  25. L. Tassini, W. Prestel, A. Erb, M. Lambacher, R. Hackl,  
**Relation between ordering and superconductivity in cuprates**

- Physica B **403**, 1092 (2008).
26. C. Maqueda, A.S. Romero, E. Morillo, J.L. Pérez-Rodríguez, A. Lerf, F.E. Wagner,  
**The Behavior of Fe in Ground and Acid-Treated Vermiculite from Santa Olalla, Spain**  
Clays and Clay Minerals **56**, 380-388 (2008).
  27. V. Ramírez-Valle, A. Lerf, F.E. Wagner, J. Poyato, J.L. Pérez-Rodríguez,  
**Thermal study of polypyrrole complexes with vermiculites of different layer charge**  
J. Thermal Analysis and Calorimetry **92**, 43-51 (2008).
  28. V. Ramírez-Valle, A. Lerf, F.E. Wagner, J. Poyato, J.L. Pérez-Rodríguez,  
**Fe<sup>3+</sup> intercalation/deposition on vermiculites and interaction with pyrrole. A Mössbauer spectroscopic investigation**  
Clay Minerals **43**, 487-499 (2008).
  29. L. Kulhánková, P. Capková, V. Ramírez-Valle, J. Poyato, J.L. Pérez-Rodríguez, A. Lerf,  
**Surface and interlayer structure of vermiculite intercalated with methyl viologen**  
J. Mol. Model. **14**, 1183-1189 (2008).
  30. B.S. Chandrasekhar,  
**Have you heard of pseudoscience**  
Deccan Herald (23.02.2008).
  31. B.S. Chandrasekhar,  
**Fall of a superconductor myth**  
Deccan Herald (07.07.2008).
  32. B.S. Chandrasekhar,  
**Biodiversity**  
Deccan Herald (30.08.2008).
  33. B.S. Chandrasekhar,  
**Waves, waves, everywhere and not a drop to drink**  
Deccan Herald (19.09.2008).
  34. B.S. Chandrasekhar,  
**The large hadron collider**  
Deccan Herald (23.09.2008).
  35. E. Schuberth, M. Tippmann, M. Kath, C. Krellner, C. Geibel, T. Westerkamp, C. Klingner, F. Steglich,  
**Magnetization Measurements on YbRh<sub>2</sub>Si<sub>2</sub> at Very Low Temperatures**  
J. Phys. C, in press (2008).
  36. S. Geprägs, F.D. Czeschka, M. Opel, S.T.B. Gönnenwein, W. Yu, W. Mader, R. Gross,  
**Epitaxial growth and magnetic properties of Sr<sub>2</sub>CrReO<sub>6</sub> thin films**  
J. Magn. Magn. Mater., accepted for publication (2008).
  37. M.V. Kartsovnik, D. Andres, W. Biberacher, H. Müller,  
**Magnetic field induced charge-density-wave transitions: the role of the orbital and Pauli effects**  
Physica B, in press (2008).
  38. L. Klam, D. Einzel, D. Manske,  
**Electronic Raman scattering in non-centrosymmetric superconductors**  
Phys. Rev. Lett., accepted for publication (2008).
  39. M. Wagenknecht, M. Rahlenbeck, D. Koelle, R. Kleiner, A. Tsukada, S.T.B. Goennenwein, R. Gross,  
**Grain Boundary Tunnel Spectroscopy of the Electron Doped Cuprate Superconductor La<sub>2-x</sub>Ce<sub>x</sub>CuO<sub>4</sub> in Low and High Magnetic Fields**  
Phys. Rev. B, submitted for publication (2008).
  40. M.V. Kartsovnik, P.D. Grigoriev, W. Biberacher, N.D. Kushch,  
**Magnetic field induced coherence-incoherence crossover in the interlayer conductivity of a layered organic metal**

- Phys. Rev. Lett., submitted for publication (2008).
41. J.M. Büttner, C.L. Rohr, F.A. Palitschka, N.D. Kushch, M.V. Kartsovnik, W. Biberacher, B.A. Hermann,  
**Organic Superconductors Revisited**  
Eur. Phys. J. B, submitted for publication (2008).
  42. D. Andres, M.V. Kartsovnik, W. Biberacher, K. Neumaier, I. Sheikin, H. Müller,  
**Field-induced charge-density-wave transitions in the organic metal  $\alpha$ -(BEDT-TTF)<sub>2</sub>KHg(SCN)<sub>4</sub> under hydrostatic pressure**  
Phys. Rev. Lett., submitted for publication (2008), arXiv:0801.2696.
  43. K. Uhlig,  
**<sup>3</sup>He/<sup>4</sup>He dilution refrigerator with high cooling capacity and direct pulse tube pre-cooling**  
Cryogenics, submitted for publication (2008).
  44. D. Venkateshvaran, M. Althammer, A. Nielsen, S. Geprägs, M.S.R. Rao, S.T.B. Gönnenwein, M. Opel, R. Gross,  
**Epitaxial Zn<sub>x</sub>Fe<sub>3-x</sub>O<sub>4</sub> Thin Films: A Spintronic Material with Tunable Electrical and Magnetic Properties**  
Phys. Rev. B, submitted for publication (2008).
  45. T. Niemczyk, F. Deppe, M. Mariani, E.P. Menzel, E. Hoffmann, G. Wild, L. Eggenstein, A. Marx, R. Gross,  
**Fabrication Technology of and Symmetry Breaking in Superconducting Quantum Circuits**  
Superconductor Science and Technology, submitted for publication (2008).
  46. R. Miller, S. Altmannshofer, E.-W. Scheidt, M. Herzinger, C. Gold, F. Mayr, D. Einzel, W. Scherer,  
**Discovery of a predominant paramagnetic Meißner effect in superconducting dichalcogenides**  
Phys. Rev. B, submitted for publication (2008).
  47. J.S. White, V. Hinkov, R.W. Heslop, R.J. Lycett, E.M. Forgan, C. Bowell, S. Straessle, A.B. Abrahamson, M. Laver, C.D. Dewhurst, J. Kohlbrecher, J.L. Gavilano, J. Mesot, B. Keimer, A. Erb,  
**Fermi surface and order parameter driven vortex lattice structure transitions in twin-free YBa<sub>2</sub>Cu<sub>3</sub>O<sub>7</sub>**  
Phys. Rev. Lett., submitted for publication (2008).
  48. N. Munnikes, B. Muschler, F. Venturini, L. Tassini, W. Prestel, S. Ono, Y. Ando, A. Damascelli, H. Eisaki, M. Greven, A. Erb, R. Hackl,  
**Possible origin of the second energy scale in superconducting cuprates**  
Phys. Rev. Lett., submitted for publication (2008).
  49. J. Poyato, J.L. Pérez-Rodríguez, V. Ramírez-Valle, A. Lerf, F.E. Wagner,  
**Sonication induced redox reactions of the Ojén (Andalucía, Spain) vermiculite**  
Ultrason. Sonochem., submitted for publication (2008).

## **Theses, Appointments, Honors and Awards, Membership in Advisory Boards, etc.**

### **Completed and ongoing Ph.D. Theses**

1. **Charge Ordering Phenomena and Superconductivity in Underdoped Cuprates**  
Leonardo Tassini, TU München, Januar 2008.
2. **Ursache der magnetischen Kopplung in Kobalt-dotiertem ZnO**  
Karl-Wilhelm Nielsen, TU München, Januar 2008.
3. **Crystal Growth and Normal State Transport of Electron Doped High Temperature Superconductors**  
Michael Lambacher, TU München, Oktober 2008
4. **Superconducting Flux Quantum Circuits: Properties, Decoherence, Coupling, and Controlled Symmetry Breaking**  
Frank Deppe, TU München, seit April 2002.
5. **Circuit-QED Experiments with Superconducting Quantum Bits**  
Matteo Mariani, TU München, seit November 2003.
6. **Magnetisierungsmessungen an festem  $^3\text{He}$  bei ultratiefen Temperaturen**  
Matthias Kath, TU München, seit April 2004.
7. **Supraleitende Quantenbits mit Supraleiter-Ferromagnet-Supraleiter Josephson-Kontakten**  
Georg Wild, TU München, seit September 2004.
8. **Spin-Engineering in funktionalen Schichtsystemen aus Übergangsmetalloxiden**  
Stephan Geprägs, TU München, seit Oktober 2004.
9. **Untersuchung der Wechselwirkungspotenziale in Kupratsupraleitern durch quantitativen Vergleich spektroskopischer Resultate**  
Wolfgang Prestel, TU München, seit November 2004.
10. **Tunnelkontakte und Spininjektoren auf der Basis von ferromagnetischen Übergangsmetalloxiden**  
Andrea Boger, TU München, seit März 2005.
11. **Kohärente Dynamik und Dekohärenz in supraleitenden Quantenbits**  
Edwin Menzel, TU München, seit Januar 2006.
12. **Quantenelektrodynamik mit supraleitenden Schaltkreisen**  
Thomas Niemczyk, TU München, seit Juli 2006.
13. **Multiferroisches Verhalten und steuerbarer Magnetismus in oxidischen Heterostrukturen**  
Andreas Brandlmaier, TU München, seit Dezember 2006.
14. **Tiefemperatur-Rastersondenmikroskopie an Molekülsystemen und Nanotubes**  
Carsten Rohr, LMU München, seit Januar 2007.
15. **Hybride Nanostrukturen auf der Basis von Materialsystemen mit elektronischen Korrelationen**  
Franz Czeschka, TU München, seit Juli 2007.
16. **Integrierte Induktivitäten in permeablen keramischen Mehrlagen-Strukturen**  
Thomas Florian Goßner, TU München, seit Juli 2007.
17. **(Bio) Sensorik mit Cantileverarrays und Oberflächenkontrolle mittels Rastersondentechniken**  
Kathrin Gruber, LMU München, seit November 2007.

18. **Korrelierte Systeme untersucht mit Tieftemperatur-Rastersondenmikroskopie**  
Johannes Büttner, LMU München, seit Januar 2008.
19. **Magnetotransporteigenschaften von dünnen ferromagnetischen Schichten und Heterostrukturen**  
Mathias Weiler, TU München, seit Februar 2008.
20. **Untersuchung von Kupraten nahe des Einsatzpunktes der Supraleitung**  
Bernhard Muschler, seit Februar 2008.
21. **Multifunktionale magnetische Heterostrukturen**  
Matthias Althammer, TU München, seit April 2008.
22. **Herstellung und Charakterisierung von supraleitenden Schaltkreisen zur Realisierung von gekoppelten supraleitenden Quantenbauelementen**  
Elisabeth Hoffmann, TU München, seit April 2008.
23. **Quantenexperimente mit elektromechanischen Systemen**  
Fredrik Hocke, TU München, seit Mai 2008.
24. **Spininjektion und Spintransport in ZnO-basierten Schichtsystemen**  
Deepak Venkateshvaran, TU München, seit Oktober 2008.
25. **Untersuchung von Ladungs- und Spinordnung in gering dotierten Kupraten: Eine Raman Studie**  
Hans-Martin Eiter, TU München, seit Oktober 2008.

The following PhD students of the Walther-Meißner-Institute have finished their theses in 2008:



**Karl-Wilhelm Nielsen**



**Leonardo Tassini**



**Michael Lambacher**

**Completed and ongoing Diploma, Bachelor, Master Theses**

1. **Preparation and Raman Studies of Cuprates with Low and Intermediate Doping**  
Nathalie Munnikes, Januar 2008.
2. **Untersuchung von  $\text{La}_{2-x}\text{Sr}_x\text{CuO}_4$  und  $\text{Re}_{2-x}\text{Ce}_x\text{CuO}_4$  (Re=Nd, Pr) nahe des Einsatzpunktes der Supraleitung bei hoher Dotierung**  
Bernhard Muschler, Januar 2008.
3. **Superconducting Hybrid Rings for Homodyne Detection of Microwave Signals**  
Elisabeth Hoffmann, Februar 2008.
4. **Untersuchung von Ladungs- und Spinordnung in gering dotierten Kupraten: Eine Raman-Studie**  
Hans-Martin Eiter, Mai 2008
5. **Dielektrische und magnetische Eigenschaften multifunktionaler Dünnschichtstrukturen**  
Daniel Pantel, Mai 2008.
6. **Mikroskopie und Spektroskopie mit Rastersondentechniken an (organischen) Supraleitern**  
Florian Palitschka, LMU München, Juni 2008
7. **Fabrication and Characterization of  $\text{Zn}_x\text{Fe}_{3-x}\text{O}_4$  Epitaxial Films**  
Deepak Venkateshvaran, Juni 2008
8. **Magnetisierungsmessungen an dem Schwere-Fermionen-System  $\text{YbRh}_2\text{Si}_2$  bei ultratiefen Temperaturen**  
Marc Tippmann, August 2008.
9. **Rastertunnelmikroskopie an Molekülsystemen**  
Cornelia Höhl, LMU München, September 2008.
10. **Mesoscopic Shelving Readout of Superconducting Qubits in Circuit Quantum Electrodynamics**  
Barbara Englert, Oktober 2008.
11. **Aufbau und Charakterisierung eines FMR-Spektrometers für X- und K-Band**  
Manuel Johannes Schwarz, Oktober 2008.
12. **Aufbau und Charakterisierung eines Spektrometers für magnetooptischen Kerr-Effekt**  
Matthias Pelkner, November 2008.
13. **A Setup for Quantum Signal Detection in a Circuit QED Architecture**  
Miguel Ángel Araque Caballero, November 2008.
14. **Transportmessungen an 214-Hochtemperatur-Supraleitern**  
Toni Helm, TU München, seit November 2007.
15. **Reibungsoptimierungspotentiale von amorphen Kohlenstoffen**  
Andreas Oancea, TU München, seit Dezember 2007.
16. **Non-linear Spin-based Nano-devices: Magnetic Diodes and Transistors**  
Arndt von Bieren, TU München, seit Januar 2008.
17. **Optimierung und Charakterisierung von supraleitenden Quantenschaltkreisen auf der Basis von Fluss-Quantenbits**  
Lars Eggenstein, TU München, seit Juni 2008.

18. **Herstellung, Charakterisierung und Untersuchung hochgeordneter Y-123 Einkristalle**  
Timo Buttler, seit Juni 2008
19. **Synthesis and Characterization of FeAs-based High- $T_c$  Superconductors**  
Monika Bahurupi, seit Juni 2008
20. **Herstellung und Charakterisierung von multifunktionalen ferromagnetischen/ferroelektrischen Hybridstrukturen**  
Matthias Brasse, seit Oktober 2008
21. **Herstellung und Charakterisierung von epitaktischen  $\text{Fe}_3\text{O}_4/\text{ZnO}$ -Dünnschichtstrukturen für die Spininjektion**  
Michael Albert Wagner, seit Oktober 2008
22. **Herstellung und Charakterisierung von metallischen Nanostrukturen**  
Daniel Ruffer, seit November 2008
23. **Supraleitende Quantenschalter**  
Thomas Weißl, seit November 2008

## Honors and Awards

In 2008, the following acknowledgements and awards have been achieved by members of the WMI:

### Arnold Sommerfeld Award of the Bavarian Academy of Sciences and Humanities

**Dr. Sebastian Gönnerwein** of WMI received the *Arnold Sommerfeld-Award 2008* of the Bavarian Academy of Sciences and Humanities in recognition of his pioneering work on thin film systems consisting of superconducting, magnetic and semiconducting materials and their application in novel spintronic devices.

The Bavarian Academy annually gives the Arnold Sommerfeld Award for outstanding achievements in the fields of natural sciences. The prize has been presented to Sebastian Gönnerwein on December 6, 2008 by the president of the Academy within an Annual Meeting of the Bavarian Academy of Sciences and Humanities in the Munich Residence.



Sebastian T.B. Gönnerwein

### Venia Legendi in Theoretical Physics for Dietrich Einzel

**Dr. habil. Dietrich Einzel** of WMI received the *Venia Legendi in Theoretical Physics* from the Technische Universität München.

### Goldene Kreide for Best Seminar in SS 2008

The physics students awarded the *Goldene Kreide* for the best seminar in SS 2008 to the "Proseminar Physik/Technik: Makroskopische Quantenphänomene". The seminar was organized by S.T.B. Gönnerwein, R. Gross, A. Marx and R. Hackl of WMI together with Ch. Pfeleiderer of the Physics Department of TUM.

### Best Poster and Best Presentation Awards at Joint European Magnetism Conference

**Matthias Althammer** of WMI received a *Best Poster Presentation Award* for his poster entitled "*Magnetization Control in Multifunctional Heterostructures*", which he presented at the Joint European Magnetism Conference held from September 14 – 19, 2008 at Dublin, Ireland.

At the same conference, **Dr. Matthias Opel** of WMI received a *Best Oral Presentation Award* for his oral presentation entitled "*Ferromagnetism or Magnetic Clusters in Cobalt-Doped ZnO?*".

**Appointments, Membership in Advisory Boards, etc.**

1. **Rudolf Gross** has been appointed member of the Scientific Advisory Board of the Leibniz Institute for Solid-State and Materials Research, Dresden.
2. **Rudolf Gross** has been appointed member of the Kuratorium of the Physik Journal of the German Physical Society.
3. **Rudolf Gross** has been appointed spokesman of the section *Low Temperature Physics* of the Condensed Matter Division of the German Physical Society.
4. **Sebastian Gönnerwein** has been appointed associate member of the Cluster of Excellence *Nanosystems Initiative Munich (NIM)*.
5. **Werner Biberacher** has been appointed member of the Selection Panel EuroMagNet II of the Joint European High Magnetic Field Laboratories.
6. **Dietrich Einzel** is one of the four spokesmen of the scientific staff of the Bavarian Academy of Sciences and Humanities.
7. **Rudolf Gross** is member of the International Advisory Board of the Institute for Nanoscale Physics and Chemistry (INPAC), which has been established by the Katholieke Universiteit Leuven in 2006 in the framework of its Excellence Programme.
8. **Rudolf Gross** is member of the Board of Editors of the European Physical Journal B.

## Research Projects and Cooperations

A large number of our research projects are benefiting from the collaboration with external groups in joint research projects, as well as from individual collaborations, exchange programs and visitors. Most collaborations are based on joint projects, which are funded by different research organizations (see list below). A considerable number of collaborations also exists with universities, other research institutions and industry without direct financial support.

### Funded Projects

#### German Science Foundation: Excellence Initiative

##### Cluster of Excellence "Nanosystems Initiative Munich"

1. Project Area A: Single Electron and Spin Systems  
R. Gross, S.T.B. Gönnerwein
2. Project Area C: Quantum Information Nanosystems  
R. Gross, A. Marx
3. Project Area F: Nanoanalytics and Enabling Techniques  
B.A. Hermann

#### German Science Foundation: Collaborative Research Centers

##### Collaborative Research Center 631: "Solid-State Quantum Information Processing: Physical Concepts and Materials Aspects"

1. Project A3: *Superconducting Quantum Circuits as Basic Elements for Quantum Information Processing*  
R. Gross, A. Marx
2. Project A8: *Cavity Quantum Electrodynamics with Superconducting Devices*  
A. Marx, R. Gross
3. Project S: *Coordination of the Collaborative Research Center*  
R. Gross

#### German Science Foundation: Research Units

##### Research Unit 538: "Doping Dependence of Phase Transitions and Ordering Phenomena in Cuprate Superconductors"

1. Project: *Single Crystal Growth of p- and n-doped Cuprate Superconductors*  
A. Erb, R. Gross

2. Project: *Raman Studies of Competing Ordering Phenomena in Cuprates*  
R. Hackl, R. Gross
3. Project: *Coordination of the Research Unit*  
R. Hackl

### German Science Foundation: Priority Programs

1. Project: *Novel functional layer structures based on artificial heteroepitaxial multilayers of transition metal oxides*  
within the DFG Priority Program 1157 *Integrated Electroceramic Functional Structures*  
R. Gross (Az. GR 1132/13-1, GR 1132/13-2 und 1132/13-3)
2. Project: *Spin injection, spin transport and controllable ferromagnetism in transition metal doped ZnO*  
within the DFG Priority Program 1157 1285 *Halbleiter-Spinelektronik*  
R. Gross, S.B.T. Gönnerwein, M. Opel (Az. GR 1132/14-1)

### German Science Foundation: Research Projects

1. Development of a very precise rotation sensor based on superfluid  $^3\text{He}$   
E. Schuberth (Az. Schu 450/4-1+2)
2. Effect of pressure, magnetic fields, and crystal quality on the electronic ground states of low-dimensional organic conductors  
W. Biberacher (Az. 436 RUS 113/926/0-1)
3. Local Magnetotransport Properties of Thin Ferromagnetic Layers and Heterostructures  
S.T.B. Gönnerwein (Az. GO 944/3-1)

### European Union

1. European Science Foundation Network "*Thin Films for Novel Oxide Devices: THIOX*"  
R. Gross; coordination by Prof. D. Blank, University of Twente, The Netherlands  
partners: several European Universities and research facilities.
2. Research and Training of Young Researchers on the "*Magnetic Properties of  $^3\text{He}$  by Means of Neutron Diffraction*"  
E. Schuberth; coordination by Dr. Konrad Siemensmeyer, Hahn–Meitner Institute Berlin GmbH  
European Community, Contract No.: HPRN-CT-2000-00166  
Partners: Hahn–Meitner Institut, Berlin, Univ. of Florida, Royal Holloway College, London, Univ. Liverpool, CNRS, Grenoble and Univ. Paris, Saclay.
3. ERA-Chemistry-network: *Hierarchically organized chemical structures: from molecules to hybrid materials*, project: *Probing Hierarchical Self-Assemblies Relevant for Drug and Vaccine Design by Employing STM*  
B.A. Hermann (project number ERA HE 5162/1-1)

4. Marie Curie Network for Initial Training (ITN) "*Cavity-confined Luminophores for Advanced Photonic Materials: A Training Action for Young Researchers*" (FINELUMEN)  
R. Hackl, Grant Agreement Number 215399  
partners: several European Universities and research facilities.
5. COST Action CM0601: *Electron Controlled Chemical Lithography (ECCL)*, project in Working Group 3: *Chemical control by scanning tunneling microscopy*  
B.A. Hermann

### **Alexander von Humboldt Foundation**

1. Humboldt Forschungspreis "Di Castro"  
R. Hackl (Förderkennzeichen IV-ITA/111548 6 GSA)
2. Humboldt Forschungspreis "Zawadowski" (Wiedereinladungsprogramm)  
R. Hackl (Förderkennzeichen 3-3-UNG/1052138)
3. Institutspartnerschaft "Kamaras-Hackl"  
R. Hackl (Förderkennzeichen 3-Fokoop-DEU/1009755)

### **Ministerio de Educacion y Ciencia, Spanien**

1. Intercalación de minerales de la arcilla por medio de tratamiento con ultrasonidos y reacciones de transferencia de electrones. Producción de arcillas funcionalizadas con estructuras complejas jerarquizadas en el espacio interlamilar.  
J.L. Perez-Rodriguez, A. Lerf (Reference No. : MAT2005-04838)

### **International Doctorate Program NanoBioTechnology – IDK-NBT**

1. STM on magnetic layers and self-organized magnetic molecules  
B.A. Hermann, coordination by C. Bräuchle and J. Rädler (IDK-NBT 1506-42501-1)

### **Bavaria California Technology Center (BaCaTeC)**

1. Collaboration on "Materials with coupled order parameter under extreme conditions"  
R. Hackl,  
partners: Profs. T.P. Devereaux, I. Fischer, W.L. Mao

## Conferences and Workshops

The Walther-Meißner-Institute has organized/co-organized the following conferences and workshops in 2008:

1. **Workshop “Properties of Cuprate Superconductors III”**  
November 02 – 07, 2008, Ringberg Castle, Rottach-Egern, Germany.



The workshop was jointly organized by the Max-Planck-Institute for Solid State Research, Stuttgart, and the DFG Research Unit 538 (spokesman: R. Hackl).

2. **International Conference on “Quantum Dynamics in Dots and Junctions: Coherent Solid State Systems”**  
October 05 – 10, 2008, Riva del Garda, Italy.



The conference was jointly supported by the European Science Foundation programme *Arrays of Quantum Dots and Josephson Junctions (AQDDJJ)* and by the Cooperative Research Center 631 on *Solid State Quantum Information Processing* of the German Science Foundation (spokesman: R. Gross).

3. **Course 3 on “Applied Physics and Electronics” of the Ferienakademie 2008**  
September 21 – October 03, 2008, Sarntal, Italy.



The course was held together with Prof. Bertho from the University of Stuttgart within the Ferienakademie, which is organized by the Technische Universität München, the University of Erlangen/Nürnberg, and the University of Stuttgart and takes place in the Italian Alps.

## Collaborations

Other collaborations without direct project funding involve:

- Stanford University, Stanford, USA (Prof. T.P. Devereaux, M. Greven, Z.-X. Shen, I. Fisher)
- Institute for Quantum Computing, University of Waterloo, Waterloo, ON, Canada (Prof. Dr. F.K. Wilhelm)
- Departamento de Química Física, Universidad del País Vasco - Euskal Herriko Unibertsitatea, Bilbao, Spain (Prof. E. Solano)
- NTT Basic Research Laboratories, Japan (Prof. H. Takayanagi, Dr. K. Semba)
- Instituto de Ciencia de Materiales de Sevilla, Spain (Prof. J. Poyato, Prof. J.L. Perez-Rodriguez)
- Research Institute for Solid State Physics and Optics, Hungarian Academy of Sciences, Budapest, Hungary (Prof. K. Kamaras and Prof. I. Tüttö)
- University of Rome "La Sapienza", Rome, Italy (Prof. S. Caprara, Prof. C. Di Castro and Prof. M. Grilli)
- Hungarian Academy of Sciences, Budapest University of Technology and Economics, Budapest, Hungary (Dr. A. Virosztek, Prof. A. Zawadowski, Prof. A. Janossy)
- Central Research Institute of the Electric Power Industry, Tokyo, Japan (Dr. S. Ono and Dr. Y. Ando)
- University of Fribourg (Prof. C. Bernhard)
- University of Basel, Institute of Inorganic Chemistry, Switzerland (Prof. E. Constable, Prof. C. Housecroft)
- University of Basel, Institute of Physics, Switzerland (Prof. H.-J. Güntherodt)
- European Synchrotron Radiation Facility (ESRF), Grenoble (Dr. H. Müller, Dr. J. Criginski Cezar, Dr. D. Mannix)
- LEPES, CNRS, Grenoble (Dr. J. Dumas and Prof. C. Schlenker)
- Materials Science Research Centre, IIT Madras, India (Prof. M.S. Ramachandra Rao)
- Trinity College, Physics Department, Dublin, Ireland (Prof. I.V. Shvets)
- Kungliga Tekniska Högskolan (KTH) Stockholm, Sweden (Dr. G. Vaitheeswaran, Dr. V. Kanchana)
- ETH-Zurich, Switzerland (Prof. P. Seeberger)
- Chalmers University of Technology Gothenburg, Sweden (Prof. P. Delsing)
- Universidad del País Vasco, San Sebastian, Spain (Prof. A. Rubio)
- MINT Center, University of Alabama (Prof. A. Gupta)
- Materials Physics Laboratory, Helsinki University of Technology, Finland (Dr. Tero Heikkilä)
- Department of Condensed Matter Physics, The Weizmann Institute of Science, Israel (Dr. Moshe Schechter)
- Kavli Institute of NanoScience, Delft University of Technology, Delft, The Netherlands (Prof. T.M. Klapwijk)
- Institute for Experimental Physics, Slovakian Academy of Sciences, Kosice (Prof. K. Flachbart)
- High-Magnetic-Field Laboratory, Grenoble, France (Dr. I. Sheikin)

- B. Verkin Institute for Low Temperature Research and Engineering, Kharkov, Ukraine (Prof. V.G. Peschansky)
- Landau Institute for Theoretical Physics, Chernogolovka, Russia (Dr. P. Grigoriev)
- Russian Academy of Sciences, Chernogolovka, Russia (N. Kushch, A. Palnichenko)
- High Magnetic Field Laboratory, Dresden (M. Bartkowiak)
- University of Bonn, Germany (Prof. W. Mader)
- IFW Dresden, Germany (Prof. B. Büchner, Prof. J. Fink, Dr. S.V. Borisenko, Dr. M. Knupfer)
- Max-Planck-Institut für Festkörperforschung, Stuttgart (Prof. B. Keimer)
- University of Tübingen, Germany (Prof. R. Kleiner, Prof. D. Kölle)
- University of Würzburg, Germany (Prof. W. Hanke, Prof. F. Assaad, Prof. C. Honerkamp, Dr. M. Potthoff)
- University of Augsburg, Germany (Dr. S. Kohler, Prof. Dr. P. Hänggi)
- Brandenburgisch-Technische Universität Cottbus, Germany (Prof. D. Schmeißer)
- University of Hamburg, Germany (Dr. G. Meier, Prof. W. Wurth)
- Abt. Halbleiterphysik, University of Ulm, Germany (Dr. W. Limmer)
- RWTH Aachen, Germany (Dr. B. Beschoten)
- Universität Duisburg-Essen, Germany (Dr. A. Ney)
- University of British Columbia, Vancouver, Kanada (Prof. D. Bonn, Prof. A. Damascelli)
- Max-Planck-Institut für Chemische Physik fester Stoffe, Dresden, Germany (Prof. F. Steglich)
- Walter Schottky Institut, TU München, Germany (Prof. G. Abstreiter, Prof. J. Finley, Dr. M. Brandt, Dr. D. Bougeard, Prof. A. Holleitner)
- Ludwig-Maximilians-Universität München, Germany (Prof. J.P. Kotthaus, Prof. J. von Delft, Prof. E. Frey, Prof. T. Franosch, Prof. J. Rädler, Dr. F. Marquardt, Dr. B. Nickel)
- Lehrstuhl E10, Physik Department, TU München, Germany (Prof. D. Grundler)
- Institut für Festkörperforschung, Forschungszentrum Jülich, Germany (Prof. Dr. H. Kohlstedt)
- University of Birmingham, UK (Prof. E.M. Forgan)
- Paul Scherrer Institute, ETH Zürich (Prof. Joel Mesot)
- University of Geneva, Switzerland (Ø. Fischer)
- HMI Berlin, Germany (Dr. A. Buchsteiner, Dr. J. Pieper, Dr. K. Siemensmeyer)
- Royal Holloway University, London UK (Prof. J. Saunders)
- University of Liverpool, UK (Dr. J. Goff)
- CNRS Grenoble, France (Prof. H. Godfrin)
- University of Florida, USA (Prof. D. Adams, Prof. Y. Takano)
- Vericold Technologies, Ismaning, Germany (Dr. J. Höhne, Dr. M. Bühler)
- BMW Group, Munich, Germany (Dr. J. Schnagl)
- Siemens AG, CT MM 2, Munich, Germany (Dr. R. Matz)
- Attocube, Munich, Germany
- Concentris GmbH, Basel, Switzerland
- BASF AG, Mannheim, Germany
- THEVA Dünnschichttechnik, Ismaning, Germany (Dr. W. Prusseit)

## Research visits

Extended visits of members of the Walther-Meißner-Institute at other research laboratories:

1. **Anton Lerf**  
Instituto de Ciencia de Materiales de Sevilla, Spain  
20. 02. – 28. 02. 2008
2. **Bianca Hermann**  
Columbia University, NSEC Nanocenter, New York, USA  
26. 02. – 08. 04. 2008
3. **Bianca Hermann**  
Indian Institute of Technology (IIT) Madras, Chennai, India  
25. 11. – 30. 11. 2008
4. **Anton Lerf**  
Nanotechnology Centre, Technical University of Ostrava, Czech Republic  
01. 09. – 04. 09. 2008
5. **Werner Biberacher, Anton Lerf**  
IPCP, Russian Academy of Sciences, Chernogolovka, Russia  
18. 09. – 23. 09. 2008
6. **Mark Kartsovnik, Toni Helm**  
High Magnetic Field Laboratory Grenoble, France  
22. 06. – 30. 06. 2008
7. **Mark Kartsovnik, Toni Helm**  
Dresden High Magnetic Field Laboratory, Dresden  
19. 10. – 31. 10. 2008
8. **Matthias Opel**  
European Synchrotron Radiation Facility, Grenoble, France  
22. 02. – 29. 02. 2008
9. **Rudolf Hackl**  
MIT Boston, USA  
28. 04. – 01. 05. 2008
10. **Rudolf Hackl**  
Stanford University, Stanford, USA  
04. 05. – 19. 05. 2008
11. **Rudolf Hackl**  
University of British Columbia, Canada  
04. 07. – 08. 07. 2008
12. **Rudolf Hackl**  
University of Alberta, Edmonton, Canada  
10. 07. – 12. 07. 2008



## Conference Talks and Seminar Lectures

### Werner Biberacher

1. **Anisotropy of the superconducting state in  $\alpha$ -(BEDT-TTF)<sub>2</sub>KHg(SCN)<sub>4</sub> under pressure**  
Institute of Problems of Chemical Physics, Chernogolovka, Russia  
22. 09. 2008

### Frank Deppe

1. **Two-photon probe of the Jaynes-Cummings model and controlled symmetry breaking in circuit QED**  
LMU München, Germany  
21. 07. 2008
2. **Symmetry breaking in circuit QED, the quantum switch, and a cross-correlation measurement technique for quantum signals**  
Universität Regensburg, Germany  
12. 11. 2008
3. **Two-photon probe of the Jaynes-Cummings model and controlled symmetry breaking in circuit QED**  
International Workshop on Solid-State Quantum Information, Scuola Normale Superiore, Pisa, Italy  
December 03 – 06, 2008

### Dietrich Einzel

1. **The centennial of helium liquefaction - a century of low temperature physics**  
Frühjahrstagung der DPG, Berlin, Germany  
February 25 – 29, 2008
2. **Theorie der Supraleitung für Experimental-Physiker und Chemiker**  
Lehrstuhl für Chemische Physik und Materialwissenschaften, Universität Augsburg, Germany  
01. 07. 2008
3. **Viscous transport in Fermi superfluids**  
Workshop on Nanoelectronics, Garching, Germany  
September 14 – 18, 2008

### Andreas Erb

1. **Crystal growth and characterization of Cuprate and FeAs based High T<sub>c</sub> superconductors**  
International Workshop on the "Properties of Cuprate Superconductors III", Schloss Ringberg, Rottach-Egern, Germany  
November 03 – 07, 2008

### Sebastian Gönnerwein

1. **Magnetic properties of transition metal-doped semiconductors**  
Seminar des IV. Physikalischen Instituts, Universität Göttingen, Germany  
10. 01. 2008
2. **Magnetization Control in Multifunctional Heterostructures**  
Seminar des Instituts für Halbleiterphysik, Universität Ulm, Germany  
04. 02. 2008
3. **Triplet supercurrent through a half-metallic ferromagnet**  
Workshop on Nanoelectronics, Garching, Germany  
16. 09. 2008

4. **Magnetoelastic magnetization manipulation in ferromagnet/ferroelectric hybrids**  
International Workshop on Nanoferronics, Aachen, Germany  
10. 10. 2008

### Rudolf Gross

1. **Spin Injection, Spin Transport and Controllable Ferromagnetism in Transition Metal Doped ZnO**  
Workshop of the DFG Priority Program 1285 on Semiconductor Spintronics, Hannover, Germany.  
June 06 – 07, 2008
2. **Pulsed Laser Deposition of Complex Oxides: An Ongoing Success Story**  
1<sup>st</sup> European Conference on Pulsed Laser Deposition Process Technology, Hückelhoven, Germany.  
June 11 – 12, 2008
3. **Multifunctional Oxide Heterostructures: From Basic Physics to New Functionalities**  
24. 06. 2008  
Physikalisches Kolloquium, Technische Universität Dresden.
4. **Supraleitung: von schwebenden Zügen und Stromfluss ohne Widerstand**  
Wissenschaftsmeile, Altstadtringfest zum 850. Geburtstag der Landeshauptstadt München, Germany.  
July 19 – 20, 2008
5. **Application of Superconducting Quantum Circuits in Quantum Information Systems**  
International Conference on Superconductivity and Magnetism, Side-Antalya, Turkey.  
August 25–29, 2008
6. **Magnetolectric Multiferroic Oxide Heterostructures: From Basic Physics to New Functionalities**  
International Conference on Superconductivity and Magnetism, Side-Antalya, Turkey.  
August 25–29, 2008
7. **Conference Summary**  
International Conference on Superconductivity and Magnetism, Side-Antalya, Turkey.  
August 25–29, 2008
8. **Solid-State Quantum Systems: From New Regimes in Quantum Optics to Quantum Information Processing**  
Humboldt-Kolleg on “Modern Trends in Mathematics and Physics”, Varna, Bulgaria.  
September 05–10, 2008
9. **Symmetry Makes the Difference: Controlled Symmetry Breaking in Superconducting Circuit QED**  
International Workshop on “Nanostructured Superconductors: From Fundamentals to Applications”, Lauterbad, Germany.  
September 03–17, 2008
10. **Two-photon Probe of the Jaynes-Cummings Model and Controlled Symmetry Breaking in Circuit QED**  
International Conference on “Quantum Dynamics in Dots and Junctions Coherent Solid State Systems”, Riva del Garda, Italy.  
October 05–10, 2008
11. **Faszination Supraleitung – von schwebenden Zügen und Stromfluss ohne Widerstand**  
Evening Lecture at the Gymnasium Raubling, Germany  
27. 11. 2008

## Rudolf Hackl

1. **Single- vs Two-Particle Properties in High Temperature Superconductors**  
Spring Meeting of the German Physical Society, Berlin, Germany  
February 24 – 29, 2008
2. **Search for the pairing glue in High Temperature Superconductors**  
University of Konstanz, Germany  
26. 03. 2008
3. **Energy scales in cuprates: results from Raman scattering**  
MIT, Boston, MA, USA  
30. 04. 2008
4. **Exploring the onset points of superconductivity in the cuprates: ordering, renormalization effects, energies**  
Stanford University, Stanford, USA  
15. 05. 2008
5. **Evolution of electronic interactions in  $\text{La}_{2-x}\text{Sr}_x\text{CuO}_4$**   
International Conference "Stripes 2008", Erice, Italy  
27. 07. - 02.08. 2008
6. **Raman scattering as a probe of (local) electronics, lattice and structural properties**  
Kick-off meeting of the EU project (FINELUMEN), Rimini, Italy  
October 15 – 18, 2008
7. **Evolution of electronic interactions in cuprates below and above half filling**  
International Workshop on the "Properties of Cuprate Superconductors III", Schloss Ringberg, Rottach-Egern, Germany  
November 03 – 07, 2008

## Bianca Hermann

1. **Our Recent Work on Low Dimensional System with Scanning Probe Methods**  
Department of Chemistry, Columbia University, New York, USA  
21. 03. 2008
2. **Attaching Fréchet Dendrons? A Route to Constructing Functional Supramolecular Assemblies on a Graphite Surface**  
Nanocenter NSEC, Columbia University, New York, USA  
02. 04. 2008
3. **Moleküle unter der Lupe - Einblicke in die Nanowelt mit Rastersondentechnik**  
Wissenschaftsmeile, Altstadttringfest zum 850. Geburtstag der Landeshauptstadt München, Germany.  
19. 07. 2008
4. **Self-Organized Molecular Structures and Dynamics Pattern Reorganization Investigated with Scanning Tunneling Microscopy (STM)**  
Conference on Functional Materials, Chennai, India.  
27. 11. 2008

## Elisabeth Hoffmann

1. **Hybrid Rings for Homodyne Detection of Microwave Signals**  
Workshop über Festkörperbasierte Quanteninformationsverarbeitung, Wildschönau, Austria  
31. 05. 2008
2. **Two-Resonator Circuit QED: a Superconducting Quantum Switch**  
International Workshop on Solid-State Quantum Information, Scuola Normale Superiore, Pisa, Italy  
December 03 – 06, 2008

### Mark Kartsovnik

1. **Magnetic field induced charge-density-wave transitions in an organic conductor: role of orbital and Pauli effects**  
International Workshop on Electronic Crystals, ECRYS-2008, Cargèse, Corsica  
August 24 – 30, 2008

### Anton Lerf

1. **Graphite oxide: an old, but still fascinating story**  
Nanotechnology Centre, Technical University of Ostrava, Czech Republic  
September 01 – 04, 2008
2. **Graphite oxide: an old, but still fascinating story**  
IPCP, Russian Academy of Sciences, Chernogolovka, Russia  
September 18 – 23, 2008

### Matteo Mariani

1. **Playing with the microwave vacuum**  
University of Augsburg, Germany  
20. 11. 2008
2. **Playing with the microwave vacuum**  
CEA Saclay, Paris, France  
11. 12. 2008
3. **Playing with the microwave vacuum**  
ENS, Paris, France  
12. 12. 2008

### Achim Marx

1. **Two-photon probe of the Jaynes-Cummings model and controlled symmetry breaking in circuit QED**  
Kryoelektronische Bauelemente 2008, Königslutter, Braunschweig, Germany  
October 06 – 08, 2008

### Edwin Menzel

1. **High Frequency Aspects of Experiments at the WMI**  
CoC Microwave Development and Production Microelectronics, Rohde & Schwarz GmbH, Germany  
01. 08. 2008

### Matthias Opel

1. **Spintronics**  
Lüscher Lectures - Magnetismus, Dillingen, Germany  
17. 10. 2008
2. **Ferromagnetism or magnetic clusters in cobalt-doped ZnO**  
Joint European Magnetic Symposia, Trinity College, Dublin, Ireland  
17. 09. 2008
3. **Ferromagnetism or magnetic clusters in cobalt-doped ZnO**  
Kristallographisches Kolloquium, LMU München, Germany  
20. 06. 2008

**4. Nanosized Superparamagnetic Precipitates in Cobalt-Doped ZnO Thin Films**

THIOX Meeting on Advances and New Challenges in Oxide Electronics, Convento dell'Annunziata, Sestri Levante, Italy  
10. 04. 2008

**Erwin Schubert****1. Magnetization measurements on  $\text{YbRh}_2\text{Si}_2$  at very low temperatures**

Max-Planck-Institut für Chemische Physik fester Stoffe, Dresden, Germany  
April 10 and June 06, 2008

**Leonardo Tassini****1. Ordering versus Superconductivity in High-Tc Superconductors**

Spring Meeting of the German Physical Society, Berlin, Germany  
February 24 – 29, 2008

**2. Spontaneous formation of 1D charge structures in a 2D electron gas**

Szeged International Workshop on Advances in Nanoscience (SIWAN), Szeged, Hungary  
October 08 – 11, 2008

**Kurt Uhlig****1. Dilution Refrigerator with Direct Pulse Tube Precooling**

15<sup>th</sup> International Cryocooler Conference, Long Beach, California, USA  
10. 06. 2008

**2. Cryogen-free Dilution Refrigerators**

Ultralow Temperature Conference, ULT2008, London, UK  
15. 08. 2008



## Lectures, Seminars, Courses and other Scientific Activities

### Lectures

#### A: Technical University of Munich

##### Dietrich Einzel

- WS 2007/2008
- Mathematische Methoden der Physik I (Mathematical Methods of Physics I)
  - Übungen zu Mathematische Methoden der Physik I (Mathematical Methods of Physics I, Problem Sessions)
  - WMI-Seminar über aktuelle Fragen der Tieftemperatur-Festkörperphysik (WMI Seminar on Current Topics of Low Temperature Solid State Physics, with R. Gross, S.B.T. Gönnerwein, A. Marx, M. Opel, R. Hackl)
- SS 2008
- Mathematische Methoden der Physik II (Mathematical Methods of Physics II)
  - Übungen zu Mathematische Methoden der Physik II (Mathematical Methods of Physics II, Problem Sessions)
  - Theorie der Supraleitung (Theory of Superconductivity)
  - WMI-Seminar über aktuelle Fragen der Tieftemperatur-Festkörperphysik (WMI Seminar on Current Topics of Low Temperature Solid-State Physics, with R. Gross, S.B.T. Gönnerwein, A. Marx, M. Opel, R. Hackl)
- WS 2008/2009
- Mathematische Methoden der Physik I (Mathematical Methods of Physics I)
  - Übungen zu Mathematische Methoden der Physik I (Mathematical Methods of Physics I, Problem Sessions)
  - WMI-Seminar über aktuelle Fragen der Tieftemperatur-Festkörperphysik (WMI Seminar on Current Topics of Low Temperature Solid-State Physics, with R. Gross, S.B.T. Gönnerwein, A. Marx, M. Opel, R. Hackl)

##### Rudolf Gross

- WS 2007/2008
- Angewandte Supraleitung (Applied Superconductivity, with A. Marx)
  - Festkörperkolloquium (Colloquium on Solid-State Physics, with D. Einzel)
  - WMI-Seminar über aktuelle Fragen der Tieftemperatur-Festkörperphysik (WMI Seminar on Current Topics of Low Temperature Solid State Physics, with D. Einzel, S.B.T. Gönnerwein, A. Marx, M. Opel, R. Hackl)
  - Seminar on Advances in Solid-State Physics (with M. Opel, A. Marx, S.T.B. Gönnerwein)

- SS 2008
- Supraleitung und Tieftemperaturphysik II (Superconductivity and Low Temperature Physics II)
  - Proseminar Physik/Technik: Makroskopische Quantenphänomene (Introductory Seminar Course Engineering/Physics: Macroscopic Quantum Phenomena, with S.T.B. Gönnerwein, A. Marx, R. Hackl)
  - Seminar on Advances in Solid-State Physics (with M. Opel, A. Marx, S.T.B. Gönnerwein)
  - Festkörperkolloquium (Colloquium on Solid-State Physics, with D. Einzel)
  - WMI-Seminar über aktuelle Fragen der Tieftemperatur-Festkörperphysik (WMI Seminar on Current Topics of Low Temperature Solid-State Physics, with D. Einzel, S.B.T. Gönnerwein, A. Marx, M. Opel, R. Hackl)
- WS 2008/2009
- Einführung in die Festkörperphysik (Introduction to Solid-State Physics)
  - Tutorium zur Einführung in die Festkörperphysik (Introduction to Solid-State Physics, Tutorium)
  - Übungen zur Einführung in die Festkörperphysik (Introduction to Solid-State Physics, Problem Sessions, with D. Einzel)
  - Angewandte Supraleitung (Applied Superconductivity, with A. Marx)
  - WMI-Seminar über aktuelle Fragen der Tieftemperatur-Festkörperphysik (WMI Seminar on Current Topics of Low Temperature Solid-State Physics, with D. Einzel, S.B.T. Gönnerwein, A. Marx, M. Opel, R. Hackl)
  - Seminar on Advances in Solid-State Physics (with M. Opel, A. Marx, S.T.B. Gönnerwein)
  - Festkörperkolloquium (Colloquium on Solid-State Physics, with D. Einzel)

### Sebastian T.B. Gönnerwein

- WS 2007/2008
- Magnetismus (Magnetism)
  - Seminar on Advances in Solid-State Physics (with R. Gross, A. Marx, M. Opel)
  - WMI-Seminar über aktuelle Fragen der Tieftemperatur-Festkörperphysik (WMI Seminar on Current Topics of Low Temperature Solid-State Physics, with R. Gross, D. Einzel, A. Marx, M. Opel, R. Hackl)
  - Seminar zu aktuellen Fragen der Magneto- und Spinelektronik (Seminar on Current Topics in Magneto and Spin Electronics, with M. Brandt, M. Opel)
- SS 2008
- Spinelektronik (Spin Electronics)
  - Seminar on Advances in Solid-State Physics (with R. Gross, A. Marx, M. Opel)
  - WMI-Seminar über aktuelle Fragen der Tieftemperatur-Festkörperphysik (WMI Seminar on Current Topics of Low Temperature Solid-State Physics, with R. Gross, D. Einzel, A. Marx, M. Opel, R. Hackl)

- Seminar zu aktuellen Fragen der Magneto- und Spinelektronik (Seminar on Current Topics in Magneto and Spin Electronics, with M. Brandt, M. Opel)
  - Proseminar Physik/Technik: Makroskopische Quantenphänomene (Introductory Seminar Course Engineering/Physics: Macroscopic Quantum Phenomena, with R. Gross, A. Marx, R. Hackl)
- WS 2008/2009
- Magnetismus (Magnetism)
  - WMI-Seminar über aktuelle Fragen der Tieftemperatur-Festkörperphysik (WMI Seminar on Current Topics of Low Temperature Solid State Physics, with R. Gross, D. Einzel, A. Marx, M. Opel, R. Hackl)
  - Seminar zu aktuellen Fragen der Magneto- und Spinelektronik (Seminar on Current Topics in Magneto and Spin Electronics, with M. Brandt, M. Opel)
  - Seminar on Advances in Solid-State Physics (with R. Gross, A. Marx, M. Opel)

### Rudi Hackl

- WS 2007/2008
- Supraleitung und Tieftemperaturphysik I (Superconductivity and Low Temperature Physics I)
  - WMI-Seminar über aktuelle Fragen der Tieftemperatur-Festkörperphysik (WMI Seminar on Current Topics of Low Temperature Solid-State Physics, with R. Gross, S.B.T. Gönnerwein, A. Marx, M. Opel, D. Einzel)
- SS 2008
- WMI-Seminar über aktuelle Fragen der Tieftemperatur-Festkörperphysik (WMI Seminar on Current Topics of Low Temperature Solid-State Physics, with R. Gross, S.B.T. Gönnerwein, A. Marx, M. Opel, D. Einzel)
  - Proseminar Physik/Technik: Makroskopische Quantenphänomene (Introductory Seminar Course Engineering/Physics: Macroscopic Quantum Phenomena, with R. Gross, S.B.T. Gönnerwein, A. Marx)
- WS 2008/2009
- Supraleitung und Tieftemperaturphysik I (Superconductivity and Low Temperature Physics I, with E. Schuberth)
  - WMI-Seminar über aktuelle Fragen der Tieftemperatur-Festkörperphysik (WMI Seminar on Current Topics of Low Temperature Solid-State Physics, with R. Gross, S.B.T. Gönnerwein, A. Marx, M. Opel, D. Einzel)
  - Seminar zu den Grundlagen der Supraleitung (Seminar on Foundations of Superconductivity, with C. Pfeleiderer)

### Anton Lerf

- WS 2007/2008
- Moderne Aspekte der Chemie für Physiker I (Modern Aspects of Chemistry for Physicists I)

- |              |  |
|--------------|--|
| SS 2008      | <ul style="list-style-type: none"> <li>• Moderne Aspekte der Chemie für Physiker I (Modern Aspects of Chemistry for Physicists I)</li> <li>• Nanostrukturierte Materie (Nanostructured Matter)</li> <li>• Heterogene Katalyse-Präparative Aspekte (Heterogenous Catalysis: Preparative Aspects, zusammen mit Prof. K. Köhler)</li> </ul>                             |
| WS 2008/2009 | <ul style="list-style-type: none"> <li>• Moderne Aspekte der Chemie für Physiker I (Modern Aspects of Chemistry for Physicists I)</li> <li>• Anorganisch chemische Technologie II: Festkörper (Inorganic Chemical Technology: Solid Materials)</li> <li>• Stoffströme in Natur und Technik (Material Flow in Nature and Technology, with Prof. K. Köhler)</li> </ul> |

### Erwin Schubert

- |              |  |
|--------------|--|
| WS 2007/2008 | <ul style="list-style-type: none"> <li>• Höhere Physik I (Advanced Physics I)</li> <li>• Übungen zur Höheren Physik I (Exercises to Advanced Physics I)</li> </ul>     |
| SS 2008      | <ul style="list-style-type: none"> <li>• Höhere Physik II (Advanced Physics II)</li> <li>• Übungen zur Höheren Physik II (Exercises to Advanced Physics II)</li> </ul> |
| WS 2008/2009 | <ul style="list-style-type: none"> <li>• Supraleitung und Tieftemperaturphysik I (Superconductivity and Low Temperature Physics I, with R. Hackl)</li> </ul>           |

## B: Ludwig-Maximilians University of Munich

### Bianca Hermann

- |              |   |
|--------------|---|
| WS 2007/2008 | <ul style="list-style-type: none"> <li>• Seminar über die aktuelle Literatur im Bereich Supraleitung und Selbst-Organisierende Moleküle</li> </ul>  |
| SS 2008      | <ul style="list-style-type: none"> <li>• Seminar über spezielle Fragen der Rastertunnelmikroskopie</li> <li>• Moderne Rastersondenmikroskopie- und Spektroskopietechniken</li> <li>• Seminar über die aktuelle Literatur zu korrelierten Phänomenen insbesondere der molekularen Selbstorganisation und der Supraleitung</li> <li>• Seminar über spezielle Fragen der Rastertunnelmikroskopie</li> </ul>                                |
| WS 2008/2009 | <ul style="list-style-type: none"> <li>• PNI: Einführung in die Physik (für Chemie- und Biochemiestudierende)</li> <li>• Übungen zu PNI: Einführung in die Physik (für Chemie- und Biochemiestudierende)</li> <li>• Seminar über die aktuelle Literatur zu korrelierten Phänomenen insbesondere der molekularen Selbstorganisation und der Supraleitung</li> <li>• Seminar über spezielle Fragen der Rastertunnelmikroskopie</li> </ul> |

## The WMI Seminars

### The Friday Seminar –

### Walther-Meißner-Seminar on Current Topics in Low Temperature Physics

- 1. Modulation of functional molecular nanostructures and construction of molecular electronic devices**  
Dr. Haiming Guo, Institute of Physics, Chinese Academy of Sciences, China.  
01. 02. 2008
- 2. New synthesis schemes for functional materials, interfaces and heterostructures**  
Dr. Gennady Logvenov, Brookhaven National Laboratory, Upton, USA.  
04. 04. 2008
- 3. Internal Stress in Solid Materials and the Glassy State**  
Prof. Dr. Klaus Andres  
18. 04. 2008
- 4. Polarization Control in Optical Fibers and Long Distance Atom Photon Entanglement**  
Dipl.-Phys. Fredrik Hocke, Sektion Physik, LMU München.  
22. 04. 2008
- 5. Magnetic flux dynamics in  $O$ ,  $\pi$  and  $O$ - $\pi$  SIFS Josephson junctions**  
Dipl.-Phys. Judith Pfeiffer, Physikalisches Institut, Universität Tübingen.  
25. 04. 2008
- 6. Upper critical field and other properties of superconductivity, appearing on the density wave background**  
Dr. Pavel D. Grigoriev, Landau Institute, Russia.  
09. 05. 2008
- 7. Experiments on Superconducting Josephson Phase Quantum Bits**  
Dr. Jürgen Lisenfeld, Physikalisches Institut, Universität Erlangen-Nürnberg.  
16. 05. 2008
- 8. Dynamics in superconductors excited by femtosecond optical pulses**  
Prof. Dr. Jure Demsar, Fachbereich Physik, Universität Konstanz.  
30. 05. 2008
- 9. Landau-Zener transitions of a qubit: From state preparation to monitoring the dynamics**  
Dr. Sigmund Kohler, Institut für Physik, Universität Augsburg.  
13. 06. 2008
- 10. Vibrational properties of glasses with different annealing histories: relationship between characteristic length scales and low-frequency Raman spectra**  
Dr. Giovanna Giulia Simeoni, Department of Physics, Universita di Roma La Sapienza, Italy.  
20. 06. 2008
- 11. Two-dimensional magnetism in the organic Mott insulator  $\kappa$ - $\text{ET}_2\text{Cu}[\text{N}(\text{CN})_2]\text{Cl}$**   
Prof. A. Janossy, Budapest University of Technology, Budapest, Hungary.  
25. 06. 2008
- 12. Electrical triggering of phase-coherent spin packets by pulsed electrical spin injection across a Fe/GaAs Schottky barrier**  
Dr. Bernd Beschoten, Physikalisches Institut, RWTH Aachen.  
27. 06. 2008
- 13. Optomechanics**  
Dr. Florian Marquardt, Sektion Physik, LMU München.  
27. 06. 2008
- 14. Functional properties of oxide based materials and nanostructures**  
Prof. M.S. Ramachandra Rao, Indian Institute of Technology Madras, India.  
04. 07. 2008
- 15. Growth, characterization, and functionalization of multiferroic  $\text{BiFeO}_3$  epitaxial thin films**  
Dr. Helene Béa, Université de Genève.  
11. 07. 2008
- 16. (Ga,Mn)As auf hochindizierten Substraten**  
Lukas Dreher, Institut für Halbleiterphysik, Universität Ulm.

18. 07. 2008
17. **Multi-bit Storage in Phase Change Memory**  
Dr. Jan-Boris Philipp, Qimonda.  
25. 07. 2008
18. **Entwicklung und Produktion von YIG (Yttrium-Eisen-Granat)-Filter für Mikrowellen Spektrumanalysatoren**  
Dr. Gerd Hechtfisher, Rohde & Schwarz.  
25. 07. 2008
19. **Wiedemann-Franz violation at a quantum-critical point: reports of quasiparticle's death may be exaggerated!**  
Dr. Michael Smith, University of Queensland, Australia.  
05. 11. 2008
20. **Transport properties of new organic superconductors  $\kappa'$ -(BEDT-TTF)<sub>2</sub>Cu[N(CN)<sub>2</sub>]X, where X = Cl, Br**  
Prof. Vladimir Zverev, Russian Academy of Sciences, Chernogolovka.  
07. 11. 2008
21. **Interplay of thermomagnetic and nonequilibrium effects in nonlocal vortex transport in mesoscopic NbGe channels**  
Dipl.-Phys. Florian Otto, University of Regensburg.  
14. 11. 2008
22. **Cavity optomechanics at low temperatures**  
Dr. René Rivière, Max-Planck-Institut für Quantenoptik, Garching.  
14. 11. 2008
23. **Manipulating spins by light and current: what is our insight on Terahertz (THz) to Gigahertz (GHz) frequency scale?**  
Prof. Dr. Markus Münzenberg, Physikalisches Institut, Georg-August-Universität Göttingen.  
21. 11. 2008
24. **Domain wall dynamics and magneto-transport in (Ga, Mn)As epilayers**  
Dr. Jan Honolka, Max-Planck-Institut für Festkörperforschung, Stuttgart.  
28. 11. 2008
25. **Superconductivity and crystal chemistry of iron arsenides**  
Prof. Dr. Dirk Johrendt, Ludwig-Maximilians-Universität München.  
05. 12. 2008
26. **Cobalt-doped ZnO epitaxial films: from an ideal Brillouin-like paramagnet to a phase-separated superparamagnetic ensemble**  
Dr. Verena Ney, Fachbereich Physik, Universität Duisburg-Essen.  
12. 12. 2008

### Topical Seminar on Advances in Solid State Physics – WS 2007/2008, SS 2008 and WS 2008/2009

- Introduction and Presentation of Seminar Topics for WS 2007/2008**  
Prof. Rudolf Gross, WMI.  
16. 10. 2007
- Charakterisierung von Nanolöchern und deren Befüllung mit Metallen**  
Marc Saitner, Universität Ulm.  
06. 11. 2007
- Josephson-Kontakte mit ferromagnetischen Barrieren: Magnetfeldabhängigkeit des Josephson-Stromes und Fiske-Resonanzen**  
Georg Wild, WMI.  
13. 11. 2007
- Kopplung von Festkörper-Quantenbits an Resonatoren: Quantenelektrodynamik mit Festkörperschaltkreisen**  
Elisabeth Hoffmann, WMI.  
20. 11. 2007

5. **Tunneln zwischen Supraleitern und Ferromagneten – physikalische Grundlagen und Messung der Spinpolarisation**  
Franz Czeschka, WMI.  
27. 11. 2007
6. **Der Riesenmagnetwiderstand – Nobelpreis für Physik 2007**  
Timo Buttler, TU-München.  
04. 12. 2007
7. **Supraleitende Quantenbits: Typen, Funktionsweise und Kopplung**  
Andreas Baust, TU-München.  
11. 12. 2007
8. **Lasing mit künstlichen supraleitenden Atomen**  
Prof. Rudolf Gross, WMI.  
08. 01. 2008
9. **Untersuchung von  $\text{La}_{2-x}\text{Sr}_x\text{CuO}_4$  und  $\text{RE}_{2-x}\text{Ce}_x\text{CuO}_4$  (RE=Nd, Pr) nahe des Einsatzpunktes der Supraleitung bei hoher Dotierung**  
Bernhard Muschler, WMI.  
15. 01. 2008
10. **Untersuchung von Y-123 in der Umgebung des Einsatzpunktes der Supraleitung**  
Nathalie Munnikes, WMI.  
22. 01. 2008
11. **Introduction, presentation of seminar topics for SS 2008, and assignment of topics to interested students**  
Rudolf Gross, WMI.  
15. 04. 2008
12. **High  $T_c$  Superconductivity in the New Quaternary REOFeAs Compounds**  
Andreas Erb, WMI.  
22. 04. 2008
13. **Mesoscopic Shelving Readout of Superconducting Qubits in Circuit QED**  
Barbara Englert, WMI.  
29. 04. 2008
14. **Preparation and characterization of thin films of  $\text{Fe}_{3-x}\text{Zn}_x\text{O}_4$**   
Deepak Venkateshvaran, Indian Institute of Technology Madras, India.  
20. 05. 2008
15. **Untersuchung von Ladungs- und Spinüberstrukturen in gering dotierten  $\text{CuO}_2$ -Verbindungen**  
Hans-Martin Eiter, WMI.  
27. 05. 2008
16. **80 Jahre Chandra**  
Dietrich Einzel, WMI.  
03. 06. 2008
17. **Dielektrische und magnetische Eigenschaften multifunktionaler Dünnschichtstrukturen**  
Daniel Pantel, WMI.  
10. 06. 2008
18. **A setup for quantum signal detection in a circuit QED architecture**  
Miquel Àngel Araque Caballero, WMI.  
17. 06. 2008
19. **Magneto-optischer Kerr-Effekt in magnetischen dünnen Filmen**  
Matthias Pelkner  
01. 07. 2008, WMI.
20. **Time Domain Measurements of Superconducting Flux Quantum Bits**  
Edwin Menzel, WMI.  
08. 07. 2008
21. **Aufbau eines Messplatzes zur ferromagnetischen Resonanz**  
Manuel Schwarz, WMI.  
15. 07. 2008

22. **Optical probe of carrier doping effect by X-ray irradiation in organic dimer-Mott insulator**  
Prof. Dr. T. Sasaki, Tohoku University, Japan.  
05. 08. 2008
  
23. **Introduction, presentation of seminar topics for WS 2008/2009, and assignment of topics to interested students**  
Rudolf Gross, WMI.  
14. 10. 2008
24. **Magnetisierungsmessungen an dem Schwere-Fermionen-System  $\text{YbRh}_2\text{Si}_2$  bei ultratiefen Temperaturen**  
Marc Tippmann, WMI.  
28. 10. 2008
25. **Two-Resonator Circuit QED: A Superconducting Quantum Switch**  
Elisabeth Hoffmann, WMI.  
04. 11. 2008
26. **Superconducting Quantum Circuits: Building Blocks for cQED experiments**  
Thomas Niemczyk, WMI.  
11. 11. 2008
27. **Playing with the Microwave Vacuum and Measuring its Covariance Matrix**  
Matteo Mariani, WMI.  
18. 11. 2008
28. **Kuprate beim Einsatzpunkt der Supraleitung**  
Bernhard Muschler, WMI.  
25. 11. 2008
29. **Spintronics based on the wide bandgap semiconductor zinc oxide**  
Matthias Althammer, WMI.  
09. 12. 2008
30. **Die neuen FeAs-Supraleiter: Experimenteller Status und Stand der Forschung**  
Reinhard Roßner, TU München.  
16. 12. 2008
31. **Materialien mit negativem Brechungsindex**  
Christian Siebenwirth, TU München.  
13. 01. 2009
32. **Erzeugung von Mikrowellen-Fock-Zuständen mit supraleitenden Quantenschaltkreisen**  
Christian Heeg, TU München.  
20. 01. 2009
33. **Der Spin-Hall-Effekt**  
Alexander Krupp, TU München.  
27. 01. 2009
34. **Surface acoustic waves at piezoelectric/ferromagnetic interfaces**  
Mathias Weiler, WMI.  
03. 02. 2009
35. **Quantenexperimente mit elektromagnetischen Systemen**  
Fredrik Hocke, WMI.  
10. 02. 2009

### C: Solid State Colloquium

The WMI has organized the Solid-State Colloquium of the Faculty of Physics in WS 2007/2008, SS 2008, and WS 2008/2009. The detailed program can be found on the WMI webpage: <http://www.wmi.badw-muenchen.de/teaching/Seminars/fkkoll.html>

## Staff of the Walther-Meißner-Institute

### Director

Prof. Dr. Rudolf Gross

### Deputy Director

Dr. Werner Biberacher

### Technical Director

Dr. Achim Marx

### Head of the Scanning Probe Division

Prof. Dr. Bianca Hermann

### Administration/Secretary's Office

Tina Pinkert

Ludwig Ossiander

Emel Dönertas

### Scientific Staff

Dr. Werner Biberacher

Dr. habil. Dietrich Einzel

PD Dr. habil. Andreas Erb

Dr. Sebastian Gönnewein

Dr. habil. Rudolf Hackl

Dr. Mark Kartsovnik

Prof. Dr. Anton Lerf

Dr. Achim Marx

Dr. Matthias Opel

Prof. Dr. Erwin Schubert

Dr. Leonardo Tassini

Dr. Kurt Uhlig

Dipl.-Phys. Matthias Althammer

Dipl.-Phys. Andreas Brandlmaier

Dipl.-Phys. Franz Czeschka

Dipl.-Phys. Frank Deppe

Dipl.-Phys. Hans-Martin Eiter

Dipl.-Phys. Stephan Geprägs

Dipl.-Phys. Fredrik Hocke

Dipl.-Phys. Elisabeth Hoffmann

Dipl.-Phys. Matthias Kath

Dipl.-Phys. Michael Lambacher

Dipl.-Phys. Matteo Mariani

Dipl.-Phys. Edwin Menzel

Dipl.-Phys. Bernhard Muschler

Dipl.-Phys. Andrea Nielsen

Dipl.-Phys. Thomas Niemczyk

Dipl.-Phys. Wolfgang Prestel

Dipl.-Phys. Deepak Venkateshvaran

Dipl.-Phys. Mathias Weiler

Dipl.-Phys. Georg Wild

### Technical Staff

Peter Binkert

Dipl.-Ing. (FH) Thomas Brenninger

Joachim Geismann (until 31.10.2008)

Dipl.-Ing. (FH) Ulrich Guggenberger

Dieter Guratzsch

Astrid Habel

Karen Helm-Knapp

Dipl.-Ing. (FH) Josef Höss

Julius Klaus

Jean-Claude Kremer

Robert Müller

Jan Naundorf

Georg Nitschke

Christian Reichlmeier

Harald Schwaiger

Helmut Thies

Siegfried Wanninger

**Assistants**

Sybilla Plöderl

Brigitte Steinberg

**Permanent Guests**

Prof. Dr. B. S. Chandrasekhar

Dr. Robert Doll

Dr. Karl Neumaier

Dr. Christian Probst

Prof. Dr. Robert Schöllhorn

## Guest Researchers

1. Prof. Dr. B.S. Chandrasekhar  
permanent guest
2. Dr. Robert Doll  
permanent guest
3. Dr. Karl Neumaier  
permanent guest
4. Dr. Christian Probst  
permanent guest
5. Prof. Dr. Robert Schöllhorn  
permanent guest
6. Deepak Venkateshvaran, Materials Science Research Centre IIT Madras, Chennai, India  
01. 10. 2007 - 31. 05. 2008
7. H. Guo, Chinese Academy of Science, Nanophysics and Devices, Beijing, China  
15. 12. 2007 - 30. 04. 2008
8. Prof. Dr. Jose-Luis Pérez-Rodríguez, Instituto de Ciencia de Materiales de Sevilla, Spain  
11. 01. - 15. 01. 2008
9. Dr. Pavel Grigoriev, Landau Institute, Chernogolovka, Russia  
06. 05. - 10. 05. 2008, 13. 07. - 16. 07. 2008
10. Prof. Dr. I. Tüttö, Research Institute for Solid State Physics and Optics, Hungarian Academy of Sciences Budapest, Hungary  
09. 06. - 22. 06. 2008, 10. 08. - 17. 08. 2008
11. J. Koeser, Concentris GmbH, Basel, Switzerland  
23. 06. - 27. 06. 2008
12. Prof. A. Jánossy, Budapest University of Technology and Economics, Budapest, Hungary  
23. 06. - 25. 06. 2008
13. Prof. Dr. M.S. Ramachandra Rao, Materials Science Research Centre, IIT Madras, Chennai, India  
26. 06. - 06. 07. 2008
14. Prof. Dr. Juan Poyato Ferrera, Instituto de Ciencia de Materiales, Sevilla, Spain  
19. 07. - 14. 08. 2008
15. Prof. Valentin Peschansky, B.I. Verkin Institute, Kharkov, Ukraine  
01. 08. - 06. 08. 2008
16. Prof. Alfred Zawadowski, Budapest University of Technology and Economics, Budapest, Ungarn  
10. 08. - 17. 08. 2008
17. Michaela Lavagnini, ETH, Zürich  
05. 08. - 16. 08. 2008, 24. 11. - 05. 12. 2008
18. Prof. T. Sasaki, Tohoku University, Japan  
03. 08. - 06. 08. 2008

19. Prof. Vladimir Zverev, Institute of Solid Physics, Chernogolovka, Russia  
29. 09. - 29. 11. 2008
20. Prof. Jeevak M. Parpia, LASSP, Cornell University, Ithaca, USA  
06. 10. - 10. 10. 2008
21. Dr. Michael Smith, Queensland University, Brisbane, Australia  
03. 11. 05. 11. 2008

## Commission for Low Temperature Physics

Members of the Commission for Low Temperature Research of the Bavarian Academy of Sciences and Humanities:

Kaiser, Wolfgang, Leiter (Technische Universität München)  
Abstreiter, Gerhard, stellv. Leiter (Technische Universität München)  
Gross, Rudolf (Walther-Meißner-Institut)  
Landwehr, Gottfried (Universität Würzburg)  
Hänsch, Theodor (Max-Planck-Institut für Quantenoptik, Garching)  
Kotthaus, Jörg Peter (Ludwig-Maximilians-Universität München)  
Schwoerer, Markus (Universität Bayreuth)  
Vollhardt, Dieter (Universität Augsburg)  
Weiss, Dieter (Universität Regensburg)